Bending Behavior of Thick-Walled Composite Tubes

Mohamed Ibrahim El-Geuchy

A thesis

In the Department

Of

Mechanical and Industrial Engineering

Presented in Partial Fulfillment of the Requirements

For the Degree of

Doctor of Philosophy (Mechanical Engineering) at

Concordia University

Montreal, Quebec, Canada

April 2013

CONCORDIA UNIVERSITY
SCHOOL OF GRADUATE STUDIES

This is to certify that the thesis prepared

By: Mohamed Ibrahim El-Geuchy

Entitled: Bending Behavior of Thick-Walled Composite Tubes

and submitted in partial fulfillment of the requirements for the degree of

DOCTOR OF PHILOSOPHY (Mechanical Engineering)

complies with the regulations of the University and meets the accepted standards with respect to originality and quality.

Signed by the final examining committee:

_____ Chair
Dr. A.G. Aghdam

_____ External Examiner
Dr. C. Poon

_____ External to Program.
Dr. M. Nokken

_____ Examiner
Dr. M. Pugh

_____ Examiner
Dr. R. Sedaghati

_____ Thesis Supervisor
Dr. S.V. Hoa

Approved by _____
Dr. A. Dolatabadi, Graduate Program Director

April 19, 2013

_____
Dr. Robin A.L. Drew, Dean
Faculty of Engineering & Computer Science

AUTHOR'S DECLARATION

I hereby declare that I am the sole author of this thesis. This is a true copy of the thesis, including any required final revisions, as accepted by my examiners.

I understand that my thesis may be made electronically available to the public.

Abstract

Bending Behavior of Thick-Walled Composite Tubes

Mohamed Ibrahim El-Geuchy, Ph.D.

Concordia University, 2013

This research presents the bending behavior of thick-walled composite tubes addressing the bending stiffness property theoretically and experimentally, and investigating the failure behavior experimentally. A theoretical formulation, based on 3D elasticity theory, is adopted for calculating the bending stiffness. An interesting bending stiffness behavior is brought up for thick-walled composite tubes made of two thick layers of [θ/-θ] stacking sequence. It is found that the bending stiffness value is decreasing when the wall thickness exceeds a specific value, for tubes have equal layers thickness and constant outer diameter (D_o). A new parameter is defined from the used bending stiffness formulation, for each layer in the composite tube, denoted as "$E_{eff,n}$", the effective extensional stiffness of the composite layer "n". This new parameter represents the layer mechanical properties contribution in its bending stiffness, involving the effects of layer geometry and its interaction with adjacent layers in the tube. A novel parametric study is carried out using "$E_{eff,n}$" and it is found that the interaction effect improves highly the bending stiffness property. The responsible layer properties that control the interaction effect are specified and the improvement mechanism for the bending stiffness property is explained. Also the effective layer geometric parameters are specified and their role in the discovered bending stiffness behavior is investigated.

Making use of the obtained results, the bending stiffness of a tube made of two thick layers of equal thickness and [θ/-θ] stacking sequence is compared to another tube made of repeated units of [θ/-θ] stacking sequence within the tube wall thickness "Multi-sublaminates configuration". It is found that the second tube has higher bending stiffness value, noting that the two tubes have the same geometry

and made of the same composite material. This is because the configuration of the second tube permits higher interaction effect between tube layers and cancels the negative effect of geometric parameters. According to that a simple and accurate equation is derived for designing the bending stiffness of multi-sublaminates composite tubes including only the interaction effects.

In order to validate the superiority of the bending stiffness of multi-sublaminates composite tubes over tubes made of one sublaminate of thick layers, two thick-walled thermoplastic composite tubes are manufactured using automated fiber placement technique (AFP) and tested using a pure bending test setup. For the manufacturing process, a study is carried out to specify the process parameters for an AFP-made thermoplastic composite tube with acceptable quality. It is found that increasing the number of compaction passes improves the intimate contact between the composite layers and reduces the voids content. For the testing process, an adaptor ring is designed to permit fixing of the manufactured specimen in the pure bending test setup and to allow smooth conveying for the pure bending loading to the tested specimen. The pure bending test setup is shown to be a superior alternative test compared to the conventional 3-point and 4-point bending tests in testing composite tubes. The experimental results validate the obtained theoretical values and the used bending stiffness formulas.

Lastly, the failure behavior of multi-sublaminates thick-walled composite tube is investigated according to the bending test results. The mode of failure of the tube under bending is due to delamination of the outer layers. Also, it is found that thick-walled composite tubes failed safely compared to thin-walled composite tubes.

Acknowledgements

First of all, greatest thanks to **Our Creator,** glory is to him, we have no knowledge except whatever he have taught us. He is the all-knowing, the all wise.

I would like to express my deepest sense of gratitude and thanks to my supervisor Dr. Suong V. Hoa, for his guidance, generous advice, criticism, continuous encouragement and support throughout this research. I have learned a lot from his morals, ethics, humbleness and sense of humor besides being among one of the best scholars in composites. I am really admiring him so much.

I also would like to thank my examination committee members, Dr. Cheung Poon, Dr. Martin Pugh, Dr. Ramin Sedaghati, and Dr. Michelle Nokken for their support and helpful comments.

Special thanks to the Egyptian government that financially supported my program, giving me this golden opportunity to complete my graduate studies at Concordia University, one of the best universities here in Canada.

Also, many thanks for all the members of Concordia Center for Composites (CONCOM) for their help, especially in completing my experimental work.

I would like to introduce my thanks to my colleagues for all their efforts. Special thanks for Mr. Ali Naghashpour, Mr. Majed Muslumani, Mr. Jeffery Simpson, Mr. Hassan Al Shahrani, Mr. Davood Rahmani, and Dr. Farjad Shadmehri for helping me in manufacturing of the test specimens and their installation in the pure bending test setup.

Last, but not least, I would like to thank my parents, my wife and all my family for their encouragement and patience throughout all this work.

Dedication

This thesis is dedicated to:

my Creator "**ALLAH**", hope to be accepted

my mother and my father,

my wife, Fatma,

and my kids, Khadega and Yousef

Table of Contents

List of Figures

List of Tables

Chapter 1

Introduction and Literature review

1.1 Introduction

Due to their light weight and high stiffness characteristics, composite tubes have been recently used in many applications ranging from piping systems to robot arms, power drive shafts, and the printing rollers in printing industry. The progress in composite material science and manufacturing techniques permit the existence of thick-walled tubes composite tubes made of advanced composites to be used as primary structures in aerospace applications such as satellite truss structures and landing gears of helicopters. A research project is held for designing a thermoplastic composite landing gear, replacing the conventional aluminum one. The first step in this project is to design a straight composite tube to match the aluminum counterpart in deformability, bending stiffness and strength. A previous work was done on deformability of thermoplastic composite tubes [1] and it is needed to understand both bending stiffness and strength properties of thick-walled composite tubes to complete this project.

In this thesis, the research work is focused on understanding the bending stiffness phenomenon theoretically and experimentally, and studying the failure behavior experimentally for thick-walled composite tubes under bending.

A theoretical method is needed to calculate and understand the bending stiffness property of thick-walled composite tube accurately. Also, samples of thick-walled thermoplastic composite tubes have to be manufactured with an acceptable quality, and a convenient testing method is needed in order to validate the theoretical calculations and to specify the failure mode and failure strength of thick-walled composite tubes accurately. In order to do that, the literature is searched about theoretical analysis of composites tubes under bending, focusing on the bending stiffness calculation. Also, the context is reviewed about the available manufacturing methods for thermoplastic composite tubes and how to have tubes with acceptable quality. Also, testing methods are reviewed to specify the suitable

testing method for the manufactured samples. In the next section, the literature review is presented for the previously stated topics.

1.2 Literature review

A thick-walled composite tube is a special case of a composite cylinder, having a large value of t/Do, where t denotes the tube wall thickness and Do is its outer diameter. So, it is convenient to review the bending of thin and thick-walled composite cylinders to have a general idea about this issue.

1.2.1 Analysis of composite cylinders under bending

The case of a composite cylinder subjected to bending loading is a repeated situation in different structural applications which motivates researchers to pay large attention for the analysis of this issue. Several studies have applied the three-dimensional elasticity theories for analysis of composite cylinders under bending. Lekhnitskii [2] was known to be the first who used elasticity theory to solve the boundary value problem of a single layered anisotropic cylinder subjected to pure bending, and axisymmetric loading. Various publications used the work of Lekhnitskii.

Jolicoeur and Cardou [3] extended Lekhnitskii's theory to obtain the three-dimensional solutions of multilayered coaxial orthotropic straight cylinders under bending, torsion, and extension loads. Tarn and Wang [4] reformulated the governing equations of Lekhnitskii [2] to be decoupled into three sets of first order differential equations, allowing simpler formulation for multilayered anisotropic cylinders.

These theories provide exact analysis for composite cylinders under bending or axisymmetric loading while the case of transverse shear loading cannot be handled because of the used assumption of constant stresses along the cylinder axis.

Equivalent single layer theories can handle a general loading condition, by assuming approximated displacement fields. A considerable amount of literature has been published on the basis of these two-dimensional theories for composite cylinders. Khdeir et al., [5] proposed a solution technique to study the bending of cross-ply cylindrical shells. This technique was applied to classical, first order and higher order shell theories neglecting the effect of layers curvature in the derivation of the two dimensional stress resultants. Qatu [6], [7] derived more accurate governing equations for composite deep thick shells, based on the first order shell theory and including the effect of the mid plane curvature in deriving the two dimensional stress resultants. It was stated that t/Do should be ≤ 0.05 to have accurate results. Assadi [8] modified Qatu's formulation [7], considering the curvature of every layer instead of using only the mid plane curvature in stress resultants derivation. Xia et al., [9] applied the classical lamination theory with Lekhnitskii's stress function approach [2] for studying filament-wound fiber-reinforced sandwich pipes.

There exist various publications considering the composite cylinder as a circular hollow composite beam when its length is very large compared to its diameter. Librescu and Song [10] derived a nonconventional beam theory based on first order plate theory for the analysis of composite beams of closed cross-section contour under general loading conditions. The theory was assumed to handle thin to thick-walled composite cylinders, by incorporating the effect of the three dimensional elastic effects and considering the transverse shear deformation. Kim and White [11] proposed a similar theory for analysis of thick hollow composite beams.

Equivalent single layer (ESL) theories are based on assuming a continuous displacement field through the thickness of the composite laminate causing unreal situation for the interlaminar stresses and strains. This unreal situation has a large negative impact on the analysis of structures having thick laminates. Layerwise theories allow the in-plane displacements to vary in a layerwise manner through the laminate thickness giving better representation for kinematical relations in thick laminates [12].

Reddy presented a layerwise theory for analysis of cross-ply cylindrical shell under bending ([12], [13] and [14]).

There are many publications that used the finite element method for analysis of composite cylinders under bending. Bathe and Almeida [15] presented an effective beam element for analysis of both straight and curved composite tubes including cross section ovalization effects. Yan et al., [16] proposed an enhanced version of this element for elastic and non-linear plastic analysis of composite tubes. Qi and Jiang [17] presented a different beam element for analysis of straight and tapered composite tubes under general loading. Xu et al., [18] used a three dimensional solid element to model the four-point bending of a thermoplastic composite tubes until its ultimate failure.

1.2.2 Bending stiffness of composite tubes

Bending stiffness is the mechanical property which governs the deformation of composite structures under bending. Tsai and Hahn [19] devoted one chapter in their book to study the bending stiffness of symmetric sandwich laminates using the classical lamination theory. Despite all the previously mentioned publications for analysis of composite cylinders under bending, few attempts are reported to calculate the bending stiffness of composite tubes and their applicability for thick-walled composite tubes are not checked. Jolicoeur and Cardou [3] presented an equation to calculate the bending stiffness of composite cylinders. This formula is considered to be accurate for thick-walled composite as its derivation is based on the three-dimensional elasticity theory. Chan and Demirhan [20] presented a closed form solution to estimate the bending stiffness of laminated composite tubes based on classical lamination theory. Cunha and Piranda [21] tried to identify the stiffness properties of composite tubes by conducting vibration tests and comparing measured Eigenvalues with those calculated using numerical modal analysis. It was shown that the method sensitivity for the bending stiffness is very low compared to other properties. Shadmehri et al., [22] derived a formula for

calculating the bending stiffness of composite tubes using Librescu beam theory [10]. The applicability of these presented methods for thick-walled composite tubes was not evaluated.

1.2.3 Manufacturing and testing of composite tubes

Manufacturing of thermoset composite tubes are conventionally performed using filament winding or prepreg layup techniques with autoclave for the curing process. These techniques are not applicable for thermoplastic composite tubes. Automated fiber placement (AFP) is a recent technique utilized for the manufacturing of both thermoset and thermoplastic composite tubes, with a unique advantage for thermoplastic ones that the autoclave process is not needed. Some studies are recently published on this manufacturing technique. Khan et al., [23] identified some optimal manufacturing parameters to enhance the quality of a thermoplastic composite laminate using AFP technique. Croft [24] studied the strength variation for a thermoplastic composite laminate due to the induced defects from AFP process. Shadmehri et al., [25] studied the AFP manufacturing technique for thermoplastic composite rings to determine the optimum process conditions from both strength and stiffness points of view.

Regarding testing techniques, the 3-point and 4-point bending test are commonly used to apply bending loading. Saggar [26] carried out 4-point bending tests for thin-walled composite tubes using MTS machine at University of Texas at Arlington. It was required to validate the theoretical method proposed by Chan and Demirhan [20] to calculate the bending stiffness. This adopted testing technique was inappropriate, causing sudden failure for most of the tested samples due to the large local ovalization that occurred for the tubes cross sections at the loading points, as shown in Figure 1.1. The obtained results were inadequate to fulfill the goal of this research.

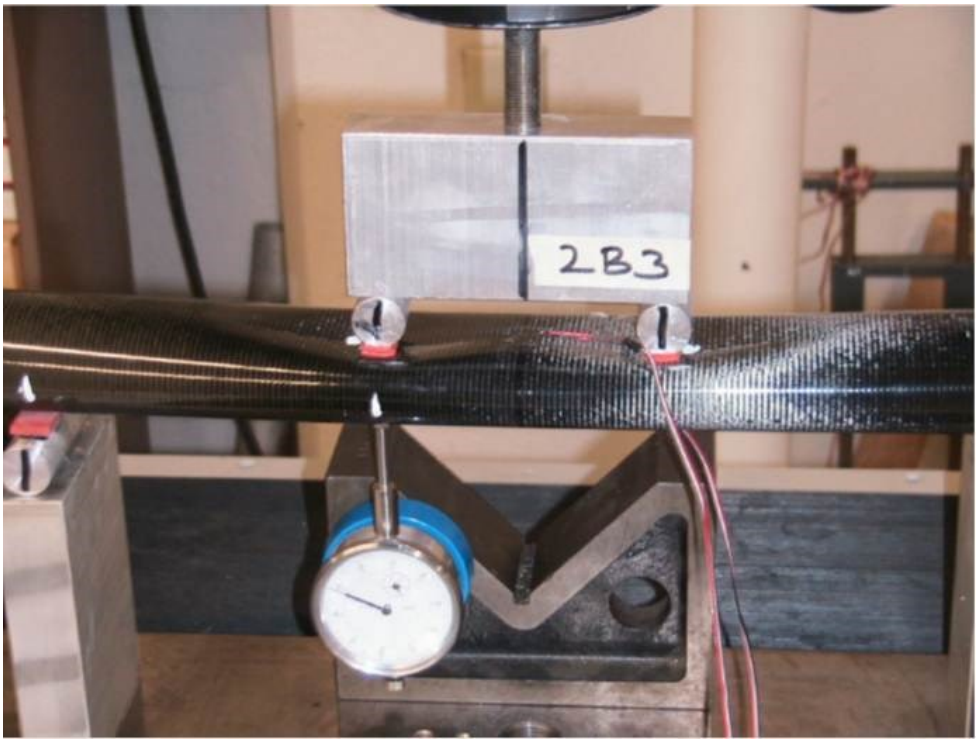

Figure 1.1: High local ovalization below loading points, [26]

Derisi [1] performed 3-point bending and 4-point bending tests for thick-walled thermoplastic composite tubes during his research on deformability phenomenon. The tests were carried out using a MTS machine of 200KN loading capacity at Concordia University. He proposed a strain controlled design technique to develop a composite tube with 2% deformability for the landing gear application. The results of these tests were better than those of Saggar, [26], because of better adopted test techniques and the thicker cross section of the used specimens. This provides more rigidity for the tube cross section which helps to get good results at the initial linear part of the experiments. Also Derisi tried to enhance the cross section rigidity by inserting an aluminum ring inside the composite tube below the loading point. However the experiments show high local damage at the loading points when going to higher loads, Figure 1.2.

Figure 1.2: Local damage in a thick-walled composite tube under loading point, [1]

These two previous studies showed a premature failure for both thin-walled and thick-walled composite tubes, and the actual bending stiffness and strength of the tubes was not accurately specified. This is thought to be due to the large applied transverse shear forces at the loading points [18].

Bending loading of composite cylinders was conducted by a different technique rather than the 3-point or 4-point bending tests. Sponsored by NASA Langley-Virginia Polytechnic Institute, Fuchs et al. [27] developed a pure bending test rig to apply an end-rotation to each end of the composite cylinder. Their objective was to study the bending and buckling behavior of thin-walled composite cylinders numerically and experimentally. Good correlation was obtained between numerical and experimental results.

Recently, Shadmehri [28] has developed a pure bending test rig of large loading capacity at Concordia University which is capable to apply large bending moments at both ends of the tested specimen. A thermoplastic tail boom of a helicopter has been tested until its failure at the predetermined load and location obtained from theoretical calculations. Thick-walled composite tubes have not been reported before to be tested on similar types of pure bending test rig.

1.3 Thesis approach

1.3.1 Objectives

Referring to the previous discussions and the presented literature in this chapter and taking into considerations the needed research to achieve a composite landing gear, it is found that there are various methods to calculate the bending stiffness of composite tubes. But there is no accurate validation for these methods for thin and thick-walled composite tubes due to the presented problems in testing composite tubes under bending using conventional 3-point and 4-point bending tests. Also, no work in the context tries to understand the bending stiffness property, or specify the design variables of this property and what parameters can affect this property.

For the manufacturing issue, it is found that the suitable method for economic manufacturing of thick-walled thermoplastic composite tubes is the AFP technique without using autoclave. Due to the absence of the autoclave process, a challenge is added to have a tube with acceptable quality. Also, it is observed from the literature that the AFP technique is controlled by many process parameters. And these parameters are dependable on the used machine specifications. This adds another challenge to specify the optimum manufacturing parameters. Finally, there is no previous work handle the failure of thick-walled composite tubes, theoretically or experimentally. From all these previous motivations, the objectives of this research are identified to be as follows:

- Understanding bending stiffness property of thin and thick-walled composite tubes.
- Manufacturing a thick-walled thermoplastic composite tube with acceptable quality.
- Alternative accurate testing method for thick-walled composite tubes under bending.
- Experimental Validation for the used bending stiffness formula.
- Investigating “failure” of thick-walled composite tubes under bending, experimentally.

The methodology of the current study is presented in the following subsection.

1.3.2 Methodology and thesis outline

Joliceur and Cardou formula [3] is used to calculate the bending stiffness of composite tubes because its formulation is based on three-dimensional elasticity theory, making it to be considered as an accurate method. A peculiar bending stiffness behavior is brought up for thick-walled composite tubes. This behavior is studied in details in Chapter 2. At first, the bending stiffness behavior of thick-walled isotropic tubes composed of two layers of different materials is investigated in section 2.2, specifying the effects of the location of the stiffer layer and the layers moments of inertia on the behavior of the tube bending stiffness property. This is followed by studying the bending stiffness behavior of thick-walled composite tubes made up of two layers in section 2.3.

The used bending stiffness formula is rearranged giving out a new term for every layer in the composite tube, denoted as the effective extensional stiffness "$E_{eff,n}$". This new term represents the contribution of the layer material properties in its bending stiffness. The variation of this term with the layer's moment of inertia is demonstrated in subsection 2.3.2.

Chapter 3 is devoted to investigating the bending stiffness property for both thin-walled and thick-walled composite tubes. A novel parametric study is performed to study $E_{eff,n}$. This is done by plotting its variation with different design variables and applying the finite difference method to calculate the partial derivatives of $E_{eff,n}$ with respect to different material properties, quantifying their contributions to the bending stiffness properties of composite layers inside the tube. The parametric study handles different configurations for a tube made of one or two composite layers in order to have a global idea about the bending stiffness, starting by identifying $E_{eff,n}$ (Section 3.1), followed by studying the effect of layers interaction on the tube bending stiffness (Section 3.2), and layer geometric effects (Section 3.3). Section 3.4 presents the configuration of multi-sublaminates composite tubes.

Experimental work is needed in this research to validate the obtained conclusions about the bending stiffness phenomenon, used theoretical methods, and to investigate the failure of thick-walled composite tubes. This is done by performing pure bending test for two thick-walled thermoplastic composite tubes having different laminate configurations. These two specimens are manufactured using the (AFP), available at Concordia center for composites (CONCOM). A pure bending test setup, available at (CONCOM) is used for performing the pure bending tests.

Chapter 4 is devoted to; presenting the manufacturing process of these two thick-walled tubes and the preparation needed for testing. A study is carried out to identify the optimum process parameters for manufacturing a thermoplastic composite tube with acceptable quality level, Section 4.1.

For the testing process, the idea of the pure bending test setup and the proposed adaptation needed for testing the manufactured samples are discussed in Section 4.2. The test preparation procedures are presented in details in Section 4.3.

The output of the experiments and their comparison with theoretical results are illustrated in Chapter 5. All the measured parameters for the pure bending test for one of the manufactured tubes are included in section 5.1. Section 5.2 is devoted to compare the calculated bending stiffness values with the specified values from the bending tests. The failure behavior for the tested thick-walled composite tubes is investigated according to the obtained experimental results, comparing their behavior with thin-walled tubes (Section 5.3).

Chapter 6 presents the conclusions from this research, the main contributions and the proposed directions for future research related to this study.

Chapter 2

Bending stiffness behavior of thick-walled composite tubes

In this chapter, the interesting bending stiffness behavior of thick-walled composite tubes is presented and explained. The bending behavior of isotropic tubes made of two layers is studied as an introduction for composite tubes of laminate configuration [θ/-θ]. The bending stiffness formula presented in [3] is arranged to define a new parameter for each layer in the composite tube in order to be used in the analysis of the bending stiffness property. The main parameters of the bending stiffness equation are studied. The influence of layers moment of inertia on their bending stiffness is identified. The effects of the layers geometry on their bending stiffness are presented.

2.1 Introduction

According to classical beam theory, the bending stiffness property describes the relation between an applied bending moment (M_x) and the obtained beam curvature (k) such that:

$$\langle EI \rangle = \frac{M_x}{k} \tag{2.1}$$

Where: $\langle EI \rangle$ is the bending stiffness of the beam. For an isotropic tube of circular cross-section, the bending stiffness is calculated using the following equation

$$\langle EI \rangle = E_x I_T = E_x \frac{\pi}{64}(D_0^4 - D_i^4) \tag{2.2}$$

Where, (E_x) is the extensional modulus of the isotropic material which has a constant value, (I_T) is the area moment of inertia of the beam cross section, and (D_i), (D_o) are the tube inner, and outer diameters, respectively.

For composite tubes, the situation is more complicated; Composite structures are normally made of (N) number of layers having different orientation angles. The anisotropic nature of these layers causes

the existence of different responses compared to isotropic ones [29]. For example, the existence of the shear-extension coupling effect makes normal stresses generate shear strains. Also, the layers interaction in composite structures leads to more complicated behavior.

In this chapter, it is necessary to study the bending stiffness behavior of thick-walled composite tubes and its variation with increasing tube wall thickness. There are some available methods in the literature to calculate the bending stiffness behavior of composite tubes ([3], [20] , [22]).

Jolicoeur and Cardou method is thought to be the most convenient method for the analysis of thick-walled composite tubes. This is because it is based on three-dimensional elasticity theory, which incorporates the thickness coordinate in the analysis with no assumption. The derived formula for calculating the bending stiffness has the following form [3]:

$$\langle EI \rangle = \sum_{n=1}^{N} \pi E_{x,n} \left\{ \sum_{i=1}^{4} K_{i,n} \left[\bar{S}_{16,n} . g_{i,n} . m_{i,n} - \bar{S}_{13,n} - \bar{S}_{12,n} (m_{i,n} + 1) \right] \left[\frac{\left(b_n^{(m_{i,n}+2)} - a_n^{(m_{i,n}+2)} \right)}{(m_{i,n} + 2)} \right] + \left[1 - \mu_{1,n} (\bar{S}_{13,n} + 3\bar{S}_{12,n}) + 2\mu_{2,n} \bar{S}_{16,n} \right] \frac{(b_n^4 - a_n^4)}{4} \right\} \quad \textbf{(2.3)}$$

Where:

- $E_{x,n}$ --- extensional modulus of the composite layer (n), function of the layer orientation angle and the composite material properties of each layer.
- $\bar{S}_{16,n}, \bar{S}_{13,n}, \bar{S}_{12,n}$ --- Off axis compliance coefficients of the composite layer (n).
- $g_{i,n}, m_{i,n}, \mu_{i,n}$ --- Different coefficients, function of the layer orientation angle, and the composite material properties.
- a_n, b_n --- Inner and outer radii of the composite layer, respectively
- $K_{i,n}$ --- Variables function of the layer orientation angle, the composite material properties, and inner and outer radii of the whole layers of the composite tube.

The presented $K_{i,n}$ are calculated assuming perfect bonding between layers. These variables are incorporating the effects of the mutual interaction between the composite layers. More details about this formula are presented in Appendix A.

In order to study the bending stiffness behavior of thick-walled composite tubes, a MATLAB program is written for this method, Appendix D. The dimensionless parameter (t/D_o) is used to represent the wall thickness (t), fixing the tube outer diameter (D_o). The tube is considered to be thick when t/D_o is greater than 0.05 [7] and the maximum value of t/D_o equal to 0.5, at which the tube becomes a solid rod.

Using equation (2.3**)**, the bending stiffness is calculated, for thick-walled composite tubes made of [θ/-θ] laminate configuration of equal layers thickness, and varying t/D_o from 0.05 to 0.45. Typical properties of carbon/epoxy material are assumed for the composite tubes, as listed in Table 2.1. The values are normalized by dividing on the bending stiffness of t/D_o=0.05. An interesting bending stiffness behavior is observed for composite tubes compared to that of isotropic counterparts, as shown in Figure 2.1. On increasing t/D_o, the bending stiffness of composite tubes decreases after a specific value of t/D_o. This is contrary to the behavior of the isotropic tube (aluminum), where the bending stiffness increases with increasing t/D_o value, and the bending stiffness approaches an asymptotic value at high t/D_o ratios.

Table 2.1: Material properties of Carbon/Epoxy used in bending stiffness analysis, [29]

E_1, GPa	155
$E_2=E_3$, GPa	12.1
$G_{12}=G_{13}$, GPa	4.4
G_{23}, GPa	3.2
$\nu_{12}=\nu_{13}$	0.248
ν_{23}	0.458

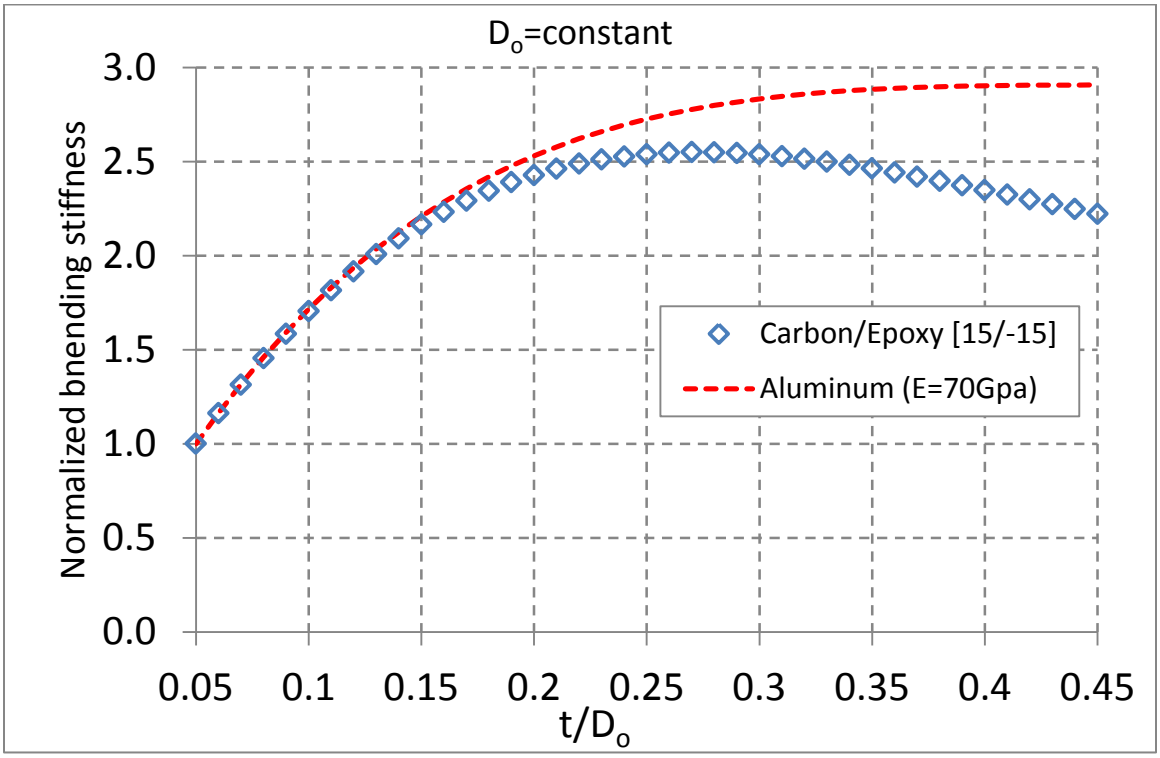

Figure 2.1: Calculated bending stiffness behavior of composite tube vs. aluminum counterpart

In order to investigate this result, the bending stiffness behavior is studied in the next sections for isotropic tubes made out of two layers, followed by studying the composite tubes of [θ/-θ] configuration, identifying the design variables and their contributions in the presented behavior.

2.2 Isotropic tubes made of two layers

For a tube composed of two layers of different types of isotropic materials, the bending stiffness has the following form:

$$\langle EI \rangle = E_{x,1} I_1 + E_{x,2} I_2 \tag{2.4}$$

The equation shows that the controlling parameters for the bending stiffness of isotropic tubes are the layers extensional stiffness with their moments of inertia. The influences of these terms on bending stiffness behavior are presented in the following paragraphs.

2.2.1 Location of the stiffer layer

In this subsection, the effect of the layer's extensional modulus on the tube bending stiffness is demonstrated through the influence of the location of the stiffer layer. The coefficient R_{Ex} is defined in the following equation:

$$R_{Ex} = \frac{E_{x,2}}{E_{x,1}} \tag{2.5}$$

R_{Ex} is the ratio of the extensional modulus of the tube outer layer ($E_{x,2}$) to ($E_{x,1}$) of the inner layer. Location of the stiffer layer can be identified according to the value of R_{Ex} such that;

- $R_{Ex}<1$, implies that the stiffer layer is the inner layer
- $R_{Ex}=1$, both layers have the same stiffness, the case of the tube made of one layer
- $R_{Ex}>1$, the stiffer layer is the outer layer

Equation (2.4) can be redefined to have the following form

$$\langle EI \rangle = E_{x,1}(I_1 + R_{Ex} I_2) \tag{2.6}$$

The following figure shows the bending stiffness behavior of isotropic tubes with increasing t/D_o for different values of R_{Ex} .

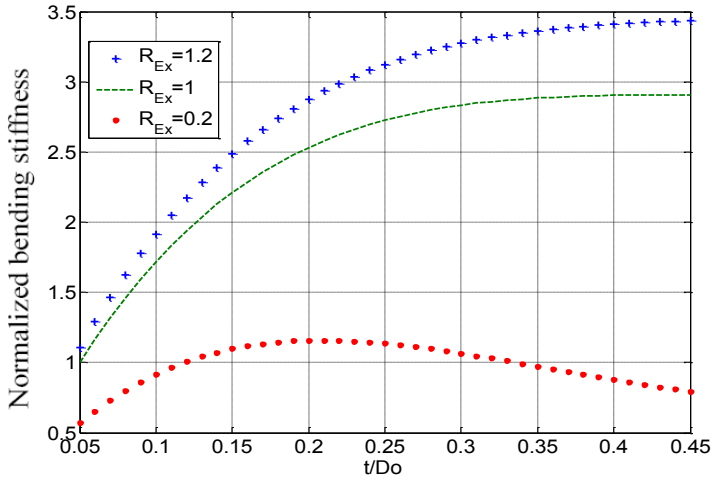

Figure 2.2: Bending stiffness behavior for different R_{Ex} values

The normalized values of bending stiffness $\langle EI^* \rangle$ are obtained using the following form

$$\langle EI^* \rangle = \frac{\langle EI \rangle}{E_{x,1} I_{min}} \tag{2.7}$$

I_{min} is the total moment of inertia of the tube at t/D_o equals 0.05. The figure shows that the bending stiffness behavior is always increasing with t/D_o for the cases of $R_{Ex}=1$ or $R_{Ex}>1$ while for the case of the stiffer layer is the inner one, the bending stiffness of the tube decreases with increasing t/D_o above specific thickness value, the same bending behavior shown in Figure 2.1 for composite tubes of [θ/-θ] configuration. From this result it is concluded for isotropic materials that the total bending stiffness of the tube decreases above a specific thickness value when the inner layer shows higher extensional stiffness than the outer layer, noting that D_o is constant. In order to have the full view of this behavior, the second parameter in the bending stiffness equation is studied

2.2.2 Layers moments of inertia

In this part, the contribution of layers' moments of inertia is studied for a tube made of two layers of different isotropic materials. This analysis is performed by identifying the design variables and investigating their variation effect on layers' moment of inertia. I_n is calculated using the following equation:

$$I_n = \frac{\pi}{4}(b_n^4 - a_n^4) \tag{2.8}$$

a_n, b_n are the inner and outer radii of layer n, respectively. The values of a_n, b_n can be calculated for a tube composed of two layers as follows:

$$\begin{gathered} a_1 = Do\left(\frac{1}{2} - \frac{t}{Do}\right) \\ b_1 = a_1 + t_1 = Do\left(\frac{1}{2} - \frac{t}{Do} + \frac{t_1}{t}\frac{t}{Do}\right) = a_2 \\ b_2 = \frac{Do}{2} \end{gathered} \tag{2.9}$$

Where: t_1/t is the ratio of the thickness of the inner layer (t_1) to the total wall thickness (t). Substituting equation (2.9) into equation (2.8), the total moment of inertia (I_T), and the layers moment of inertia (I_n) are written in the following forms

$$I_T = \frac{\pi}{8}\frac{t}{Do}Do^4\left(1 - 3\frac{t}{Do} + 4\left(\frac{t}{Do}\right)^2 - 2\left(\frac{t}{Do}\right)^3\right)$$

$$I_1 = \frac{\pi}{8}\frac{t}{Do}Do^4\left(1 - \left(1 - \frac{t_1}{t}\right) - 3\frac{t}{Do}\left(1 - \left(1 - \frac{t_1}{t}\right)^2\right) + 4\left(\frac{t}{Do}\right)^2\left(1 - \left(1 - \frac{t_1}{t}\right)^3\right) - 2\left(\frac{t}{Do}\right)^3\left(1 - \left(1 - \frac{t_1}{t}\right)^4\right)\right) \quad \textbf{(2.10)}$$

$$I_2 = I_t - I_1 = \frac{\pi}{8}\frac{t}{Do}Do^4\left(\left(1 - \frac{t_1}{t}\right) - 3\frac{t}{Do}\left(1 - \frac{t_1}{t}\right)^2 + 4\left(\frac{t}{Do}\right)^2\left(1 - \frac{t_1}{t}\right)^3 - 2\left(\frac{t}{Do}\right)^3\left(1 - \frac{t_1}{t}\right)^4\right)$$

From previous equations, the design variables of I_n are specified to be D_o, t/D_o, and t_1/t, while I_T is function of D_o and t/D_o only.

Also, one can observe the significant effect of D_o on I_n and I_T. The behavior of I_n will be studied on the following ranges of the design variables

- t/D_o= 0.05:0.5 --- representing relatively thick to the case of solid circular bar.
- t_1/t=0:1 --- zero for first layer means that the tube is composed of only the second layer and vice versa for 1
- D_o is assumed to be constant in this study

2.2.2.1 Effect of t/Do

The effect of t/D_o on I_n is studied by two ways: plotting I_n and I_T with respect to t/D_o, and differentiating I_n and I_T with respect to t/D_o, checking the monotonicity of these functions, while fixing the values of D_o and t_1/t.

Figure 2.3 demonstrates the change of the moments of inertia with t/D_o, taking $t_1/t=0.5$, and normalizing the values by dividing on (I_{min}). From this figure, one can observe the following points:

- I_T is always increasing over the values of t/D_o till $t/D_o=0.5$ where I_T has its maximum value.
- I_1 is increasing till certain value of t/D_o, and then it decreases again.
- I_2 is always increasing over the range of t/D_o.

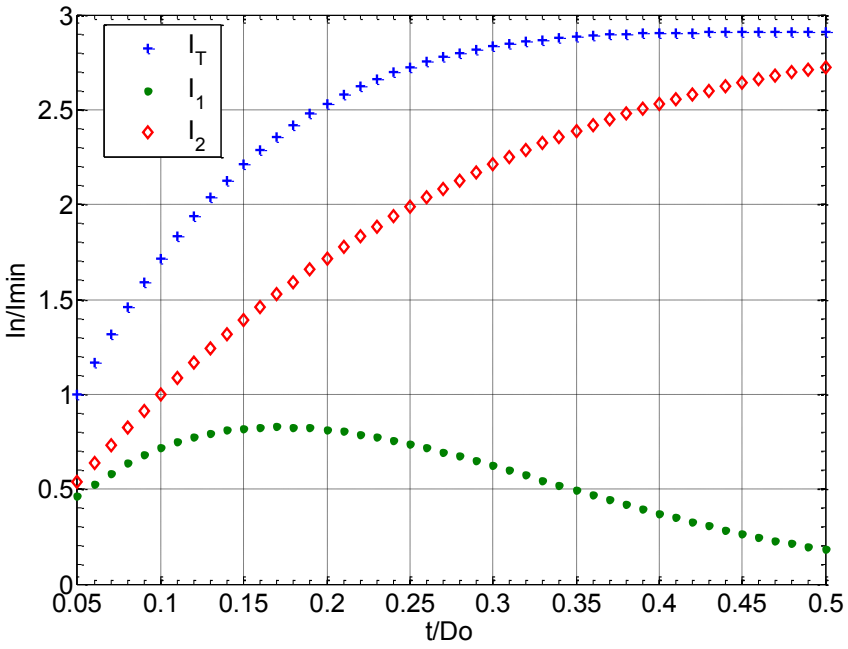

Figure 2.3: Layers moments of inertia versus t/D_o, $t_1/t=0.5$

It is shown that the values of I_1, I_2 are close to each other when t/D_o is small, then their values diverge from each other when t/D_o increases. Also one can observe the large value of I_2 at the expense of I_1 when the value of t/D_o is large, despite of having the same wall thickness. The reasons are discussed in the following subsection.

2.2.2.2 Reasons of dominance of I_2 over I_1 for layers of equal thickness

It is required to understand the reasons that make I_2 to be greater than I_1 when the two layers have the same thickness in a tube. First, consider a sandwich plate composed of four layers of isotropic materials of equal thickness "H", having an empty core making the layers to be apart from X axis by a distance a_1, as shown in Figure 2.4

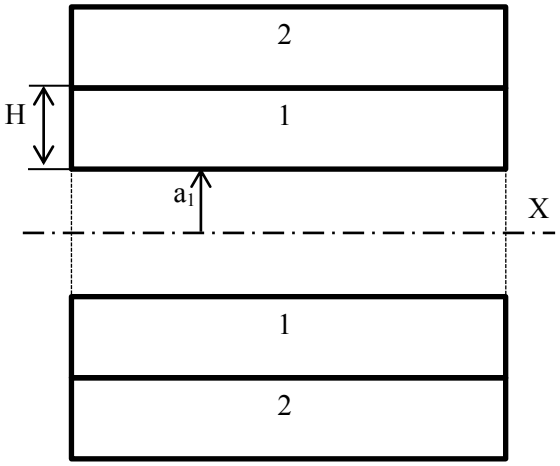

Figure 2.4: Cross section of sandwich plate of equal layer thickness and empty core

The moments of inertia with respect to x of layers "1" and layers "2" in the figure can be obtained using parallel axis theorem

$$I_x = I_{x0} + Area * a^2 \quad \textbf{(2.11)}$$

Where:

- I_x --- the moment of inertia with respect to x axis
- I_{xo} --- the moment of inertia of the layer with respect to its own centroid
- a --- the distance from x axis to the layer centroid

The ratio of I_1 to I_2 for the shown plate is calculated to be in the following form

$$\left.\frac{I_1}{I_2}\right|_{plate} = \frac{\frac{1}{12}H^3 + H\left(\frac{1}{2}H + a_1\right)^2}{\frac{1}{12}H^3 + H\left(\frac{3}{2}H + a_1\right)^2} = \frac{H^2 + 3Ha_1 + 3a_1^2}{7H^2 + 9Ha_1 + 3a_1^2} \quad \textbf{(2.12)}$$

By subtracting the denominator from the numerator, the following equation is obtained

$$7H^2 + 9Ha_1 + 3a_1^2 - (H^2 + 3Ha_1 + 3a_1^2) = 6H^2 + 6Ha_1 \quad \textbf{(2.13)}$$

So it is clear that for the two positive variables a_1 and H, I_2 is larger than I_1. This is because layers "2" are in farther location from x axis than layer 1. It is important to note that the plate width value has no effect on the ratio of I_1 to I_2 as its value is canceled with each other when dividing I_1 by I_2.

Now, assuming that the same Figure 2.4 is considered to be a longitudinal cross section of a tube made of two layers such that the notation "1" is for the inner layer and "2" is for the outer layer, x axis is the longitudinal axis of the tube and a_1 is equal to the tube inner radius. The ratio of I_1 to I_2 can be calculated as shown in the following equation:

$$\left.\frac{I_1}{I_2}\right|_{tube} = \frac{(H + a_1)^4 - a_1^4}{(2H + a_1)^4 - (H + a_1)^4} = \frac{H^3 + 4H^2a_1 + 6Ha_1^2 + 4a_1^3}{15H^3 + 28H^2a_1 + 18Ha_1^2 + 4a_1^3} \quad \textbf{(2.14)}$$

From this equation, one can observe that I_2 is also larger than I_1 for tubes. By subtracting equation (2.14**)** from (2.12**)**, the following equation is obtained:

$$\left.\frac{I_1}{I_2}\right|_{plate} - \left.\frac{I_1}{I_2}\right|_{tube} = \frac{2H(4H^4 + 18H^3a_1 + 33H^2a_1^2 + 24Ha_1^3 + 6a_1^4)}{(15H^3 + 28H^2a_1 + 18Ha_1^2 + 4a_1^3)(7H^2 + 9Ha_1 + 3a_1^2)} \quad \textbf{(2.15)}$$

The result shows that the ratio of I_1 to I_2 for the sandwich plate is larger than that for the tube when the layers thicknesses are equal. This means that I_2 has superior value over I_1 in the case of the tube more than that of the sandwich plate.

The reason of that is explained by calculating the limit of equation **(2.15)** when a_1 tends to infinity. It is found that the difference between these two ratios is equal to zero, at a_1 equal to infinity, the situation of zero curvatures for the layers. This result indicates that the curvature of layers is the reason of this difference between the sandwich plate and the tube.

In summary, the moment of inertia of the outer layer of a sandwich plate is larger than that of the inner layer due to the farther location of the outer layer from the mid plane, despite having equal thickness, while the moment of inertia of the outer layer of a tube of equal layer thickness is larger than that of the inner layer due to two effects; the farther location of the outer layer and its larger radius of curvature.

Figure 2.5 shows the variation of the ratio of layers moment of inertia over t/D_o range, comparing the case of the tube to that of the sandwich plate when $t_1/t=0.5$. The figure shows the large effect of layer location such that the inner layer shows small moment of inertia compared to the outer layer for the plate and the tube.

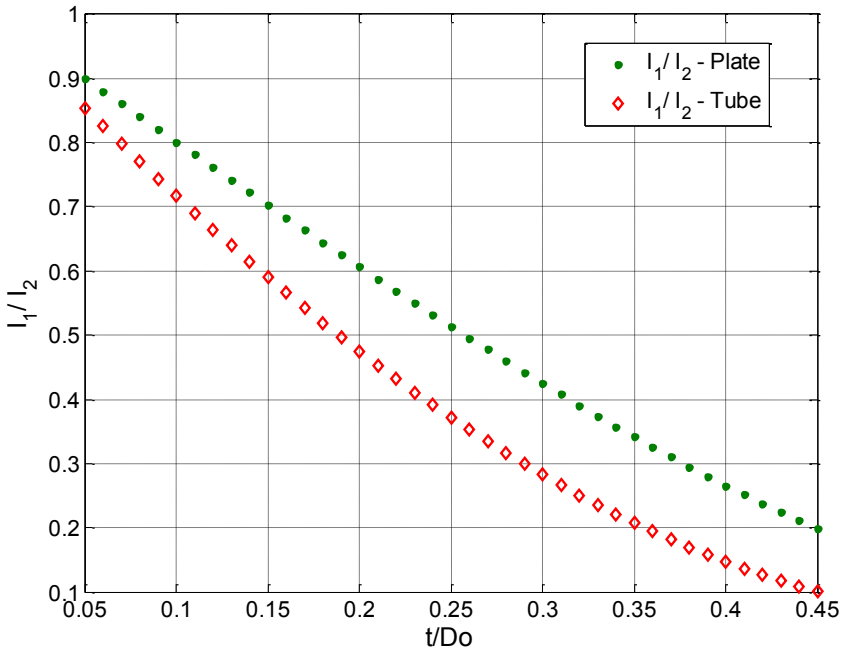

Figure 2.5: I_1/I_2 ratios vs. t/D_o for sandwich plates and tubes of equal layer thickness

Also one can observe the significant effect of the radii of curvature of layers when $t_1/t=0.5$, especially for larger wall-thickness. The situations of other values of t_1/t are presented in the following subsection.

2.2.2.3 Effect of t_1/t

The effect of t_1/t is analyzed in the same way as presented for t/D_o; plotting I_n and I_T functions with respect to t_1/t and differentiating them with respect to t_1/t, fixing the values of D_o and t/D_o. Figure 2.6 demonstrates the change of the moments of inertia with t_1/t, using t/D_o=0.05,0.45.The values are normalized using the total moment of inertia of the tube. From this figure, one can see the following points:

- The equation of I_T is not function of t_1/t; which means that I_T is constant for all t_1/t.
- The value of I_1 is always increasing with t_1/t
- The value of I_2 is always decreasing with increasing t_1/t

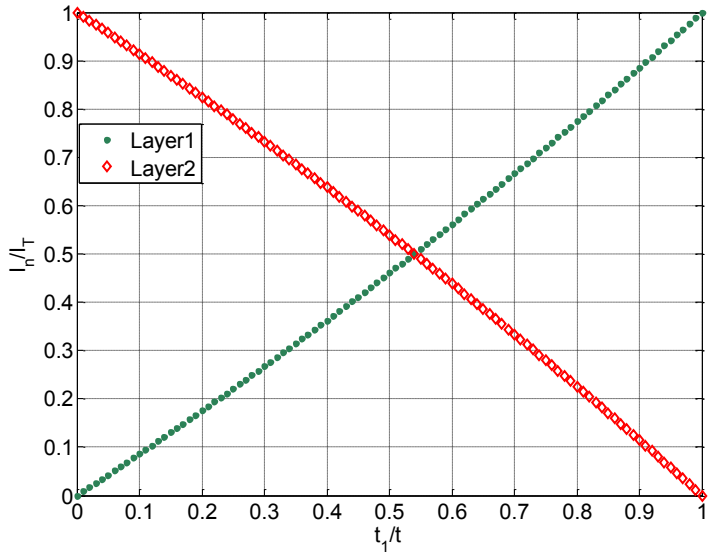

(a)

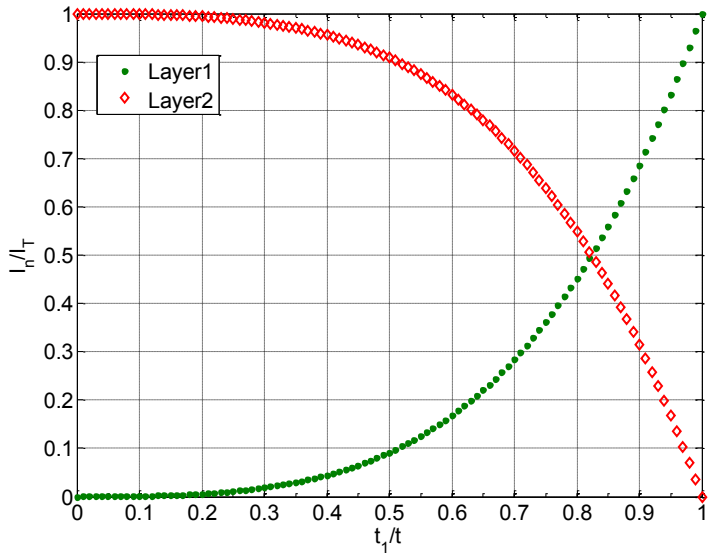

(b)

Figure 2.6: Layers moments of inertia vs. t_1/t. (a) t/D_o=0.05, (b) t/D_o=0.45

The figures illustrate that when t/D_o is small, the variation of I_1 and I_2 is linear while as t/D_o increases, the nonlinearity of their functions increases. Also, it is shown that at t_1/t=0.5, the values of $I_1$and I_2 are not equal even for the smallest value of t/D_o due to effects of layer location and radius of curvature.

The value of t_1/t that permits equal I_n can be calculated by solving I_1 and I_2 functions to get the point of intersection of the two curves of I_1 and I_2 ($I_1=I_2$) for every value of t/D_o, such that:

$$\frac{t_1}{t} = 1 - \frac{\left\{1 - \left(1 - 4\left(\frac{t}{D_o}\right) + 12\left(\frac{t}{D_o}\right)^2 - 16\left(\frac{t}{D_o}\right)^3 + 8\left(\frac{t}{D_o}\right)^4\right)^{1/4}\right\}}{2\left(\frac{t}{D_o}\right)} \qquad \textbf{(2.16)}$$

Figure 2.7 shows the values of t_1/t obtained from equation (2.16) over the range of t/D_o.

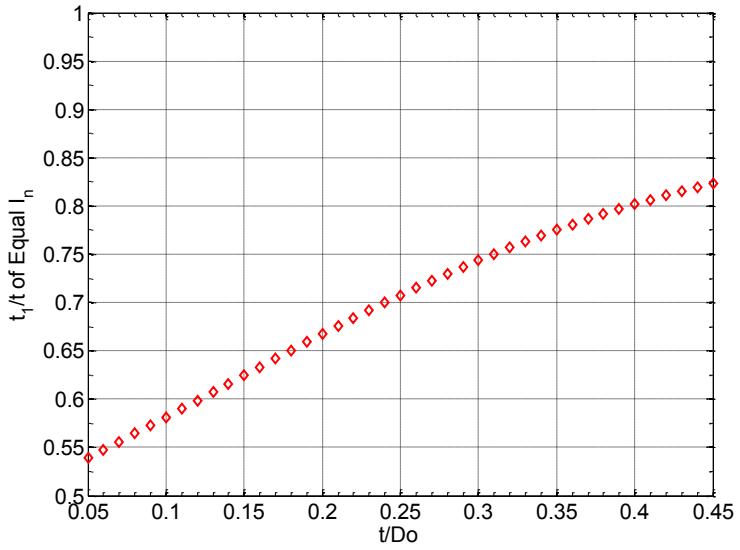

Figure 2.7: t_1/t values of ($I_1=I_2$) vs. t/D_o

It is shown that as the wall thickness of the tube increases, a higher value of t_1/t is required to achieve equal area moments of inertia for the two layers, shifting its value from $t_1/t=0.5$. The cases of equal moments of inertia are presented in more details later in this chapter.

2.2.3 Tube of stiffer inner layer

The bending behavior of the tube of stiffer inner layer can be discussed after the presented analysis for layers moment of inertia. First, it is convenient to define the new variable for the layer moment of inertia, ($I_{fr,n}$) to indicate the moment of inertia fraction of layer "n"; which is the contribution of I_n in the total moment of inertia of the tube "I_T". So, for a tube composed of two layers:

$$I_{fr,\mathrm{n}} = I_{\mathrm{n}}/I_T \qquad I_{fr,1} + I_{fr,2} = 1 \tag{2.17}$$

Equation **(2.6)** is redefined using the term $I_{fr,n}$:

$$\langle EI \rangle = E_{x,1} I_{\mathrm{T}} (I_{fr,1} + R_{Ex} I_{fr,2}) \tag{2.18}$$

For the case of stiffer inner layer, $R_{Ex}<1$ and the monotonicity of the term ($I_{fr,1}+R_{Ex}I_{fr,2}$) with respect to t/D_o is decreasing while the term ($E_{x,1}I_T$) is always increasing.

The overall monotonicity of equation 2.10 is tested by differentiation with respect to t/D_o. The derivative is found to be positive at one interval of t/D_o and negative in the other interval which means the existence of a local maximum for the bending stiffness at a certain value of t/D_o and it decreases after this value. The specified value of t/D_o of maximum bending stiffness can be obtained when substituting by the values of R_{Ex}, and t_1/t to have the following equation

$$\frac{d\langle EI \rangle}{d\left(\frac{t}{D_o}\right)} = 0 \rightarrow \frac{t}{D_o} = \frac{\left\{(1-R_{Ex})^{1/3}\left(1-\frac{t_1}{t}\right)^{1/3} - 1\right\}}{2\left\{(1-R_{Ex})^{1/3}\left(1-\frac{t_1}{t}\right)^{4/3} - 1\right\}} \tag{2.19}$$

The following numerical examples are used to demonstrate the bending stiffness behavior for $t_1/t=0.5$ with R_{Ex} =0.2, and 0.5, as shown in Figure 2.8. The values are normalized using equation (2.7).

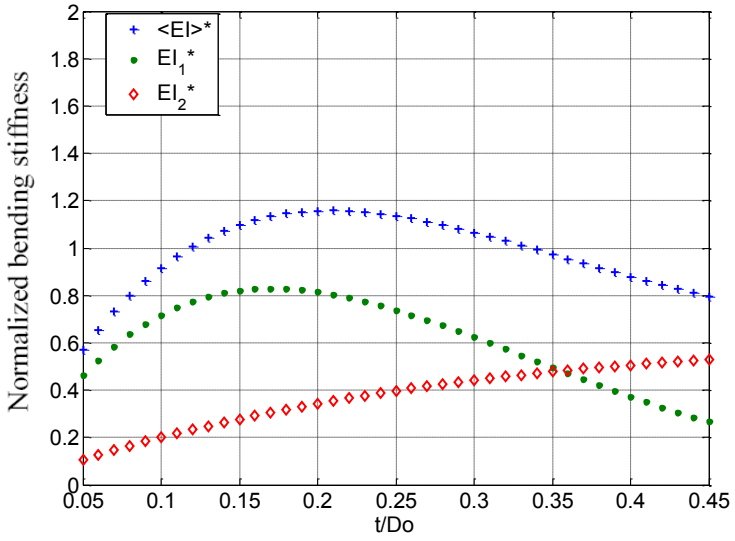

(a)

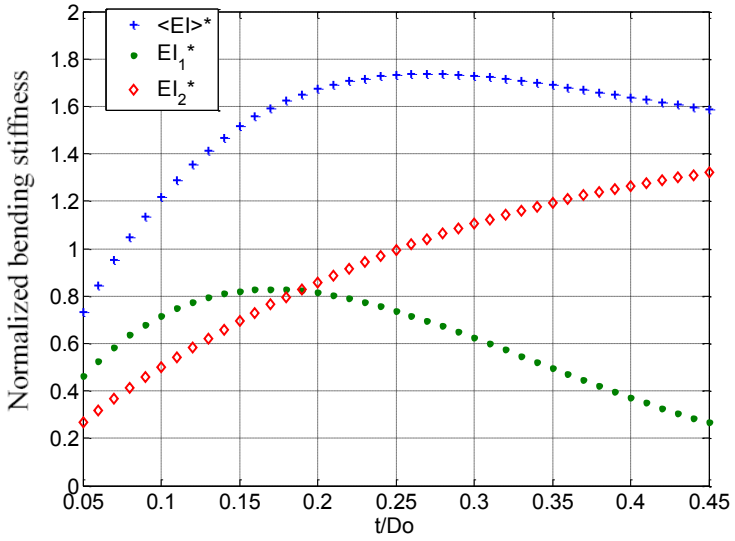

(b)

Figure 2.8: Bending stiffness variation over the range of t/D_o when $E_{x,1}>E_{x,2}$

The plots (a,b) in these figures show the effect of R_{Ex} on the bending stiffness of the outer layer "EI_2" and the total bending stiffness of the tube "EI_T". For smaller value of R_{Ex}, the value of bending stiffness of the outer layer (EI_2) is lower. It is also shown that the bending stiffness of the inner layer (EI_1) is larger for small values of t/D_o, and then it decreases after specific value of t/D_o due to the

effect of I_1. So, it is concluded that the decrease in the total bending stiffness of the tube beyond a certain t/D_o is because of the lower contribution of the outer layer extensional stiffness and adding to that the lower value of the inner layer moment of inertia when $t_1/t=0.5$ and R_{Ex} is less than unity.

2.2.4 Tube of layers having equal moments of inertia

The moments of inertia fractions for the tube layers are satisfying the following equation:

$$I_{fr,1} = I_{fr,2} = 0.5 \tag{2.20}$$

This case can be achieved at specified value of t_1/t, which can be calculated using equation (2.16) for any value of t/D_o. The main benefit of having equal $I_{fr,n}$ is that both effects of the layers location with respect to the tube axis and the difference in layers radii of curvature are vanished. This situation has a special influence on the bending stiffness of the tube. The bending stiffness is calculated using equation **(2.18)**, such that:

$$\langle EI \rangle = E_{x,1} I_T (0.5 + 0.5 R_{Ex}) = 0.5 E_{x,1} (1 + R_{Ex}) I_T = 0.5 (E_{x,1} + E_{x,2}) I_T \tag{2.21}$$

From this equation, one can observe that this case is similar to a tube made of one layer of isotropic material of extensional stiffness value equal to the average of the extensional modulus of the two layers. The bending stiffness behavior for this tube is increasing with the tube thickness, not affected by the location of the stiffer layer.

2.2.5 Summary

The bending stiffness of isotropic tubes has been studied to identify the controlling variables for this property. The design variables for an isotropic tube made of two different isotropic materials are D_o, t/D_o, and t_1/t with $E_{x,n}$ of the isotropic layers. The bending stiffness behavior has been presented for thick-walled isotropic tubes composed of two layers of equal thickness at different values of R_{Ex}, showing that the bending stiffness is decreasing with increasing t/D_o after specified value of t/D_o,

when the inner layer is stiffer than the outer one. This is because of lower value of inner layer moment of inertia causing lower contribution in the tube bending stiffness even if it is the stiffer layer. Adding to that, the small contribution exhibited by the outer layer in the total bending stiffness is because of its smaller extensional stiffness. It is also concluded that the cases of having equal moments of inertia cancel the effect of the location of the stiffer layer and the bending stiffness is always increasing with t/D_o as if the tube is made of one material of extensional stiffness equal to the average of the extensional stiffness of the two layers. These cases are achieved at specific value of t_1/t for every value of t/D_o.

After presenting the bending stiffness of isotropic tubes and explaining its behavior in the case of a stiffer inner layer, new questions come up; Is this the case for a composite tube of laminate configuration [θ/-θ] having equal layers thickness?, and if the answer is yes, how can these layers have different stiffness when they are of the same material and they have the same value of layer extensional stiffness in the direction of the tube axis. The following section presents the answers for these questions.

2.3 Bending stiffness of Composite tubes

In this section, the bending stiffness behavior for thick-walled composite tubes is analyzed.

2.3.1 Effective extensional stiffness

Equation **(2.3)** is rearranged in order to have analogous form to bending stiffness equation of isotropic tubes equation, equation (2.4), defining new parameters helping in the analysis of the bending stiffness property, such that:

$$\langle EI\rangle = \sum_{n=1}^{N} E_{x,n}\left\{\sum_{i=1}^{4}\frac{\pi K_{i,n}}{I_n}\left[\bar{S}_{16,n}.g_{i,n}.m_{i,n} - \bar{S}_{13,n} - \bar{S}_{12,n}(m_{i,n}+1)\right]\left[\frac{\left(b_n^{(m_{i,n}+2)} - a_n^{(m_{i,n}+2)}\right)}{(m_{i,n}+2)}\right] + \left[1-\mu_{1,n}(\bar{S}_{13,n}+3\bar{S}_{12,n}) + 2\mu_{2,n}\bar{S}_{16,n}\right]\right\} I_n \quad \textbf{(2.22)}$$

So, the formula is redefined in the following form

$$\langle EI\rangle = \sum_{n=1}^{N}\langle EI(n)\rangle = \sum_{n=1}^{N} E_{x,n}\{Coef_n\}I_n \quad \textbf{(2.23)}$$

Where:

$$Coef_n = \sum_{i=1}^{4}\frac{\pi K_{i,n}}{I_n}\left[\bar{S}_{16,n}.g_{i,n}.m_{i,n} - \bar{S}_{13,n} - \bar{S}_{12,n}(m_{i,n}+1)\right]\left[\frac{\left(b_n^{(m_{i,n}+2)} - a_n^{(m_{i,n}+2)}\right)}{(m_{i,n}+2)}\right] + \left[1-\mu_{1,n}(\bar{S}_{13,n}+3\bar{S}_{12,n}) + 2\mu_{2,n}\bar{S}_{16,n}\right] \quad \textbf{(2.24)}$$

Studying equations (2.23) and (2.24), it is found that $Coef_n$ is a dimensionless parameter function of the geometric parameters, material properties, and the orientation angle of the composite layer with the layers interaction parameters $K_{i,n}$. By multiplying $Coef_n$ with $E_{x,n}$ a new parameter will be defined called "$E_{eff,n}$", which is denoting the effective extensional stiffness of the composite layer (n). This new has the same units as E_x. This new parameter represents the contribution of the layer mechanical properties in its bending stiffness property, including the effects of the layer geometry and the

interaction within the layers of the tube. $E_{eff,n}$ is used in this study in order to understand the bending stiffness phenomenon of composite tubes. Equation (2.23) is modified to the following form:

$$\langle EI \rangle = \sum_{n=1}^{N} E_{eff,n} I_n \tag{2.25}$$

Such that $E_{eff,n}$ is equal to the following equation:

$$E_{eff,n} = E_{x,n} \left\{ \sum_{i=1}^{4} \frac{\pi K_{i,n}}{I_n} \left[\bar{S}_{16,n}.\, g_{i,n}.\, m_{i,n} - \bar{S}_{13,n} - \bar{S}_{12,n}(m_{i,n}+1) \right] \left[\frac{\left(b_n^{(m_{i,n}+2)} - a_n^{(m_{i,n}+2)} \right)}{(m_{i,n}+2)} \right] + \left[1 - \mu_{1,n}(\bar{S}_{13,n} + 3\bar{S}_{12,n}) + 2\mu_{2,n}\bar{S}_{16,n} \right] \right\} \tag{2.26}$$

$E_{eff,n}$ is a function of a_n, b_n, $g_{i,n}, m_{i,n}, \mu_{i,n}$, $\bar{S}_{16,n}, \bar{S}_{13,n}, \bar{S}_{12,n}$, $K_{i,n}$, $1/I_{fr,n}$ and $E_{x,n}$. The independent design variables of $E_{eff,n}$ are functions of t/D_o, t_1/t, θ_n, and all on axis composite material properties of layer n. It should be emphasized that D_o is not among the design variables of $E_{eff,n}$.

2.3.2 Composite tube formed of two layers

For a tube composed of two layers:

$$\langle EI \rangle = E_{eff,1} I_1 + E_{eff,2} I_2 \tag{2.27}$$

Comparing equation (2.27) with equation (2.4) of isotropic tubes, the following points are observed:

- The design variables for the total bending stiffness of composite tubes are D_o, t/D_o, t_1/t, composite material properties and fiber orientation angles of the composite layers.
- Moments of inertia of the composite tube layers have the same behavior of those of the isotropic tube; the outer layer has larger moment of inertia than the inner one when $t_1/t=0.5$, because of its location farther from the tube axis and its larger radius of curvature.

- The constant values of extensional stiffness of isotropic layers are replaced by the parameter $E_{eff,n}$, which is a complicated function in the case of composites, incorporating both geometric and material properties of the composite layer with the interaction effects among the total layers of the tube.

According to these observations, it is shown that the parameter $E_{eff,n}$ is not constant. It could be expected that the value of $E_{eff,1}$ can be different from $E_{eff,2}$ even in the situation of equal thickness of layers for [θ/-θ] laminate configuration, and this inequality would give a chance that $E_{eff,1}$ can be larger than $E_{eff,2}$, leading to the existence of the observed curious bending stiffness behavior in Figure 2.1. In the next subsection, more investigation for $E_{eff,n}$ is presented to verify this expectation.

2.3.2.1 Effect of t/D_o

It is required to study the effect of the geometric design variable t/D_o and how the geometry of composite layers can alter $E_{eff,n}$ when the layers have equal thickness. In order to demonstrate the variation of $E_{eff,n}$ versus t/D_o, the other design variables have constant values: $t_1/t=0.5$, and $\theta=15^o$ for [θ/-θ] configuration, using Carbon/Epoxy in the analysis. For this laminate configuration:

$$E_{x,1} = E_{x,2} = E_x \tag{2.28}$$

Since E_x is not function of any geometric design variable, $E_{eff,n}/E_x$ can be used as a normalized value of $E_{eff,n}$ when considering constant value of θ. The variation of the normalized $E_{eff,n}$ with respect to t/D_o is plotted in Figure 2.9:

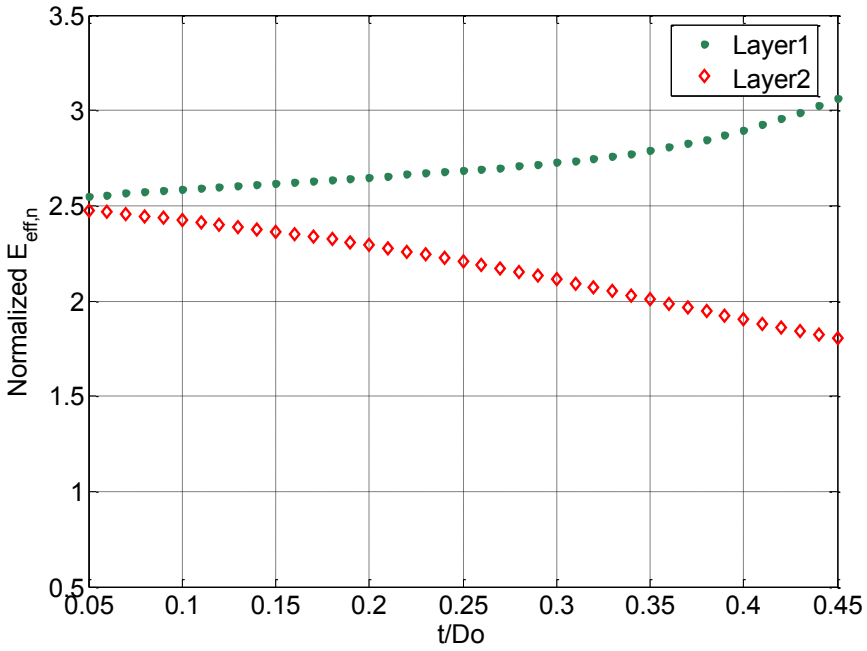

Figure 2.9: Normalized $E_{eff,n}$ ($E_{eff,n}/E_x$) versus t/D_o for [θ/-θ], t_1/t=0.5, θ=15°

From this figure, one can observe that at t/D_o =0.05, that $E_{eff,1}$ of inner layer and $E_{eff,2}$ of the outer layer have close values however as t/D_o increases the value of $E_{eff,1}$ increases while $E_{eff,2}$ decreases. For t/Do=0.45, $E_{eff,1}$ is highly larger than $E_{eff,2}$. This means that the ratio of $E_{eff,2}/ E_{eff,1}$ is decreasing with increasing t/D_o . This makes the inner layer to have a stiffer behavior compared to the outer layer. This result validates the expected inequality, explaining the reason of having this interesting bending behavior for composite tubes of [θ/-θ] configuration, and equal layers thickness.

The reason of this variation is because $E_{eff,n}$ is a function of $(1/I_{fr,n})$. Figure 2.10 shows the variation of $I_{fr,n}$ with t/D_o.

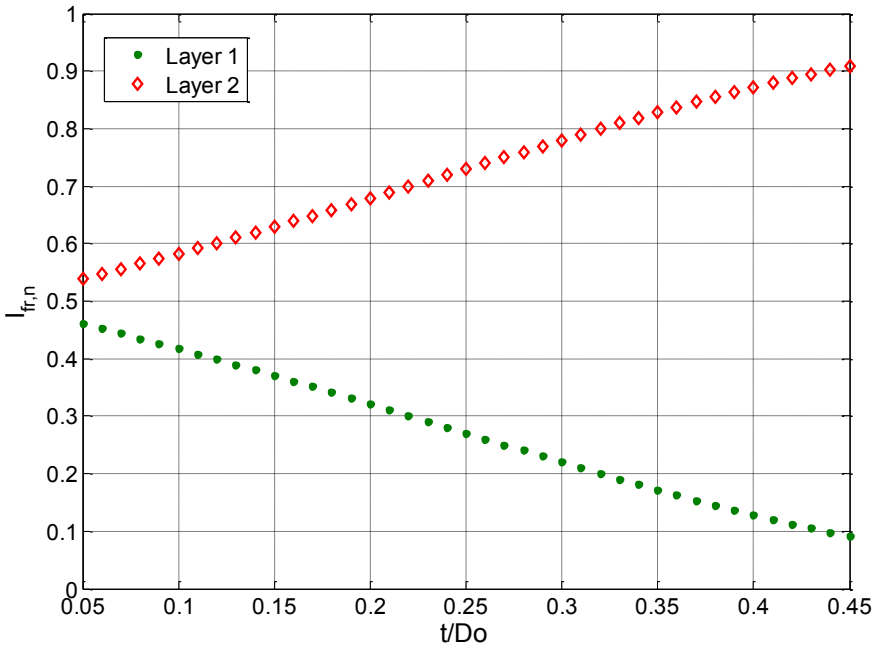

Figure 2.10: Moment of inertia fractions versus t/D_o for $t_1/t=0.5$

Comparing Figure 2.9 to Figure 2.10, one can observe the inverse proportional relation between $E_{eff,n}$ and $I_{fr,n}$. The bending stiffness values of the layers and of the total tube are calculated over the range of t/D_o, as shown in Figure 2.11. The values are normalized using equation (2.7), using E_x of composite layer at $\theta=15^o$ instead of the extensional modulus of the isotropic layer $E_{x,1}$.

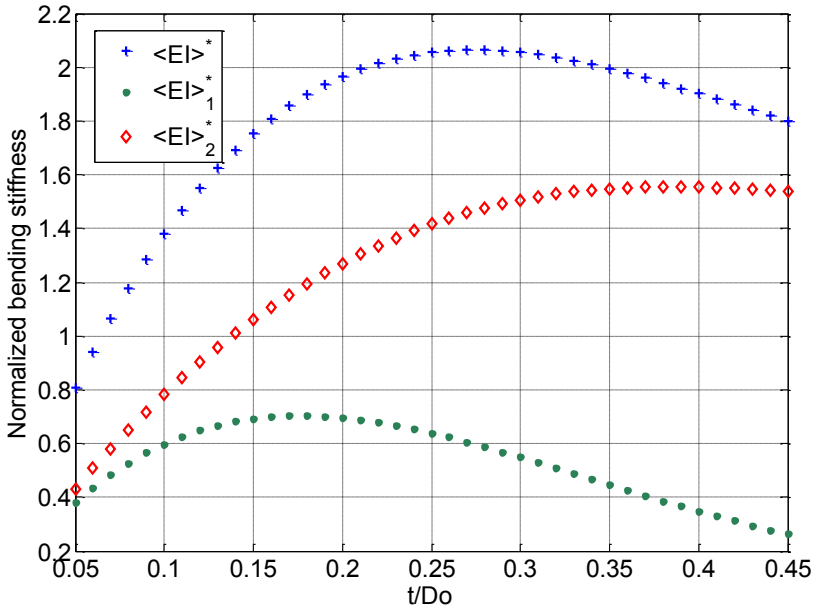

Figure 2.11: Normalized bending stiffness of a composite tube vs. t/D_o for $[\theta/-\theta]$, $t_1/t=0.5$, $\theta=15^o$

EI_1 and EI_2 are the bending stiffness of the inner and outer layers of the composite tube, respectively. Comparing Figure 2.2 to Figure 2.11, one can see a similar bending behavior for the composite tube and the isotropic one when R_{Ex} is less than unity. It is important to note that the case of composite tube is more complicated compared to the isotropic tube; For isotropic tubes $E_{x,1}$ and $E_{x,2}$ of the layers are constant values such that when R_{Ex} is constant when changing t/D_o, while for the composite tube layers, the ratio of $E_{eff,2}$ to $E_{eff,1}$ is decreasing with increasing t/D_o.

Also it is important to note that although $E_{eff,1}$ is much higher than that of layer2 at $t/D_o=0.45$, its moment of inertia is much lower than that of outer layer, making EI_2 to be five times of EI_1, because of the small contribution of I_1 compared to I_2 at $t_1/t=0.5$, as demonstrated in Figure 2.3. From this result, one can observe a double effect of I_n on the bending stiffness of composite tubes. The first effect is on $E_{eff,n}$ via $I_{fr,n}$ and the second effect is by itself as the second parameter in the bending stiffness equation, equation (2.4). It is important to check the bending behavior for other values of t_1/t. In the following subsection, the effect of t_1/t is investigated.

2.3.2.2 Effect of t_1/t

The normalized values of parameter $E_{eff,n}$ is plotted for the range of t_1/t , taking t/D_o=0.45, and θ=15°, as shown in Figure 2.12.

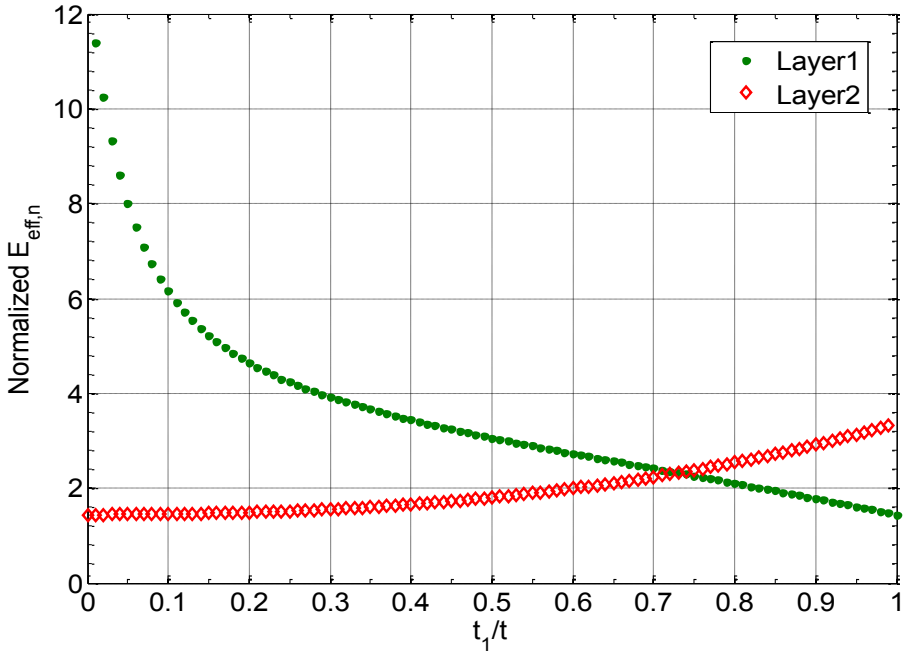

Figure 2.12: : ($E_{eff,n}/E_x$) versus t_1/t for [θ/-θ], t/D_o=0.45, θ=15°

The figure shows that $E_{eff,1}$ is decreasing with increasing the thickness of the inner layer, while $E_{eff,2}$ is increasing. This can be explained from the inverse behavior of $I_{fr,n,}$ demonstrated in Figure 2.6. Also one can observe that the intersection point in Figure 2.12 is at t_1/t=0.73 which is different than that of equal $I_{fr,n}$ at t_1/t=0.82. The reason of that is because $E_{eff,n}$ is also function of a_n and b_n of the composite layers leading to different intersection points. The case of equal $E_{eff,n}$ is presented in details latter on.

Now, turning to study the effect of $E_{eff,n}$ variation on the bending stiffness of the composite tube. Using D_o=60mm, t/D_o=0.45, and θ=15°, the bending stiffness is calculated over the t_1/t range. The results are presented Figure 2.13.

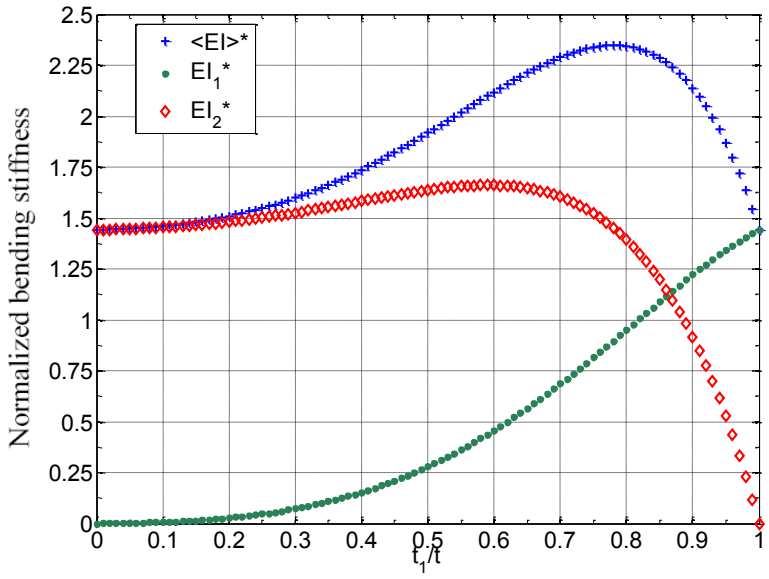

Figure 2.13: Normalized bending stiffness of a composite tube vs. t_1/t for [θ/-θ], t/D_o =0.45, θ=15°

The following points are observed from this figure

- The figure shows a large variation in the bending stiffness over the range of t_1/t; despite the tubes have constant D_o, t/D_o, and θ. In other words, the composite tubes are of the same inner and outer diameters, having the same mass, same material and same value of E_x. However a large variation in the total bending stiffness is illustrated. This is because of the large variation of $I_{fr,n}$ and $E_{eff,n}$ values as presented in Figure 2.6 and Figure 2.12, respectively. This causes a large change in the contributions of the bending stiffness of the tube layers in the total bending stiffness.
- For t_1/t=0 or 1, this means that the tube is made of one layer of θ or –θ orientation. One can observe that these two cases have the smallest value of bending stiffness, compared to the tube configuration [θ/-θ] for other values of t_1/t. This is because the value of $E_{eff,n}$ of one composite layer is very small, as shown in Figure 2.13.

- It is also presented in Figure 2.6 that at t/D_o=0.45, the case of equal $I_{fr,n}$ is obtained at t_1/t=0.82, and Figure 2.12 shows that the case of equal $E_{eff,n}$ is achieved at t_1/t=0.73 for θ=15°. Figure 2.13 illustrates that the maximum value of bending stiffness is obtained at t_1/t=0.78, a different value from the former cases. This is because the maximum bending stiffness is obtained at a point providing optimum combination of the layers moments of inertia with their effective extensional stiffnesses. In other words the maximum bending stiffness is achieved at optimum contribution from layers moments of inertia and layers material properties.

2.3.2.3 Cases of equal $E_{eff,n}$

The cases of equal $E_{eff,n}$ provide a special feature: the tube is similar to that made of one isotropic material of extensional modulus equal to E_{eff} and the bending stiffness has the following form

$$\langle EI \rangle = E_{eff}(I_1 + I_2) = E_{eff} I_T \tag{2.29}$$

In this situation, the bending stiffness behavior over t/D_o is similar to that presented in Figure 2.2 when R_{Ex} equal to unity. The values of t_1/t providing equal E_{eff} are obtained numerically for every t/D_o, fixing the value of θ. This is done by plotting $E_{eff,n}$ over t_1/t range to specify the point of intersection of the $E_{eff,1}$ with $E_{eff,2}$. Figure 2.12 shows that equal E_{eff} is located at t_1/t=0.73 for t/D_o=0.45, and θ=15°. The intersection points and the corresponding values of E_{eff} over t/D_o are plotted in Figure 2.14 for carbon-epoxy composite material at θ=15°.

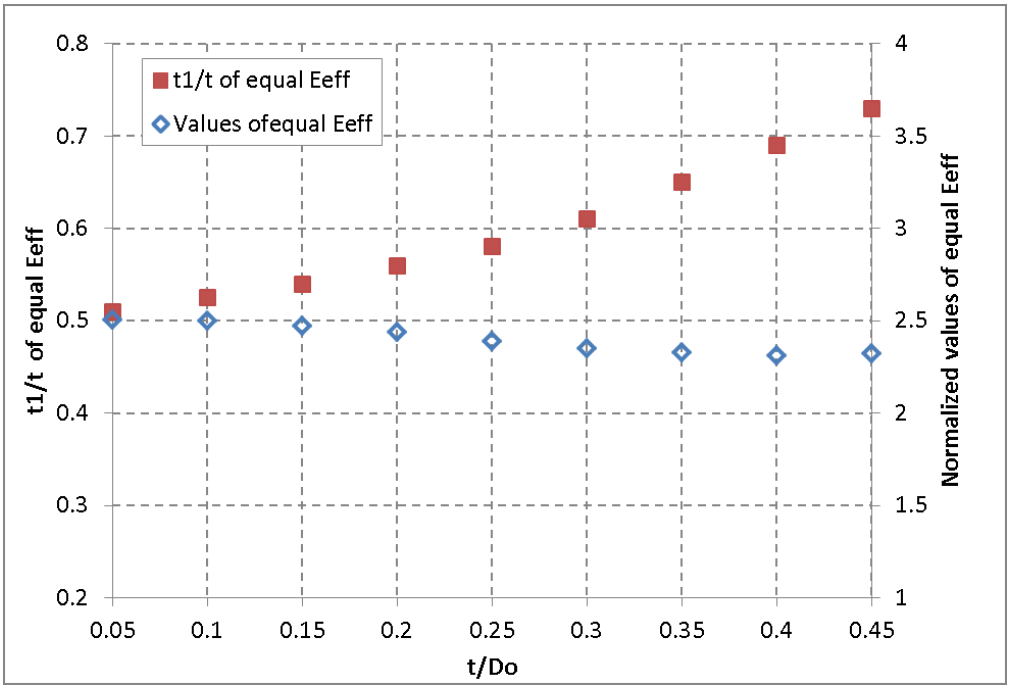

Figure 2.14: Cases of equal E_{eff} versus t/D_o for [θ/-θ], θ=15°

The figure shows that the points permitting equal E_{eff} are shifting away from $t_1/t=0.5$ as t/D_o increases as the case for equal I_n presented in Figure 2.7. Also one can notice the values of E_{eff} at these points are slightly decreasing, which is explained in details in chapter 3.

2.4 Summary

The shared design variables of isotropic tubes and composite tubes are D_o, t/D_o, t_1/t. Adding to them the composite material properties with θ for the case of composite tubes. A new parameter $E_{eff,n}$ is defined, based on three-dimensional elasticity theory presented in [3]. This parameter is utilized in this parametric study as an indicator for the contribution of the mechanical properties of the composite layer in the bending stiffness property of the composite tube. The interesting bending behavior of composite tubes of equal layers thickness and [θ/-θ] configuration is investigated and the reason of this behavior is known to be due to lower contribution of the inner layer moment of inertia,

adding to that the lower contribution of the mechanical properties of the outer one, represented in $E_{eff,2}$.

It is also illustrated that for $t_1/t=0.5$, the moment of inertia of the outer layer of the tube is larger than the inner layer due to the location of the outer layer farther from the tube axis and due to its bigger radius of curvature. It is important to say that these two effects are included in the formula used for calculating the bending stiffness of composite tubes since it is based on three-dimensional elasticity theory.

Also, the double effect of I_n on the bending stiffness of composite layer is identified: The first effect is on $E_{eff,n}$ which is inversely proportional to $I_{fr,n}$ and the second one is by itself as the second parameter in the bending stiffness equation.

More questions arose about the bending stiffness phenomenon. First, Figure 2.9 shows that the value of $E_{eff,n}$ is more than twice of that of E_x which motivates one to know the reason for this large improvement in E_x contribution to the bending stiffness of the layer. Also, what do the cases of equal $E_{eff,n}$ mean from the structural point of view? And why are these E_{eff} values decreasing over the t/D_o shown in Figure 2.14? Lastly, it is necessary to check the effect of θ on the bending stiffness behavior. These new questions are discussed in the next chapter.

Chapter 3

More understanding for the bending stiffness property

3.1 Introduction

In last chapter, the bending stiffness equation for composite tubes is rearranged to have the following equation:

$$\langle EI \rangle = \sum_{n=1}^{N} E_{eff,n} I_n \tag{3.1}$$

And $E_{eff,n}$ is found to have the following form:

$$E_{eff,n} = E_{x,n} \left\{ \sum_{i=1}^{4} \frac{\pi K_{i,n}}{I_n} \left[\bar{S}_{16,n} . g_{i,n} . m_{i,n} - \bar{S}_{13,n} - \bar{S}_{12,n} (m_{i,n} + 1) \right] \left[\frac{\left(b_n^{(m_{i,n}+2)} - a_n^{(m_{i,n}+2)} \right)}{(m_{i,n} + 2)} \right] + \left[1 - \mu_{1,n} (\bar{S}_{13,n} + 3\bar{S}_{12,n}) + 2\mu_{2,n} \bar{S}_{16,n} \right] \right\} \tag{3.2}$$

Where:

$E_{x,n}$ is the extensional stiffness of the composite layer (n). Noting that $E_{x,n}$ of (θ)= $E_{x,n}$ of (-θ)=E_x. The closed form equation of E_x for an orthotropic layer is known to have the following form [29]:

$$E_x = \frac{E_1}{\cos^4\theta + \left(\frac{E_1}{G_{12}} - 2\nu_{12} \right) \cos^2\theta \sin^2\theta + \frac{E_1}{E_2} \sin^2\theta} \tag{3.3}$$

Where:

E_1, E_2 --- extensional moduli in fiber and transverse directions of layer n, respectively

G_{12}, ν_{12} --- Shear modulus and in-plane Poisson's ratio of layer n, respectively

One can observe that the design variables of E_x are E_1, E_2, G_{12}, ν_{12}, and θ. This means that E_x is only a function of the composite material properties of the layer. In other words the layer geometry and layer interaction with adjacent layers has no effect on E_x.

While from equation (3.2), one can see that $E_{eff,n}$ is function of E_x and the dimensionless quantity between braces. This quantity contains material dependent parameters and geometric parameters. This is added to coefficients solved from the solutions of the differential equations of elasticity theory for the pure bending loading and variables obtained from the solution of the equilibrium equations for the whole tube as stated in Appendix A.

$E_{eff,n}$ can be defined as the contribution of composite material properties in the bending stiffness of the layer (n) in the composite tube including interaction effect between adjacent layers and the effect of geometric parameters of the layer.

In this chapter, both E_x and $E_{eff,n}$ are investigated by plotting and differentiation techniques. The effects of the composite material properties (E_1, E_2, E_3, G_{12}, G_{13} and G_{23}) are identified by differentiation of E_x and $E_{eff,n}$ with respect to these properties. These derivatives are considered to be quantifiers from which one can identify the contributions of the material properties in E_x and $E_{eff,n}$.

From equation (3.3), E_x can be differentiated analytically with respect to the material properties. $E_{eff,n}$ is a very complicated function containing many variables, that obtained by solving matrix equations numerically and these variables are function in the composite material properties. Due to this complication $E_{eff,n}$ cannot be differentiated analytically.

Numerical methods are alternatively used in this situation. In this parametric study, $E_{eff,n}$ is differentiated numerically using finite difference method. More details are given about this method in the next paragraph.

3.1.1 Finite difference method

This numerical method is used to calculate numerically the partial derivative of $E_{eff,n}$ with respect to any specified material property, fixing the values for all the other design variables. The partial derivative of $E_{eff,n}$ is calculated using the following equation:

$$\left.\frac{\partial E_{eff,n}}{\partial X}\right|_{X=X_i} = \frac{E_{eff,n}(X_i + \Delta X) - E_{eff,n}(X_i - \Delta X)}{2\Delta X} \quad \textbf{(3.4)}$$

Where:

X --- any independent design variable

X_i --- specified point in the range of X

ΔX --- a very small value of X with respect to its value.

In this study, the used value of ΔX is equal to 0.5% of the concerned material property. A MATLAB code is written in order to implement the finite difference method (FDM) in calculating the partial derivatives of $E_{eff,n}$ with respect to the material properties, Appendix D.

3.2 Effect of layers Interaction on the bending stiffness of composite tubes

It is important to explain what the interaction effect is and how this effect improves the bending stiffness property of the composite layers. In order to discuss the interaction effect, the existing coupling effects in a composite layer of fibers orientation angle θ is first presented.

3.2.1 Composite layer coupling effects

For any composite layer, there are several coupling effects that make the composite layer to deform in one direction due to a generated deformation in the other directions [29].

Assuming a composite plate of fibers orientation angle θ, subjected to axial tension, one can see the deformation occurred in this layer as a result of this axial tension as shown in Figure 3.1-a.

The axial tensile (σ_x) generates a positive axial strain (ε_x), a transverse strain ($-\varepsilon_y$) and an in-plane shear strain ($-\gamma_{xy}$). However assuming that the same composite plate is subjected to a positive shear stress (τ_{xy}), one can observe the deformation occurred in this layer as a result of this shear stress as shown in Figure 3.1-b. This shear stress generates a positive in-plane shear strain (γ_{xy}), an axial strain ($-\varepsilon_x$), and a transverse strain ($-\varepsilon_y$).

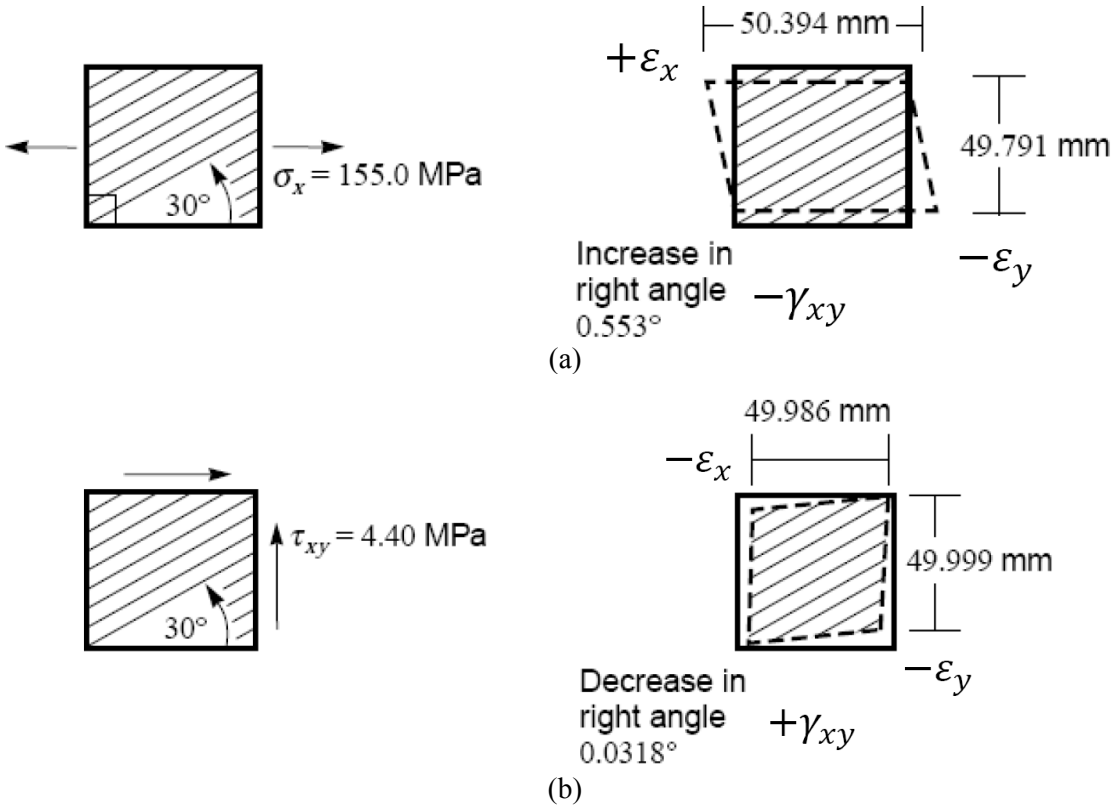

Figure 3.1: Deformations of a composite layer of fibers orientation θ, [29]

(a) Subjected to axial tension (b) Subjected to in plane shear

Some of the coupling effects that occurred in the composite layer are stated as follows:

At first, the coefficient of mutual influence of the second kind ($\eta_{xy,x}$) relates the generated in-plane shear strain (γ_{xy}) to the axial strain (ε_x) in the layer when the layer is subjected to only axial loading such that:

$$\eta_{xy,x} = \frac{\gamma_{xy}}{\varepsilon_x} = \frac{\bar{S}_{16}}{\bar{S}_{11}} = \bar{S}_{16}E_x \tag{3.5}$$

Noting that the sign of the generated (γ_{xy}) is specified according to the sign of both (ε_x) and ($\eta_{xy,x}$). The maximum value of ($\eta_{xy,x}$) is obtained at $\theta=9^o$ for carbon-epoxy as shown in Figure 3.2.

The second coupling effect is the coefficient of mutual influence of the first kind ($\eta_{x,xy}$) which relates the generated the axial strain (ε_x) to in-plane shear strain (γ_{xy}) in the layer when the layer is subjected to shear loading so that:

$$\eta_{x,xy} = \frac{\varepsilon_x}{\gamma_{xy}} = \frac{\bar{S}_{16}}{\bar{S}_{66}} = \bar{S}_{16}G_{xy}$$
$$\varepsilon_x = \eta_{x,xy}\gamma_{xy} = \bar{S}_{16}G_{xy}\gamma_{xy} \tag{3.6}$$

The maximum value of ($\eta_{x,xy}$) is at $\theta=35^o$ as illustrated in Figure 3.3.

Another coupling effect is the Poisson's ratio (ν_{xy}) which relates the generated hoop strain (ε_y) due to the axial strain (ε_x) in the layer when it is subjected to axial force as shown in the following form:

$$\nu_{xy} = -\frac{\varepsilon_y}{\varepsilon_x} = -\frac{\bar{S}_{12}}{\bar{S}_{11}} = -\bar{S}_{12}E_x$$
$$\varepsilon_y = -\nu_{xy}\varepsilon_x = \bar{S}_{12}E_x\varepsilon_x \tag{3.7}$$

The maximum value of (ν_{xy}) is at $\theta=24^o$ as illustrated in Figure 3.4

Lastly, the Poisson's ratio (ν_{xz}) relates the generated interlaminar normal strain (ε_z) due to the axial strain (ε_x) in the layer when it is subjected to axial force as shown in the following form:

$$\nu_{xz} = -\frac{\varepsilon_z}{\varepsilon_x} = -\frac{\bar{S}_{13}}{\bar{S}_{11}} = -\bar{S}_{13}E_x$$
$$\varepsilon_z = -\nu_{xz}\varepsilon_x = \bar{S}_{13}E_x\varepsilon_x \tag{3.8}$$

This variation of the Poisson's ratio (ν_{xz}) is presented in Figure 3.5

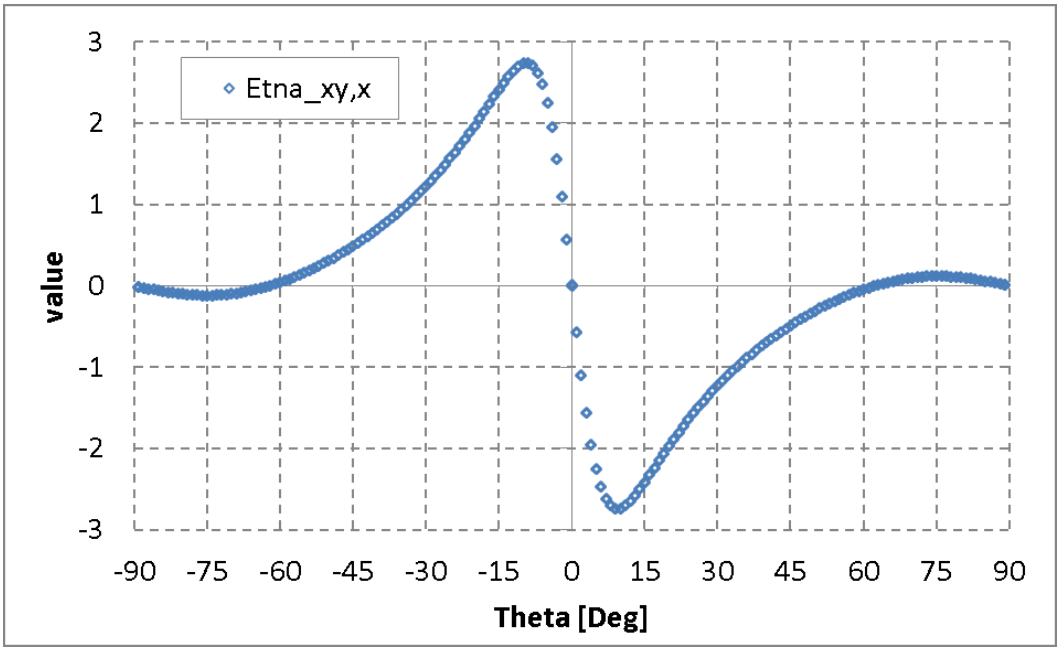

Figure 3.2: $\eta_{xy,x}$ variation with θ for carbon/epoxy

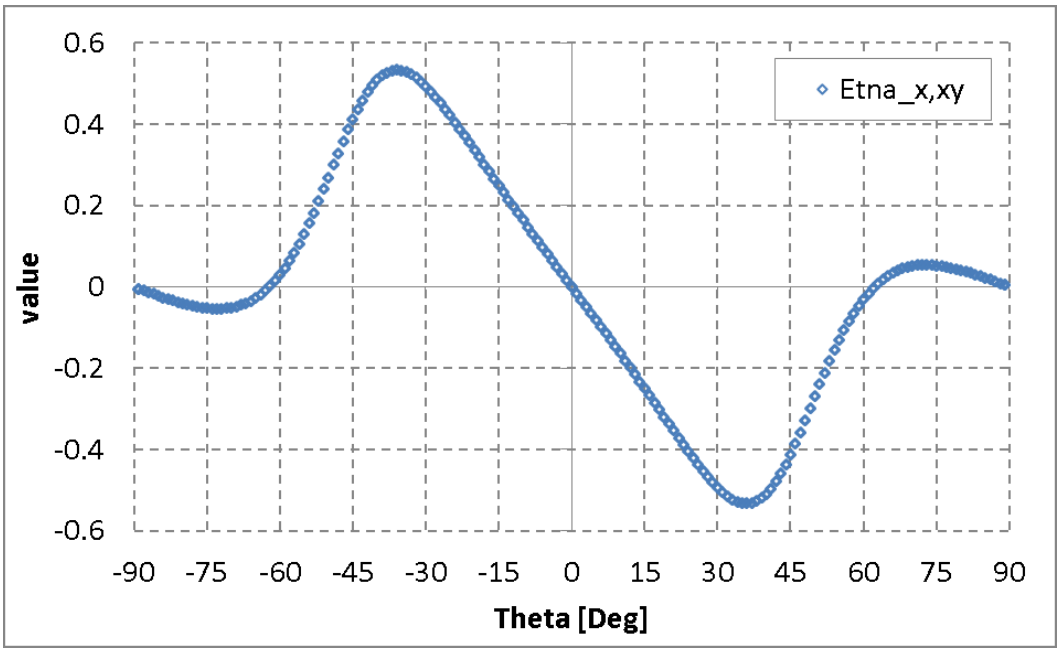

Figure 3.3: $\eta_{x,xy}$ variation with θ for carbon/epoxy

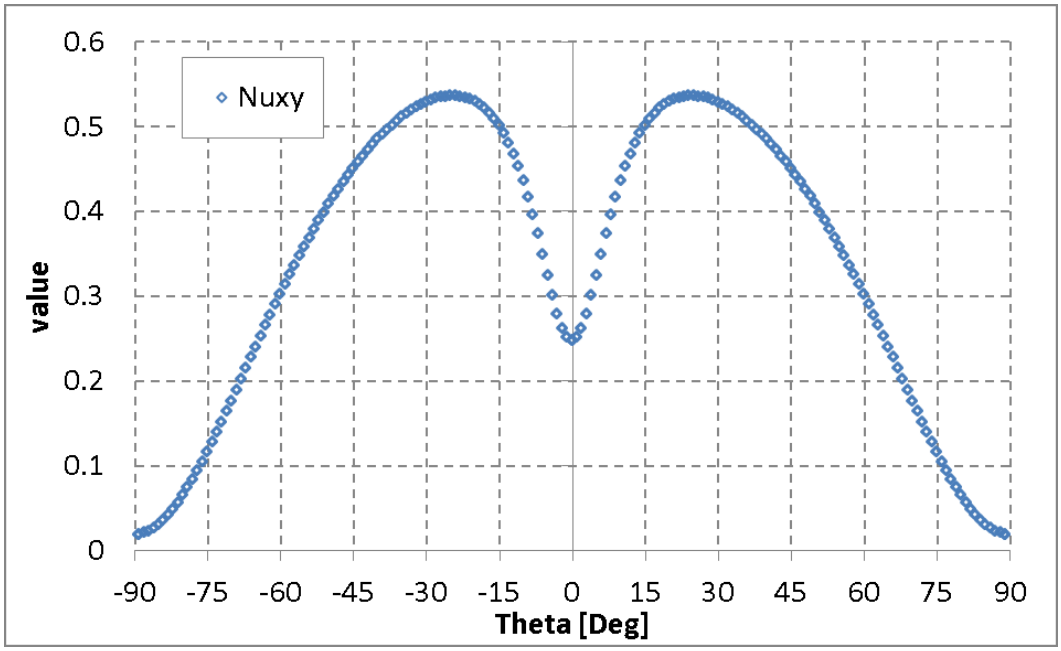

Figure 3.4: ν_{xy} variation with θ for carbon/epoxy

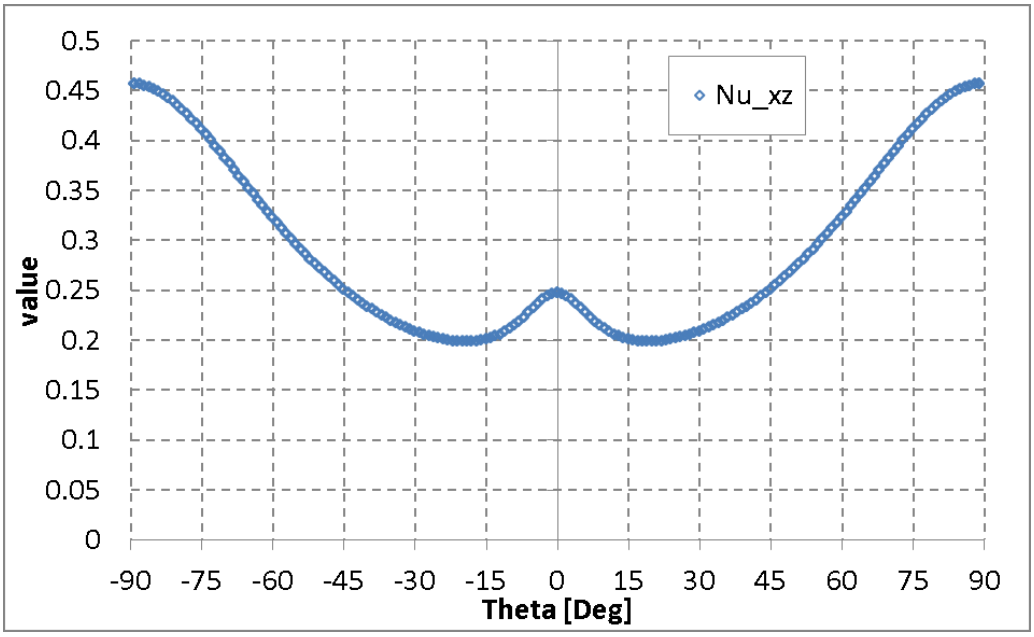

Figure 3.5: ν_{xz} variation with θ for carbon/epoxy

3.2.2 Responsible coefficients for interaction effect

It is found that ($\eta_{xy,x}$) and ($\eta_{x,xy}$) are the responsible coefficients for the interaction effect between adjacent layers in tubes of [θ/-θ] configuration under bending. In order to illustrate their role, the following examples will be presented.

3.2.2.1 Thin-walled tube made of one layer of [θ]

Turning for a composite tube made of one thin layer of [θ] stacking sequence, the tube cross section is assumed to be composed of small plate elements and each element is located at different position angle (α), as shown in Figure 3.6. Consider a pure bending moment is applied on this tube such that the elements of the upper part of the tube are subjected to axial compression while those of the lower part are subjected to axial tension.

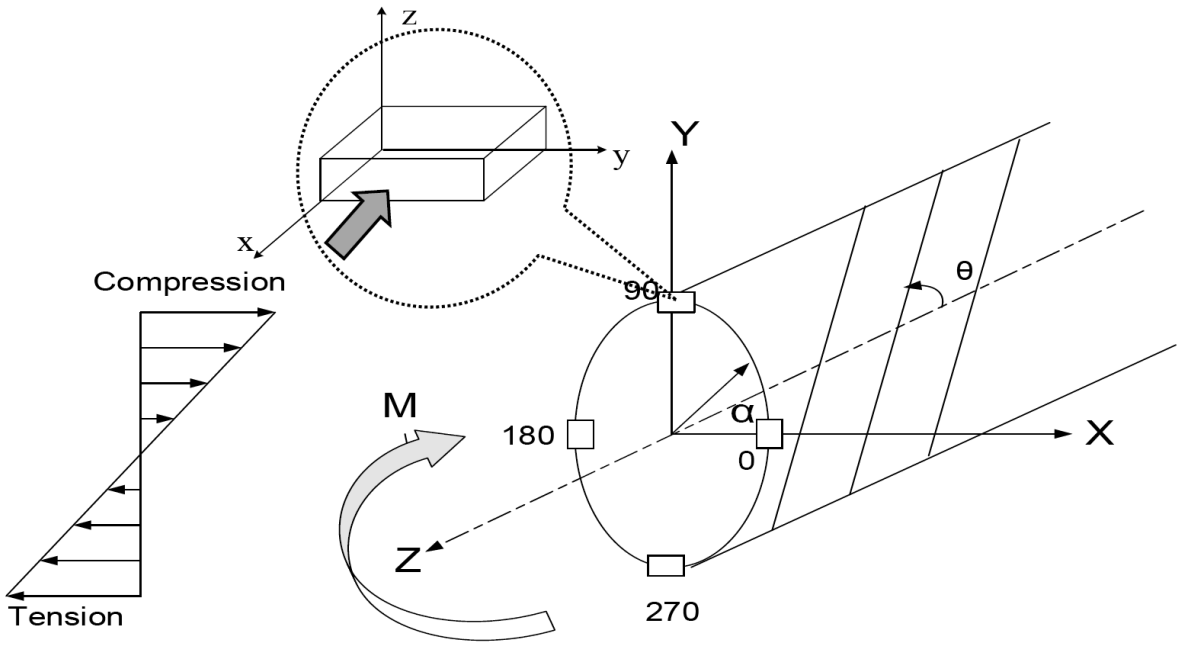

Figure 3.6: Composite tube subjected to pure bending moment

Concerning the plate element at $\alpha=90^{o}$, shown in Figure 3.6, one can observe that the applied compressive forces will generate a negative axial strain (ε_x), and a positive in-plane shear strain (γ_{xy}) as shown in Figure 3.7.

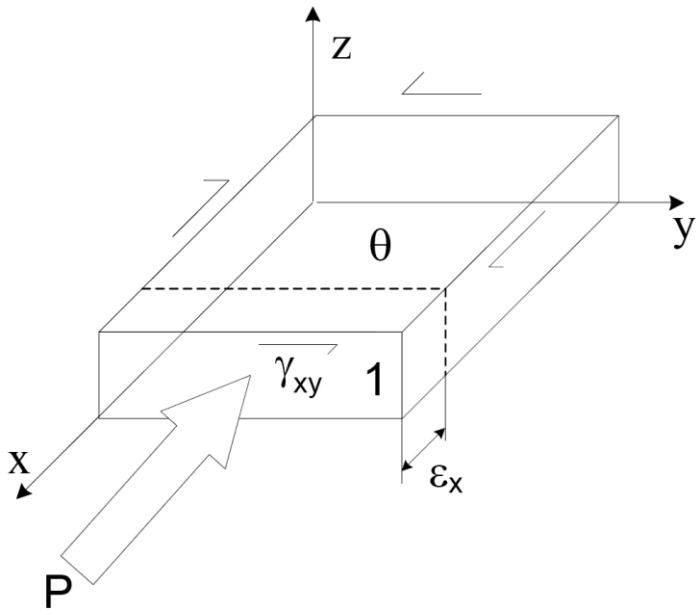

Figure 3.7:Plate element of a single layered tube under bending, at the compression side

The constitutive equations for this element have the following matrix equation:

$$\begin{Bmatrix} \varepsilon_x \\ \varepsilon_y \\ \varepsilon_z \\ \gamma_{yz} \\ \gamma_{xz} \\ \gamma_{xy} \end{Bmatrix} = \begin{bmatrix} \bar{S}_{11} & \bar{S}_{12} & \bar{S}_{13} & 0 & 0 & \bar{S}_{16} \\ \bar{S}_{12} & \bar{S}_{22} & \bar{S}_{23} & 0 & 0 & \bar{S}_{26} \\ \bar{S}_{13} & \bar{S}_{23} & \bar{S}_{33} & 0 & 0 & 0 \\ 0 & 0 & 0 & \bar{S}_{44} & \bar{S}_{45} & 0 \\ 0 & 0 & 0 & \bar{S}_{45} & \bar{S}_{55} & 0 \\ \bar{S}_{16} & \bar{S}_{26} & \bar{S}_{36} & 0 & 0 & \bar{S}_{66} \end{bmatrix} \begin{Bmatrix} \sigma_x \\ \sigma_y \\ \sigma_z \\ \sigma_{yz} \\ \sigma_{xz} \\ \sigma_{xy} \end{Bmatrix} \quad \textbf{(3.9)}$$

Since the element is subjected to only axial stress, the in-plane shear strain is calculated from the following equation:

$$\gamma_{xy} = \bar{S}_{16}\sigma_x \quad \textbf{(3.10)}$$

Since from equation (3.5), the generated in-plane shear strain have the following value:

$$\gamma_{xy} = \eta_{xy,x}\varepsilon_x \tag{3.11}$$

So, from equations (3.11) and (3.12), one can observe that:

$$\frac{\sigma_x}{\varepsilon_x} = \frac{\eta_{xy,x}}{\bar{S}_{16}} = E_x \tag{3.12}$$

Since $E_{eff,n}$ is considered as the effective extensional stiffness including the interaction effects and the geometric effects, and as the tube is made of one thin layer of [θ], so:

$$\begin{aligned} E_{eff,n} &= fn\left(\frac{\sigma_x}{\varepsilon_x}, layer\ geometric\ effects\right) \\ E_{eff,n} &= fn(E_x, layer\ geometric\ effects) \end{aligned} \tag{3.13}$$

In order to validate equation (3.13), the variation of E_x versus θ is plotted in Figure 3.8, for carbon-epoxy composite material. The values are normalized using E_1.

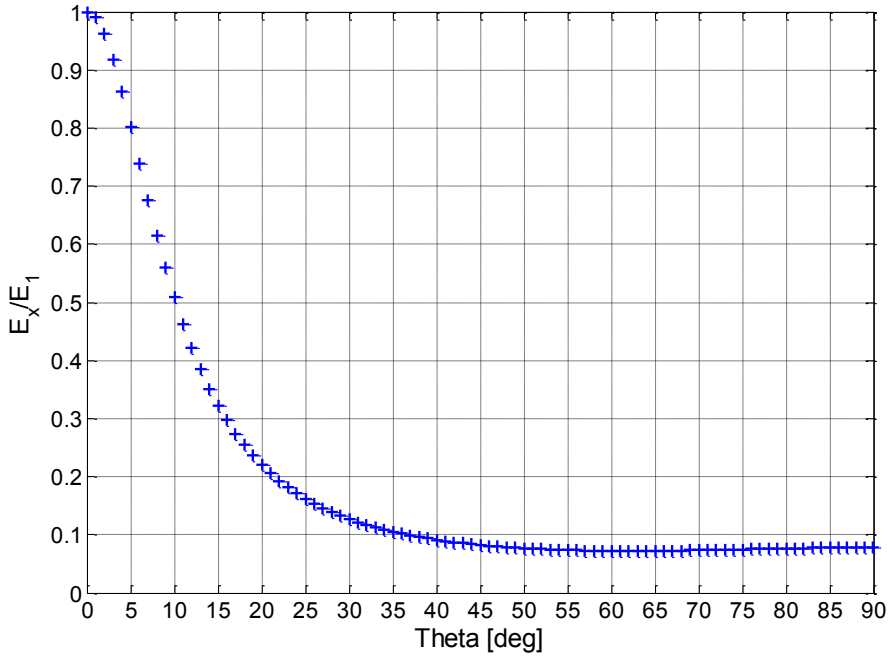

Figure 3.8: Variation of Ex with θ for Carbon/Epoxy

The figure shows that the value of E_x drops severely when θ value goes away from zero such that E_x loses nearly 70% of its value at $\theta=15^o$.

The variation of E_{eff} with θ is calculated for a relatively thin-walled composite tube made of one layer, of $t/D_o=0.05$. The calculated values of E_{eff} are compared to E_x and plotted in Figure 3.9. The values are normalized by dividing by E_1.

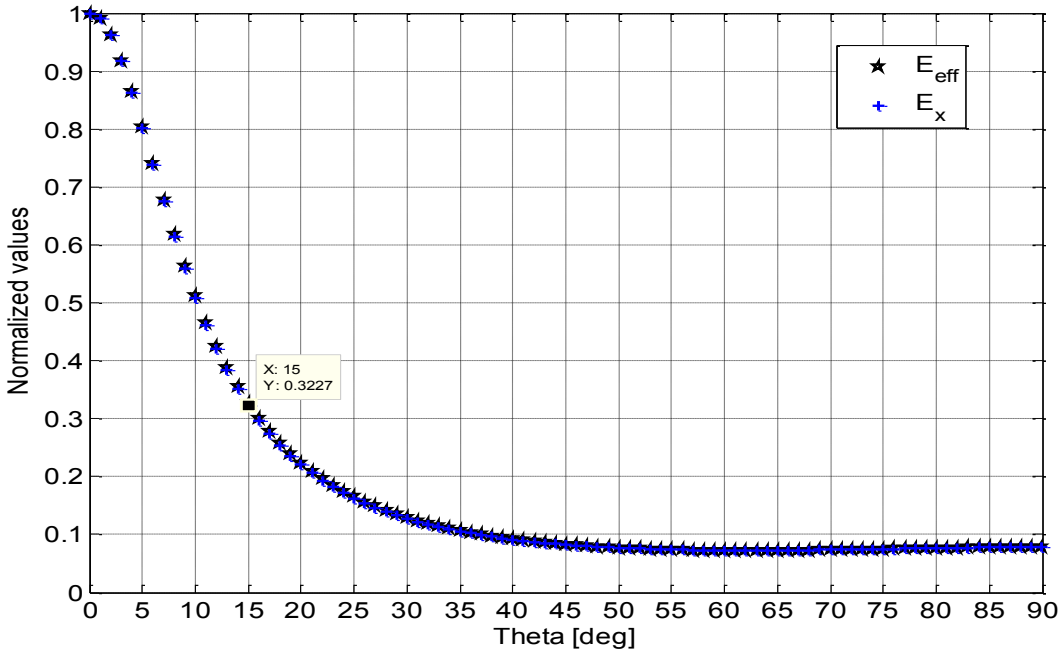

Figure 3.9: $E_{eff,n}$ versus E_x for single layered tube of [θ], $t/D_o=0.05$

One can see that the curve of E_{eff} coincides with E_x which validates equation (3.13). Also one can observe that the layer geometry has no effect on E_{eff}. This is because the layers are thin.

The tube bending stiffness is calculated using equation (3.1), and the values are normalized using the following equation:

$$\langle EI^* \rangle = \frac{\langle EI \rangle}{E_1 I_T} \tag{3.14}$$

Figure 3.9 is also considered to be the normalized values of the tube bending stiffness. This is explained when substituting in equation (3.14) by the moment of inertia of the layer which is equal to the total moment of inertia of the tube. The normalized value of the tube bending stiffness is equal to 0.3227 at $\theta=15^{o}$.

3.2.2.2 Thin-walled tube made of [θ/-θ] having equal layers thickness

Considering the composite tube, shown in Figure 3.6, is made of two thin layers of [θ/-θ], the plate element at $\alpha=90^{o}$ will be as shown in Figure 3.10.

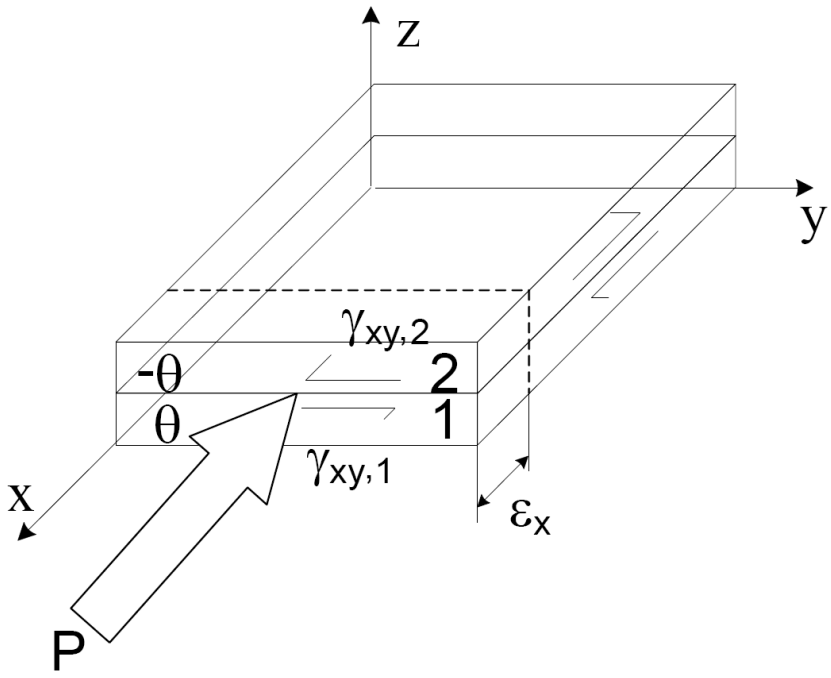

Figure 3.10: Plate element of a tube made of [θ/-θ] under bending, at the compression side

Due to compression, one can observe that a negative axial strain (ε_x) is generated in both layers. From Figure 3.10, one can see that:

$$\eta_{xy,x}\big|_{Layer1} = -\eta_{xy,x}\big|_{Layer2} \qquad \textbf{(3.15)}$$

So, the generated in-plane shear strain (γ_{xy}) in the inner layer (Layer1) is opposing the generated in-plane shear strain in the outer layer (Layer2), such that:

$$\gamma_{xy} = 0 \; at \; interface \tag{3.16}$$

This constrained the interface causing generation of an in-plane shear stress (τ_{xy}). Substituting by equation (3.16) in the constitutive matrix equation (3.9), to have the following equation:

$$\gamma_{xy} = 0 = \bar{S}_{16}\sigma_x + \bar{S}_{66}\tau_{xy} \tag{3.17}$$

The in-plane shear stress will have the following equation:

$$\tau_{xy} = -\frac{\bar{S}_{16}}{\bar{S}_{66}}\sigma_x = -\eta_{xy,x}\sigma_x \tag{3.18}$$

Also since from constitutive matrix equation (3.9)

$$\varepsilon_x = \bar{S}_{11}\sigma_x + \bar{S}_{16}\tau_{xy} \tag{3.19}$$

Substituting by equation (3.18) into equation (3.19), one can observe that:

$$\varepsilon_x = (\bar{S}_{11} - \bar{S}_{16}\eta_{x,xy})\,\sigma_x \tag{3.20}$$

And

$$\frac{\sigma_x}{\varepsilon_x} = \frac{1}{(\bar{S}_{11} - \bar{S}_{16}\eta_{x,xy})} \tag{3.21}$$

By multiplying equation (3.21) with E_x/E_x, it is found that:

$$\frac{\sigma_x}{\varepsilon_x} = \frac{E_x}{1 - \eta_{xy,x}\eta_{x,xy}} = E_{eff,av} \tag{3.22}$$

So, $E_{eff,n}$ is for the tube made of two thin layers of [θ/-θ] is as follows:

$$E_{eff,n} = fn(\frac{\sigma_x}{\varepsilon_x}, layer\ geometric\ effects)$$

$$E_{eff,n} = fn(E_{eff,av}, layer\ geometric\ effects) \tag{3.23}$$

In order to validate equation (3.23), the variation of $E_{eff,n}$ and $E_{eff,av}$ versus θ are calculated, assuming the tube is made of carbon-epoxy composite material and laminate configuration [θ/-θ], t/D_o=0.05, and t_1/t=0.5. The values are normalized by dividing by E_1 and plotted in Figure 3.11.

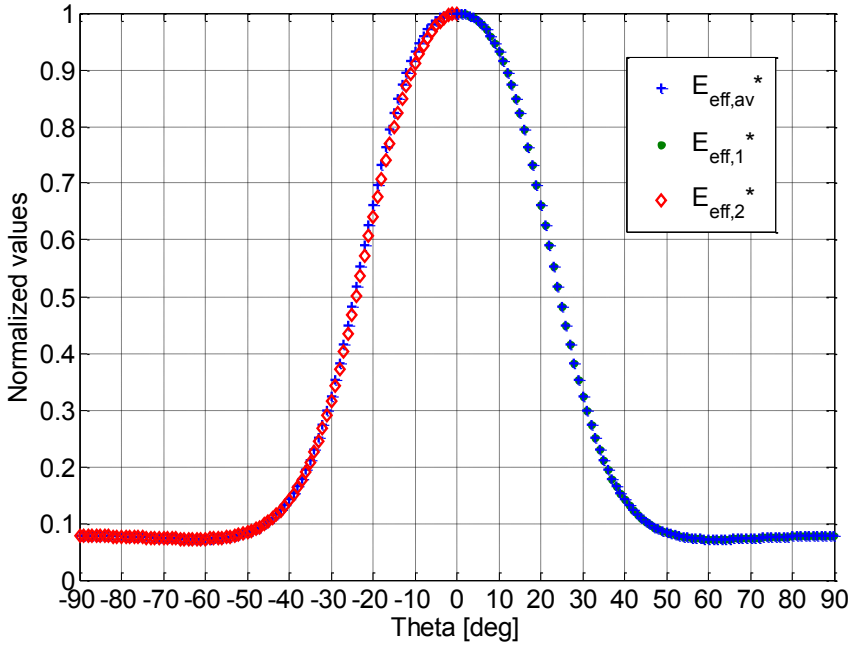

Figure 3.11: $E_{eff,n}$ versus $E_{eff,av}$ for composite tube of [θ/-θ] configuration, t/D_o=0.05, t_1/t=0.5

The Normalized bending stiffnesses for the composite layers and for the total tube are calculated over the range of θ and plotted in Figure 3.12.

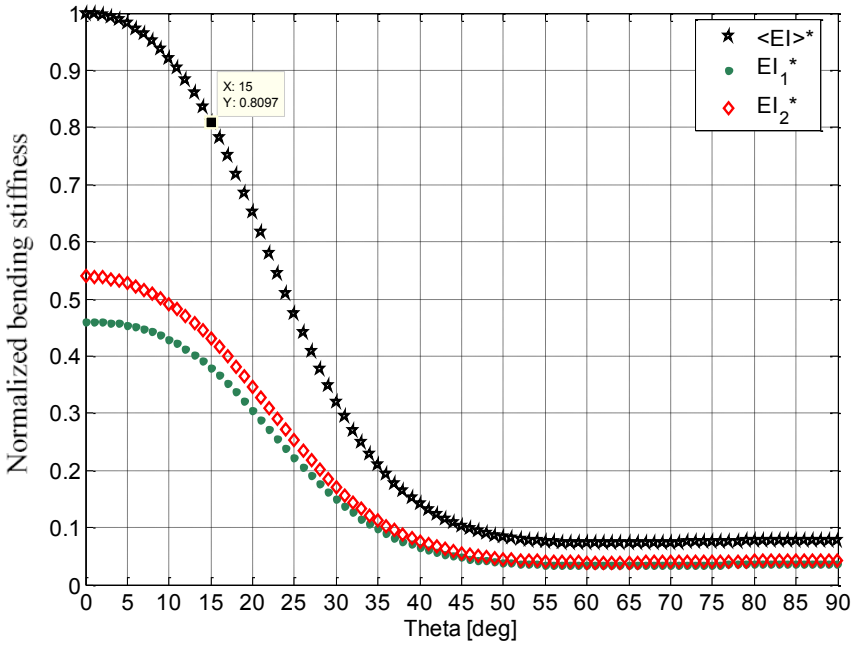

Figure 3.12: Bending stiffness versus θ for tubes of [θ/-θ], t/D_o=0.05, t_1/t=0.5

The figure shows nearly equal contribution from the two layers in the total bending stiffness of the tube. Also one can observe the improved values of bending stiffness of the tube made of [θ/-θ] compared to that made of only one layer such that at θ=15°, the normalized bending stiffness increased to be (0.8097), which is 2.5 times of the normalized bending stiffness of the tube made of one layer. It is important to note that the two tubes have the same dimensions (D_o and t/D_o). More comparison between the two tubes is presented in the following subsection.

3.2.2.3 Tubes comparison

In order to realize the reason of the improved bending stiffness of the tube made of [θ/-θ] over θ range, Normalized $E_{eff,n}$ is plotted for the two tubes in Figure 3.13. Noting that E_{eff} of the tube made of one layer is equal to E_x as presented in Figure 3.9.

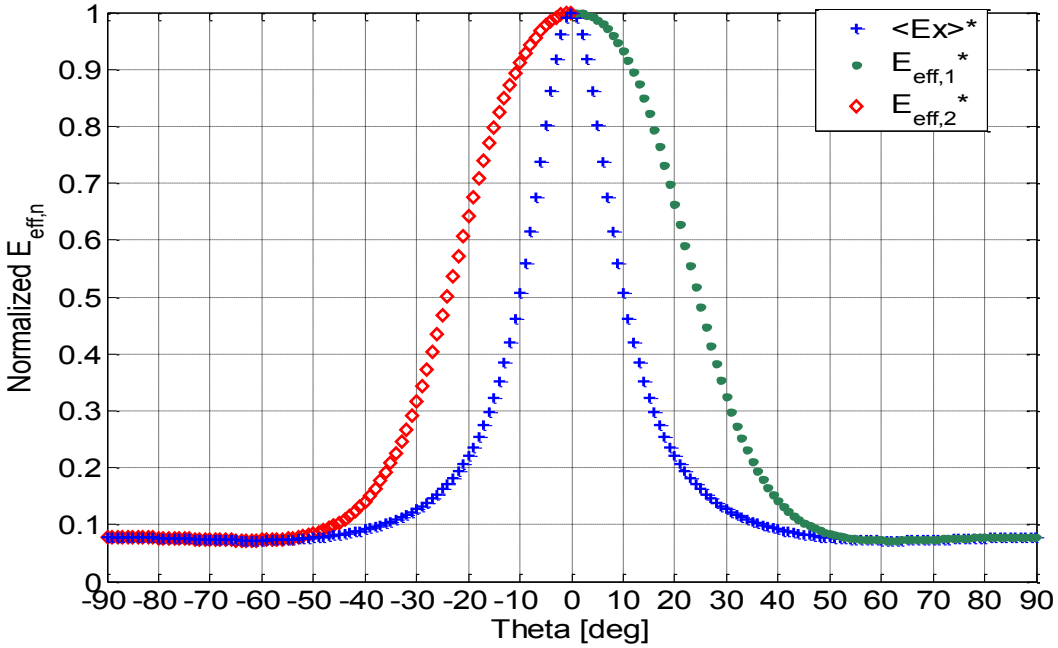

Figure 3.13: $E_{eff,n}$ versus E_x for composite tube of [θ/-θ] configuration, t/D_o=0.05, t_1/t=0.5

The figure shows higher values of $E_{eff,n}$ compared to that of E_x over θ range. This high improvement in $E_{eff,n}$ is because of the interaction between the two layers of [θ/-θ] stacking sequence. Also, one can observe that both $E_{eff,1}$ and $E_{eff,2}$ have similar variation over the range of θ. This is expected at t/D_o=0.05, making $E_{eff,1}$ value to be close to $E_{eff,2}$, as presented in Figure 2.9.

The area between E_x and $E_{eff,n}$ curves represents the enhancement values at different θ. The difference between $E_{eff,n}$ and E_x are obtained in percentage of E_1 for each θ, and plotted in Figure 3.14.

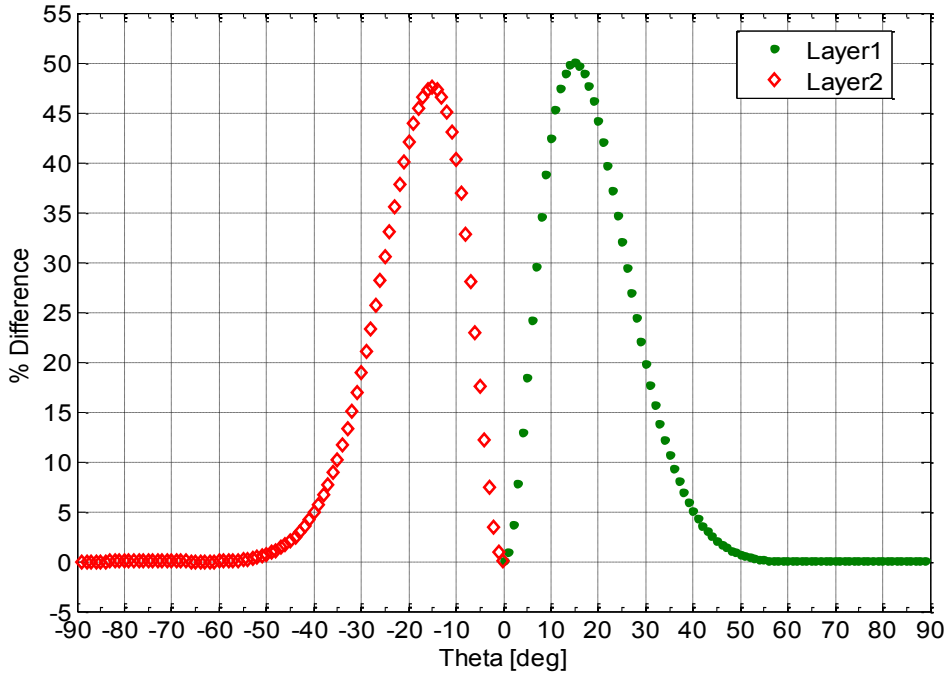

Figure 3.14: ($E_{eff,n}$ - E_x)/E_1 for tubes of [θ/-θ] configuration, t/D_o=0.05, t_1/t=0.5

One can observe the large difference between the two parameters such that the maximum difference is about 50% of E_1, obtained at θ=15°. Also it is shown that the percentage difference for the inner layer (Layer1) is somewhat larger than that of the outer layer (Layer2) at θ=15°, which is due to $I_{fr,1}$ being somewhat smaller than $I_{fr,2}$ for t/D_o=0.05, as shown in Figure 2.10. Lastly, one can notice that for carbon/epoxy composite tube, the percentage difference has a significant value when θ is greater than zero and less the 60° while its value vanishes for any other value out of this range, making $E_{eff,n}$ equal to E_x. This means ceasing the layers interaction. This can be explained from equation (3.22), that at θ=0° or 90°, the values of ($\eta_{xy,x}$) and ($\eta_{x,xy}$).are equal to zero and at θ>60° , their values are very small as shown in Figure 3.2 and Figure 3.3. This makes $E_{eff,n}$ to be equal E_x.

In order to realize the interaction effect on the tubes bending stiffness, their normalized values are compared the layers material properties in bending over E_x value, the calculated bending stiffness of the composite tube is compared to the obtained values from multiplying E_x with I_T in Figure 3.15.

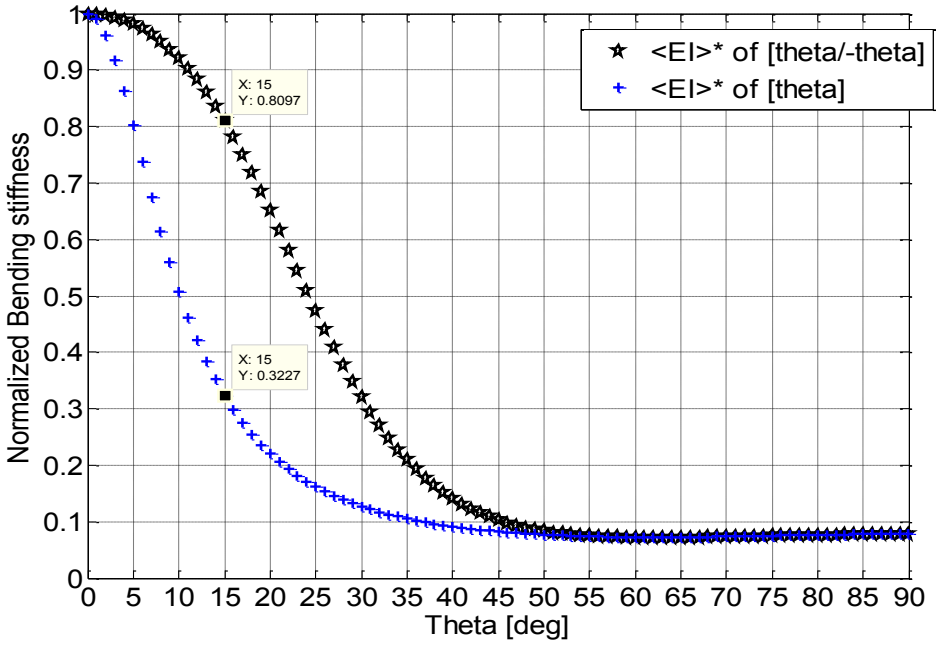

Figure 3.15:Normalized bending stiffnesses vs. θ for the two tubes of t/D_o=0.05, t_1/t=0.5

The figure shows the improved effect of layers interaction on the total bending stiffness of the tubes, and the maximum improvement is obtained at $\theta=15^0$ causing the bending stiffness for a tube made of [θ/-θ] to be 2.5 times compared to that made of [θ] only.

3.2.3 Explaining how interaction improves the bending stiffness

In order to explain how layers interaction improves the bending stiffness of the tube composed of [θ/-θ] compared to that made of [θ], the contributions of the composite material properties in $E_{eff,n}$ and E_x are quantified over θ range. This quantification is obtained by calculating the partial derivatives of $E_{eff,n}$ with respect to the material properties using FDM. For E_x, the derivatives are calculated

analytically using equation (3.3) and numerically using FDM in order to validate the used numerical method. The obtained values from the analytical and numerical differentiation Coincide with each other, which validates the numerical method.

The calculated partial derivatives of $E_{eff,n}$ are plotted in Figure 3.16 for the inner and outer layers at $\theta=15^{o}$, the point of maximum percentage difference between $E_{eff,n}$ and E_x. The partial derivatives of E_x with respect to the material properties are plotted in Figure 3.17 at the same angle for comparison.

Figure 3.16 shows nearly equal contributions in both layers from the material properties, such that the derivative with respect to E_1 in the inner layer (Layer 1) is equal to that of the outer layer (Layer 2). Comparing Figure 3.16 to Figure 3.17, one can observe that derivatives in case of E_x show very small effects from E_1 and E_2, while for $E_{eff,n}$, the derivatives indicate higher effects for E_1 and E_2 and lower effect for G_{12}. Also it is shown that the material properties G_{13} and G_{23} show some added contributions in $E_{eff,n}$ while they have no effect on E_x. This is due to the absence of layers interaction in the tube made of one layer.

Now, in order to have a comprehensive understanding for the contributions of the material properties, the partial derivatives for both $E_{eff,n}$ and E_x are calculated for selected values over θ range and presented in Figure 3.18 and Figure 3.19, respectively.

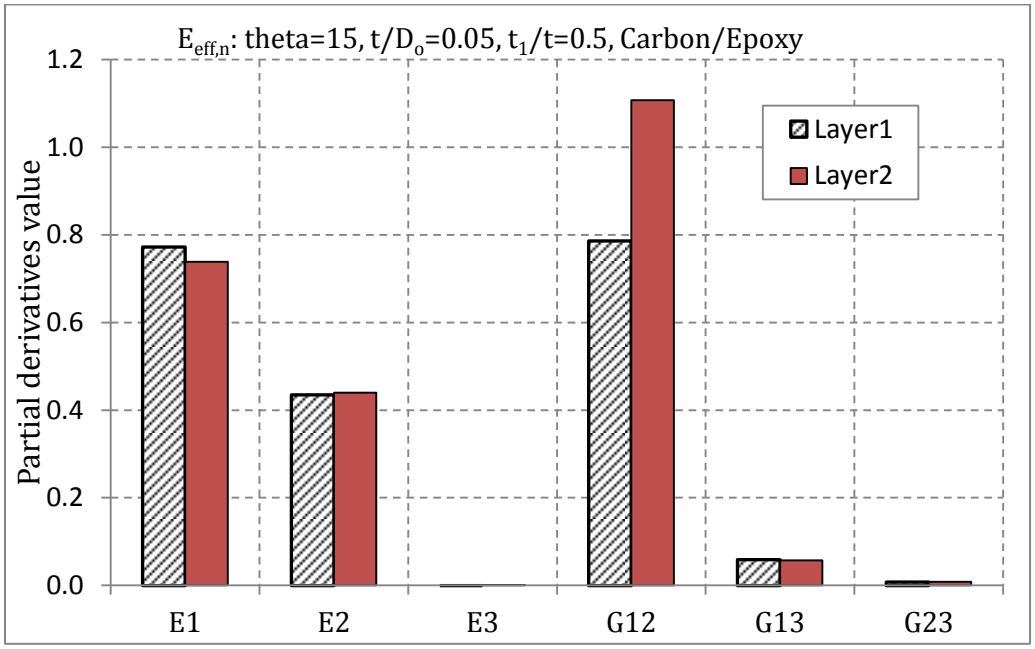

Figure 3.16: Derivatives of $E_{eff,n}$ to material properties for tubes of [θ/-θ], t/D_o=0.05, t_1/t=0.5

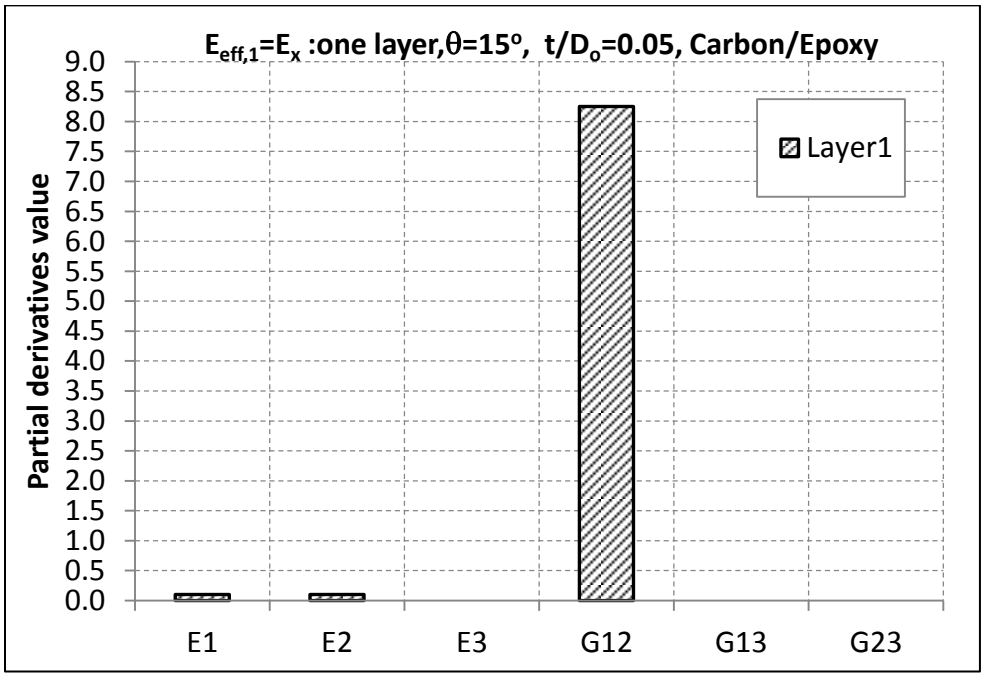

Figure 3.17: Partial derivatives of E_x with respect to material properties, θ=15°

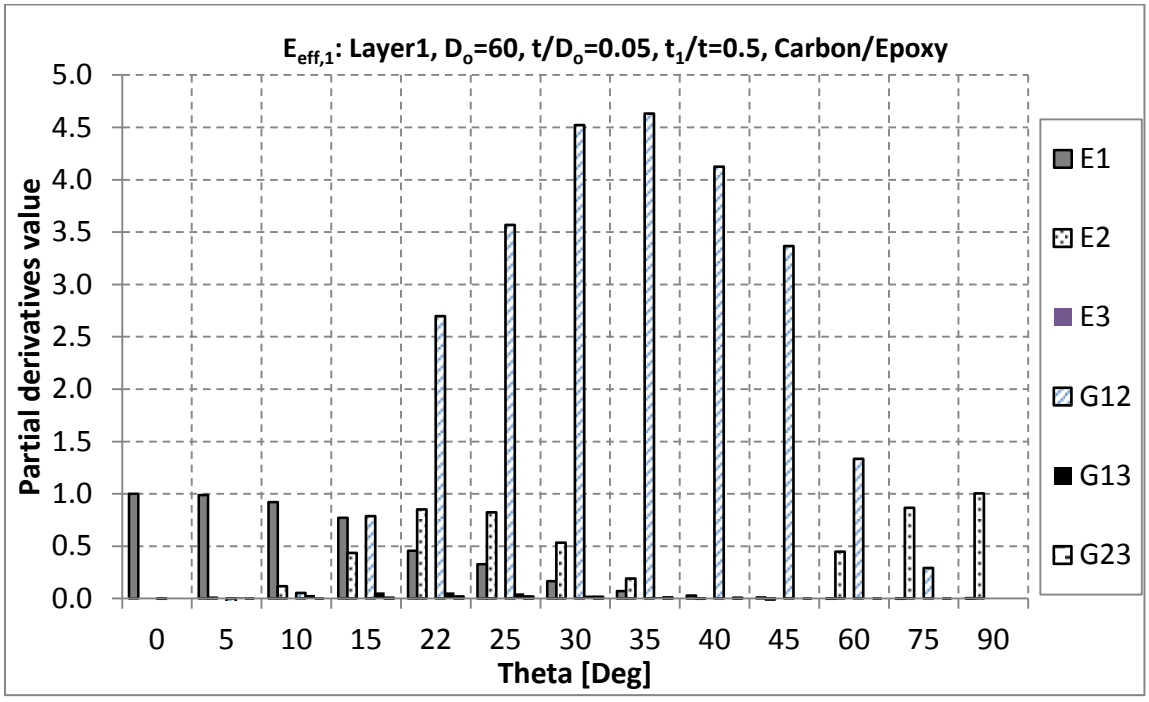

Figure 3.18: Derivatives of $E_{eff,n}$ over θ range for tubes of [θ/-θ], t/D_o=0.05, t_1/t=0.5

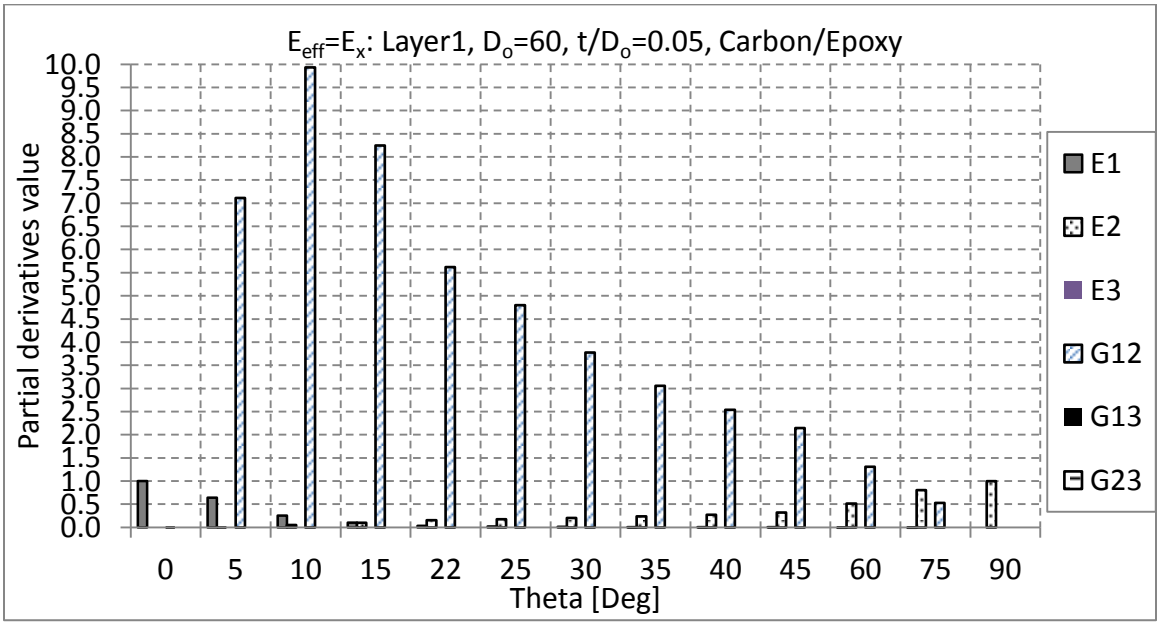

Figure 3.19: Derivatives of E_x over θ (equal to E_{eff} of single layered tube, t/D_o=0.05, t_1/t=0.5)

Comparing the two figures, one can observe the following:

- At $\theta=0^o$, E_1 is the only effective material property for E_x and $E_{eff,n}$. However for $\theta>0^o$, E_1 effect increases highly for $E_{eff,n}$ compared to E_x such that the contribution of E_1 for $E_{eff,n}$ is more than triple its contribution for E_x. at $\theta=10^o$. Also one can observe that G_{12} is most effective material property for E_x and its effect is maximum at $\theta=10^o$. This is explained from equation (3.22) that shows that ($\eta_{xy,x}$) is the main effective coefficient and one can observe that ($\eta_{xy,x}$) value is maximum at $\theta=9^o$, as shown in Figure 3.2.
- At $\theta=15^o$, the figure shows large contribution from E_1, with a considerable contribution from E_2 and G_{12} which makes the maximum improvement occurs at this θ value.
- At $\theta=22^o$, one can observe the high contribution of E_2. Also, it is shown that G_{12} has less contribution at lower values of θ with maximum effect at $\theta=35^o$ for $E_{eff,n}$. The reason of that is ($\eta_{x,,xy}$) which is maximum at $\theta=35^o$, as shown in Figure 3.3.
- For $\theta>60^o$, less contributions of the material properties since the effective coefficients ($\eta_{x,,xy}$) and ($\eta_{xy,x}$) in interaction have very low values as shown in Figure 3.2 and Figure 3.3.
- The effect of E_2 increases at larger value of θ to be the only effective property at $\theta=90^o$. This is because the layer transverse direction will coincide with the axial direction of the tube.
- The reasons of the improved contributions of the material properties for $E_{eff,n}$ compared to that of E_x are due to the interactions between the composite layers in the tube under bending loading.

3.3 Effect of layers geometry on the bending stiffness of composite tubes

The responsible parameters for layers geometry effect are t/D_o and t_l/t. t/D_o is found to have a negative effect on tubes made of two thick layers of [θ/-θ] stacking sequence. While it has somewhat positive effect on tubes made of one thick layer. For t_l/t, it is found that one specific value of this ratio gives higher bending stiffness of the tube made of two thick layers of [θ/-θ] than the other values. To explain the reasons of these effects, the following examples will be presented.

3.3.1 Thick-walled tubes made of one layer

For a single layer composite tube of t/D_o=0.45, E_{eff} versus θ is compared to E_x values, as shown in Figure 3.20.

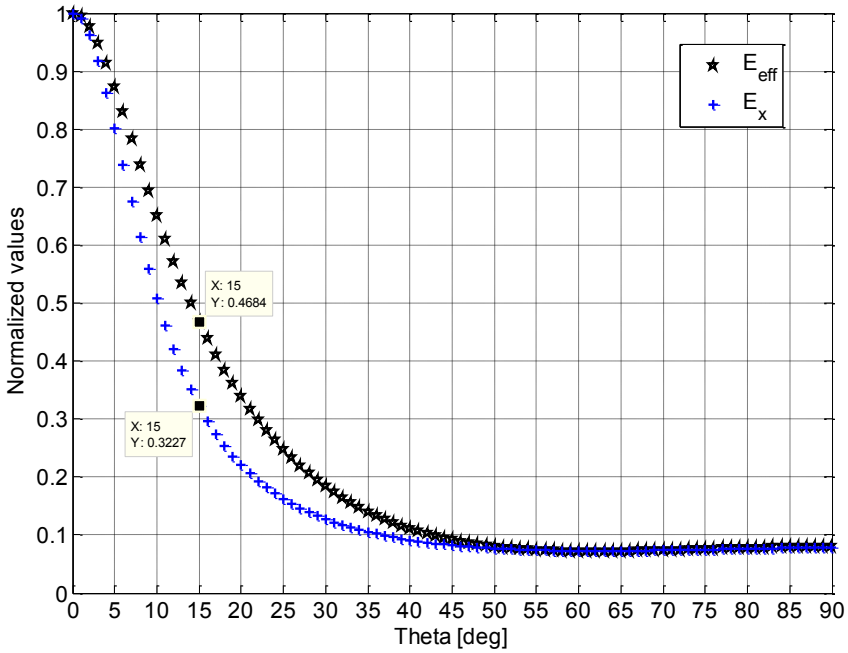

Figure 3.20: $E_{eff,n}$ versus E_x for single layered tube of [θ], t/D_o=0.45

For this thicker tube, the curve of E_{eff} shows some enhancement compared to E_x. The percentage difference between E_{eff} and E_x is plotted in Figure 3.21.

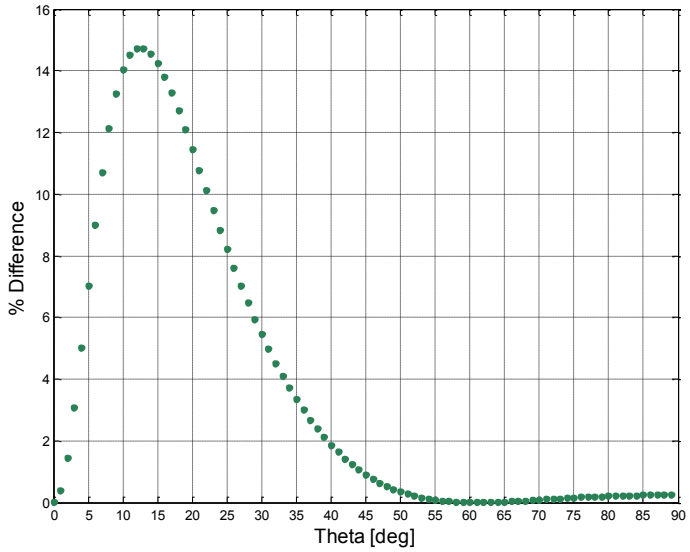

Figure 3.21: $(E_{eff,n} - E_x)/E_1$ for single layered tube of [θ], t/D_o=0.45

One can see that the percentage difference is relatively small compared to the tube made of [θ/-θ], presented in Figure 3.14. The maximum percentage difference is about 14.5% obtained at θ=12°. The contributions of the material properties are calculated and plotted in Figure 3.22, in order to explain this enhancement.

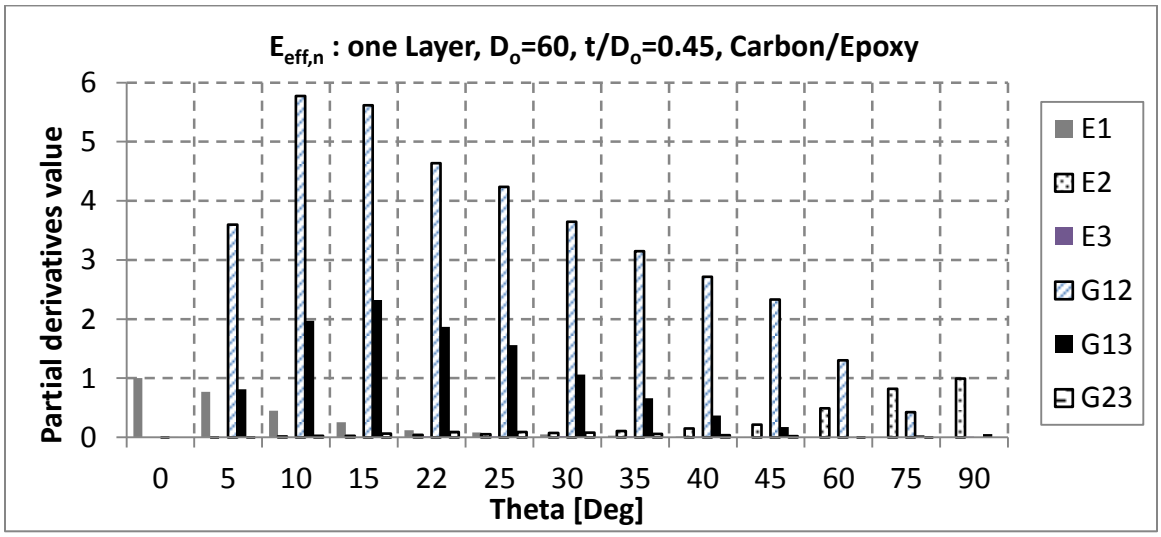

Figure 3.22: Derivatives of $E_{eff,n}$ over θ range for single layered tube of [θ], t/D_o=0.45

Comparing this figure to Figure 3.19, one can observe that the shown enhancement for the thicker tube is due to the increased contribution for G_{13} on the expense of G_{12}. Also one can see larger contribution for E_1 compared to the case of E_x such that E_1 contribution for E_{eff} is more than twice of its contribution for E_x at $\theta=15^o$. This enhancement is thought to be due to more material in thickness direction which adds more stiffness properties for the tube.

E_{eff} values in Figure 3.20 are also considered to be the normalized values of the tube bending stiffness. One can see that the bending stiffness normalized value is equal to 0.4684 at $\theta=15^o$ which is higher than the former single layer thinner tube (0.3227) but the value is still much lower than the presented tubes of balanced [θ/-θ] laminate configuration of value (0.8097), as shown in Figure 3.15.

3.3.2 Thick-walled tubes made of 2 layers of equal thickness

At first, the variation of $E_{eff,n}$ with θ is presented for this thick-walled composite tube of $t_1/t=0.5$. The values of $E_{eff,n}$ are plotted over θ range, compared to E_x in Figure 3.23.

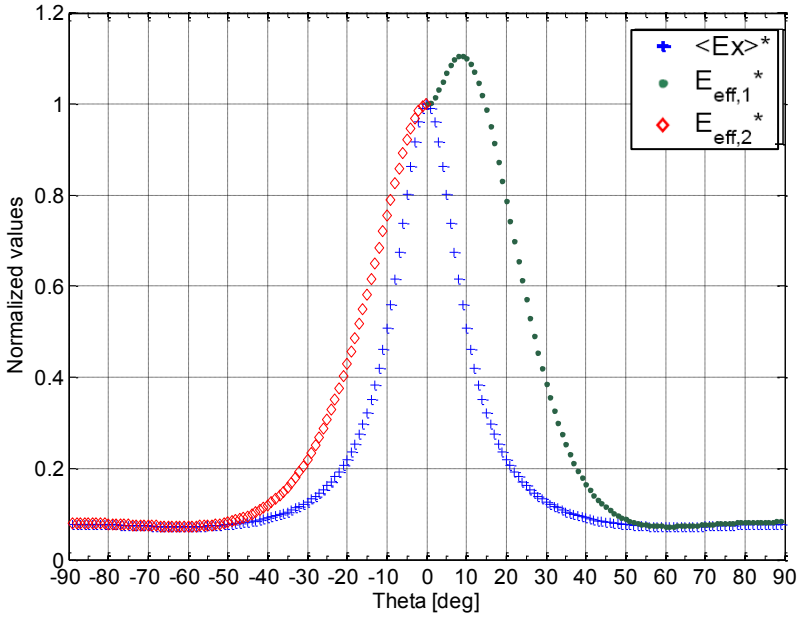

Figure 3.23: $E_{eff,n}$ versus E_x for tubes of [θ/-θ], $t/D_o=0.45$, $t_1/t=0.5$

The figure illustrates a different behavior of $E_{eff,1}$ compared to $E_{eff,2}$. One can observe that for the inner layer $E_{eff,1}$ increases with θ to have a peak value at θ=9°, then the curve exhibits a decreasing behavior while for the outer layer $E_{eff,2}$ curve is always decreasing, showing closer behavior to E_x curve. The percentage difference between $E_{eff,n}$ and E_x curves is plotted in Figure 3.24, normalizing the results to E_1.

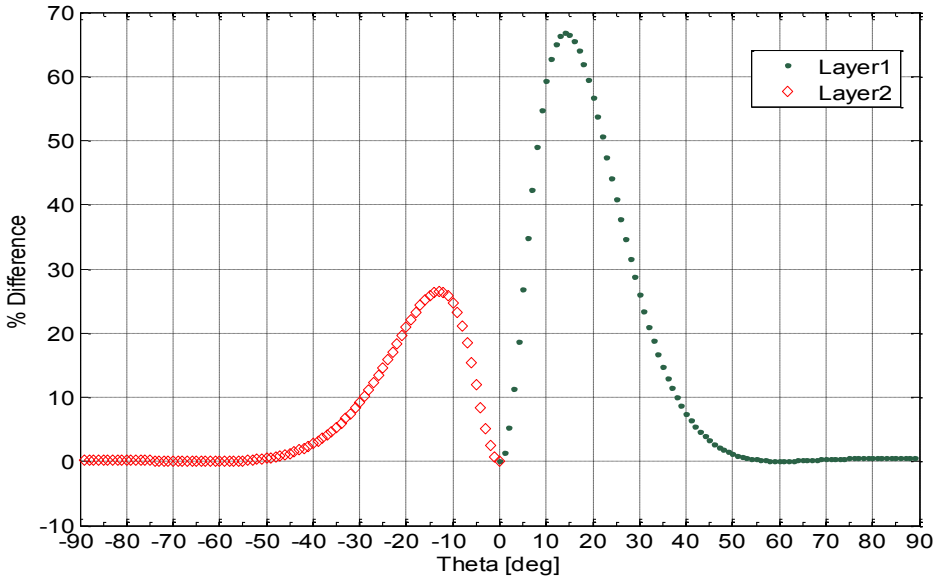

Figure 3.24: $(E_{eff,n} - E_x)/E_1$ for tubes of [θ/-θ], t/D_o=0.45, t_1/t=0.5

For this very thick-walled tube, the maximum difference reaches about 70% of E_1 for the inner layer compared to a value less than 30% for the outer layer obtaining these maximum values at θ=14°. This large difference between $E_{eff,1}$ and $E_{eff,2}$ is because $I_{fr,2}$ is very large compared to $I_{fr,1}$ and consequently this makes $E_{eff,1}$ to be very large compared to $E_{eff,2}$, as shown in Figure 2.10 for t/D_o=0.45 and t_1/t=0.5. However, this large difference in $E_{eff,n}$ is influenced by the composite material properties and θ, making the geometric parameters to be effective only in a specified range of θ while outside this range, the geometric properties have no effect, making $E_{eff,1}$ equal to both $E_{eff,2}$ and E_x when θ is greater than 55 as shown in Figure 3.15.

3.3.2.1 Material properties contributions

The partial derivatives of $E_{eff,n}$ with respect to material properties are calculated in order to show the material influence for this very thick tube. The derivatives are plotted for both inner and outer layers at $\theta=15^{o}$, as shown in Figure 3.25.

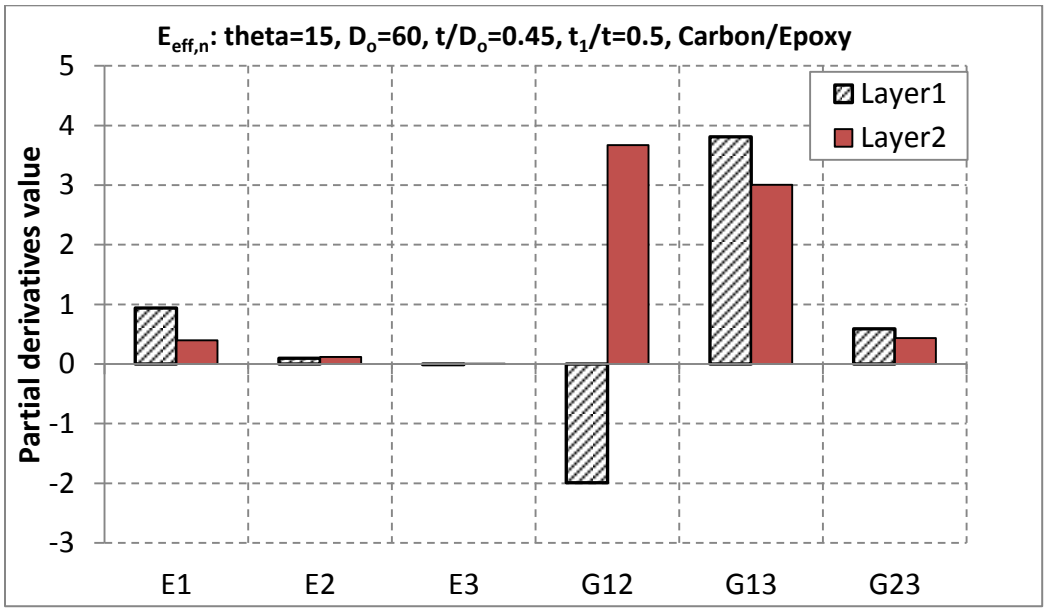

Figure 3.25: Derivatives of $E_{eff,n}$ to material properties for tubes of [θ/-θ], $t/D_o=0.45$, $t_1/t=0.5$

One can observe the unbalanced contributions of the material properties for the laminate layers in the case of thicker tube compared to those for relatively thin-walled tubes shown in Figure 3.16. A larger contribution of E_1 is presented for the inner layer compared to the outer layer, a drastic increase in G_{13} with higher effect for the inner layer, and an enhanced effect from G_{23}. Also one can notice the large decrease in the effect of E_2 for the thicker tube compared to its effect for the relatively thinner tube.

In order to have a global picture about the effect of tube geometric parameters on the contributions of the composite material properties, the material properties derivatives are plotted for the inner and outer layers in Figure 3.26.

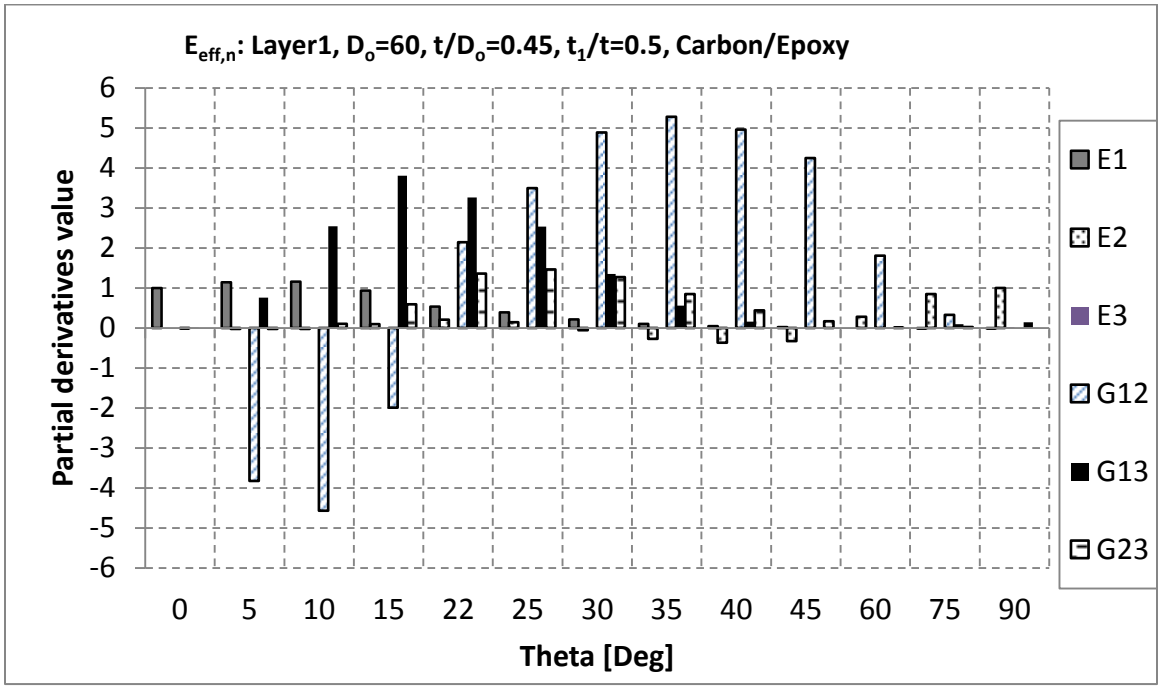

(a)Inner layer

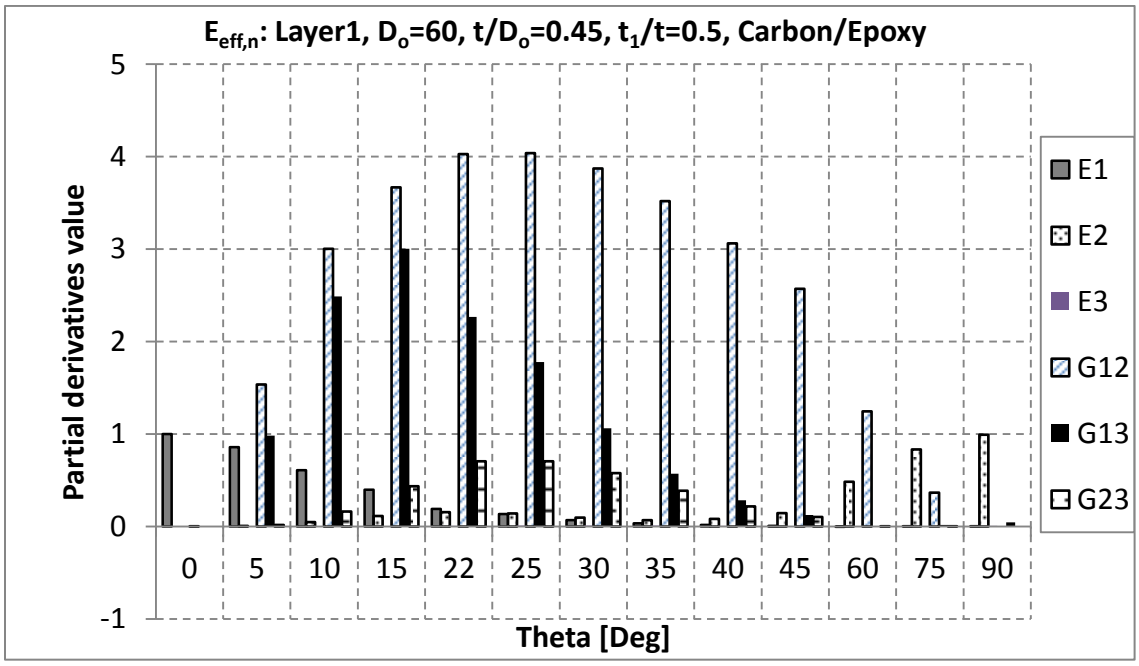

(b)Outer layer

Figure 3.26: Derivatives of $E_{eff,n}$ over θ range for tubes of [θ/-θ], t/D_o=0.45, t_1/t=0.5

From these figures one can observe the following points:

- E_1 shows unbalanced contributions for the two layers. The inner layer has higher contribution of E_1 compared to that of the outer layer which leads to higher value of $E_{eff,1}$ compared to $E_{eff,2}$.
- G_{13} effect is highly enhanced for the two layers reaching its maximum at $\theta=15^o$. This is thought to be due to the increased thickness coordinate of these thick layers, causing more contribution from its mechanical properties.
- G_{23} contribution is somewhat higher for the inner layer compared to the outer one and that the maximum contribution is at $\theta=25^o$.
- G_{12} shows negative effect for the inner layer while it has positive effect for the outer layer.
- E_2 effect is reduced for both layers.

In general, one can conclude that the material properties show unbalanced contributions in $E_{eff,n}$ for both layers in this thicker tube compared to the presented thinner tube for $t_1/t=0.5$.

3.3.2.2 Bending stiffness behavior

In order to show the influence of $E_{eff,n}$ variation with θ on the bending stiffnesses for the composite layers and for the total tube, their values are calculated over the range of θ and plotted in Figure 3.27.

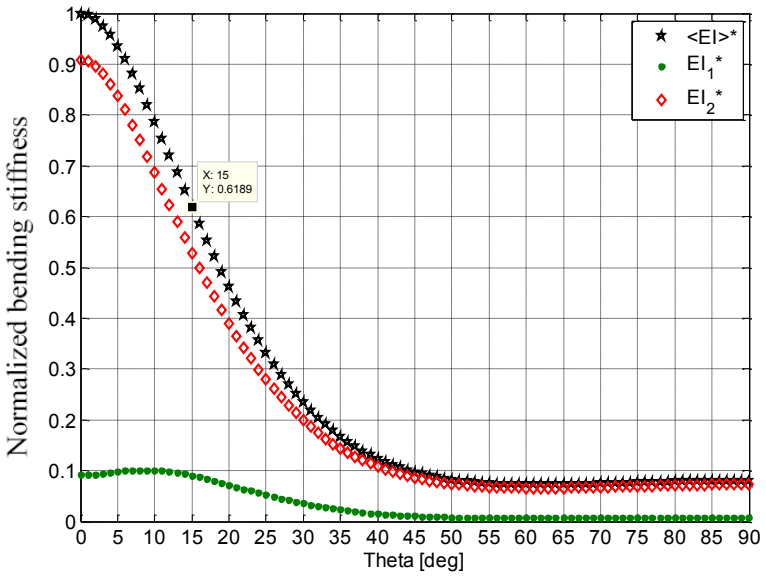

Figure 3.27: Bending stiffness versus θ for tubes of [θ/-θ], t/D_o=0.45, t_1/t=0.5

The figure shows that the bending stiffness of the inner layer is much lower than that of the outer layer despite $E_{eff,1}$ shows higher values compared to $E_{eff,2}$, Figure 3.24. This situation is explained as follows:

The bending stiffness property of each layer depends on two terms $E_{eff,n}$ and I_n . Adding to that I_n shows higher effect on the layer bending stiffness compared to $E_{eff,n}$, as explained at the end of chapter 2. For the presented tube geometry, I_2 is much larger than I_1, making the bending stiffness of the outer layer to be larger than that of the inner layer, even when $E_{eff,1}$ is larger than $E_{eff,2}$.

Also one can observe that the normalized value of the tube bending stiffness is equal to 0.6189 at $\theta=15^o$ while the corresponding normalized value for the relatively thin walled tube is equal to 0.8097, as shown in Figure 3.15. This lower value for the thicker tube is due to smaller contribution of the composite material in the bending stiffness of the outer layer, plus the smaller value of I_1, leading to a smaller bending stiffness value for the whole tube. The situation of this thick tube is different when $E_{eff,1}$ and $E_{eff,2}$ are equal, as will be discussed in the next subsection.

3.3.3 Balanced and unbalanced laminates

The cases of equal $E_{eff,n}$ are previously presented in the previous chapter, and it is shown that these cases are obtained at specific value of t_1/t for each specified t/D_o and θ, such that for $t/D_o=0.45$ and $\theta=15^o$, the case of equal $E_{eff,n}$ is obtained at $t_1/t=0.73$, as shown in Figure 2.14. In this subsection, this case is investigated to understand what does it mean physically when the tube layers have equal $E_{eff,n}$. Starting this analysis by plotting $E_{eff,n}$ versus θ and comparing its value to E_x as shown in Figure 3.28.

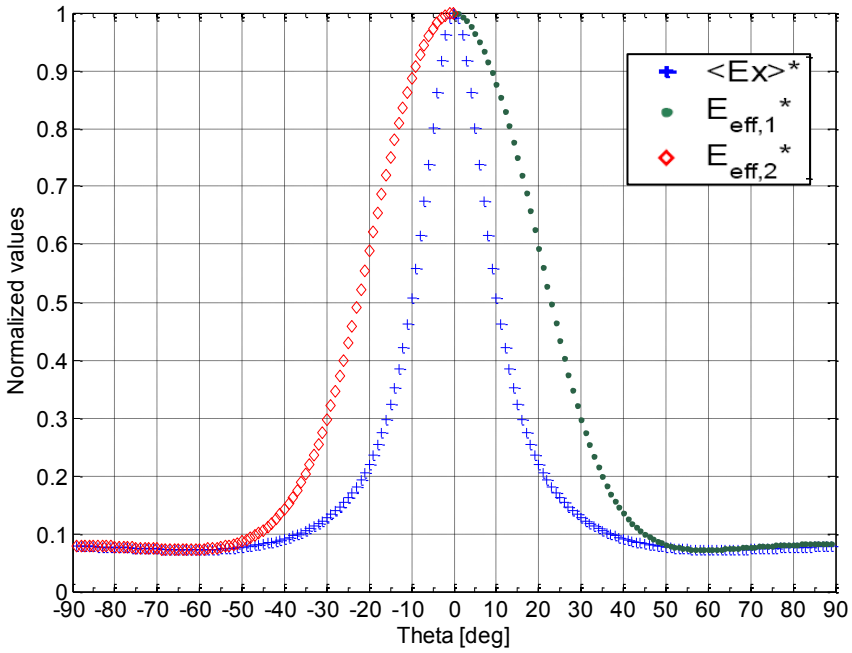

Figure 3.28: $E_{eff,n}$ versus E_x for tubes of [θ/-θ], $t/D_o=0.45$, $t_1/t=0.73$

One can observe an interesting result when comparing to the presented results of the same thick tube of $t_1/t=0.5$, shown in Figure 3.23. The case of equal $E_{eff,n}$ provides a symmetric behavior in the variation of $E_{eff,n}$ for the inner and outer layers. The difference between $E_{eff,n}$ and E_x is calculated and plotted in the Figure 3.29.

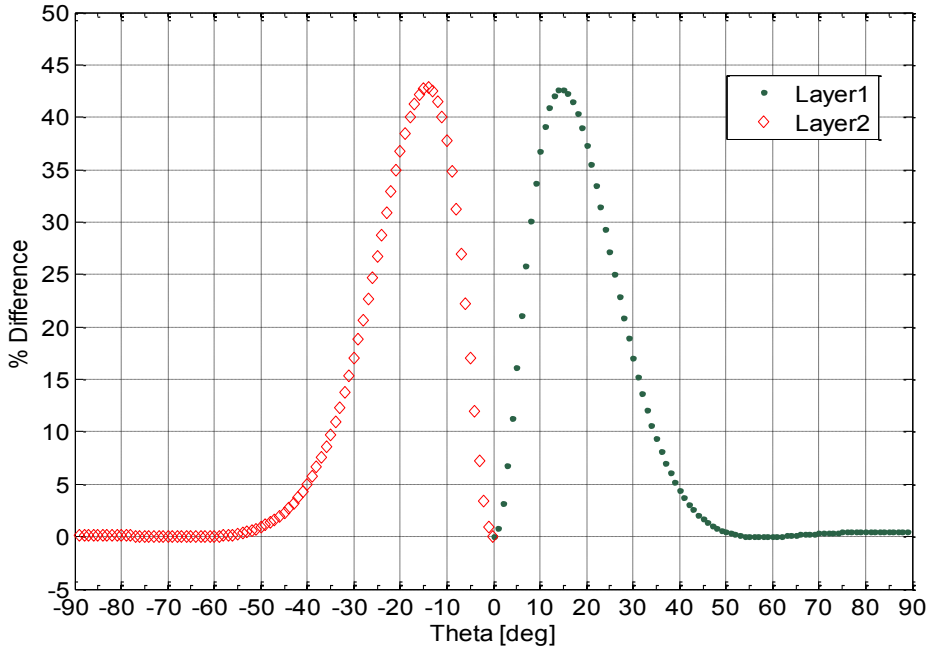

Figure 3.29: ($E_{eff,n}$ - E_x)/E_1 for tubes of [θ/-θ], t/D_o=0.45, t_1/t=0.73

One can observe similar curves for the two layers, noting that the maximum percentage is around 43% which is smaller compared to the thinner tube of t/D_o=0.05, and t_1/t=0.5, presented in Figure 3.14. The reason of this smaller value is discussed at the end of this section.

3.3.3.1 Material properties contributions

The partial derivatives of the material properties are calculated and plotted in Figure 3.30 to check their contributions for the two layers at θ=15°.

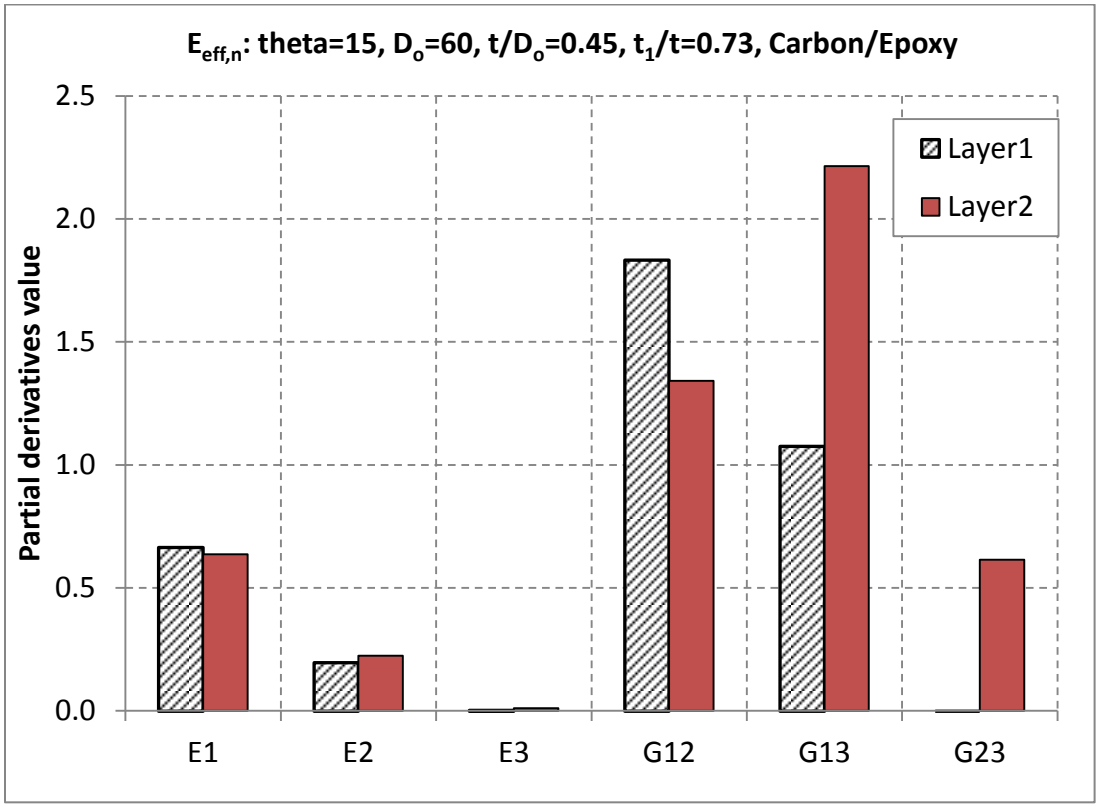

Figure 3.30: Derivatives of $E_{eff,n}$ to material properties for tubes of [θ/-θ], t/D_o=0.45, t_1/t=0.73

From the figure, one can observe the balanced contribution of E_1 and E_2 for the two layers and closer contributions of the other material properties for the tube layers compared to the former thick-walled tube of equal layer thickness, shown in Figure 3.25.

In order to have a global idea about the case of equal E_{eff}, the contributions of the composite material properties for the two layers are plotted in Figure 3.31 for selected values of θ range. From these figures, one can see the similar contributions of the material properties in the two layers.

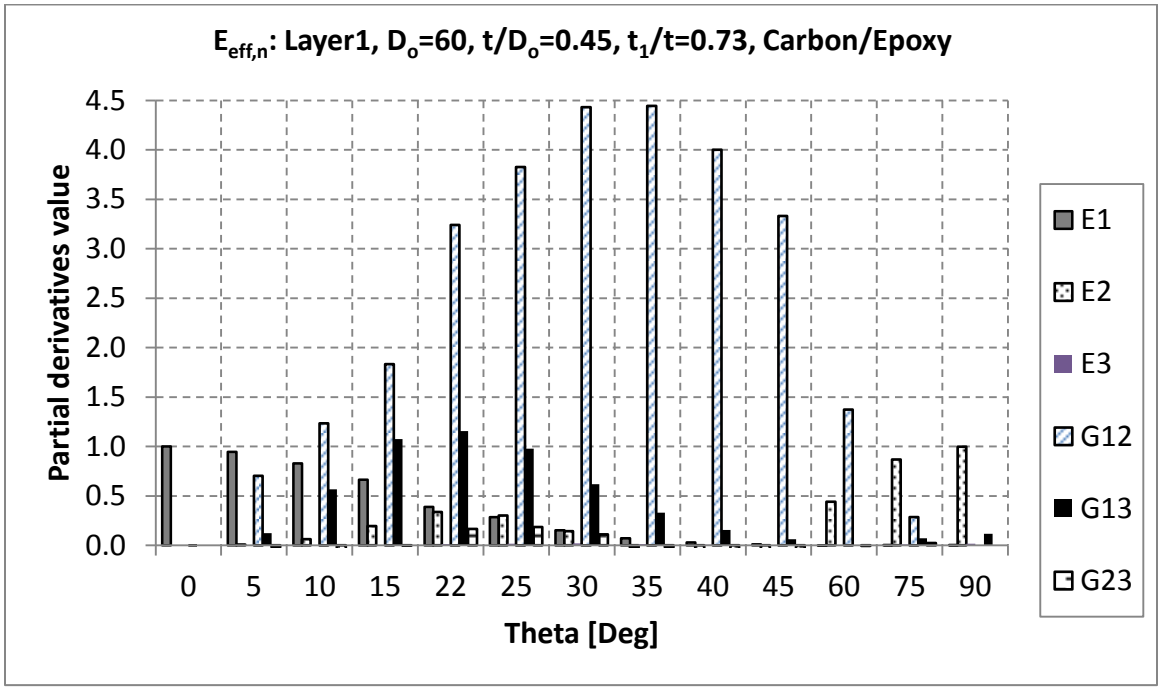

(a)Inner layer

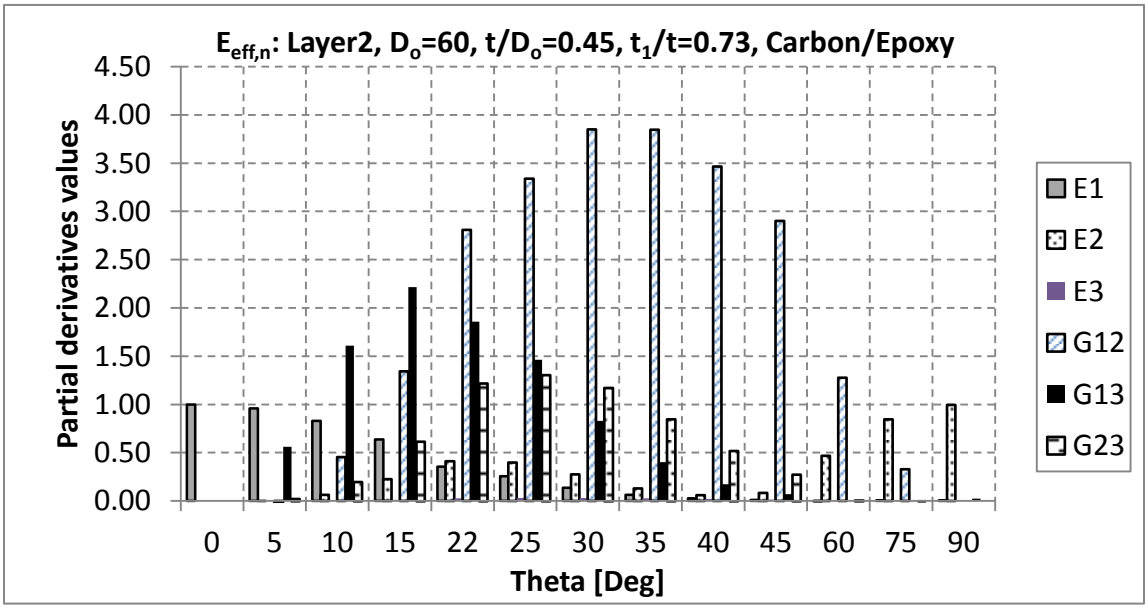

(b)Outer layer

Figure 3.31: Derivatives of $E_{eff,n}$ over θ range for tubes of [θ/-θ], t/D_o=0.45, t_1/t=0.73

Comparing these figures to Figure 3.26 of the thick tube having equal layer thickness, one can observe that the effects of the material properties are changed from unbalanced contributions to balanced ones for $t_1/t=0.73$, when $E_{eff,1}$ is equal to $E_{eff,2}$.

One can conclude that $E_{eff,n}$ term can be used as an indicator for the balanced laminate of a tube under bending using a 3D theory. This is analogous to A_{16} and A_{26} terms for equivalent single layer theories.

3.3.3.2 Bending stiffness behavior

In order to show the influence of equal $E_{eff,n}$ on the bending stiffnesses for the composite layers and for the total tube, their values are calculated over the range of θ and plotted in Figure 3.32.

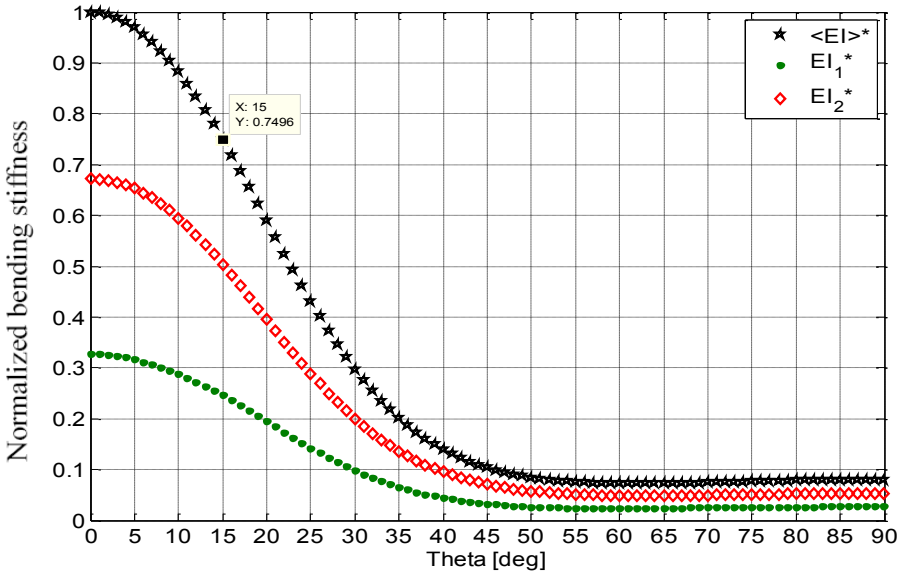

Figure 3.32: Bending stiffness versus θ for tubes of [θ/-θ], $t/D_o=0.45$, $t_1/t=0.73$

The figure shows better effect of the inner layer in the total bending stiffness compared to the previous thick-walled tube configuration presented in Figure 3.27. Also, its normalized bending stiffness has a value of 0.7496 at $\theta=15^o$ which is higher than that of the former thick-walled tube of equal thickness which has a value of (0.6189).

This result emphasizes that the laminate configuration of (t_1/t=0.73) is a balanced laminate since it provides higher bending stiffness value for the tube compared to the former laminate configuration of (t_1/t=0.5). This is despite that the former laminate is of equal wall thickness.

3.3.4 Comparing balanced thick-walled tube with relatively thinner one

Before ending this section, it is important to explain the reason making the balanced thick-walled tube to have a lower value of equal E_{eff} than that of the balanced thin-walled tube. This consequently makes the thick-walled tube to have a lower normalized value of the tube bending stiffness equal to (0.7496), see Figure 3.32, compared to the relatively thin-walled tubes which has a normalized value equal to (0.8097), as shown in Figure 3.15.

The first reason of that can be observed when comparing Figure 3.25 (balanced thick-walled tube) to Figure 3.16 (relatively thinner tube). One can see the contribution of E_1 for this balanced thick-walled tube is smaller compared to thinner one.

The second reason is explained as follows: The maximum value of bending stiffness is obtained at a value of t_1/t permitting optimum combination of I_n and $E_{eff,n}$ of each layer. Figure 3.33 shows the variation of $E_{eff,n}/E_x$, I_n, and the tube bending stiffness in t_1/t range for a relatively thin-walled tube (t/D_o=0.05), and a thick-walled tube (t/D_o=0.45). From this figure, the following points are observed:

- For the tube of small value of t/D_o, the balanced laminate configuration is seen to be at layers thickness ratio closer to t_1/t=0.5, showing higher values of $E_{eff,n}$ compared to the thick-walled tube.
- The layers bending moments I_n are equal to each other closer to t_1/t=0.5 for the thinner tube, permitting the best sharing for the composite layers in the total bending stiffness of the tube.

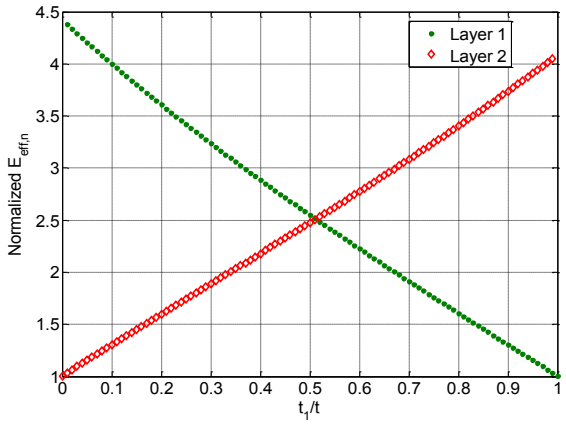

(a.1) $E_{eff,n}$ for t/D_o=0.05

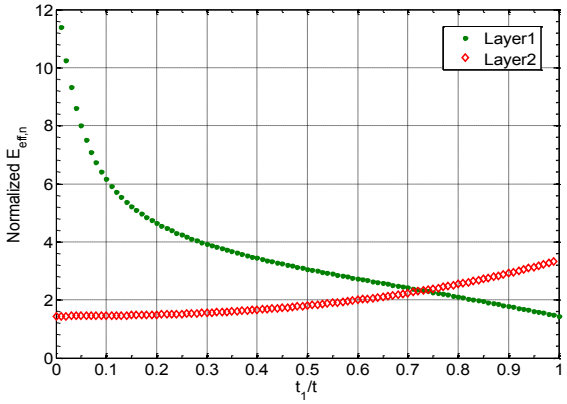

(a.2) $E_{eff,n}$ for t/D_o=0.45

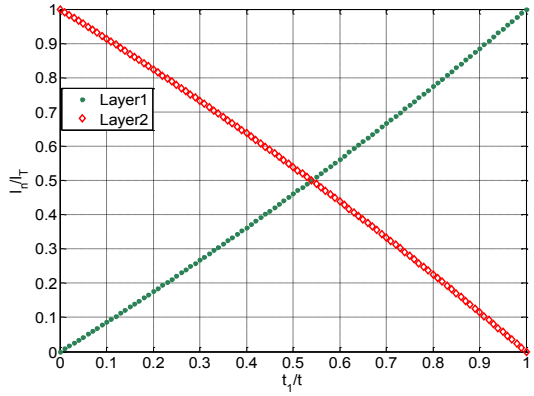

(b.1) In for t/D_o=0.05

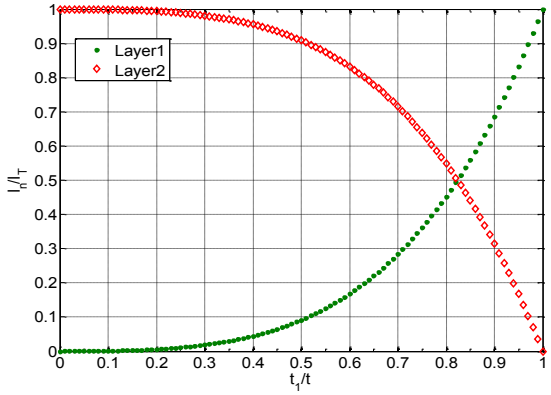

(b.2) In for t/D_o=0.45

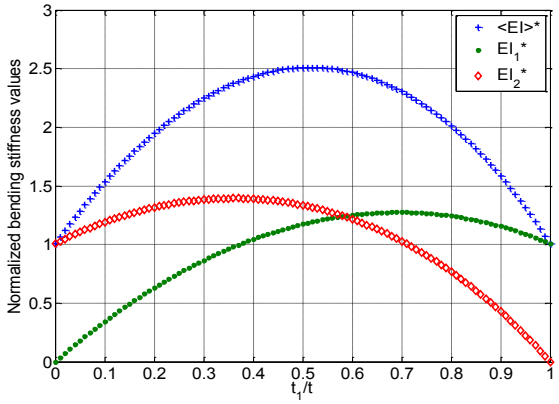

(c.1) <EI> for t/D_o=0.05

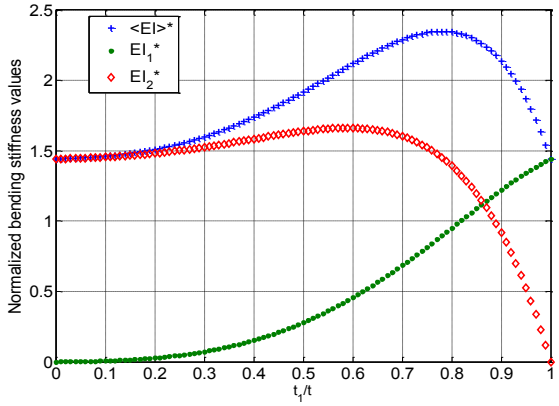

(c.2) <EI> for t/D_o=0.45

Figure 3.33: $E_{eff,n}/E_x$, I_n, and bending stiffness vs. t_1/t for (t/D_o=0.05) and (t/D_o=0.45), θ=15°

In other words, the smaller values of t/D_o permits closer balanced interaction between the composite layers at $t_1/t=0.5$, and better sharing in the tube total moment of inertia, leading to achieve maximum bending stiffness. This can explain the slight decrease in the values of equal E_{eff} for larger values of t/D_o, shown in Figure 2.14.

From the presented results in this section, one can conclude that the balanced laminate configuration permits higher bending stiffness for the composite tube due to the balanced contribution of the composite material properties in the tube layers, which implies better interaction between them. In the next subsection, the mechanism of geometric effect on the tube bending stiffness is explained

3.3.5 Explaining material properties contributions for different tube configurations

For thick-walled composite tubes of [θ/-θ] and ($t_1/t=0.5$), from the forces gradient, shown in Figure 3.6, one can observe that the compressive forces acting on the element at $\alpha=90^o$ will generate axial strains in plate element at $\alpha=90^o$ or 270^o such that:

$$(\varepsilon_x)_{Layer1} < (\varepsilon_x)_{Layer2} \tag{3.24}$$

This means that the generated in-plane shear strains in these layers (having opposite signs) will follow the relation shown in equation (3.25), assuming the layers are separated.

$$\|\gamma_{xy}\|_{Layer1} < \|\gamma_{xy}\|_{Layer2} \tag{3.25}$$

But, since these layers are in intimate contact, all the shear strain in layer1 (inner layer) will be canceled and it will not deform adding to this layer more contribution from E_1 as stated before.

While layer2 (outer layer) will still have some value of residual shear strain according to the following equation:

$$\|\gamma_{xy}\|_{Residual} = \|\gamma_{xy}\|_{Layer2} - \|\gamma_{xy}\|_{Layer1} \tag{3.26}$$

This residual strain makes the outer layer to deform losing some of the contribution from E_1, as shown in Figure 3.26.

While for fully balanced layers, $\|\gamma_{xy}\|_{Residual} = 0$, leading to equal contribution of E_1 in both the inner and the outer layer, as presented for the thin-walled composite tube and the thick-walled composite tube of balanced composite laminates in Figure 3.14 and Figure 3.28, respectively.

After presenting the analysis of single and double layered composite tube. It is convenient to study the multilayered composite tubes which are more practical configurations.

3.4 Multi-sublaminates composite tubes

The multi-sublaminates composite tube is composed of (m) repeated unit of [θ/-θ] through the wall thickness of the tube as shown in Figure 3.34. This makes the tube layers to thinner.

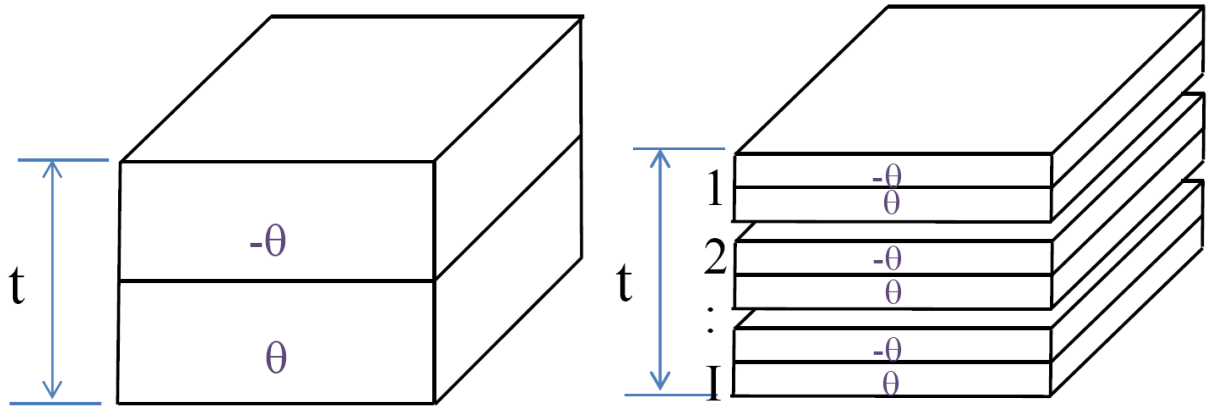

(a)One-sublaminate configuration (b) Multi-sublaminate configuration

Figure 3.34:one-sublaminate thick-walled tube vs. multi-sublaminates thick-walled tube

In this section, multilayered composite tubes of $[\theta/-\theta]_m$ laminate configuration is analyzed in order to identify the effect of increasing (m) on the total bending stiffness of the tube. (m) is the number of sublaminates in the tube laminate.

The bending stiffness of the multilayered composite tubes has the following form:

$$\langle EI \rangle = \sum_{n=1}^{N} E_{eff,n} I_n \tag{3.27}$$

Where: (N) is equal to twice of (m). The normalized values of bending stiffness for a composite tube is shown in the following equation

$$\langle EI \rangle^* = \sum_{n=1}^{N} \frac{E_{eff,n} I_n}{E_1 I_T} = \sum_{n=1}^{N} E^*_{eff,n} I_{fr,n} \tag{3.28}$$

$E^*_{eff,n}$ are the normalized values of the layer effective extensional stiffness. In order to illustrate the influence of increasing (m) on the bending stiffness of the tube, numerical examples are presented for composite tubes having D_o=60 mm, t/D_o=0.45 for the whole tube, the layers have equal thickness, and θ=15°. Figure 3.35 shows the bending stiffness variation versus (m).

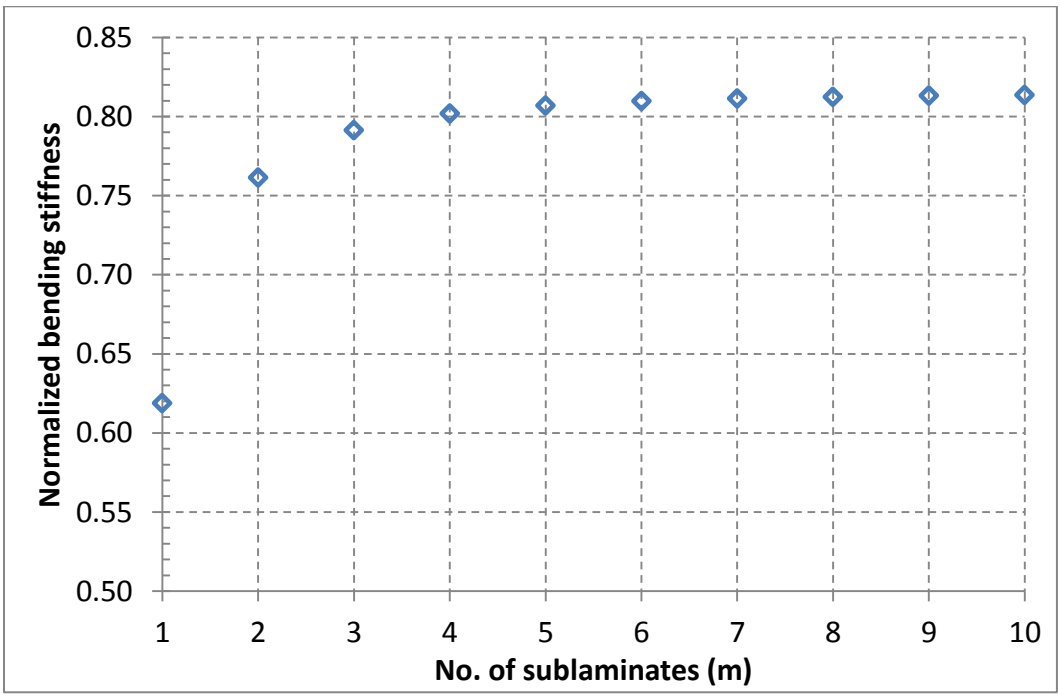

Figure 3.35: Bending stiffness variation with (m) for tubes of $[\theta/-\theta]_m$, θ=15°, t/D_o=0.45

The figure shows that the bending stiffness of the tube of (m=2) increased by 23% compared to the case of the tube of only one sublaminate. Also one can see that as the value of (m) increases, the bending stiffness increases by less rate till it converges to a specific value. This figure implies that increasing (m) improves the bending stiffness of the tube until certain point, where no more significant improvement is added such that the normalized bending stiffness is equal to (0.81) for the tube of m=6, while for m=10, the normalized value is equal to (0.814). Moreover, assume that the minimum layer thickness from manufacturing point of view is equal to (0.15mm), such that the maximum value of (m) equal to (90) for this numerical example. The normalized bending stiffness is calculated for this tube is equal to (0.816).

In order to explain the obtained results, the bending stiffness parameters of three composite tubes formed of different (m) values are compared. The normalized values of the bending stiffness parameters of the layers for these three tubes are listed in Table 3.1. The sublaminate index (i) ranges from (1) for the inner sublaminate to (m) for the outer sublaminate, and $(t/D_o)_i$ value is the wall thickness of the layers of sublaminate (i) divided by its outer diameter. The layer contribution percentage is its share in the total bending stiffness of the tube.

Table 3.1: Bending stiffness parameters for three tubes of different number of sublaminates

Tube No.	Sublaminate index. (i)	Sublaminate $(t/D_o)_i$	Layer No. (n)	$E^*_{eff,n}$	$I_{fr,n}$ [%]	Layer contribution %	$\langle EI \rangle^*$
Tube1 (m=1)	1	0.45	1	0.988	9.1	14.60	0.6189
			2	0.582	90.9	85.40	
Tube2 (m=2)	1	0.409	1	0.834	1.1	1.21	0.762
			2	0.640	8.0	6.75	
	2	0.225	3	0.908	26.9	32.10	
			4	0.714	63.9	59.94	
Tube3 (m=4)	1	0.346	1	0.732	0.2	0.18	0.802
			2	0.683	0.9	0.78	
	2	0.205	3	0.833	2.5	2.65	
			4	0.727	5.5	4.98	
	3	0.145	5	0.856	10.1	10.79	
			6	0.754	16.8	15.81	
	4	0.113	7	0.871	26.0	28.20	
			8	0.774	38.0	36.62	

From the moment of inertia fraction column ($I_{fr,n}$), one can observe that the outer layers of the tubes, which represent half their wall thickness, contribute by about 91% of the total moment of inertia. This makes these layers are the most effective layers in specifying the total bending stiffness of the tubes. For the first tube, it is shown that $E_{eff,2}$ has a smaller value compared to $E_{eff,1}$, however, due to large effect of moment of inertia, the outer layer contributes by 85% in the total bending stiffness. This tube

has the lowest bending stiffness value because of the unbalance behavior of this tube configuration for this thick tube of equal wall thickness, as presented in previous sections.

For the second tube, the bending stiffness is much higher than that of the first tube. This improvement in bending stiffness occurs due to adding more layers interface which means more interaction surfaces and consequently more improved contributions from the material properties takes place. Also, the value of $(t/D_o)_2$ of the outer sublaminate has a smaller value (0.225) compared to 0.45 for the first tube, leading to higher and closer values of $(E_{eff,3})$ and $(E_{eff,4})$ which consequently increases the share of the outer layers of the tube in the tube bending stiffness. So, it can be concluded that the large enhancement in the bending stiffness of the tube of two sublaminates is because the sublaminates have lower values of $(t/D_o)_i$ which make their configuration to be more closer to the balanced configuration and this in turn improve the values of $E_{eff,n}$ of sublaminate layers. Also the addition of more interaction surfaces improves the material properties contributions.

For the third tube, there are more interaction surfaces between layers and smaller values of $(t/Do)_i$ of the tube sublaminates, leading to closer configuration to the balanced sublaminates and increasing their contribution in the tube bending stiffness This consequently makes the third tube to have higher bending stiffness value compared to the first and second tube.

So, multi-sublaminates composite tubes have higher bending stiffness than one-sublaminate composite tubes due to thinner layers and smaller values of $(t/Do)_i$. This makes:

$$(E_{eff,1} \approx E_{eff,2})_i \tag{3.29}$$

This increases the improvement of the bending stiffness of the tube due to larger interaction effect.

$$(I_1 \approx I_2)_i \tag{3.30}$$

And that will reduce highly the geometric effect, especially when m is large to have very thin layers.

For the case of 90 sublaminates, the following curves are plotted for $E_{eff,n}/E_1$, $I_{fr,n}$, and the normalized bending stiffness values. Figure 3.36 shows that the outer sublaminates layers have maximum values of $E_{eff,n}$ and the inner layers have lower values. This is because the outer sublaminates have the smallest $(t/D_o)_i$ values.

Also, the outer layers have higher moments of inertia as shown in Figure 3.37, which in turn maximize the bending stiffness of the outer sublaminates as shown in Figure 3.38. One can observe that the bending stiffness contribution of the outer layer alone is 2% which is more than the contribution of the first 55 layers all together. This is because of the large volume of the composite material of this layer compared to the inner ones and its location at the farthest point away from the tube axis with the largest radius of curvature. It is important to note that these sublaminates are in perfect contact with each other.

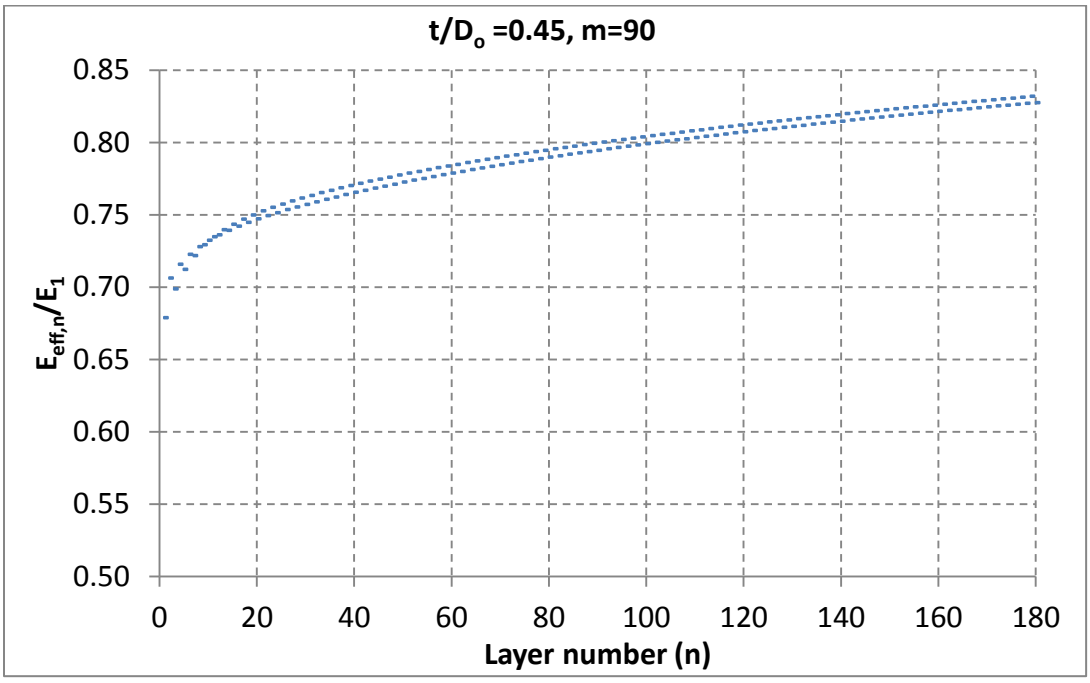

Figure 3.36: Normalized $E_{eff,n}$ of composite layers for a tube of $[\theta/-\theta]_{90}$, $\theta=15^o$
(the upper curve is for the inner layer and the lower curve is for the outer layer of each sublaminate)

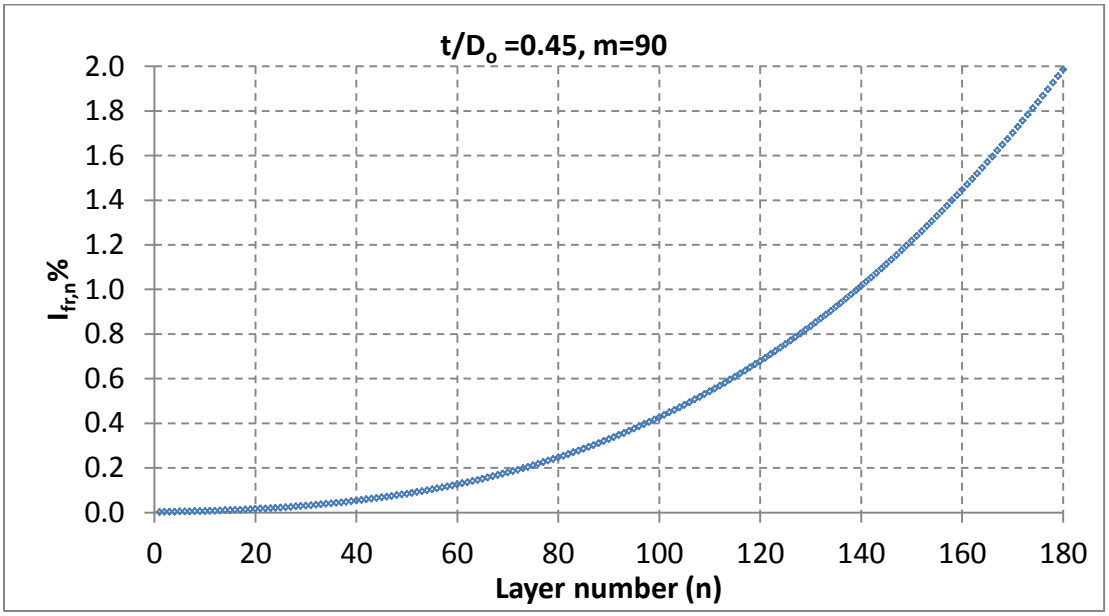

Figure 3.37: $I_{fr,n}$ of composite layers for a tube of $[\theta/-\theta]_{90}$, $\theta=15^o$

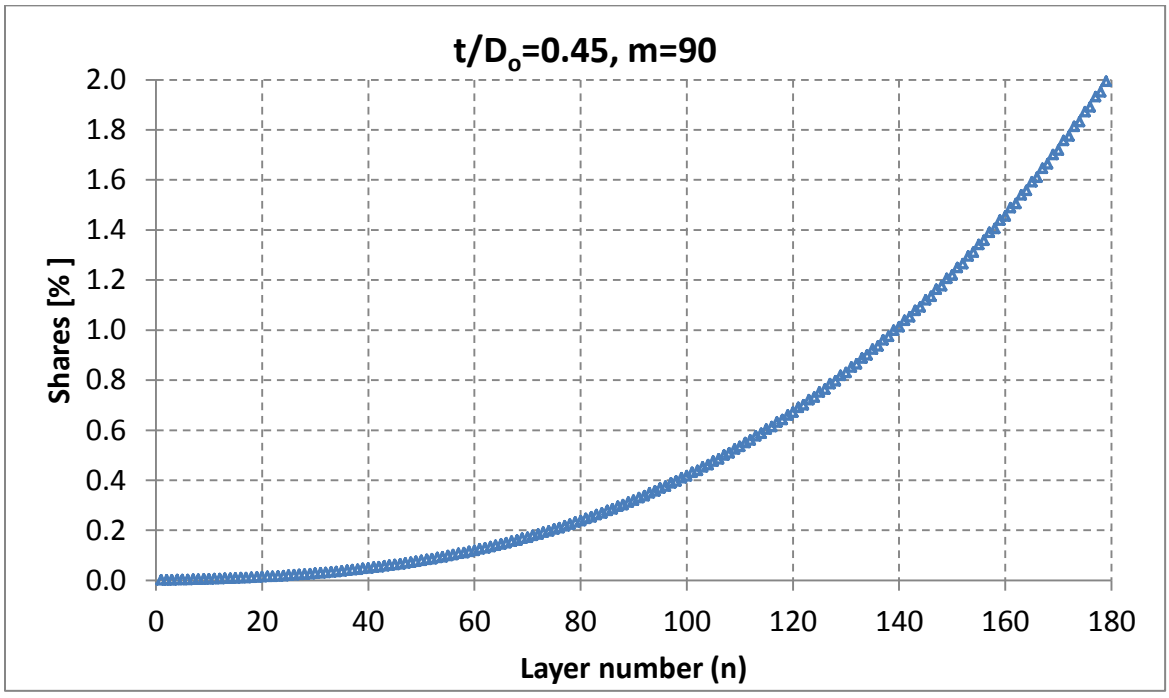

Figure 3.38:Shares of composite layers in bending stiffness for a tube of $[\theta/-\theta]_{90}$, $\theta=15^o$

3.4.1 Simple equation for bending stiffness of multi-sublaminates composite tubes

From equations (3.29) and (3.30), one can observe for multi-sublaminates composite tubes, the interaction effect is high and the geometric effects are very small. This encourages deriving a simple equation for calculating the bending stiffness of this type of tubes.

From equation (3.1), the bending stiffness of multi-sublaminates composite tubes equal to the following form:

$$\langle EI \rangle = \sum_{i=1}^{m} \left(E_{eff,1} I_1 + E_{eff,2} I_2 \right)_i \tag{3.31}$$

Form equation (3.22), and equation (3.30), assuming to cancel the geometric effects, so that:

$$E_{eff,n} = E_{eff,av} = \frac{E_x}{1 - \eta_{xy,x}\eta_{x,xy}} \tag{3.32}$$

Since from equation (3.29) and (3.32), one can assume that:

$$\left(E_{eff,1} = E_{eff,2} \right)_i = E_{eff,av} \tag{3.33}$$

Substituting by this equation in equation (3.31), to have this form:

$$\langle EI \rangle = E_{eff,av} \sum_{m=1}^{I} (I_1 + I_2)_m$$
$$\langle EI \rangle = E_{eff,av} I_T \tag{3.34}$$

Since,

$$E_{eff,av} = \frac{E_x}{1 - \eta_{xy,x}\eta_{x,xy}} \tag{3.35}$$

So, the bending stiffness of multi-sublaminates composite tubes can be calculated from the following simple equation:

$$\langle EI \rangle = \frac{E_x}{1 - \eta_{xy,x}\eta_{x,xy}} I_T \tag{3.36}$$

This simple equation is used to calculate the normalized bending stiffness for a multi-sublaminate composite tube of $t/D_o=0.45$, $\theta=15^o$, and m=90. The normalized bending stiffness is found to be equal (0.811) while the calculated value from equation (3.1) rearranged from [3] is equal to (0.816).The error % is found to be equal to (-0.06%). This result validates the high accuracy of this equation.

3.5 Conclusion

From the previous sections, it is shown that the bending stiffness property of the composite tube is specified by two parameters: the layers moment of inertia and the composite materials contributions represented in $E_{eff,n}$, such that the improvement of any of these two parameters leads to higher value of bending stiffness for the composite layers and the whole tube. Also from this chapter, one can conclude that $E_{eff,n}$ represents the contribution of the mechanical properties of the composite layer (n) in its bending stiffness property, including the influence of the tube and layer geometry, laminate configuration and incorporates the interaction effects between adjacent layers. While E_x is the extensional stiffness property of the composite layer without any of these stated effects. It is also shown that $E_{eff,n}$ is equal to E_x at the situation when the tube is made of single layer, losing the improvement due to absence of layers interaction.

Also, it is illustrated that $E_{eff,n}$ of two adjacent layers are considered as measures for the interaction between these layers in a composite tube considering bending loading. As $E_{eff,n}$ values come closer to each other, this indicates better interaction until the maximum interaction is achieved when having equal $E_{eff,n}$, the case of balanced layers. In other words, E_{eff} identifies the configuration and the geometric parameters of the balanced laminate configuration for a composite tube under bending loading using the three-dimensional elasticity theory.

The layer coefficients of mutual influences ($\eta_{xy,x}$) and ($\eta_{x,xy}$) are thought to be the key issues of the interaction effect between composite layers. This coefficient improves the contribution of E_1 in the bending stiffness of the adjacent layers especially at lower values of θ.

G_{12} is an effective material property for bending stiffness of thin layers specially the outer layers, since the largest portion of the material of the layer exists in its working plane (12). While for thick layers, the largest portion of the material is in the layer radial direction, making G_{13} to be the effective material property for bending stiffness since it controls the rigidity of this direction.

Lastly, the practical situation of multi-sublaminate composite tubes of $[\theta/-\theta]_m$ exhibit higher bending stiffness property compared to composite tubes made of only one sublaminate due to lower values of $(t/D_o)_i$ of the tube sublaminates causing closer configuration for the balanced laminate and maximizing their bending stiffness. This enhancement in the bending stiffness is required to be validated experimentally. The following chapter is devoted to illustrate the experimental work done for manufacturing and testing of two thick-walled composite tubes, the first tube is composed of one sublaminate and the second tube is of multilayered laminate configuration.

.

Chapter 4

Experimental work

The experimental work in this study has a number of goals. The first goal is to manufacture a thick-walled thermoplastic composite tube of good quality using Automated Fiber Placement technique (AFP). This is achieved by identifying the optimum parameters for the manufacturing process. The second goal is to check the feasibility of testing thick-walled composite tubes using the pure bending test setup as a better alternative testing method compared to the conventional three-point and four-point bending tests. The third goal is to investigate the bending behavior of thick-walled composite tube experimentally. This is achieved from the bending test results, by specifying the bending stiffness, the strength of the tube, and understanding the failure behavior of thick-walled composite tubes (specifying the initial mode of failure and the progressive final Modes). The last goal is to validate the used theory and the obtained explanation about the bending stiffness property.

This chapter is devoted for obtaining the optimum manufacturing parameters to have a thermoplastic composite tube of good quality, and inspection procedures for quality assurance. Also the pure bending test setup is introduced and the test preparations are presented.

4.1 Manufacturing of thermoplastic composite tubes with acceptable quality

In this section, the manufacturing process of AFP-made thermoplastic composite tubes is discussed. A study is carried out to identify the optimum parameters for the manufacturing process, in order to have a composite tube with acceptable quality. At the end of this section, the manufacturing process of the test specimen, with the performed quality assurance, is presented.

4.1.1 Automated fiber placement manufacturing technique

In the last decades, composite manufacturing processes showed large progress in automation. Automated fiber placement (AFP) technique is one of these developed processes in order to overcome some of the limitations found in filament winding and automated tape layup methods.

AFP is considered as a combination of these two techniques such that it gets the advantage of filament winding method in using continuous prepreg tapes for manufacturing structures with surfaces of revolution, and the advantage of automated tape layup methods for manufacturing structures with relatively flat surfaces using a compaction roller to place the prepreg accurately. It also can manufacture composite structures of concave surface of revolution, while filament winding method can only handle structures with convex surface. It is also important to note that filament winding techniques cannot be used to manufacture thermoplastic composite structures while AFP can be utilized with both thermoset and thermoplastic composites by changing the laying head. AFP utilizes narrow width tapes of typically 0.25–1 inches as its composite material medium.

For thermosets, the composite structure is laid down on the tool using an elastomeric compaction roller and a curing process is required using autoclaves or ovens. While, thermoplastic composites have an advantage over thermosets that the autoclave process can be avoided leading to reduction of the manufacturing cost. AFP lays down the thermoplastic tape, heating the tape via hot gas, laser, or other heating methods and applying pressure by means of a metal compaction roller simultaneously. This process forces the resin to flow between the fibers and consolidates the tape onto the tool surface, in situ, without the need for further consolidation processes [30].

Figure 4.1 shows the process of laying down a thermoplastic composite slit tape of width 0.25 inches, using a nitrogen Hot Gas Torch (HGT) as the heating source and compacting the tape on the previous layers to be consolidated.

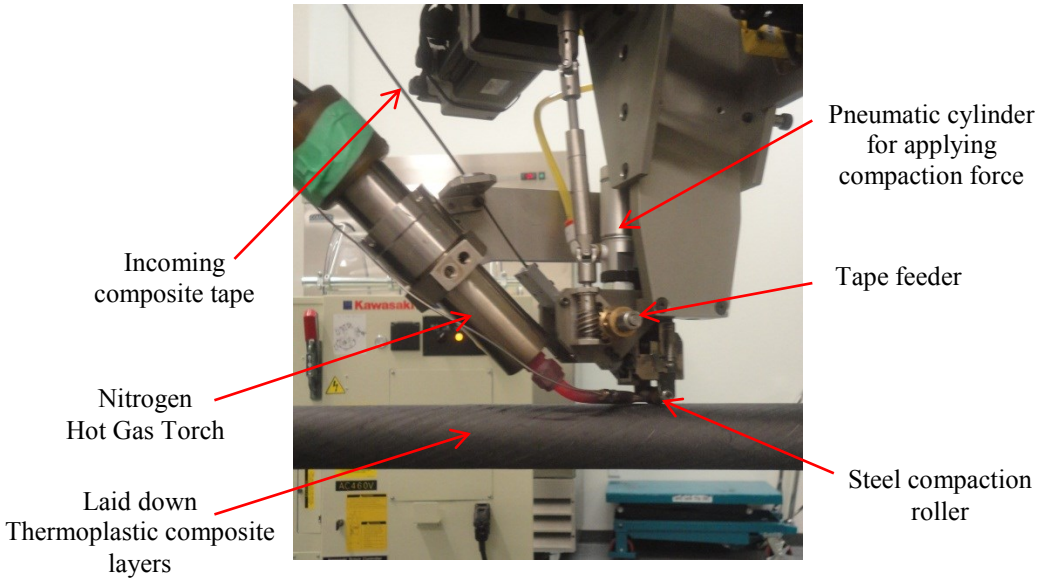

Figure 4.1: Automated fiber placement for thermoplastic composite tape

It is highly desired to achieve good consolidation for thermoplastic composites using AFP and avoid the use of post consolidation process in a high-temperature autoclave in order to reduce the cost and time of producing thermoplastic composites. However, it is a challenge to have in-situ consolidated thermoplastic composite structure with acceptable quality level. This challenge is because the manufacturing process is controlled by a large number of parameters and these parameters are different according to machine type. For example the manufacturing parameters for machines using nitrogen HGT heating source differ from those machines using laser. Also, since this manufacturing technique is recently developed, we can see a relatively small number of publications discuss the quality issue. In the next subsection, some of the optimum manufacturing parameters are discussed in order to have a thick-walled composite tube of good quality.

4.1.2 Manufacturing parameters of an AFP-made thermoplastic tube with good quality

Thermoplastic composite material is chosen to be used in manufacturing thick-walled tube specimens. This is because of the advantage that thermoplastic composite structures can be manufactured using AFP technique by instu consolidation, avoiding the autoclave process.

Carbon/PEEK is the selected thermoplastic composite material as it has high structural performance, good impact resistance, and high temperature performance with service temperature 120^{o}C. Also it offers a composite material of low moisture absorption, excellent resistance to chemicals and solvents. These characteristics make Carbon/PEEK to be ideal for structural applications in aerospace field as landing gears of helicopters. Carbon/PEEK is also flame retardant.

Two thick-walled tubes made of Carbon/PEEK thermoplastic composite material of same geometry are manufactured in order to be tested using the pure bending test setup. The first tube has a laminate configuration $[25_{45}/\text{-}25_{45}]$, meaning that the laminate is made of two thick layers; the inner layer is of orientation angle (25^{o}) and the outer layer is of orientation angle (-25^{o}). The second composite tube has a laminate configuration $[25/\text{-}25]_{45}$, which means the laminate is composite of thin layers alternatively arranged. The tubes dimensions are of D_o=61.1 mm, D_i=38.1 mm, t=11.5 mm, t/D_o=0.19. The tubes length is equal to 1016 mm.

The first thermoplastic composite tube is manufactured using an AFP machine, available at CONCOM, using the following process parameters: Nozzle temperature=825^{o}C, lay down process rate= 70 mm/sec (2.75 inches/sec), and the compaction force=178 N (40 lbf). Figure 4.2 shows small samples that are taken from the tube in order to check the quality of the tube using scanning electron microscope (SEM).

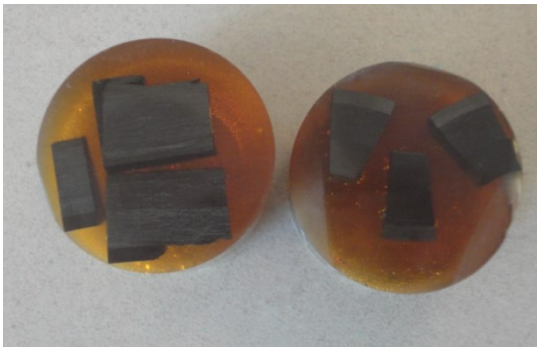

Figure 4.2: SEM sample of the first thick-walled composite tube

Figure 4.3 shows the SEM figures of the samples taken from the tube.

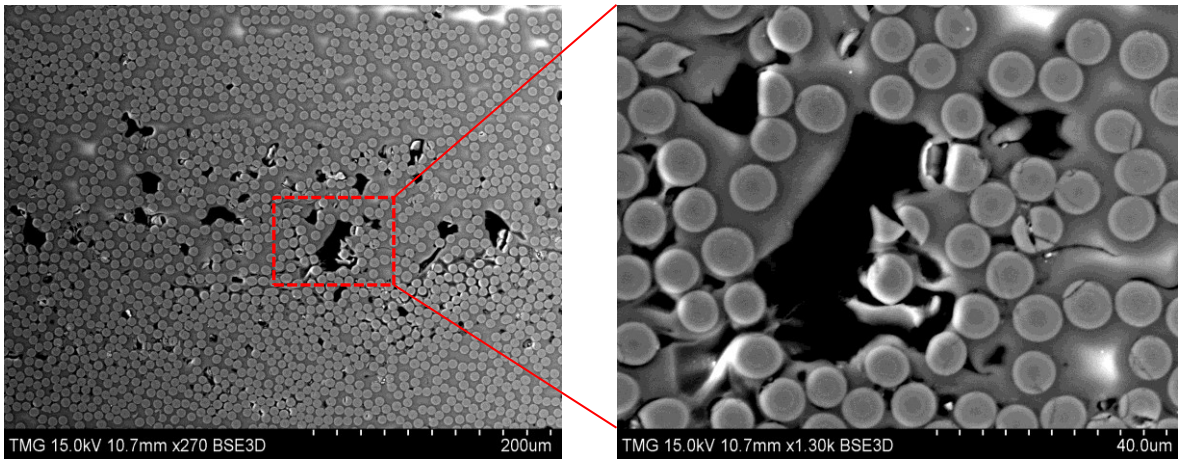

Figure 4.3: SEM figures of a sample taken from the first tube

The inspection of the sample shows a lot of voids between layers within the tube cross section which means that the tube is of poor quality. However, because of the large cost of the manufacturing expenses and the used thermoplastic material and the effort done, a decision is taken to test the tube as a trial test in order to gain experience. The tube was tested and it failed at relatively lower loading level. This motivates to carry out a study to get some of the optimum manufacturing parameters in order to have a thermoplastic composite tube with acceptable quality level, starting with reviewing the context.

Several studies studied the influence the manufacturing parameters on the fiber placed thermoplastic composite structure [25], [31], [23] such as the rate of laying down the tape, the applied heat flux from the heating source, the applied compaction pressure, and the number of compaction passes. Shadmehri et al, [25] discussed the effect of the heat flux, compaction force and the process rate on the stiffness of rings made of Carbon/PEEK. X. Cai et al, [31] have identified the optimum process parameters for thermoplastic composite rings from the strength point of view. They concluded that the compaction force is the most significant factor that affects the strength properties of the laminates. Khan et al, [23] identified some optimal parameters to achieve higher laminate quality through fiber placement process. After laying down the thermoplastic tape, they performed a number of compaction passes with the roller without adding more material. They concluded that increasing the number of compaction passes improves the quality of the samples.

This motivates to make a study in order to identify the minimum number of compaction passes required to have a sample with acceptable quality level.

4.1.2.1 Used material

The test specimens are made of Carbon/PEEK unidirectional prepreg tape of quarter inch width. The material is supplied from TenCate Advanced Composites Company, having a commercial name "Cetex TC1200 PEEK AS-4", made of a semi-crystalline poly-ether-ether-ketone thermoplastic resin with unidirectional carbon fibers. The resin content is 34% by weight and 41% by volume. The resin has glassy temperature (Tg=143^{o} C), melting temperature (Tm=343^{o} C) and typical processing temperature range (370^{o} -400^{o} C) [32]. The typical applications of this thermoplastic composite are primary and secondary aircraft structures

4.1.2.2 Plan of work

Small thin-walled composite tubes made of Carbon/PEEK are manufactured using different number of compaction passes in order to identify the optimum number providing an acceptable quality level. Then, samples are taken from these tubes in order to be inspected using SEM. The minimum number of compaction passes is chosen according to the satisfied quality level. Noting that increasing the number of compaction passes will multiply the manufacturing time.

The manufacturing process is carried out using a 6- axis robotic AFP, supplied from ADC Company, USA. Both Shadmehri and Cai [25], [31] were using an AFP machine supplied from ADC, which has a similar configuration to the AFP machine available at CONCOM, such that the obtained optimum parameters from their studies can be applied in our study. The type of the used AFP machine type has nitrogen (HGT) as the heating source, and lays down thermoplastic composite tape of 6.35 mm (0.25 inches) width.

All the samples are manufactured on a steel mandrel of 38.1 mm (1.5 inches) diameter with a stacking sequence $[90/25_{10}]$. Table 4.1 shows the samples specifications and the used number of compaction passes.

Table 4.1: Specifications of the used samples in the optimization study

Tube ID	No. of samples	No. of compaction passes
0C	6	1
1C	6	2
2C	6	3
3C	6	4

The manufacturing parameters are as follows:

Nozzle temperature=850^{o} C, lay down process rate=70 mm/sec (2.75 inches/sec), and the compaction force=333.6 N (75 lbf).

After manufacturing every sample, a power screw extractor, available at CONCOM, is used to extract the mandrel from the sample. The extractor is of two tons loading capacity, supplied from ADC. An adaptor and an extraction disc are manufactured in order to use the extractor to remove the mandrel from the manufactured samples. The extraction process is carried out by inserting the extraction disc and the adaptor at the threaded end of the mandrel, then two washers are assembled on the mandrel, and a through bolt connects the adaptor to the head of the power screw. Figure 4.4 shows the adaptor, the extraction disc assembled on the extractor. The head moves away from the extraction disc which in turns constrains the composite sample, and the mandrel is pulled out slowly from the sample through the disc. Figure 4.5 shows the manufactured tubes after extraction.

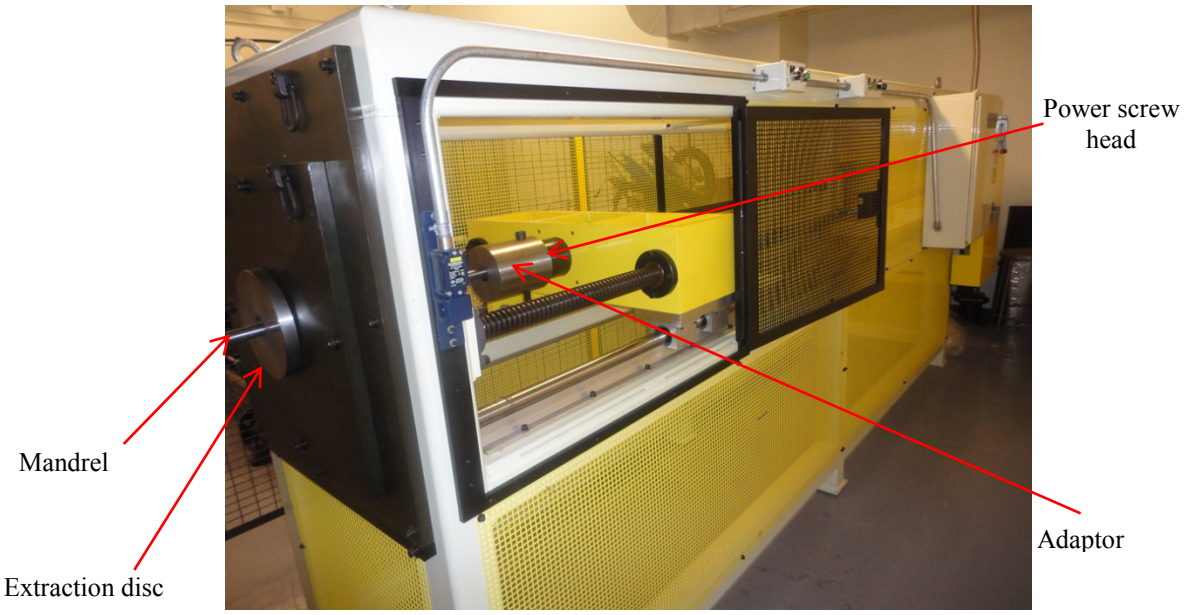

Figure 4.4: Designed parts for mandrel extraction, assembled in the power screw extractor

Figure 4.5: Thin-walled composite tubes of different compaction passes

4.1.2.3 Sample preparation

Small samples of 30 mm length and 20 mm width are taken from the tubes using a diamond cutter in order to inspect these samples using scanning electron microscope. Once the samples are cut, they are mounted in four different plastic with a resin system of 100 pph 828-Epon epoxy and 40 pph 3046-Epicure curing agent. The quantities of each material were 49.232 g and 19.691 g respectively. The material quantities are mixed and degased under vacuum for 15 minutes, and then the resin is poured over the samples, and left for six hours at room temperature to be cured. Finally, the samples are post cured for twelve hours inside an oven at 60^{o} C.

Grinding and polishing processes are carried out for the cured samples. The grinding and polishing processes are critical steps for this study as the SEM pictures are highly dependent on these processes. As an example rough grinding may take off fibers from the samples that can be interpreted as voids in the pictures. Also this rough process may shred the fibers which can be wrongly understood that the

compaction force is high during manufacturing. The following steps are suggested in order to achieve samples with good quality.

At first the grinding process is carried out using sand papers (silicon carbide) with grades 120, 240, 380 to assure flatness of the samples after removing the resin from the surface of the composite specimens, then this step is followed by fine grinding process using Grit size of 400, 600, 800, and 1200. In order to be sure that the samples microstructure does not change, water is used as a coolant, reducing the heat generated from the friction between the specimen surface and grinding paper as shown in Figure 4.6.

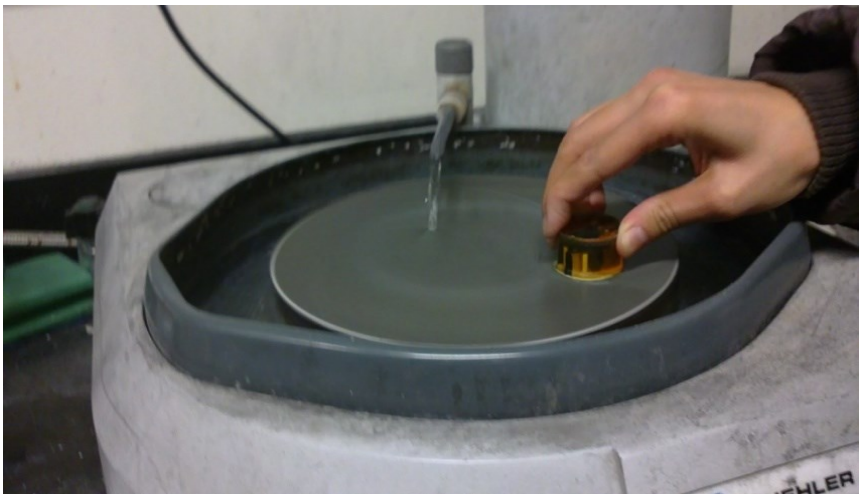

Figure 4.6: Grinding process for SEM samples using water as a coolant

After the grinding process, the specimens are polished using Arctic polishing cloths type N- 8 inches (trade mark ANAMET), with diamond suspension (3micron) and diamond Extender (water based) coolant. The process is repeated with **(**1micron) diamond suspension and diamond extender coolant, followed by polishing using Imperial polishing cloths supplied from ANAMET, with diamond suspension of (0.5micron). Figure 4.7 shows a picture for the polished samples.

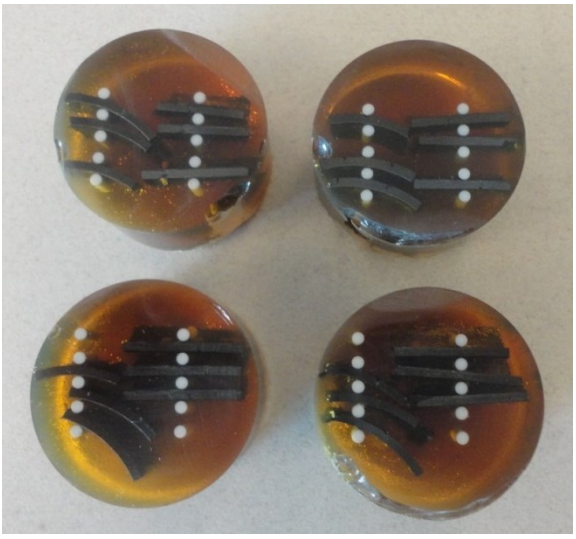

Figure 4.7: Polished samples for different number of compaction passes

4.1.2.4 SEM inspection

A Scanning Electron Microscope (SEM), available at CONCOM, is used to inspect the polished samples in order to hive high magnification. The SEM is of type "S-3400N Hitachi", supplied from Oxford Instruments, which has the ability to inspect nonconductive samples without conductive coating using variable pressure technique. Figure 4.8 shows the captured pictures from SEM.

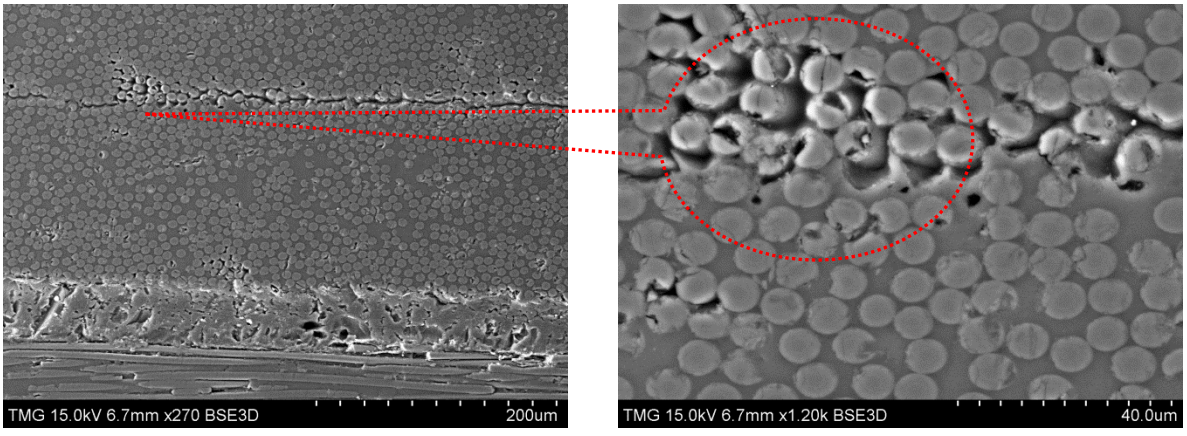

(a) (b)

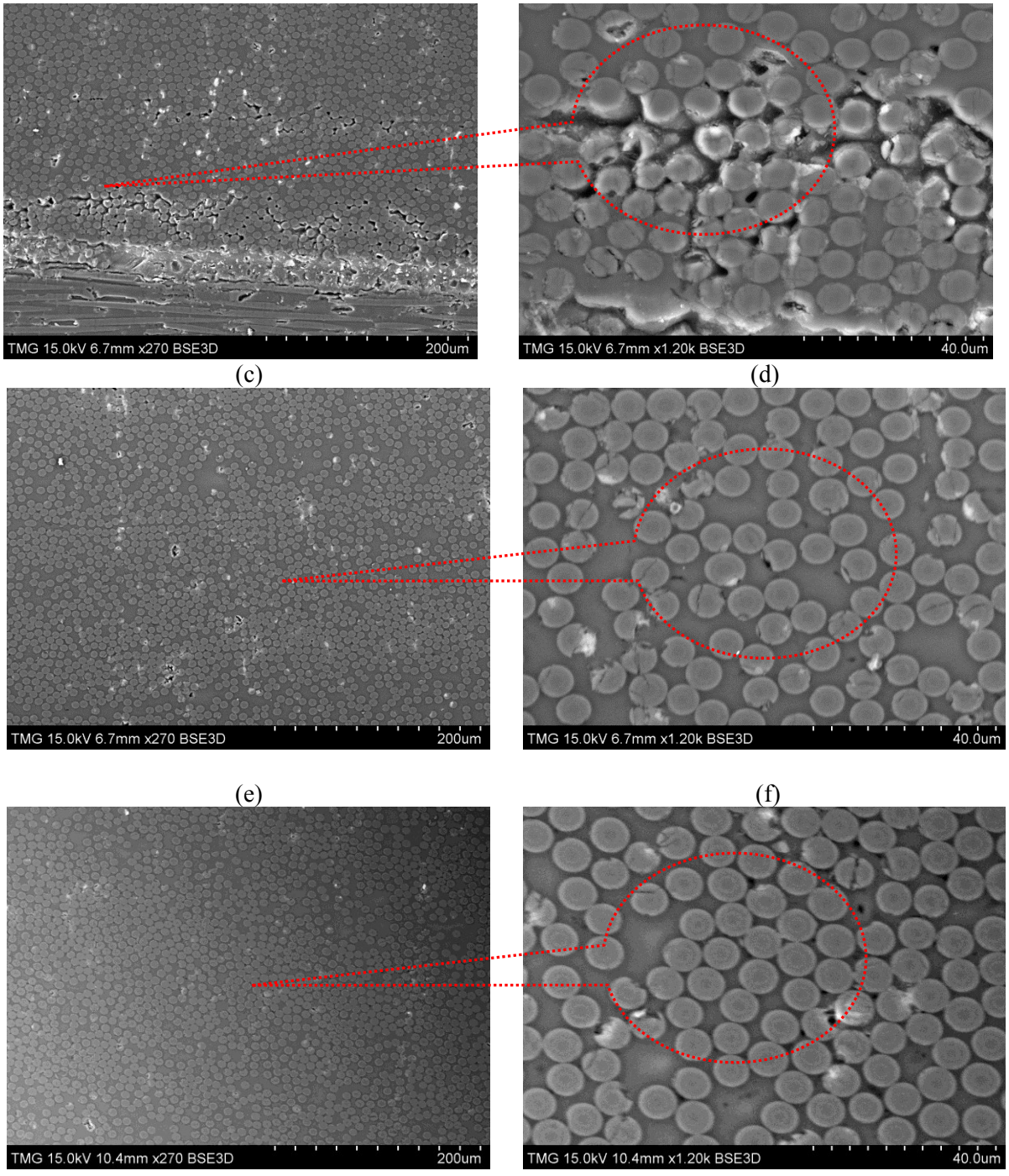

Figure 4.8 : SEM figures for different number of compaction passes
(a,b) zero compaction pass, (c,d) one compaction passes, (e,f) two compaction passes
(g,h) three compaction passes

It is observed that the samples of zero or one compaction passes have the worst quality. They have poor contact between layers, delamination, and large percent of void content. For larger number of compaction passes, better wetting of fibers are shown and better intimate contact between layers are achieved. The samples of acceptable quality are those manufactured using 2 compaction passes.

The improvement in the quality of samples is due to three reasons:

- Give a chance for the matrix material to flow in order to wet the fibers and fill the voids during the time of compaction.
- Improving the surface roughness of the laid down fiber bands.
- Increasing the intimate contacts between layers.

A Shifting angle ($\Delta\alpha$) is suggested at the start of laying down each layer in order to cover the gaps between layer bands. This shifting angle prevents building up of a ready-made crack through the tube wall thickness, as shown in Figure 4.9. The shifting angle is specified using the following equation:

$$\Delta\alpha = \frac{360}{2N_{bands}} \quad \textbf{(4.1)}$$

Where, N_{bands} are the number of bands that form the layer

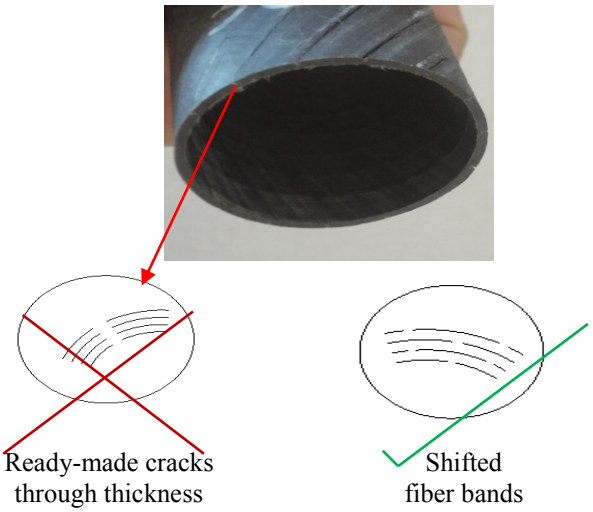

Figure 4.9: Shifting the fiber bands to avoid ready-made cracks

4.1.3 Manufacturing of the thick-walled composite tube specimen with better quality

The second test specimen is a thick-walled straight composite tube needed for pure bending test in order to measure its bending stiffness and to study its failure behavior. The tube is made out of an advanced thermoplastic composite material of a semi-crystalline poly-ether-ether-ketone thermoplastic resin with unidirectional carbon fibers. The material is supplied from TenCate Advanced Composites Company having a commercial name "Cetex TC1200 PEEK AS-4". The tube dimensions and laminate configuration are listed in Table 4.2. The manufacturing process is carried out using the AFP available at CONCOM, Figure 4.10.

Table 4.2: Dimensions and laminate configuration of the second composite tube

Tube length	1016 mm (40 inches)
Inner diameter (D_i)	38.1 mm (1.5 inches)
Outer diameter (D_o)	61.1 mm (2.405 inches)
Wall thickness/outer diameter (t/D_o)	0.19
Laminate configuration	$[90/(25/-25)_{45}]$

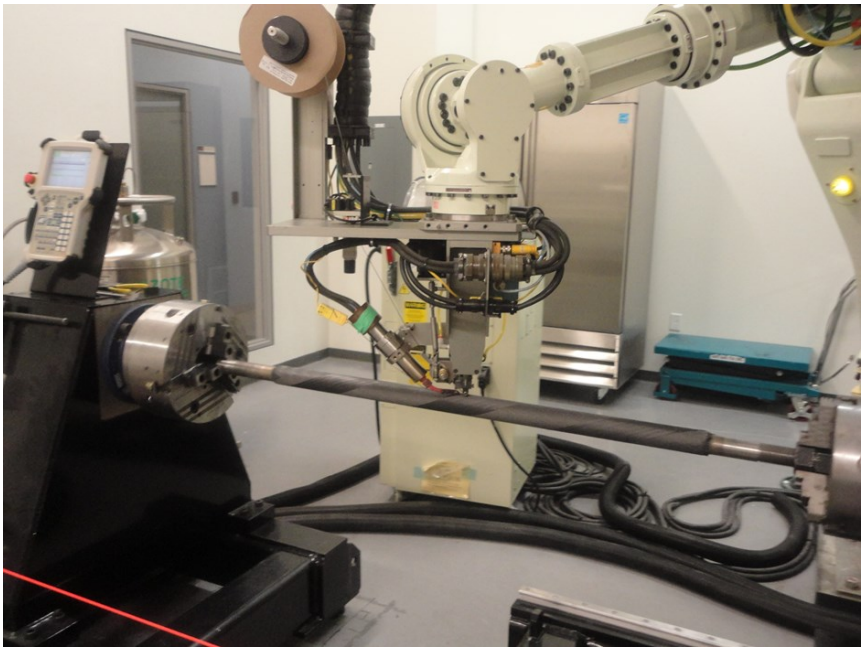

Figure 4.10: Manufacturing of the thermoplastic composite tube using a robotic AFP machine

The manufacturing parameters are listed in Table 4.3, according to the available literature and the presented study in order to have a part with acceptable quality.

Table 4.3: Manufacturing parameters of the second composite tube

Number of compaction passes	2
Compaction force	333.6 N (75 lbf)
HGT temperature	875^{o} C
Nitrogen flow rate	75 L/min
Laydown process rate	70 mm/sec (2.75 inches/sec)

A mandrel is needed for the manufacturing process which should be stiff enough to withstand the applied compaction forces during the layup process and it should be extractable from the

manufactured tube. A steel mandrel of diameter 1.5 inches is manufactured, polished and threaded at one end to be extracted easily after the manufacturing process, Appendix B.

Steel rollers are designed and manufactured in order to be used in the layup process and to apply the compaction forces. The rollers have specific profiles to guarantee a maximum contact curve for the thermoplastic tape and the previous consolidated layers on the mandrel surface, Figure 4.12. The roller profile is generated by revolving an arc of an ellipse around the roller axis. The ellipse major diameter (D_x), and minor diameter (D_y) are specified according to the diameter of the placed layer (D_L) and its inclination angle (θ) as shown in Figure 4.11, such that:

$$D_y = D_L$$
$$D_x = \frac{D_y}{\cos\theta} \qquad \textbf{(4.2)}$$

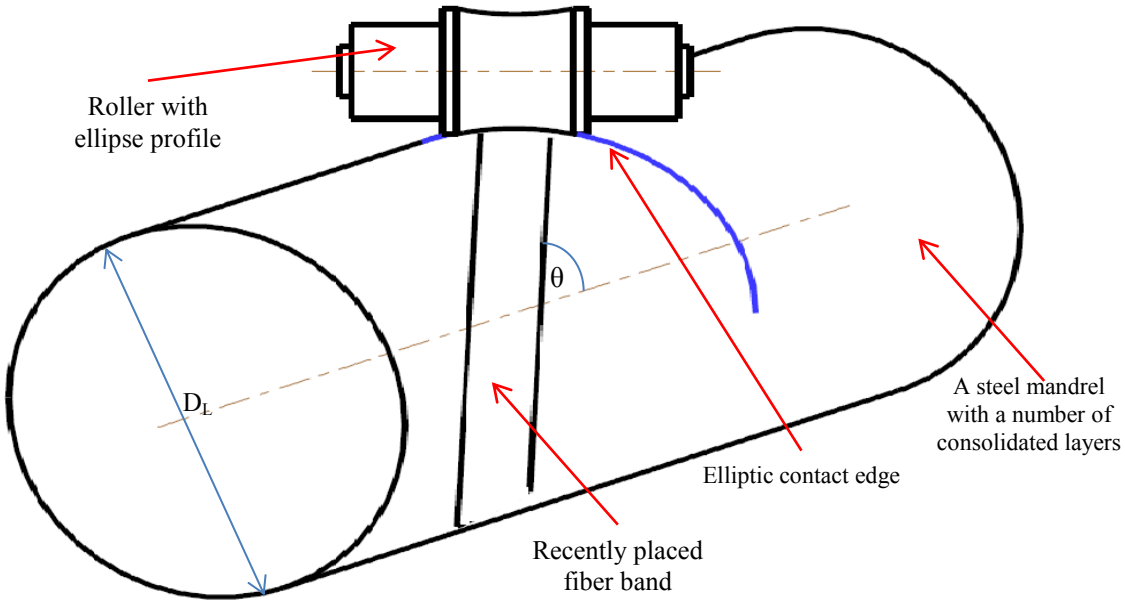

Figure 4.11: Roller profile permits a maximum contact edge with the placed fiber band

Since D_L is increasing during the manufacturing process, four steel rollers are designed such that each roller is used for a specified range of D_L. The rollers dimensions and their working range are tabulated in Table 4.4

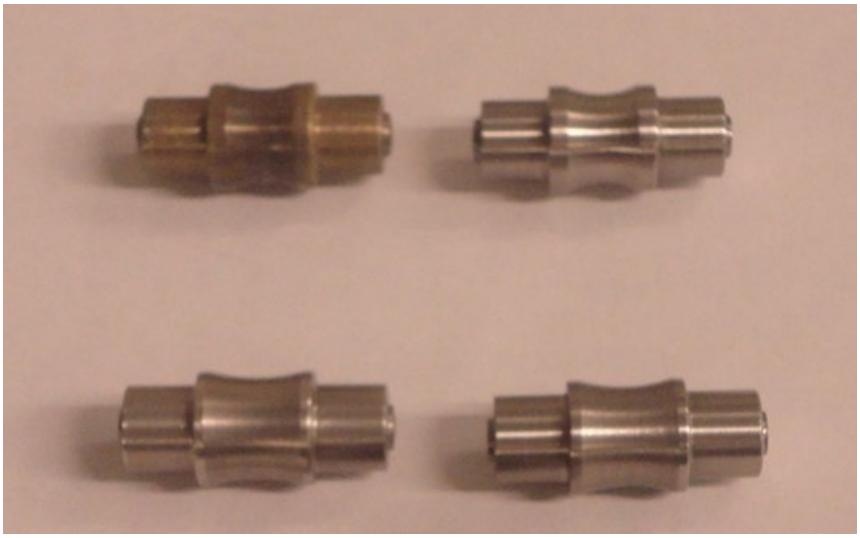

Figure 4.12: Steel rollers have elliptic profiles with different dimensions

Table 4.4: Dimensions and the working range of the used compaction rollers

Roller no	Dx [Inches]	Dy [Inches]	Diameter working range [Inches]
1	1.66	1.5	1.500 - 1.625
2	1.93	1.75	1.625 - 1.875
3	2.21	2	1.875 - 2.125
4	2.48	2.25	2.125 - 2.406

* All dimensions in inches

For the 90^o layer, a roller with a straight cylinder is manufactured. All these rollers have a polished surface in order to have good surface finish for the manufactured part.

4.1.3.1 Tube extraction and cutting

After the manufacturing process, the last step is to extract the mandrel from the composite tube. This process is a critical step so that the tube may be damaged if it is not performed properly. The mandrel with the tube is placed in a freezer of -20^{o}C for one day in order to allow shrinkage of the steel mandrel more than the composite tube, facilitating the extraction process. A plastic bag is used in order to isolate the tube from any condensed water vapour when it is removed from the freezer.

The power screw extractor is used for the extraction process. Figure 4.13 shows the extraction process of the mandrel from the tube.

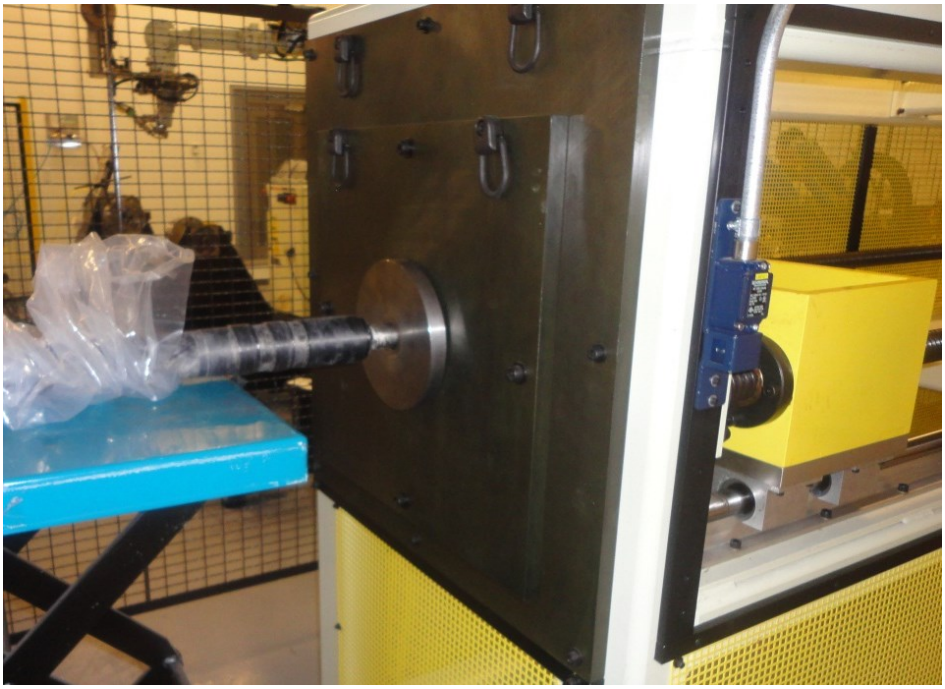

Figure 4.13: Extraction process of the mandrel from the thermoplastic composite tube

4.1.4 Quality assurance of specimen

4.1.4.1 SEM inspection

Small samples are cut out from the tube using the diamond cutter. The samples are of 20mm average width along the circumference of the tube, and of height equal to the tube thickness. The SEM samples are prepared for checking the tube quality by the same steps presented in subsection 4.1.2.3. The polished samples are inspected using a variable pressure SEM, available at CONCOM. Figure 4.14 shows the SEM picture taken for these samples

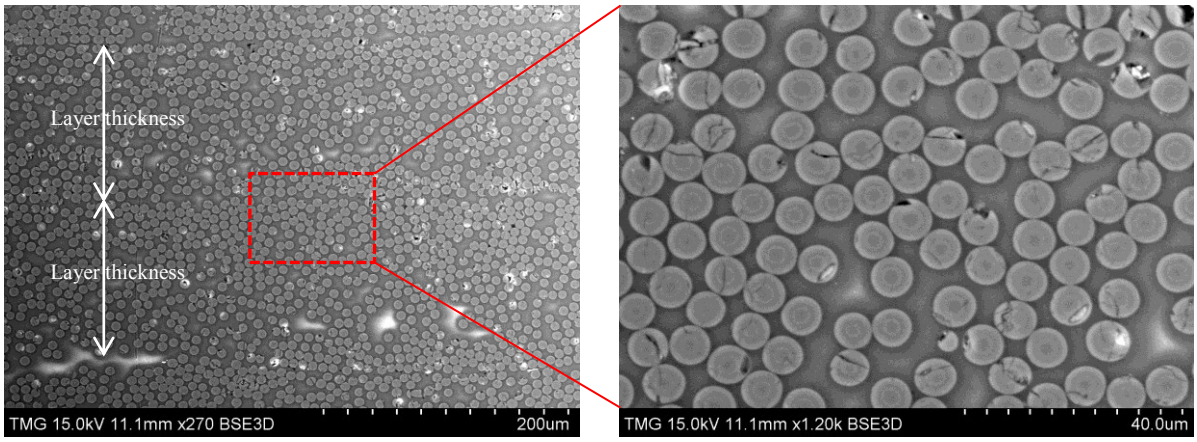

Figure 4.14: SEM figures for the second manufactured composite tube

The figure shows better quality tube compared to that of the first tube shown in Figure 4.3, as there are no delamination between layers and very small void content.

4.1.4.2 TGA test

In order to identify the volume fraction of fibers for the manufactured tube, a Thermo Gravimetric Analysis (TGA) test is carried out for a sample taken from the composite tube using TGA instrument, available at CONCOM. Figure 4.15 shows the TGA results of the sample.

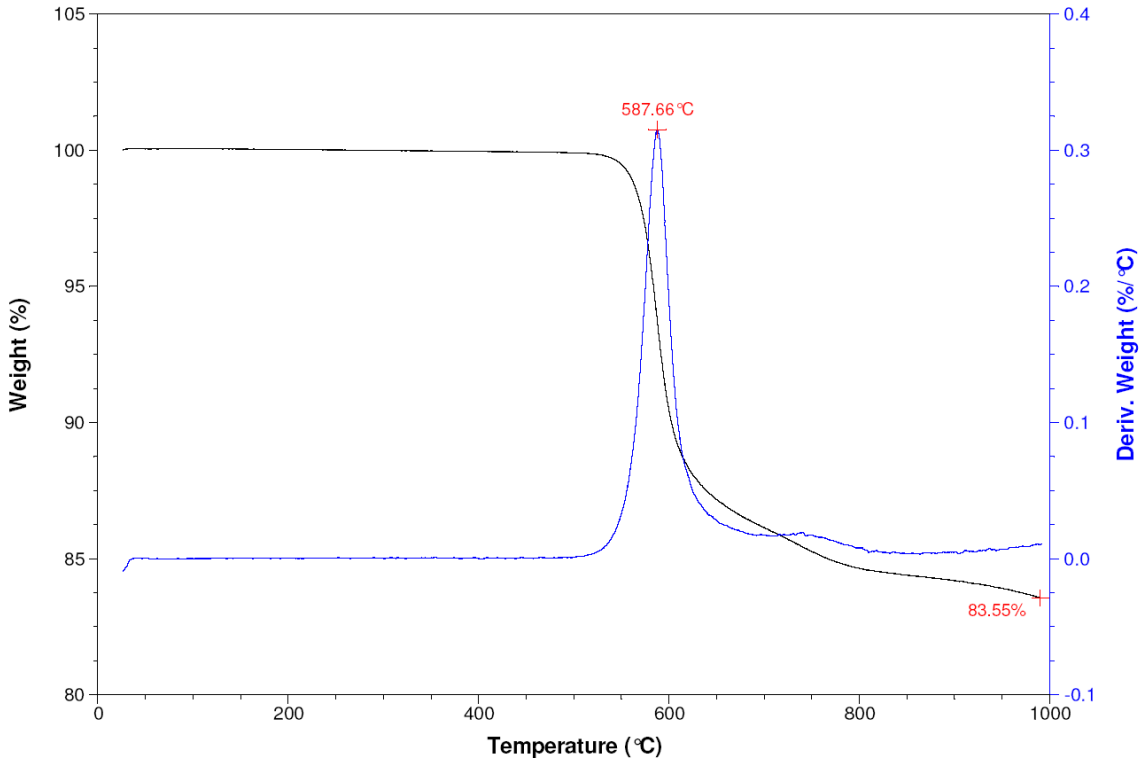

Figure 4.15: TGA result of a sample taken from the composite tube

From the TGA results, it can be observed that the degradation point of this resin is around 587.66^{o}C. By calculating the weight loss of the sample and by knowing the density of the primary materials, the volume fraction of fibers in the sample is determined to be (78% ±0.1%).

4.2 Pure bending test setup

The literature review shows the problems of using three-point bending and four-point bending tests for composite tubes [26], [1], where the bending moment is conveyed to the specimen by applying high concentrated transverse loads at the loading points. This way of loading causes high local deformation and premature failure for the test specimen under loading points. However the pure bending test setup is another different technique proposed in [27], [28] for applying bending loading to the test specimen without applying any concentrated loading points. This technique was used for thin-walled composite cylinders of quite large diameters. In this section, the feasibility of this technique is checked for testing thick-walled composite tubes. This attempt is considered to be the first time to test thick-walled composite tubes using the pure bending test setup.

The pure bending test setup in [28] has a loading capacity up to 1.5×10^6 lbf-inches (169 kN.m), Figure 4.16. The structural parts are rigid enough to prevent any deformation under the maximum loading. It can handle samples of different lengths from 30 to 48 inches (762-1219 mm). A schematic drawing for the pure bending test setup illustrates the main structural components is shown in Figure 4.17.

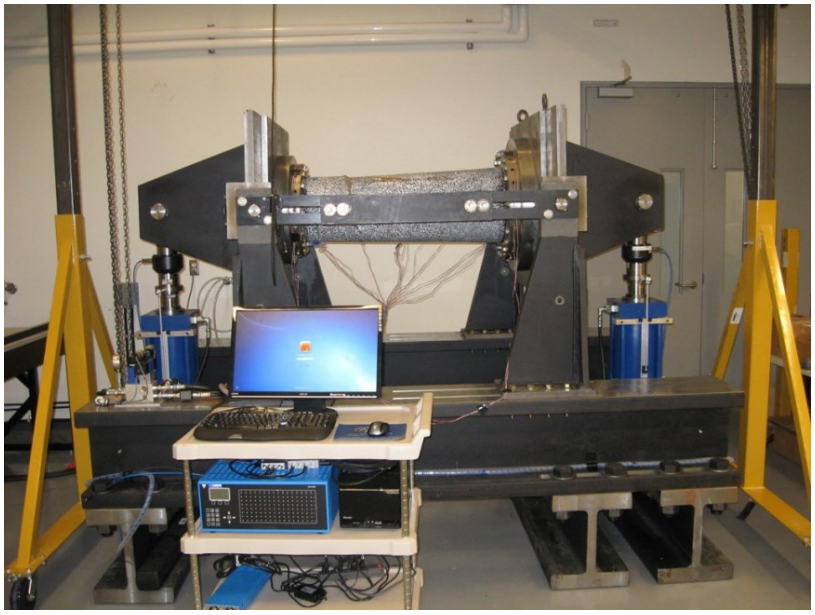

Figure 4.16: Pure bending test setup designed at CONCOM, [28]

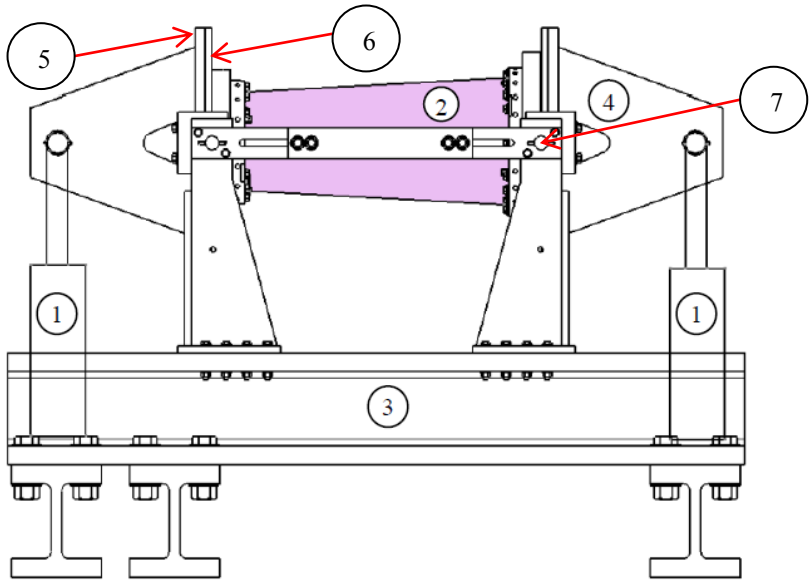

Figure 4.17: Structural components of the pure bending test setup, [28]
1-Hydraulic cylinders, 2-Test specimen, 3-Reaction frame, 4-Moment-arm, 5-back-plate, 6-Adaptor-plate, 7-Pinion

4.2.1 Idea of the pure bending test setup

The idea of the pure bending test rig is that the bending moment is conveyed to the specimen in a smoother way compared to the conventional 3-point or 4-point bending tests. The test specimen ends are fixed inside the pure bending test rig using a low melting point alloy (LMPA). The hydraulic cylinders create the required loads which are converted to equal bending moments by rotating the moment-arm assemblies (moment-arm with the adaptor-plate and back-plate) about their pinions- see Figure 4.17. This rotation generates shear forces between the LMPA and the surface of the tube ends such that the upper part of the sample is subjected to compression while the lower part is subjected to tension. These compression and tension forces form a moment at each end of the specimen without applying any concentrated load.

4.2.1.1 Low Melting Point Alloy (LMPA)

LMPA is a Bismuth alloy "Bi-Cd-Pb-Sn" which has a melting point of 75 degree of Celsius and can be melted easily and potted around the specimen. The use of a LMPA to restrain the specimen and to transfer the load to the test specimen was an idea taken from [27].

4.2.1.2 Adaptor ring

For the case of thin-walled composite cylinders of large diameter, the cylinder is fitted between inner and outer rings. Also a number of radial bolts are used to fix the specimen at the tension side with the LMPA in order to prevent the cylinder from slipping out of the rings during the test, Figure 4.18.

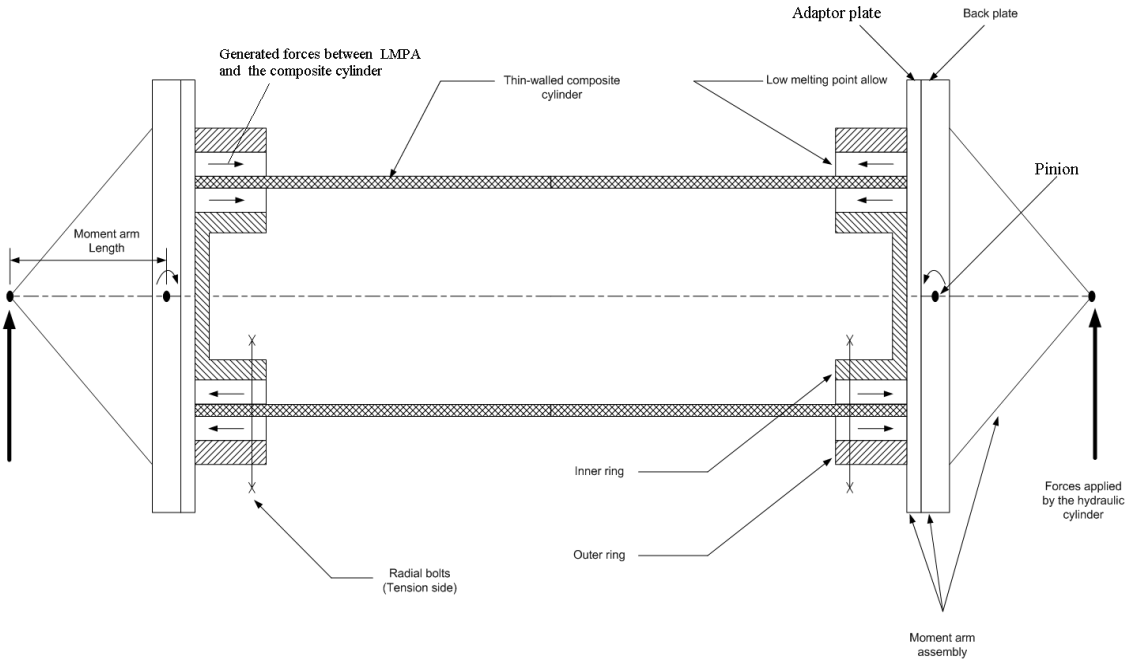

Figure 4.18: Fixation of thin-walled tubes in the pure bending test setup

For thick-walled composite tubes of smaller diameter, the tube is of small inner diameter such that no inner ring can be used and the tube has a large wall thickness preventing the usage of these radial bolts. An adaptor ring is designed to fix thick-walled composite tubes inside the test rig instead of the inner ring and the radial bolts. The idea of this design is to have a ring with large depth permitting bigger contact surface between the LMPA and the tube ends in order to compensate the absence of the radial bolts at the tension side, Figure 4.19. The design drawing of the adaptor ring is presented in Appendix B. Two adaptor rings are manufactured and fixed in the adaptor-plate of the pure bending test setup, one ring for each tube end, as shown in Figure 4.20.

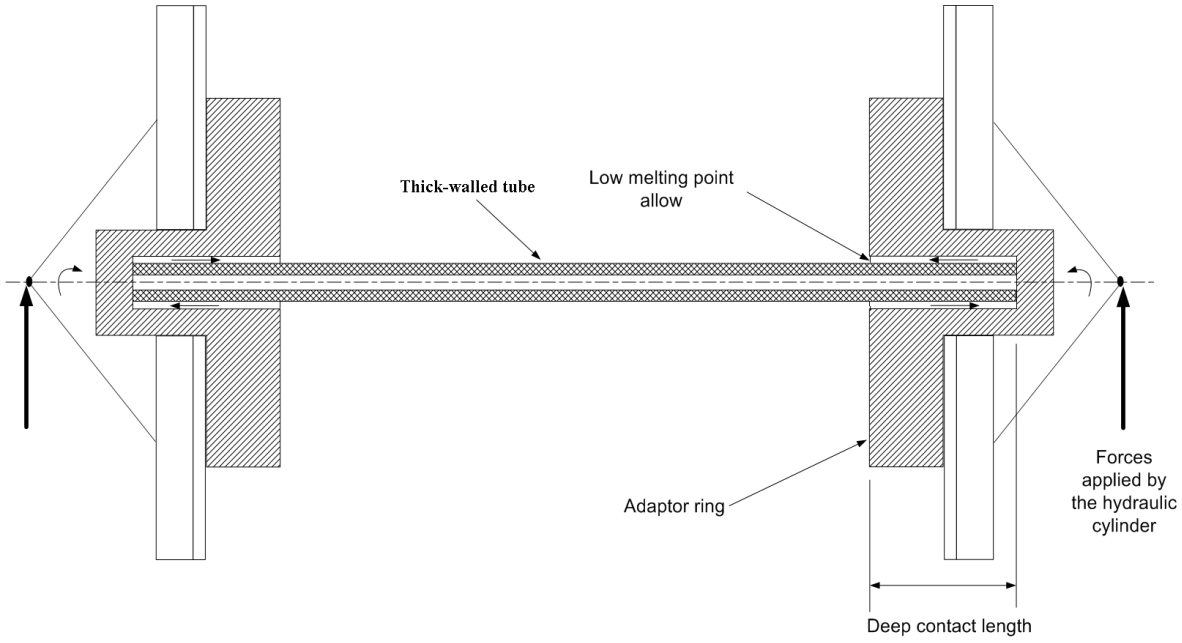

Figure 4.19: Idea of fixing thick-walled tubes in the pure bending test setup

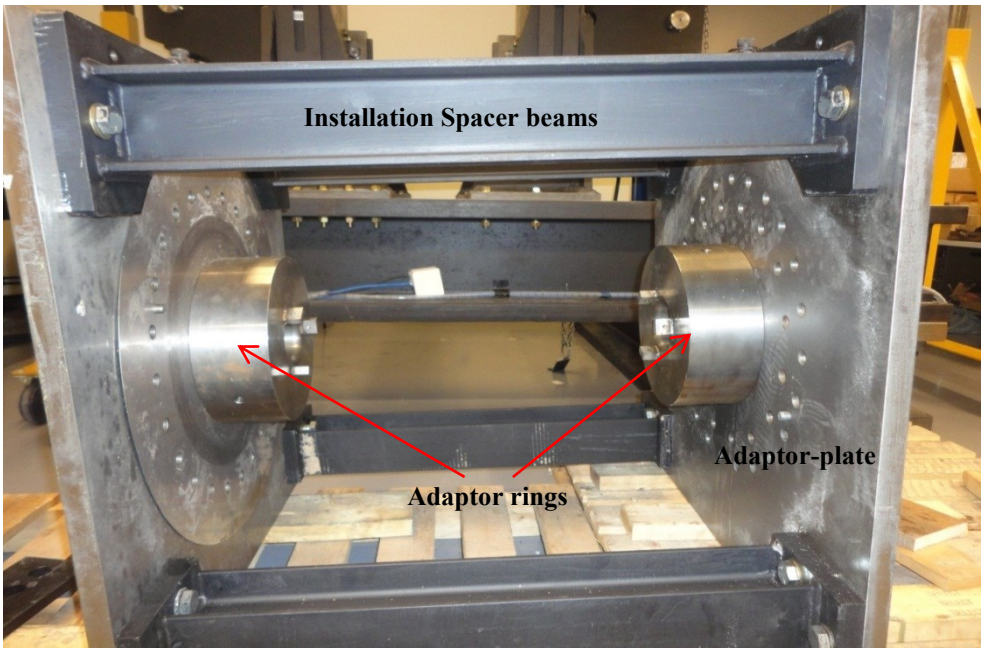

Figure 4.20: Adaptor rings fixed in adaptor plates outside the test setup

4.2.2 Measuring instruments

Different measuring instruments are utilized in the bending test in order to acquire the response of the composite tube under bending. These instruments are listed as follows:

- Digital Image Correlation (DIC) system to measure the tube deformation and strains
- Strain gages to measure strain at specified points on the tube
- Force transducers to measure the applied forces from the hydraulic cylinders
- Position transducers to measure the displacement of the hydraulic cylinders
- Dial gauge to measure the tube deflection at its mid length.
- Data acquisition system to record the signals from strain gauges and force transducers
- Data acquisition card for recording signals from the position transducers

Details of these instruments are explained in the following subsections.

4.2.2.1 DIC system

This system is used to measure the global tube deformation and strain field during the bending test. A three-dimensional DIC system is available at CONCOM, equipped to control simultaneously two pairs of optical sensors (digital cameras). This permits installing one pair of optical sensors on the top of the specimen to measure strains and deformation in the upper side of the tube (Top view) and the other pair can be installed in front side of the tube (Front view). The measuring principle and the system advantages of the DIC system are explained in the following paragraphs

4.2.2.1.1 Measuring principles

For one pair of optical sensors, each point on the tube surface is focused on a specified pixel in the image plane of each sensor. By identifying the sensors orientation with respect to each other and their imaging parameters, the three-dimensional coordinates of each point on the tube surface can be

calculated. A random pattern of points is required on the tube part such that the DIC system is able to track the position of each point in the images obtained from the two sensors using image correlation algorithms.

The tube position is recorded before the bending test to be the reference image for the DIC system calculations. The tube surface in this image is divided into small facets, then during the test the DIC system tracks the translation, rotation and distortion occurred for these small facets. The correlation algorithms calculate the tube deformation in the image plan. Using one optical sensor (two-dimensional DIC), the accuracy of calculations can reach up to 1/100 pixel. While using two optical sensors permits higher accuracy and the three-dimensional coordinates of any point on the tube surface can be calculated. By determining the 3D coordinates for every point on the tube surface, the 3D contour of the tube surface can be plotted.

Also the deformation contour of the tube surface can be plotted by calculating the displacement vector of each small facet on the tube surface. That the center point P of one facet moved from the original position in the reference image (P_u) to the deformed position (P_v) due to facet distortion, translation and rotation during the test, as shown in Figure 4.21.

The displacement vector for this facet can be calculated from the calculated positions of P_u and P_v.

From displacement vectors, the DIC system can calculate the strain at each point on the tube surface to have the strain contours [33].

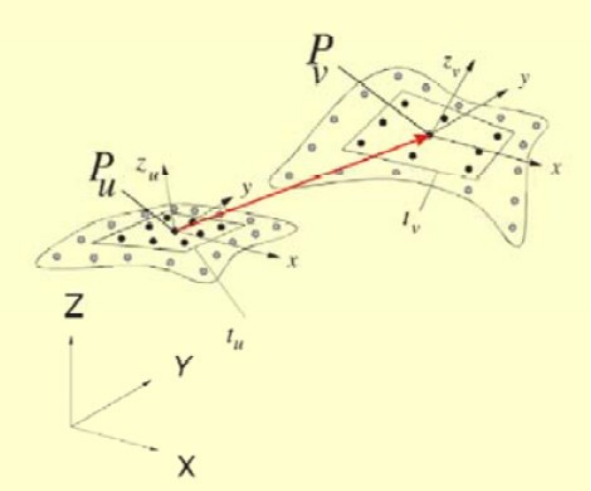

Figure 4.21: Deformation of 3D displacement vector Ref. [33]

4.2.2.1.2 Advantages of DIC System

From the previous discussions, one can see that this system has the following advantages compared to wire strain gages [34]

- Contactless strain measurement: this means that the DIC can capture strains in situations that wire strain gages cannot be used. One of these situations in large deformations that exceed the limitations of wire strain gages. Also at failure regions, the DIC can capture the strain field while wire strain gages will detach from the failure region. Adding to that the elimination of the measurement errors in wire strain gages due to misalignment, the adhesion quality, or thermal variations.
- Full-Field Measurements: this advantage provides contour plots for the tube deformation in three-dimensional coordinates, which means the global deformation the tube.

4.2.2.1.3 Validation of the DIC system

In order to validate the obtained results from the DIC system, an L-shape composite plate is manufactured and tested under tension using MTS. This plate configuration is chosen in order to involve large deformation effects. A unidirectional strain gauge is mounted on the composite plate and a random pattern of points is drawn on the plate surface, Figure 4.22. One pair of optical sensors is used with the DIC system in the test. The strain obtained from both the wire strain gage and the DIC system at the stain gage location are compared in Figure 4.23

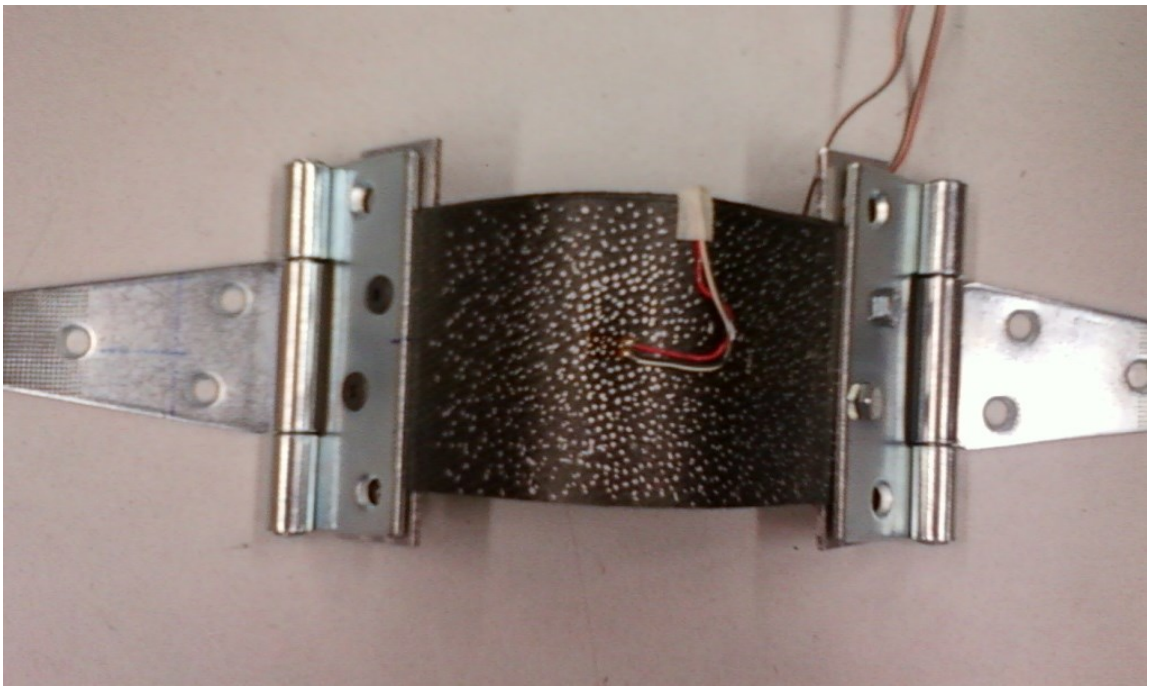

Figure 4.22: L-shape plate with the random pattern, strain gage and fixtures for the tensile test

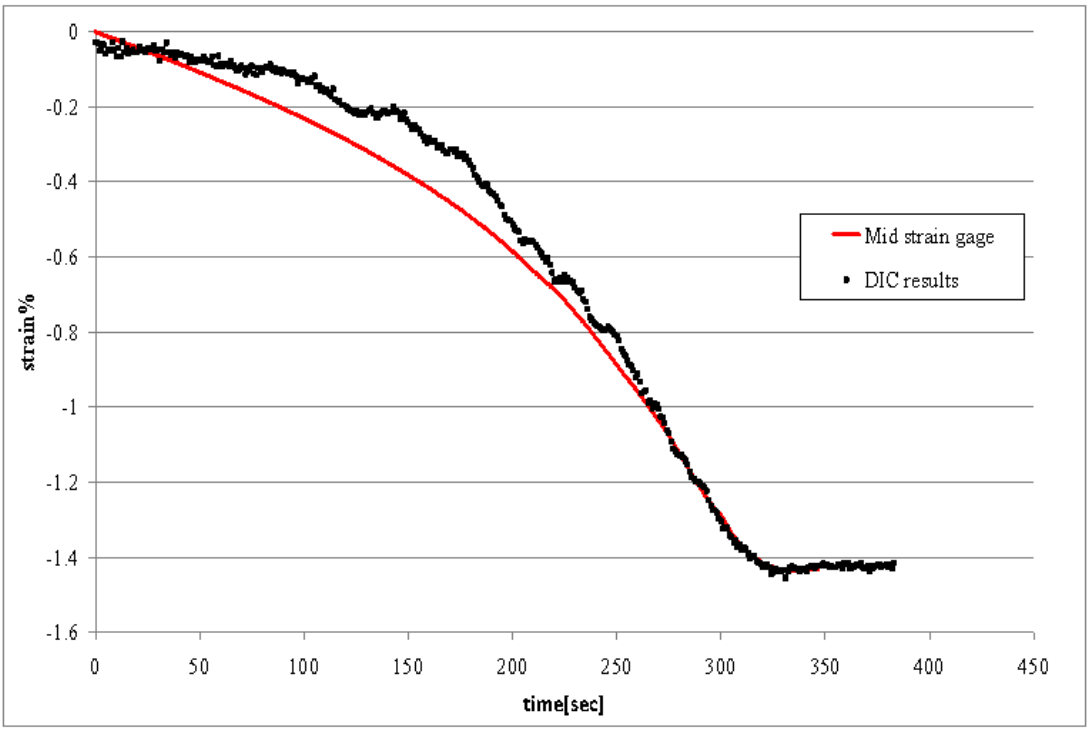

Figure 4.23: DIC results versus strain acquired from strain gage

The figure shows good agreement between the two obtained results validating the accuracy of the DIC system. One can also see more deviation in the DIC results in the time interval from 50-200 seconds. This is because of the large out-of-plane deformation of the L-shape, when its shape is changing from L-shape to become a flat plate. Large out-of-plane deformation is known to have more error percent in the DIC results since the motion of the points is perpendicular to the images plane. This result motivates us to use two pairs of optical sensors to capture the tube deformation accurately in two different imaging planes, top view and the perpendicular front view.

4.2.2.2 Force, position transducers, and data acquisition system

The applied loads from the hydraulic cylinders are measured using force transducers of strain gage type having nominal capacity of 50,000 lbf of 0.1% precision. These force transducers are fixed between the hydraulic cylinder and the moment arm of the test rig. The output signals from the force transducers and the strain gauges are recorded during the bending test using "Micro-Measurements System 7000" data acquisition system. The system can read simultaneously from 24 wire strain gages channels including the 2 force transducers.

The position transducer is of a non-contact magnetostrictive linear type. The test setup is equipped with two position transducers, one for each hydraulic cylinder in order to measure the displacement of the two cylinders during the test. The output signals are recorded using a data acquisition card which is synchronized with the DIC system.

4.3 Test preparation

4.3.1 Specimen preparation

During the bending test, the forces are transferred from the adaptor ring to the LMPA which in turn convey the forces to the tube ends located inside the rings. In order to prevent the tube failure inside the rings, more layers of composite material are laid up at the tube ends. The layers are oriented at 90^{o}. The end tapes are designed to be tapered such that more layers are added at the tube end and as it moved toward the center of the tube, some layers are dropped until no more layers are added. Adding to that, three more composite rings are manufactured at the specimen ends, Figure 4.24. The importance of these rings is to create a self-locking mechanism between the specimen ends and the LMPA which constrains the specimen from slippage at the tension side during the bending test. The

end taps and the composite rings are manufactured before the mandrel extraction from the tube. The idea of the designed end taps with the composite rings are taken from [28].

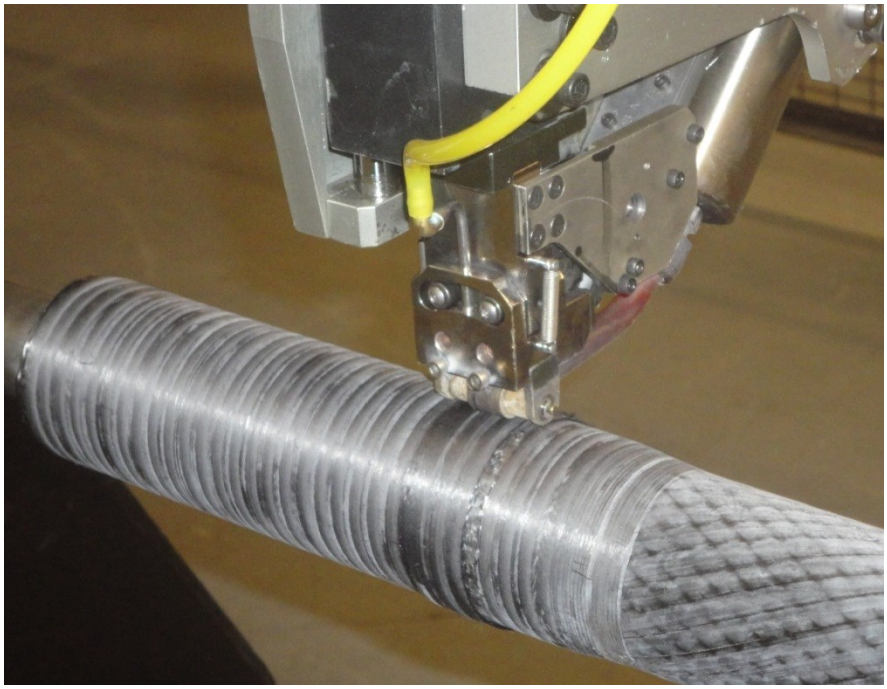

Figure 4.24: Manufacturing of end taps and composite rings

4.3.2 Mounting the tube inside the adaptor rings

After manufacturing of the end taps and the composite rings, the specimen is extracted and small portions are cut from its ends in order to have a length of 36 inches.

One end of the specimen is placed inside one adaptor ring and then the other adaptor ring with the adaptor-plate and the installation spacer beams are assembled on the other end of the specimen, Figure 4.25. The specimen is centered inside both adaptor rings using bolts and the molten LMPA is poured between the specimen end and the adaptor ring on one side, Figure 4.26. The LMPA is left to solidify and then the whole assembly is rotated upside down to pour the molten LMPA at the other specimen end.

Figure 4.25: Placing the tube inside the adaptor rings

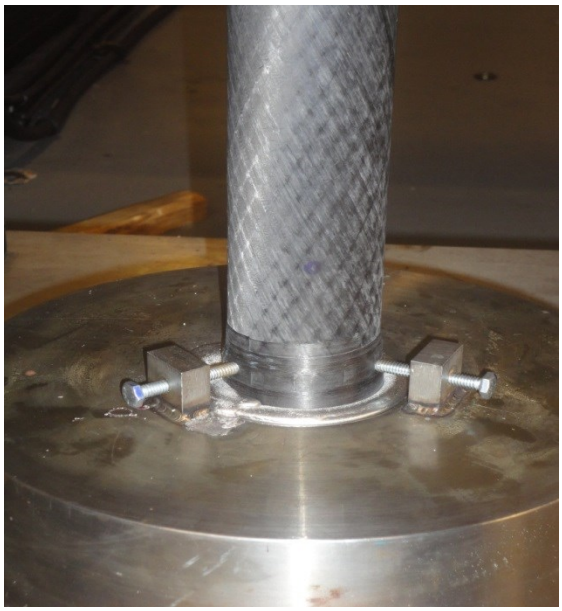

Figure 4.26: LMPA between the specimen end and the adaptor ring

4.3.3 Mounting the strain gages

Strain gages are mounted on the specimen surface at specified points, shown in Figure 4.27. These points are chosen in order to have equal number of gages at both upper and lower part of the tube covering its left side, right side and mid part of the tube.

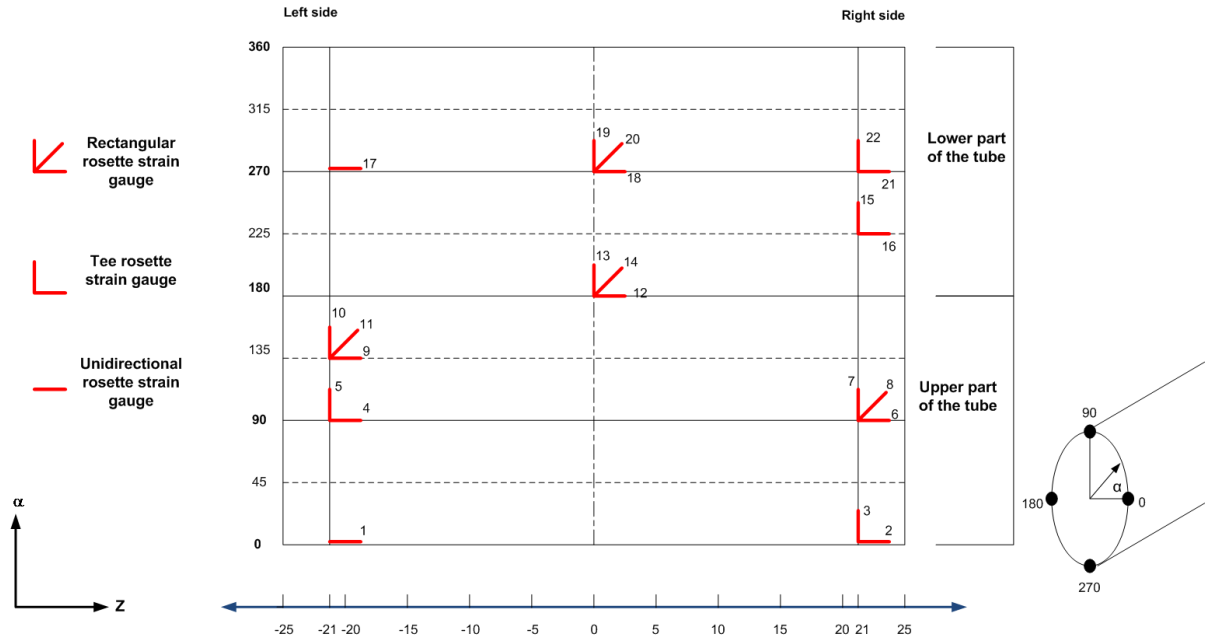

Figure 4.27: Strain gages pattern on the tube surface

Fewer points are placed at the mid part of the tube to have minimum interference with the DIC system. From Figure 4.27, one can see that (22 gages) are mounted on the tube surface at 10 different locations; (10 gages) are oriented axially, (8 gages) are oriented in the hoop direction and (4 gages) are mounted at 45^{o} in order to measure the axial strains, hoop strains and shear strains at these locations.

Also, it is important to note that the DIC system has two pairs of cameras (total four cameras) used to measure in-plane strains and out-of-plane deformation. These measurements covered the upper part of

the tube using two cameras placed at the top of the sample (Top view), and the side part of the sample using two more cameras placed in front of the sample (front view)

4.3.4 Drawing the random pattern

In order to utilize the DIC system for measuring the specimen deformation and strains, the surface of the specimen should have enough texture to be recognized by the cameras. The surface of the thermoplastic is quite black and does not have enough texture after manufacturing. Therefore, in order to have maximum contrast, a white random pattern is drawn on the specimen surface by hand using permanent markers to have the shape shown in Figure 4.28.

Figure 4.28: White random pattern drawn on the tube surface

4.3.5 Assembling in the test rig and running the test

The assembly of the specimen with the adaptor rings, adaptor-plates and the installation spacer beams are lifted to the bending test setup using a gantry crane in order to be mounted to the back-plates in the test setup. The adaptor ring and the adaptor-plate on the left are assembled with the back-plate on the fixed shoulder on the left hand side of the test setup, as shown in Figure 4.29.

Then the moving shoulder with the other back-plate on the right hand side of the test setup is pushed until it is assembled with the other adaptor ring and the adaptor-plate. After that, the installation spacer beams are disassembled from the test setup, as presented in Figure 4.30.

The two pairs of cameras of the DIC system are placed in front of the tube and above the test setup. After calibrating the cameras and connecting all the gages to the data acquisition system, the test is ready to start. The hydraulic system is started, making the hydraulic cylinders to apply the required forces which in turn generate the bending moments at the tube ends.

The measured forces from right and left cylinders are kept increasing until a loud sound is heard and the forces are dropped to half of the reached maximum value showing its failure. The test results are presented and analyzed in the next chapter

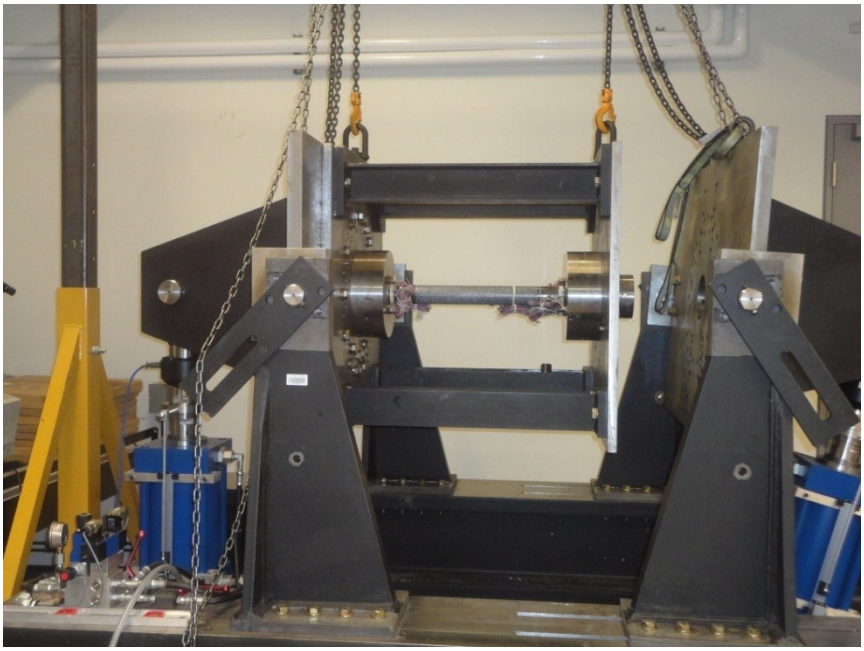

Figure 4.29: Installing the specimen assembly on the bending test setup

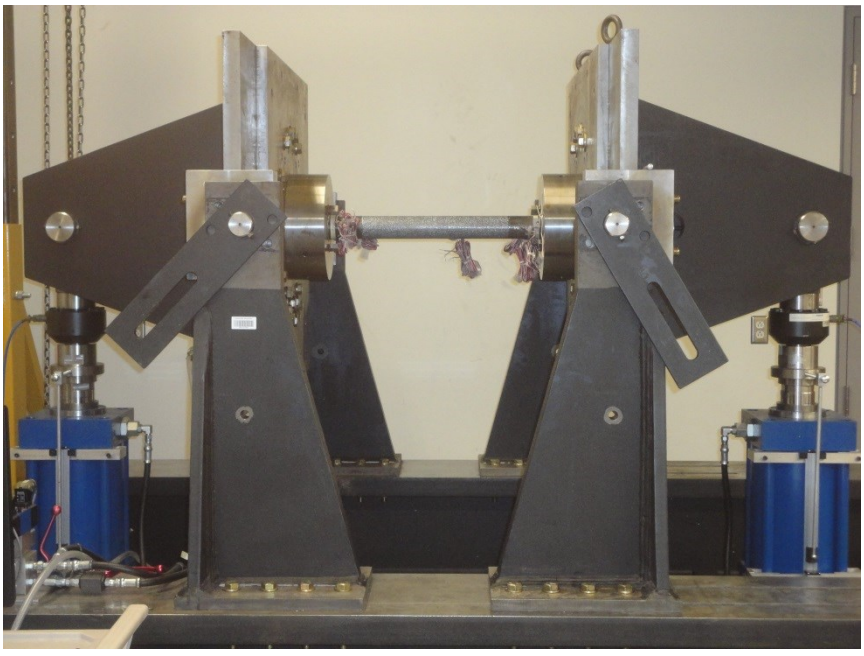

Figure 4.30: Specimen installed in the pure bending test setup

.

Chapter 5

Results and discussion

5.1 Test Results of the second tube

This section presents results of the bending test for the second manufactured composite tube, having an acceptable quality level. The tube is made of 90 layers of configuration $[25/-25]_{45}$, Do=61.1mm, t/Do=0.1856. The bending test for the composite tube is carried out using the pure bending test setup as shown in Figure 5.1. The failure load is found to be at an average moment equal to 6.78kN.m (60,046lbf.inch). The tube final failure is located closer to the right side of the tube in the upper part as shown in Figure 5.1 and Figure 5.2.

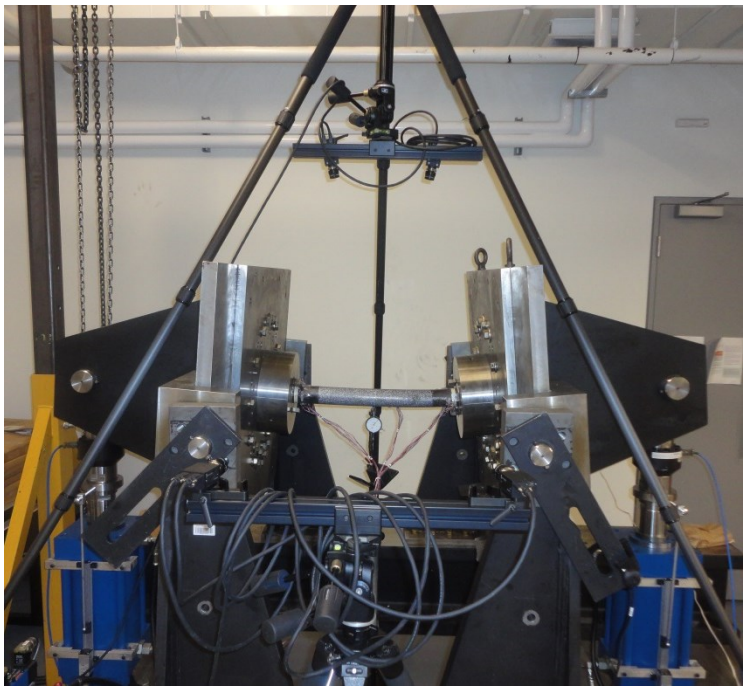

Figure 5.1: Pure bending test setup after tube failure

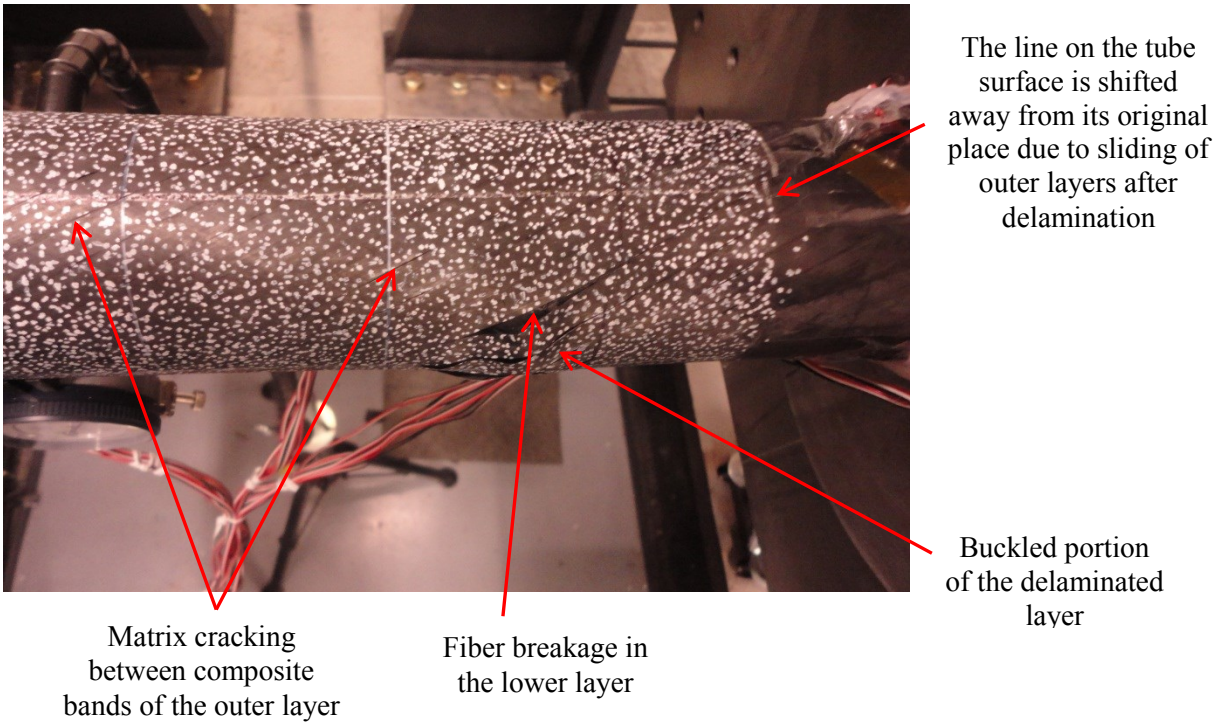

Figure 5.2: Failure location of the second tube

One can observe delamination and sliding of the outer most layers at the right side of the tube, fiber breakage at the failure zone in the layers below the outer layer, and local buckling for the delaminated fiber bands. Also one can see some location of matrix cracking on the outer layer in the upper part.

It is important to note that no failure occurred at the gripping zone at the tube ends which emphasizes the smooth conveying of the bending loading to the tube. Also there is no slipping occurred in the lower part of the tube at the gripping zones. This implies the effectiveness of the designed adaptor ring with the LMPA and the added tabs with the composite rings in preventing the slipping of the lower part of the tube under tension loading.

The following subsection is devoted to show the measured deformations, strains with the charts of the applied loads during the test.

5.1.1 Deformations results obtained from the DIC system

5.1.1.1 Front view

5.1.1.1.1 Axial deformation

The contour plot of axial deformation of the tube (U direction in the front view) is shown in Figure 5.3 before and after failure. The figure before failure shows that in the upper part, both the tube sides are deforming towards each other due to compression while in the lower part, both sides are moving away from each other. This indicates the smooth conveying of the forces from the bending test setup in order to apply the bending moment.

After failure the axial deformation shows more concentration at the zone of failure (purple colour) indicating larger deformation of the tube at failure location because of delamination of the outer most layers at this location and sliding towards the mid part of the tube.

5.1.1.1.2 Hoop deformation

The contour plot of the tube deformation in the hoop direction (V direction in the front view) before and after failure is shown in Figure 5.4. It is shown in both figures that the whole tube is deflected in the negative direction due to bending, with maximum deflection at the mid length of the tube. The interesting finding here is that the maximum deflection location is closer to the neutral axis than the lower part. This can be explained due to ovalization of the tube cross section that make the lower part deforms upward while the upper part deforms downward as will be presented later in details. After tube failure, the location of the maximum deflection moves closer to the failure location

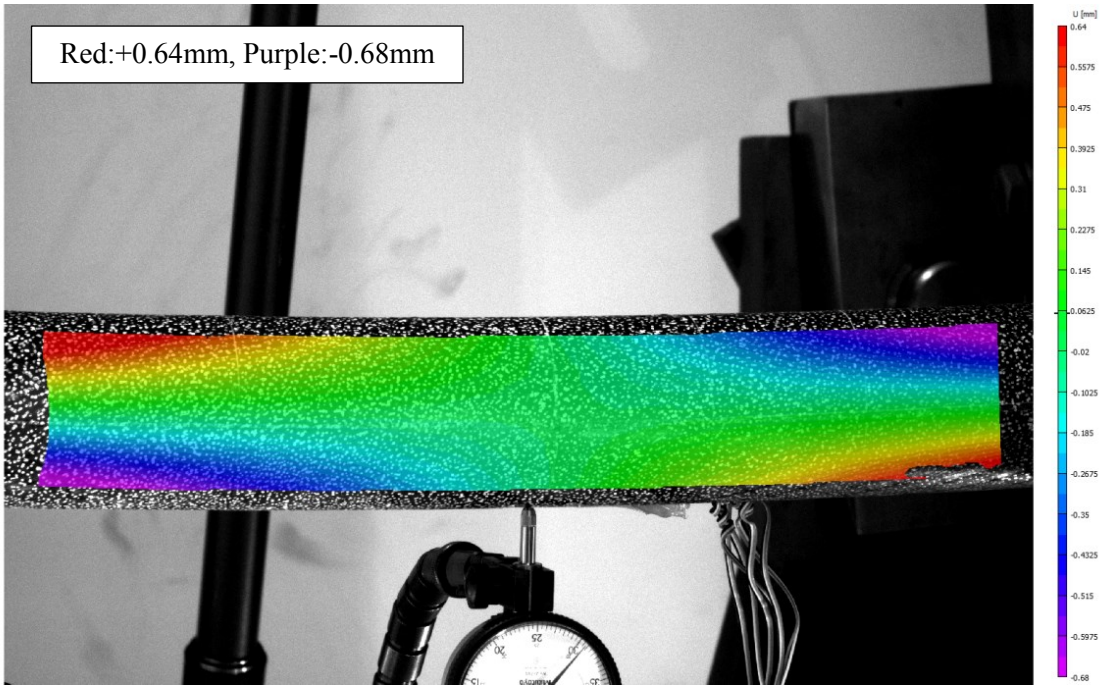

Before failure

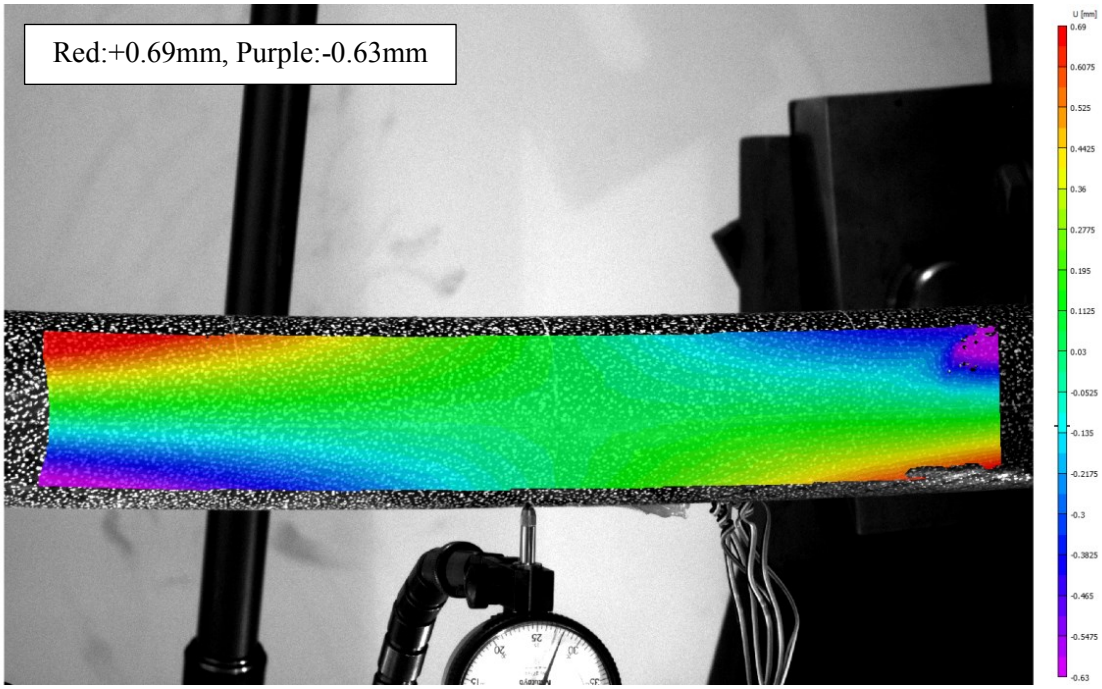

After failure

Figure 5.3: axial deformation of the tube under bending (front view)

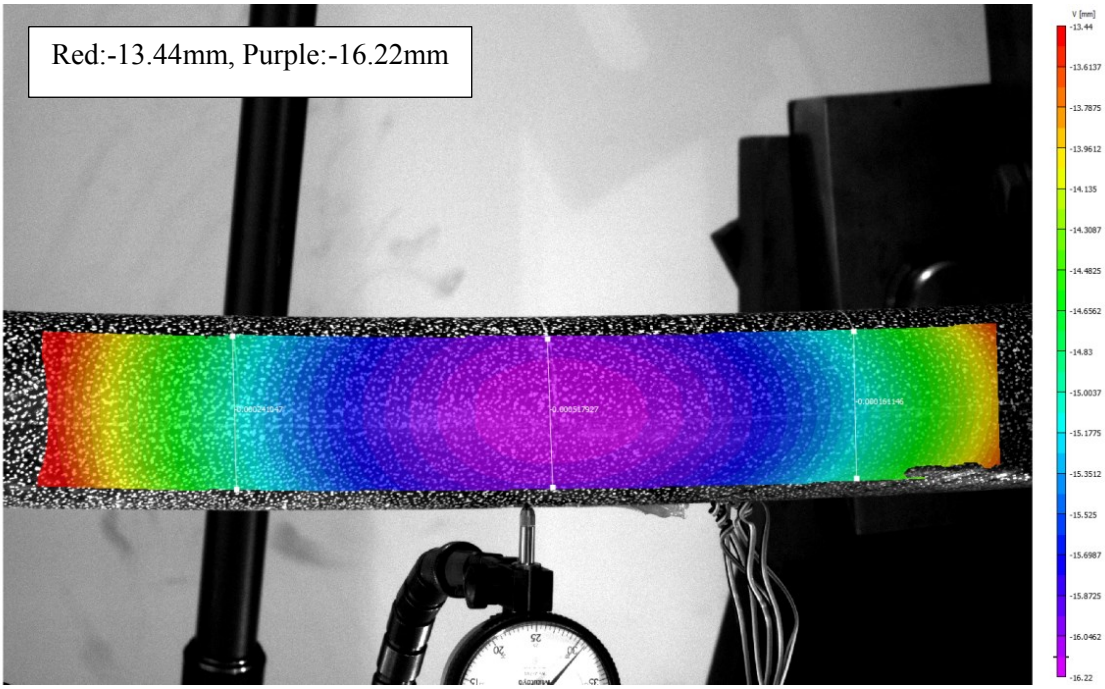

Before failure

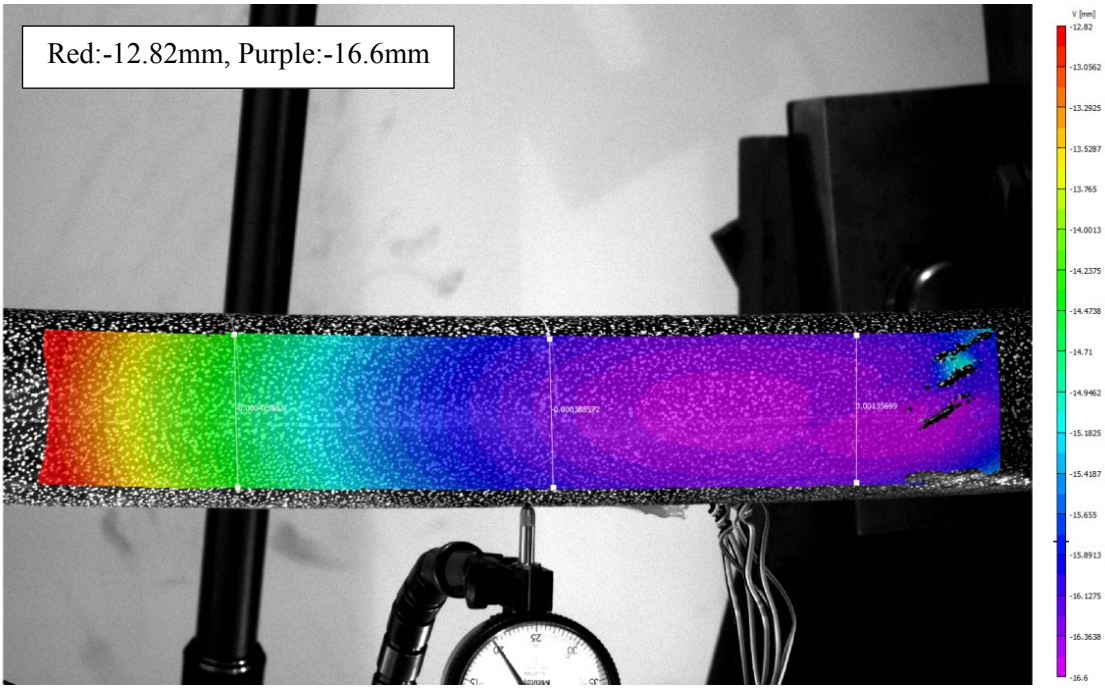

After failure

Figure 5.4 Hoop deformation of the tube under bending (front view)

5.1.1.2 Results from top view

5.1.1.2.1 Axial deformation

The contour plot of axial deformation of the tube (U direction in the top view) is shown in Figure 5.5 at the time of maximum load before and after failure of the tube. It is shown that both sides of the tube deform toward each other so that the axial deformation in the right side is negative while that of the left side is positive and the axial deformation is equal to zero at the middle of the tube length.

After failure the tube tried to deform back to its original position.

5.1.1.2.2 Hoop deformation

The contour plot of the tube deformation in the hoop direction (V direction in top view) before and after failure is presented in Figure 5.6. It is shown that the whole middle section of the tube moves in the negative direction of (V) with small deflection value. This implies that the tube exhibit small value of bending in the image plane compared to the main bending loading in the front view. This bending is thought to be due to unsymmetrical boundary conditions

After failure, the failed part deforms in the negative direction showing sliding and buckling of the delaminated part.

5.1.1.2.3 Out-of-plane deformation

Figure 5.7 shows the contour plot of the tube deformation out of plane of the top view (in Z direction of the top view). One can see that the maximum deflection occurred at the mid length of the tube.

After failure, the tube maximum deflection location became below failure zone.

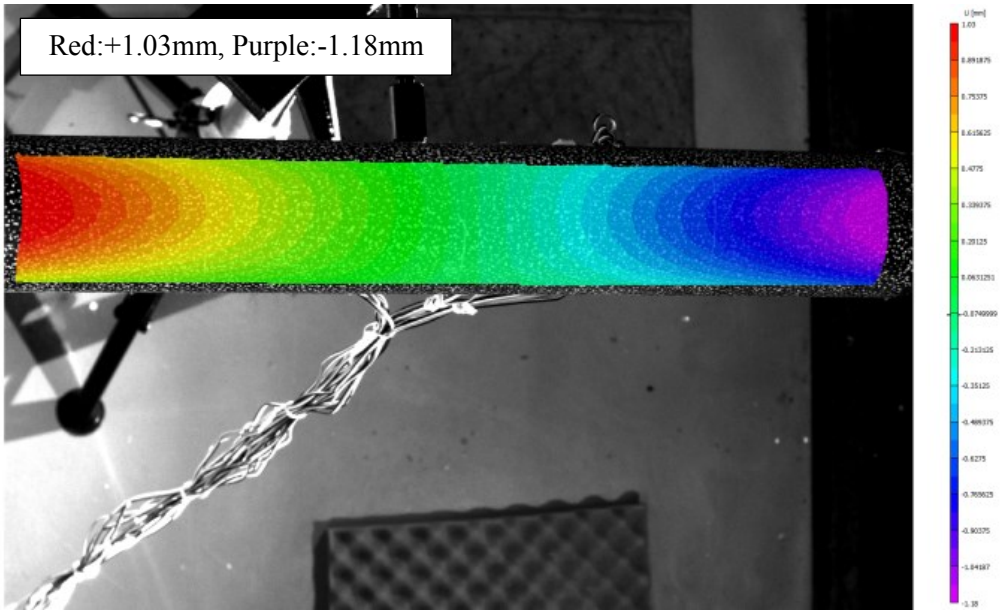

Before failure

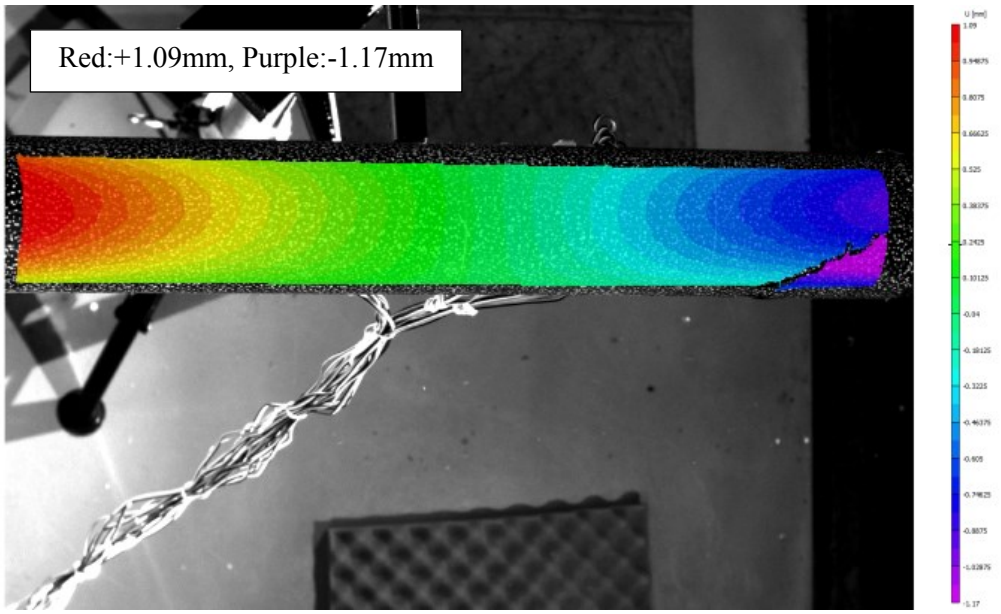

After failure

Figure 5.5: Axial deformation of the tube under bending (Top view)

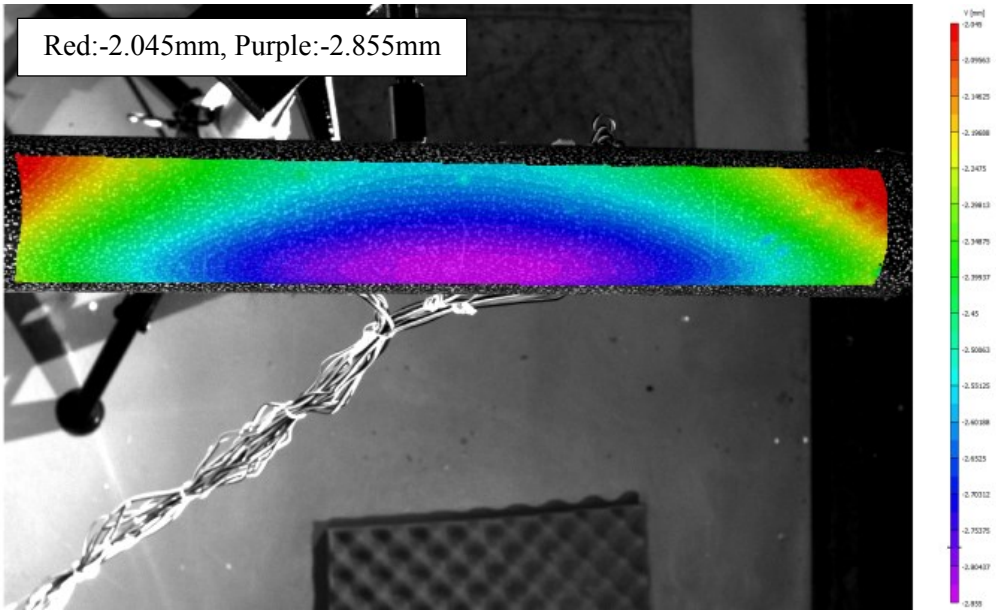

Before failure

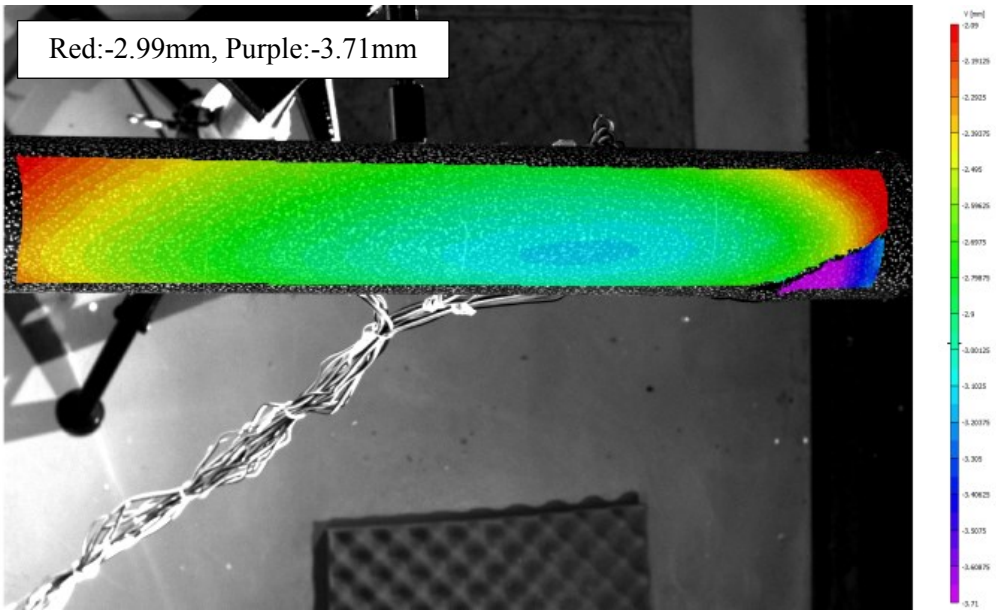

After failure

Figure 5.6: Hoop deformation of the tube under bending (Top view)

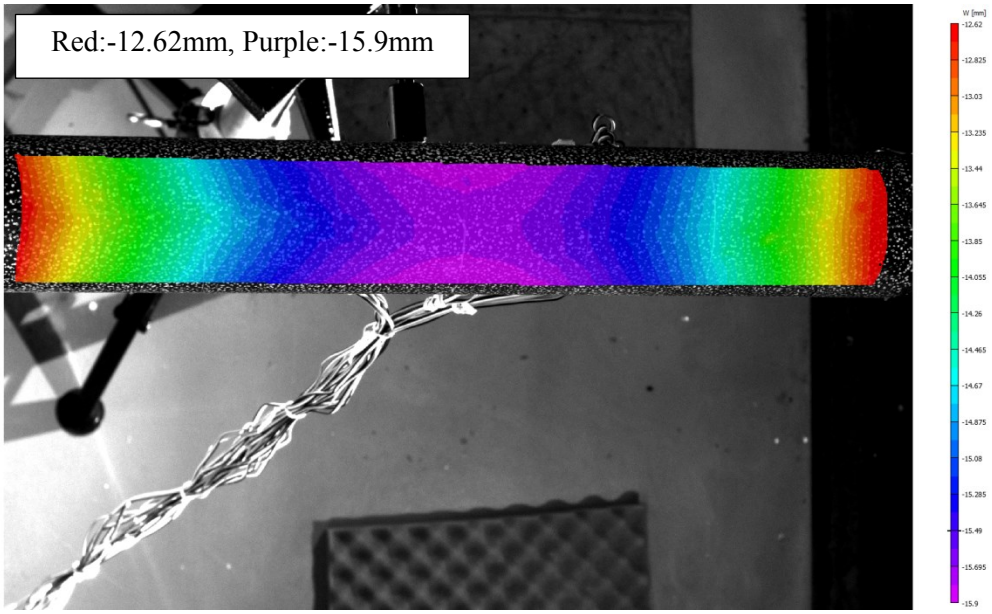

Before failure

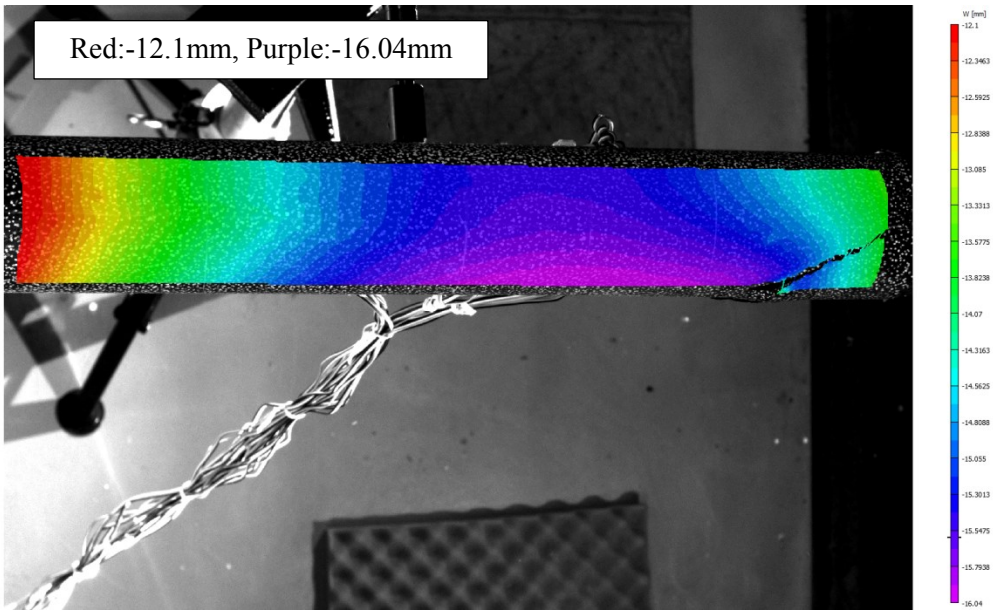

After failure

Figure 5.7: Out-of-plane deformation of the tube under bending (Top view)

5.1.2 Strains results obtained from the DIC system

5.1.2.1 Front view

From Figure 5.8, the contour plot shows the axial strain is negative in the upper part of the tube while it has positive value in the lower part and the absolute value is nearly equal in both of them before failure. This strain field emphasizes on the smooth application to the bending moment on the tube through the LMPA which smoothly transfers compressive surface load to the upper part and tension surface loading to the lower part of the tube.

After failure the maximum axial strain is more accumulated at the failure location on the failed fiber bands

For the hoop strains, Figure 5.9 illustrates very high strain values before failure on the entire tube surface. The hoop strain is positive at the upper part while it has negative values in the tube lower part. This means that the hoop strain has the opposite sign of the axial strain in both upper and lower parts of the tube. This can be explained due to the Poisson's ratio effect which makes the upper part to expand in the hoop direction when it is subjected to axial compression, while the lower part contracts since it is subjected to axial tension. Both axial and hoop strains shows large values before failure and after failure

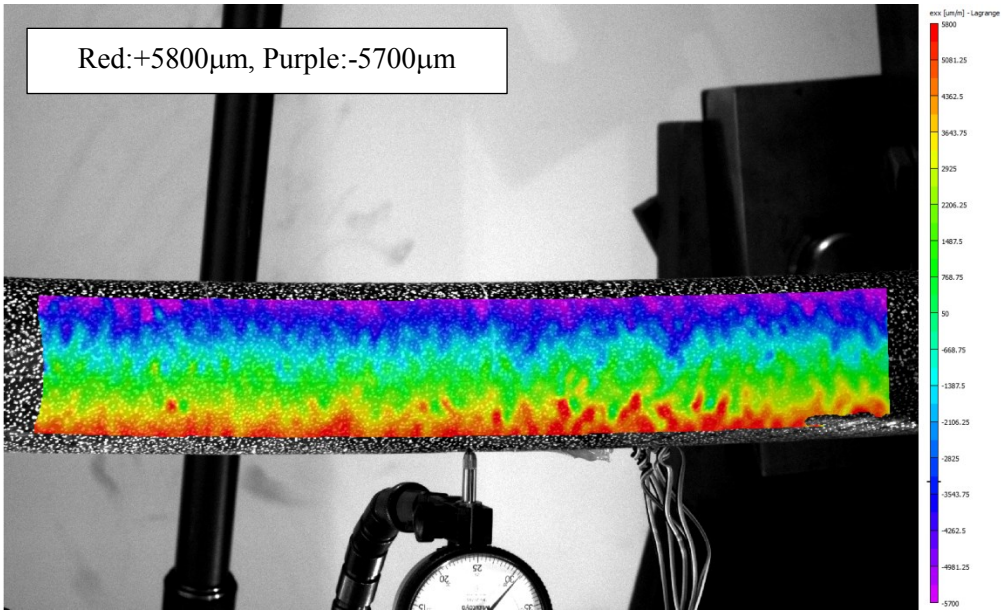

Before failure

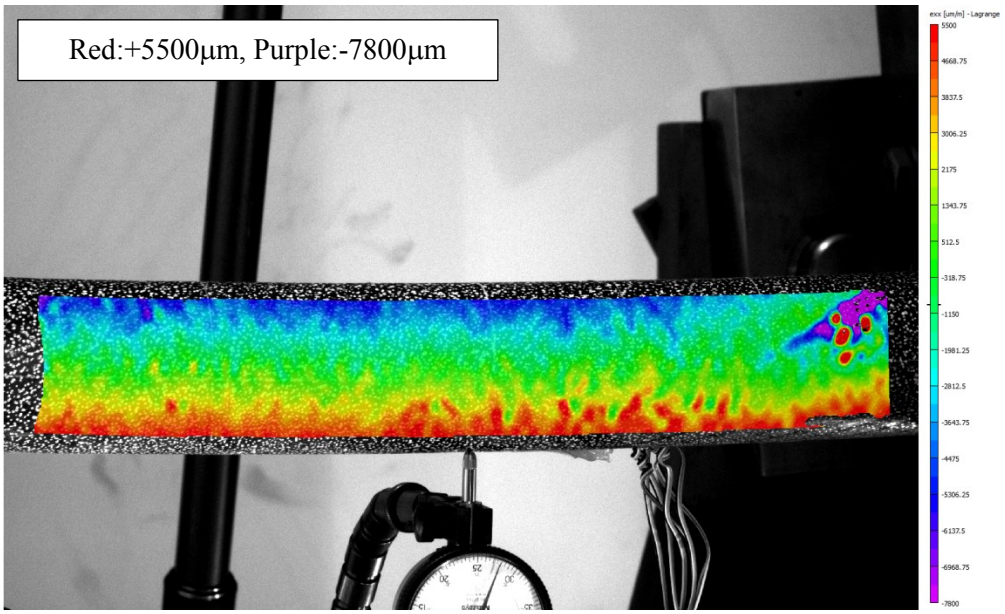

After failure

Figure 5.8: Axial strain field of the tube during bending (front view)

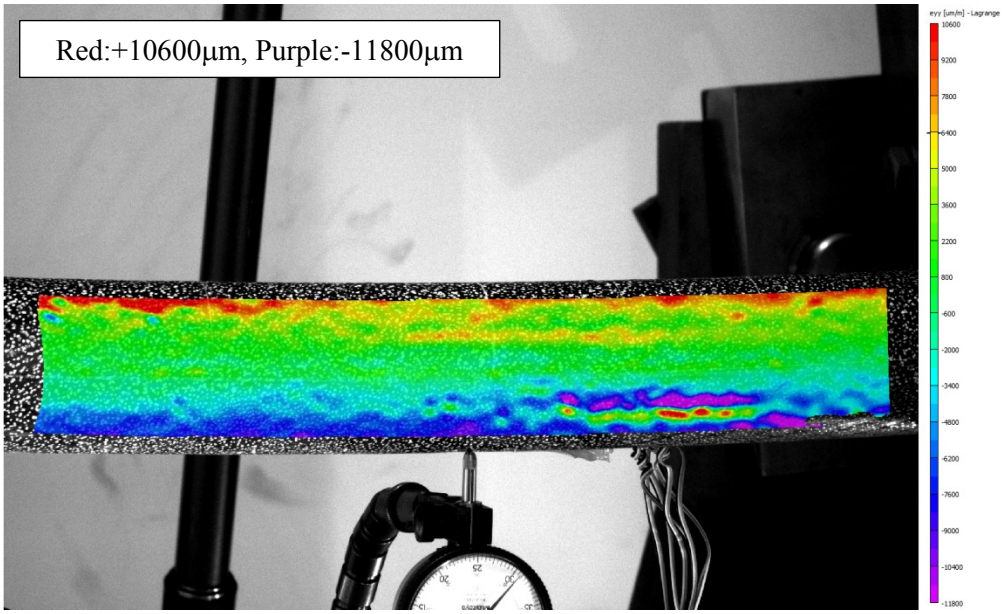

Before failure

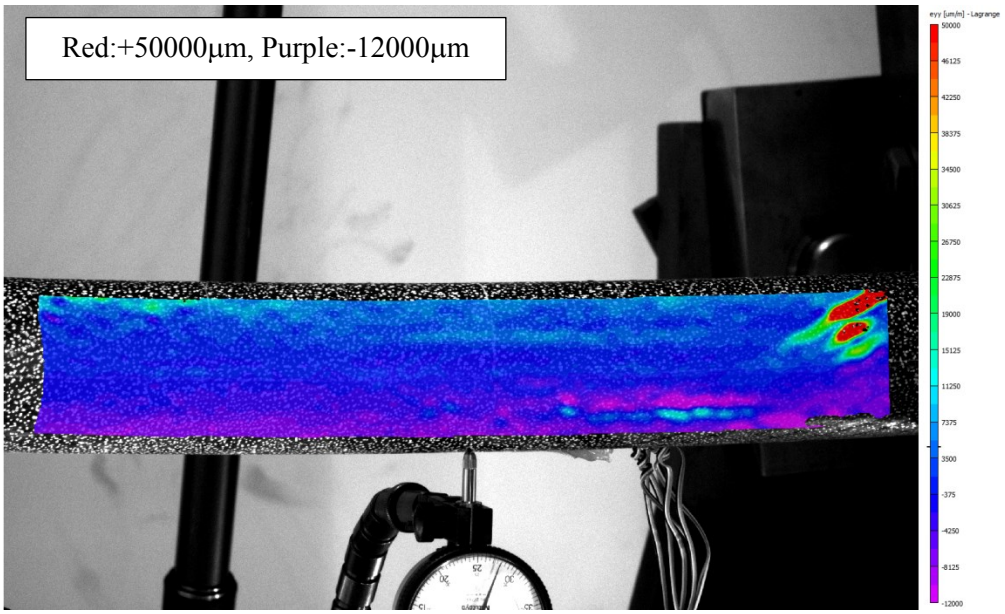

After failure

Figure 5.9: Hoop strain field of the tube during bending (front view)

5.1.2.2 Top view

Axial strain

In the top view, the axial strain field is negative on the upper part of the tube, Figure 5.10. Before failure, one can see the largest compressive strain at the highest position in the tube (at $\alpha=90^o$), which is subjected to the largest compressive load. After failure, the largest compressive strain is accumulated around the formed crack. The figure shows that the crack propagates parallel to the fiber directions of the outer layer, from the top of upper part towards the neutral axis (from $\alpha=90^o$ to $\alpha=0^o$) and the failed portion slides to form local buckling.

For hoop strain, before failure, a positive large hoop strain is accumulated at $\alpha=90^o$ close to the failure location on the fiber bands, Figure 5.11. After failure, the hoop strain is maximum at the failure side, showing very large values compared to the axial strain at the same locations.

From the presented results of the axial and hoop strain field in the tube upper part, the failure scenario can be proposed to be as follows: delamination occurred under the outer layers of the tube in right side at $\alpha=90^o$. This is accompanied with matrix cracking in the outer layer at this location causing the delaminated layers to slide in the direction of fibers of the outer layer towards the mid length of the tube. This sliding motion cuts the fibers in the layer below the outer layer and cause local buckling for the delaminated portion.

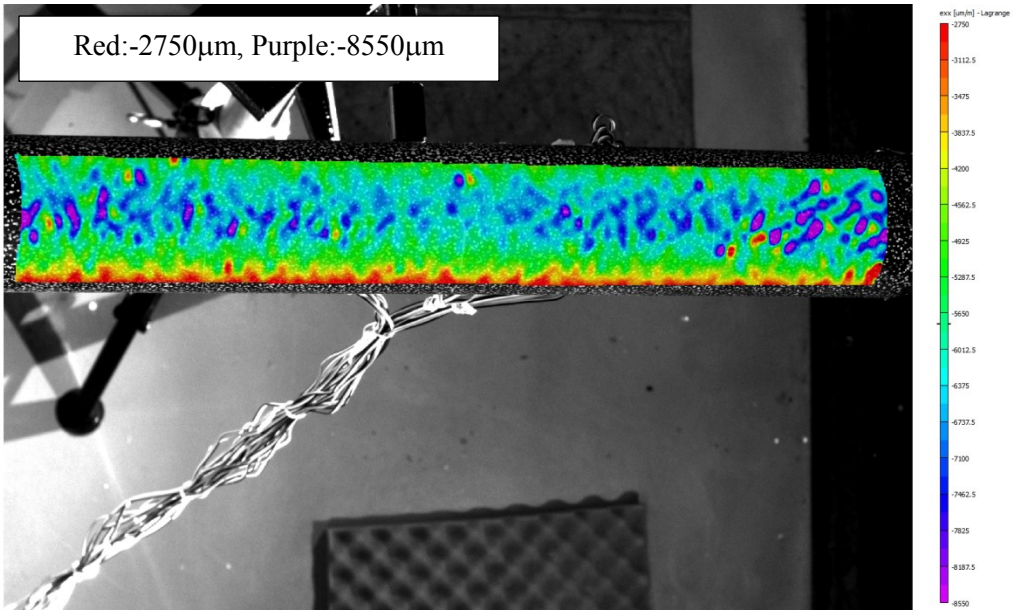

Before failure

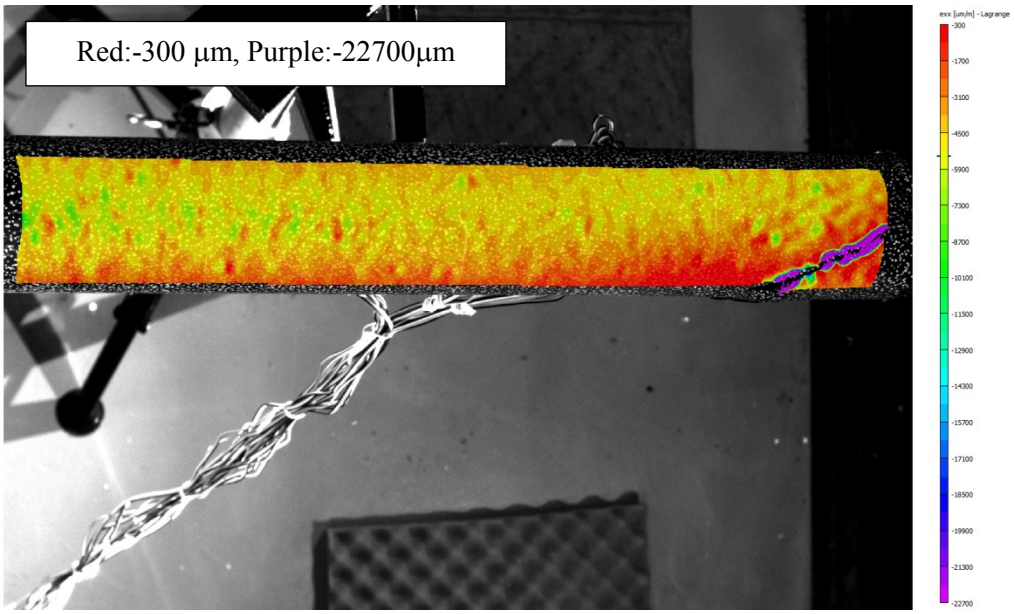

After failure

Figure 5.10: Axial strain field of the tube during bending (Top view)

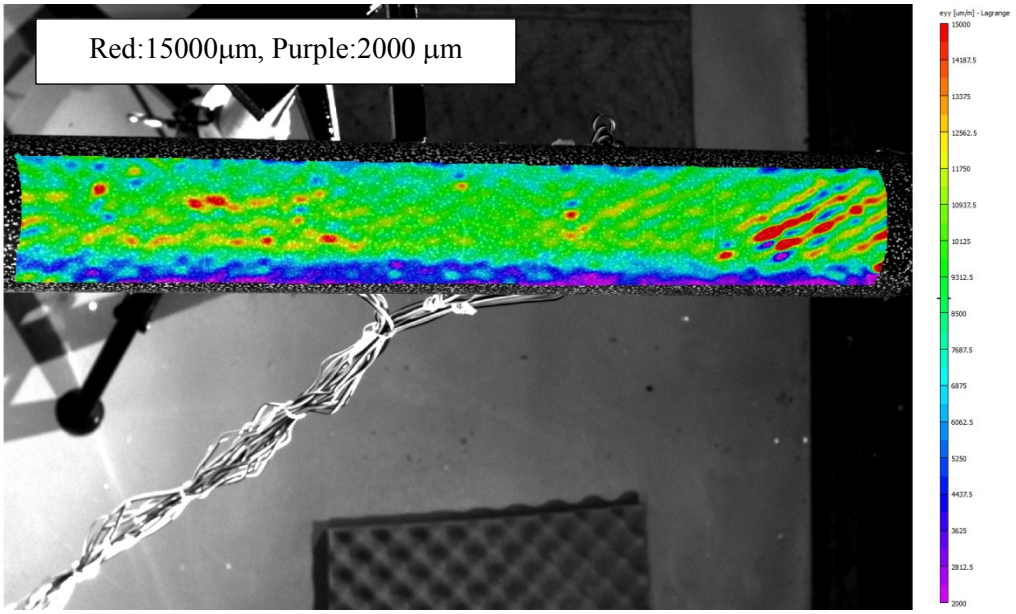

Before failure

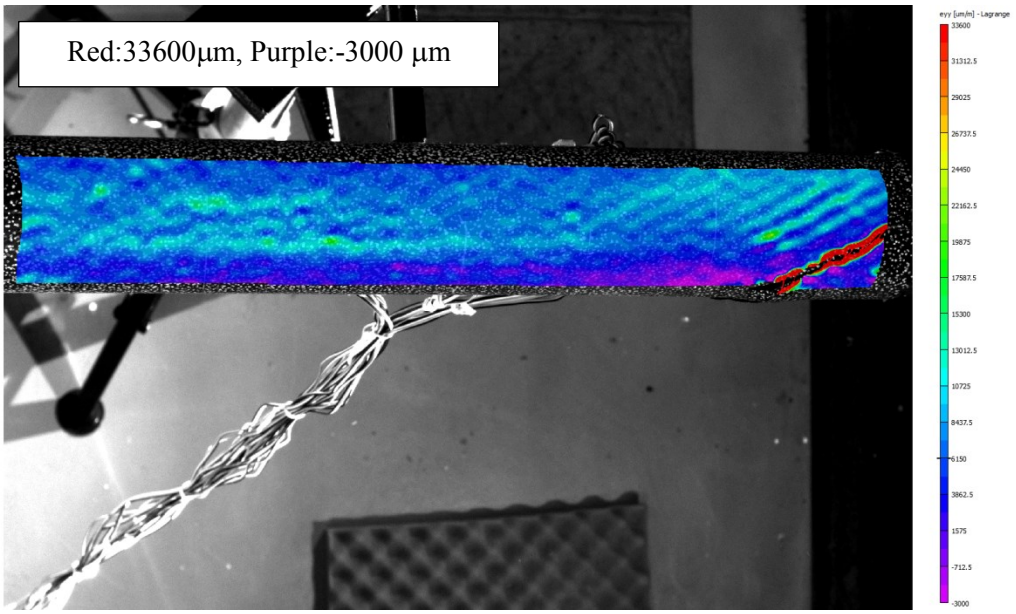

After failure

Figure 5.11:Hoop strain field of the tube during bending (Top view)

5.1.3 Strain results obtained from strain gages

The strain values recorded from strain gages are presented in this subsection, starting with the upper part of the tube (compression side) at (α=90^o).

5.1.3.1 Strains measured at the upper part

Figure 5.12 shows the axial strains at gages (#4, #6) located at the left and the right side of the tube, respectively. Both gages shows close values which implies that the tube is subjected to uniform bending moment along its length. The small difference in values between the two gages is because the hydraulic cylinder at the right side of the test setup is acting by little bit larger force that that at the left side (about 6%) as will be presented later in this chapter. In general the two gages show linear behavior except near to the time of failure indicating the initiation of the failure process. After failure, both gages show a drop in the strain values due to failure. However, gage (#6) shows larger drop in strain values because it is located closer to the failure location. The strain values do not vanish after failure which implies that the tube can withstand some load after its failure. This is attributed to the large wall thickness of the tube.

For the hoop direction at the compression side, the hoop strain is measured using gages (#5, #7) mounted at the left and the right side of the tube, respectively. It is known that the upper part of the tube is subjected to compressive loads in the axial direction. These loads cause negative axial strain and because of the effect of Poisson's ratio, the strain values are positive in the perpendicular hoop direction at gages (#5, #7) as shown in Figure 5.13. Also, one can see that the strain values are close to each other in both gages except before the time of failure, gage (#5) indicates larger values since it is located closer to the failure zone.

The positive hoop strain in the upper layer causes the expansion of the upper part in the hoop direction. This expansion deforms the tube circular cross section to be flattened (ovalization) which has a negative effect on the bending stiffness of the tube as will be discussed later in this chapter.

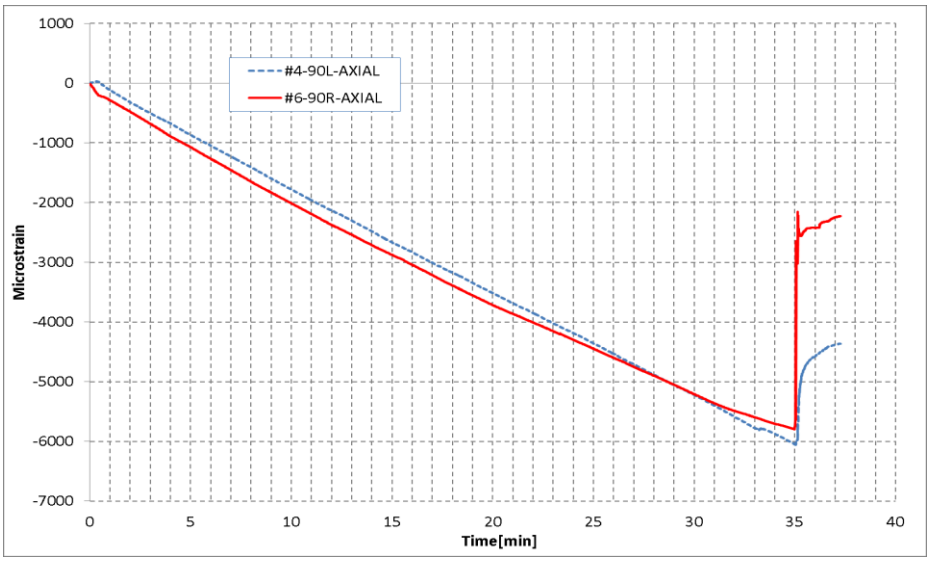

Figure 5.12: Axial strains at the upper part of the tube

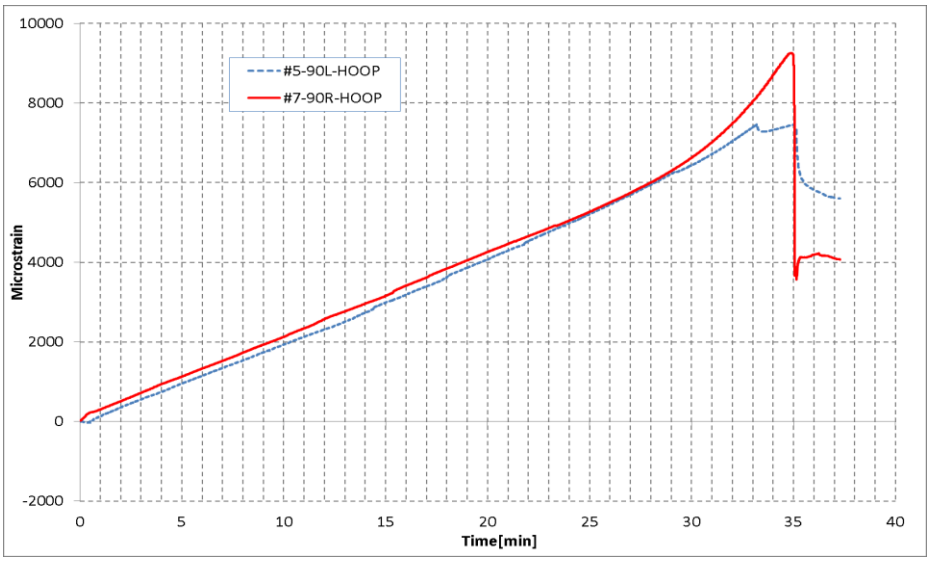

Figure 5.13: Hoop strains at the upper part of the tube

5.1.3.2 Strains measured at the lower part

For the lower part of the tube at (α=270^o), Figure 5.14 presents the axial strains acquired from gages (#18, #21) which are located at the mid length and the right side of the tube, respectively. The strain values are positive indicating that the lower part is subjected to tension. Also one can see that the strain values are close to each other until (time=12 min), at which gage (#18) shows a nonlinear strain behavior. This nonlinear behavior is thought to be due to initial failure happened closer to the location of gage (#18). At failure time, the strain at gage (#21) increased while it decreased at gage (#18). This is because the tube is deflected more at failure location –closer to gage (#21)-while the tube is relaxed at the mid length- closer to gage (#18).

For the hoop direction, the hoop strain is measured from gages (#19, #22) located at (α=270) the mid length and the right side of the tube, respectively. Figure 5.15 shows negative hoop strain at the tube lower part due to Poisson's ratio effect. Also one can see the abrupt change in the hoop strain at gage (#19) at the same time that shows a change in the axial strain at same measuring point, Figure 5.14. This sharp change indicates that the occurred initial failure is closer to the hoop direction from the axial one.

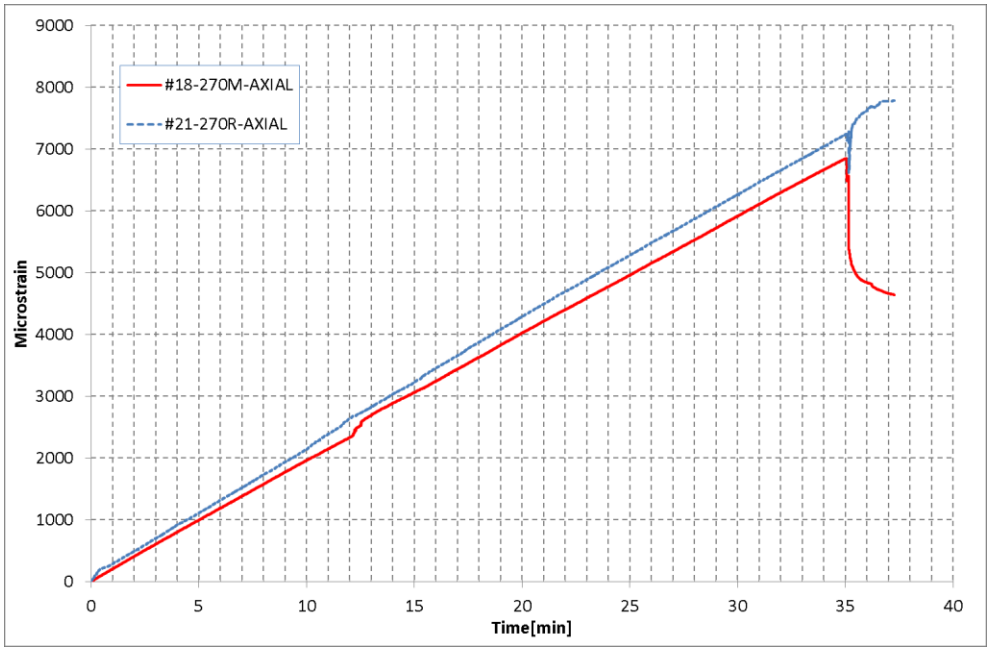

Figure 5.14: Axial strains at the lower part of the tube

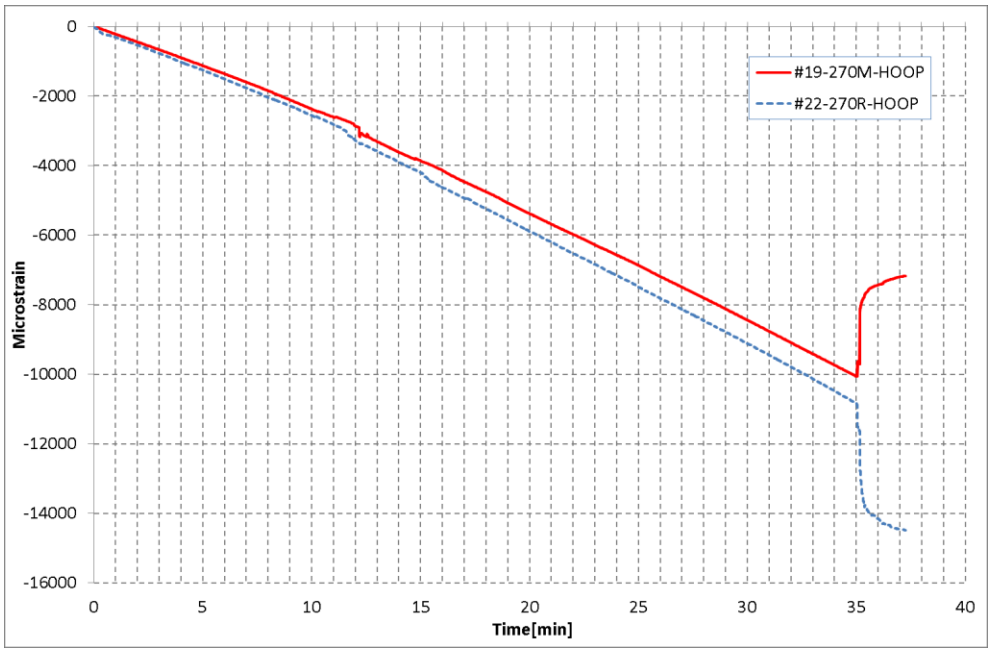

Figure 5.15: Hoop strains at the lower part of the tube

5.1.3.3 Strains measured at the neutral plane

Figure 5.16 shows the axial strain acquired from gages (#1, #2, and #12). Gage (#1, #2) are place between the upper and lower part of the tube (α=0) in the left and right side, respectively while gage (#12) is placed at (α=180) in the mid length of the tube. The three gages are supposed to measure zero strain value as they are located in the neutral plane of the tube. Both gages (#1, #2) show considerable value of positive axial strain which implies some tension in this location while gage (#12) measures equal negative axial strain, means equal compression in the opposite side of the tube. This situation means that the tube exhibits some curvature in the neutral plane of the tube which is perpendicular to the main plane of bending, emphasizing the deformation result shown in Figure 5.6 from the DIC results in the (Top view).

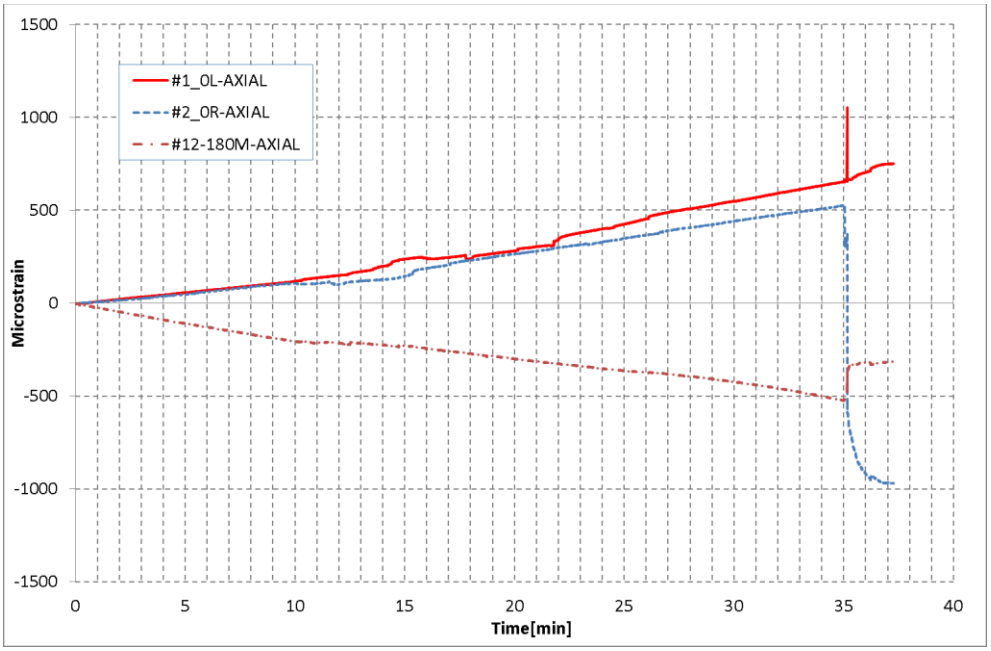

Figure 5.16: Axial strains measured from gages (#1, #2, and #12)

5.1.4 Forces

The force transducers fixed on the left and right hydraulic cylinders measured the applied forces during the test as plotted in Figure 5.17. The figure shows that the forces are kept increasing –with negative sign- for (35 minutes) then their values dropped in both sides. The maximum force measured from the right side is (-2745 lbf) then it is dropped to (-1550 lbf) after failure, losing about to (43.64%) from its maximum value. For the left side, the maximum measured force is (-2592 lbf) that is dropped to (2100 lbf), losing about (19%) of its value after failure.

One can see that the hydraulic cylinder on the right applies somewhat larger force compared to the left cylinder (about 6% difference). The deformation and strain results show that this small difference between the left and right cylinder adds some more strain on the right side of the tube compared to the left side which may cause the failure to be close to the right side instead of being in the mid length of the tube. The average moment acting on the tube is obtained by calculating the average value of the forces measured from both cylinders and multiplying it with the arm length (22.5 inches). Figure 5.18 shows that the maximum moment is equal to (60,000 lbf. Inches “6.78kN.m”).

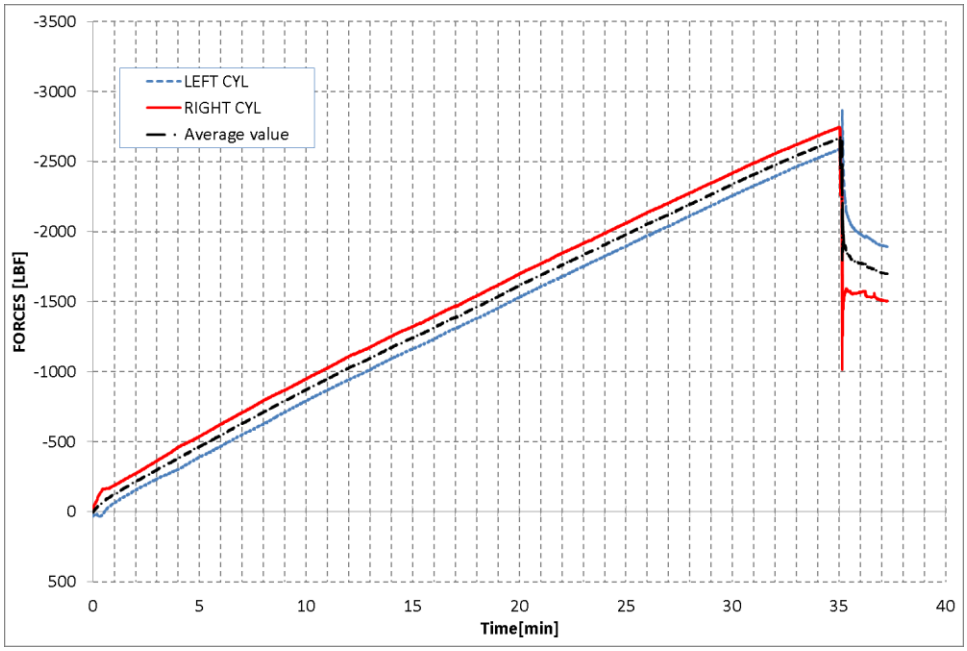

Figure 5.17: Forces applied by the hydraulic cylinders

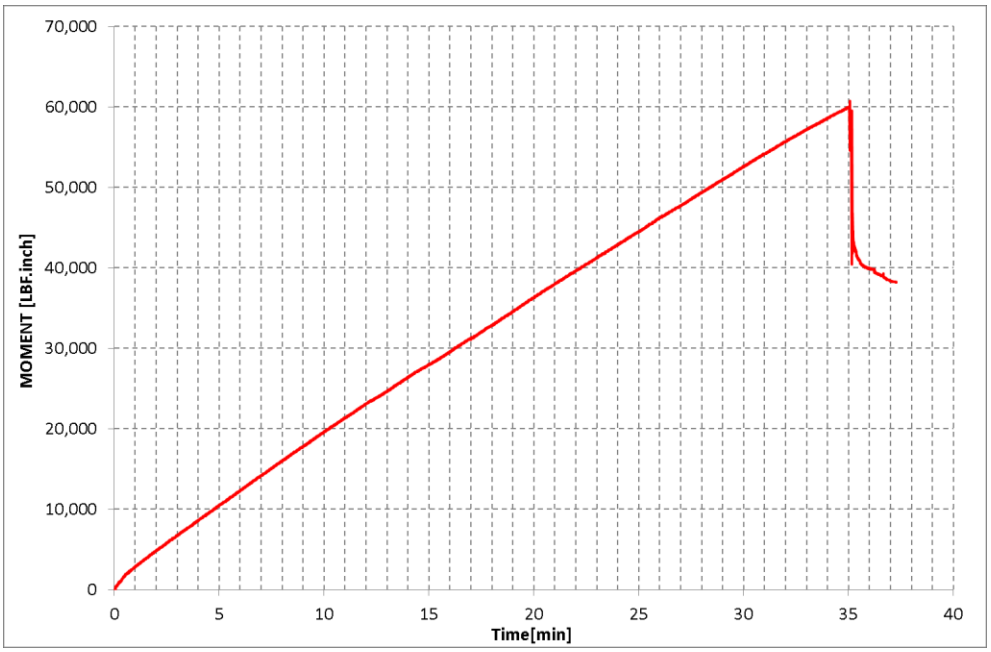

Figure 5.18: Moment applied on the composite tube during the bending test

5.2 Bending stiffness property: theoretical calculations versus experimental values

In this section, the bending stiffness values of the two tested composite tubes are obtained theoretically and from the experimental results in order to validate the theoretical values experimentally and to validate the superiority of the bending stiffness of the second composite tube due to its laminate configuration as discussed in section 3.4.

5.2.1 Theoretical calculation for the bending stiffness

At First, the bending stiffness is calculated for the two manufactured thermoplastic composite tubes using equation (2.25) in section 2.3. The inputs of bending stiffness calculations are presented in Table 5.1.

Table 5.1: Inputs for calculating the theoretical bending stiffness of manufactured tubes

	First tube	Second tube
D_o [mm]	61.1(2.4 inches)	61.1(2.4 inches)
D_i [mm]	38.1(1.5 inches)	38.1(1.5 inches)
t/D_o	0.19	0.19
t [mm]	11.5(0.45 inches)	11.5(0.45 inches)
Stacking sequence	$[-25_{45}/25_{45}]$	$[-25/25]_{45}$
No. of sublaminates	1	45

The used material for making these tubes is AS4/APC2 Carbon/PEEK thermoplastic composite. The material properties obtained from TenCate [32] are listed in Table 5.2 after reduction, according to [35]. This is because the material is in-situ consolidated, not autoclave consolidated. The calculated bending stiffness is presented in Table 5.3.

Table 5.2: Material properties of Carbon/PEEK used in bending stiffness calculation [32], [35]

E_1, GPa	115
E_2=E_3, GPa	10
G_{12}=G_{13}, GPa	5
G_{23}, GPa	3
ν_{12}=ν_{13}	0.329
ν_{12}	0.49

Table 5.3: Theoretical bending stiffness for the manufactured tubes

First tube [kN.m^2]	33.574
Second tube [kN.m^2]	35.000

The second tube has higher bending stiffness than the first tube even the two tubes have the same dimensions. This is attributed to the higher number of sublaminates in the second tube, as discussed before in section 3.4.

5.2.2 Bending stiffness specification from the pure bending tests

The bending stiffness of the tube can be specified experimentally from the measured bending moment (M_x) and the end rotation angle of the tube (β) during the bending test. An accurate end rotation can be calculated using the following equation [27]

$$\beta(s) = \frac{L}{(Do/2)}\varepsilon_z^{max}(s) \quad \textbf{(5.1)}$$

Where:

$\varepsilon_z^{max}(s)$.--- the maximum axial strain at the lower part of the tube (α=270^o) at time (s) during the test

L --- half the length of the tube under pure bending (L=11inches “278.5mm”)

The tube curvature (k) is calculated from the following equation:

$$\mathrm{k(s)} = \frac{\beta(s)}{L} \tag{5.2}$$

Substituting by equations (2.1) and (5.2) into equation (5.1), the bending stiffness equation will have the following form:

$$\langle EI \rangle = \frac{M_x(s)}{\varepsilon_z^{max}(s)}\left(\frac{D_0}{2}\right) \tag{5.3}$$

Equation (5.3) shows that the slope of (M_x - ε_z^{max}) curve is equal to the tube bending stiffness divided by the outer radius of the tube. The location of maximum axial strain is found to be measured at gage (#21) for both the first and the second tube, which is located in the right side at α=270^o.

In order to compare the experimental bending stiffness to the theoretical value, a straight line is plotted, having a slope equal to the calculated bending stiffness divided by the outer radius of the tube. Figure 5.19 compared the curve of the applied bending moment versus the maximum measured axial strain $\varepsilon_z^{max}(s)$ with the dashed line obtained from theoretical calculations for the first tube. Although the first tube is of poor quality, the measured bending stiffness shows satisfactory agreement with the theoretical value specially at the initial part of the curve . Figure 5.20 presents the comparison of the experimental curve with the theoretical one for the second tube (which has better quality). One can see that the two curves show good agreement with each other such that the tube has bending stiffness equal to (32.314kN.m^2) at a moment value equal to (1kN.m). The percentage difference between the experimental and the theoretical values is equal to (7.67%).

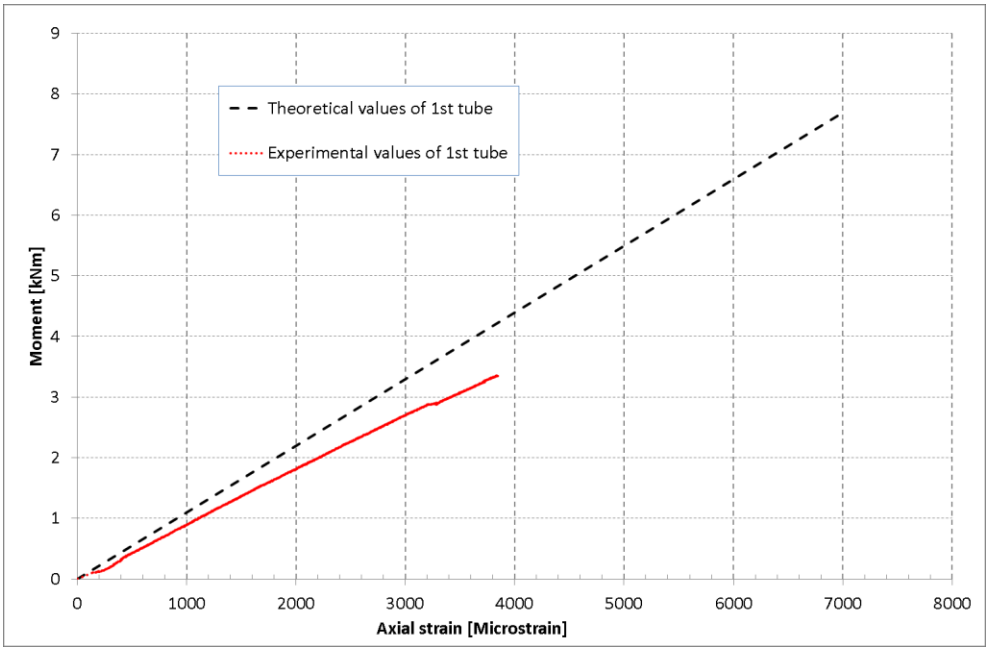

Figure 5.19: Applied Moment versus axial strain at gage (#21) for the first tube

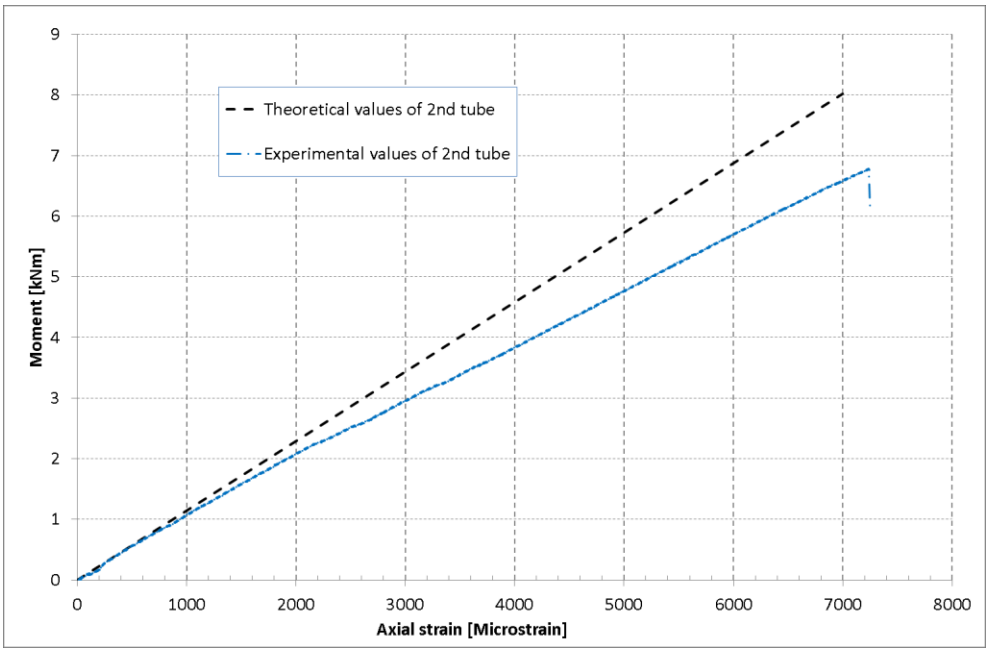

Figure 5.20: Applied Moment versus axial strain at gage (#21) for the second tube

The good agreement between the experimental and theoretical bending stiffness in both tubes validates the used theory. Also both theoretical and experimental results show that the composite tube of larger number of sublaminates within the wall thickness has higher bending stiffness, despite the two tubes have same dimensions, same number of layers, same orientation angle (-25/25), and made of the same thermoplastic composite material.

Before leaving this part it is important to discuss the reason that makes the moment-axial strain curves in Figure 5.19, and Figure 5.20 change their slope and show decrease in the bending stiffness with increasing the applied moment. This can be explained due to two reasons:

The first reason is due to ovalization effect on the tube subjected to bending loading which is called Brazier effect [36]. When a bending moment is applied on the tube, it deforms to have a curvature. This curvature makes both the compressive and tensile loads to have transverse components towards the tube axis, trying to flatten the circular cross section, as shown in Figure 5.21.

This flattening effect reduces the tube bending stiffness. It is important to note that the ovalization effect decreases as the rigidity of the tube cross section increases.

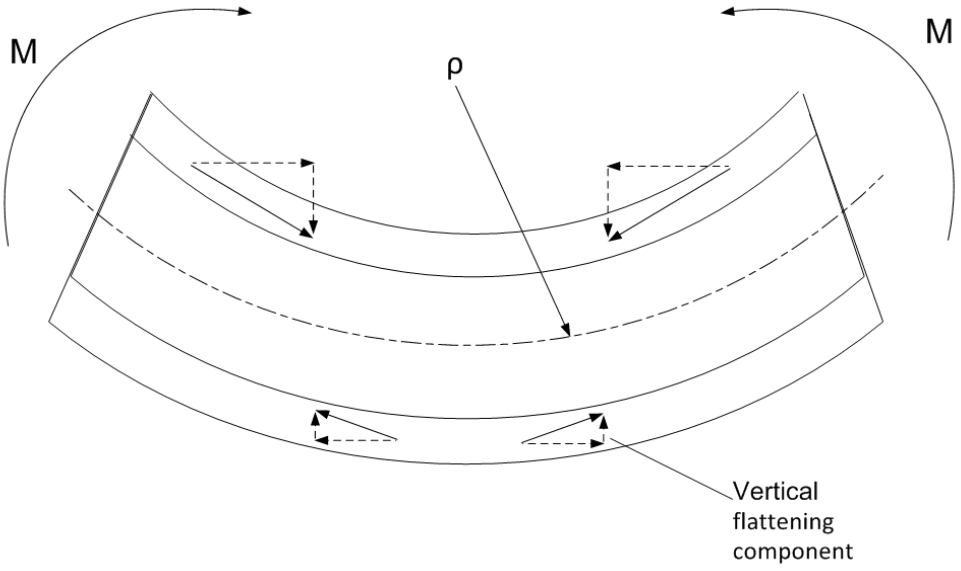

Figure 5.21: Schematic drawing for Brazier effect on bent tubes, redrawn from [36]

The second reason for the reduction of the tube bending stiffness is, as the moment value increases this may cause initiation of non linear material behavior which reduces the stiffness properties of the composite material and in turn reduces the bending stiffness. An example of this case is shown in Figure 5.19 for the first tube when some what sharp reduction in the slope of the curve occurred at a moment value close to 3kN.m

5.3 Failure behavior of thick-walled composite tubes

In this section, the failure of the second thick-walled composite tube is investigated, discussing the failure location and its mode of failure compared to thin-walled composite tubes.

5.3.1 Discussing the failure of the tested tubes

It is important to emphasize on the following observations from the bending test results of the second tube:

- The strain fields show that the tube has a constant stress field along its gauge length (since the measured strains at the right, left and mid sections are nearly equal, adding to that the theoretical calculations of stresses and strains along the tube length are constant as shown in Appendix C).
- There is no concentrated loading points that can bias the failure to happen at specific point
- Noting that the tube has a uniform thick-circular cross section

These observations imply that the tube can fail at any point along its gauge length, a situation similar to the case of testing a bar of circular cross section under tension. The only effect that can make the tube to fail at its mid-section is the ovalization effect, which reduces the tube cross section more at the mid-section compared to the right or left side. In our case the failure occurred at the right side of the tube because the right cylinder applies a little bit higher load compared to the left cylinder (%6 difference).

Turning to discussing why the failure location is in the upper part of the second tube not in its lower part. This is thought to be due to the following points:

- Existence of considerable value of positive radial strain between the outer layers at $\alpha=90^{o}$ which may cause delamination in the outer layers (Mode I) and sliding of the delaminated part under compression as shown from the theoretical stress analysis in Appendix C

- Carbon fibers in the upper part are subjected to compression, knowing that carbon fibers have lower compressive strength than the tensile strength.
- Adding to that the polymer matrix is subjected to tension, which is weaker in tension than in compression.

Also it is important to compare the failure in the two tested tube. At first, comparing Figure 5.19 to Figure 5.20, one can see that the second tube failed at a higher moment value (6.78kN.m) compared to that of the first tube (3.35kN.m). This large difference in strength may validate the quality enhancement of the second tube due to the used optimum manufacturing parameters.

Also it is important to emphasize that both tested thick-walled tubes using the pure bending test rig do not show any local deformations. While the thick-walled composite tube, tested using three-point bending, show a severe local damage under the concentrated loading point as shown in Figure 1.2. This result shows the superiority of the pure bending test setup over both three-point and four-point bending tests.

Lastly, it is important to compare the failure strength of the composite tube with an aluminum counterpart. The ultimate bending an isotropic tube can withstand under pure bending moment can be calculated from the following equation:

$$M_x = \frac{I_T}{(D_o/2)}\sigma_u \qquad \textbf{(5.4)}$$

Where: σ_u is the ultimate tensile strength of the material.

For aluminum alloy 6061-T4, the ultimate tensile strength is equal to (207 MPa), such that the maximum bending moment is (3.91 kN.m). For aluminium alloy 6061-T6, the ultimate tensile strength is equal to (300 MPa), making the tube fails at a moment equal to (5.66kN.m). From these results, one can see that the thermoplastic composite tube is of higher strength under bending compared to aluminum alloys

5.3.2 Comparing failure behavior of thick-walled composite tubes to thin-walled composite tubes

5.3.2.1 Crack direction

For the two tested thick-walled tubes, it is observed that the crack propagation occurred parallel to the fibers orientation angle of the outer layer and the crack depth is through the thickness of the outer layers only, as shown in Figure 5.22, Figure 5.23. While for thin-walled composite tubes, the crack propagates in the hoop direction of the tube through the whole wall thickness, regardless to the fibers orientation angle of the outer layer, as shown in the example in Figure 5.24 for a thin-walled thermoplastic composite cone tested on the pure bending test setup. This can be explained as follows:

- Thick-walled tube have a large t/D_o value, which makes the composite material properties have a considerable contribution in the tube bending stiffness, as discussed in chapter 3. This large contribution makes the laminate staking sequence affect the global behavior of the tube under bending such that the axes of the material coordinates of the outer layer are the principle stresses and strains directions [19].
- For a thin-walled composite tube t/D_o value is small, making the contribution of the material properties in the tube bending stiffness is smaller compared to the layers moment of inertia as stated in chapter3. This small contribution makes the laminate stacking sequence does not affect the global behavior of the tube (but only on affect localy) such that the principle stresses and strains to be in the hoop and axial direction of the tube and the crack direction in in the direction of the maximum principal stress.

This explaination agreed with the stiffness analysis of composite tubes, presented in [19].

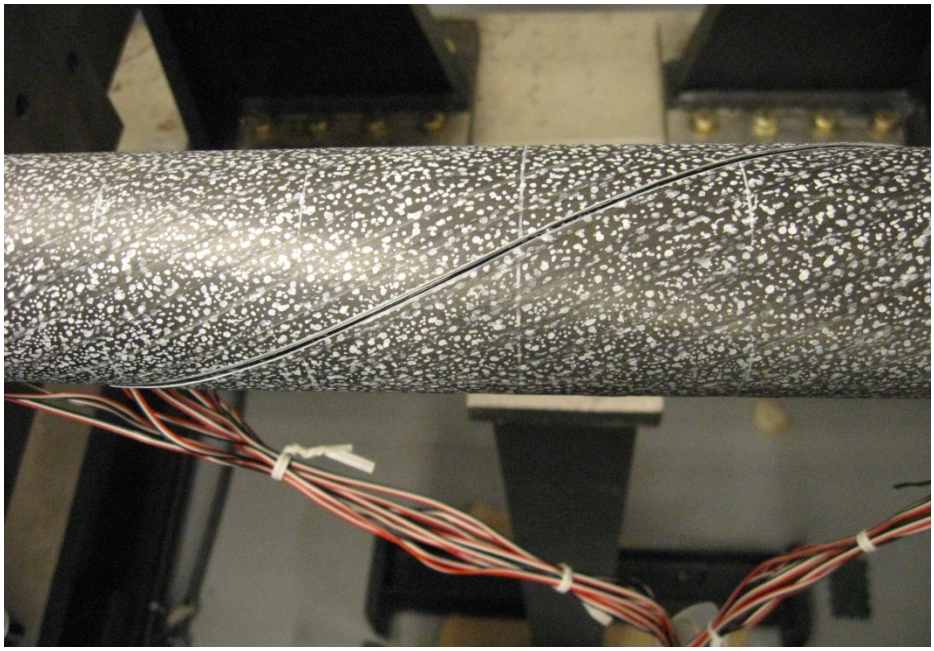

Figure 5.22: Crack propagation across outer layers, parallel to fibers orientation (first tube)

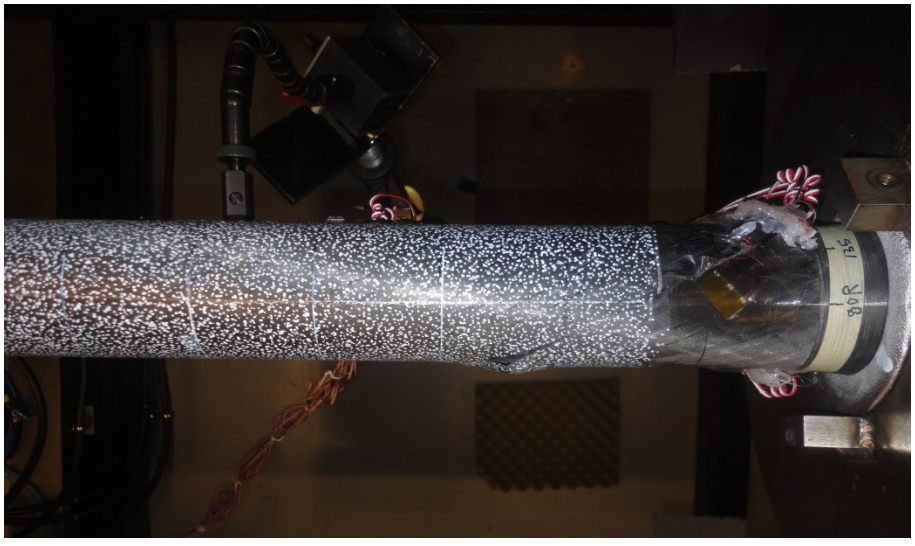

Figure 5.23: Crack propagation across outer layers, parallel to fibers orientation (second tube)

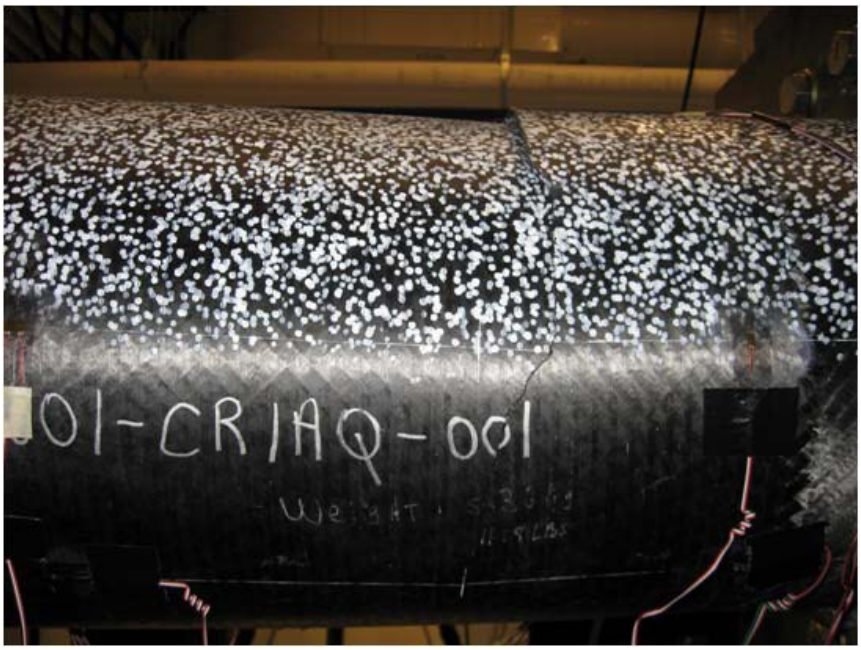

Figure 5.24: Crack propagation along hoop direction of a thin-walled thermoplastic composite cone, [28]

5.3.2.2 Mode of failure

Another point is needed to be discussed is that thick-walled composite tube shows different mode of failure compared to thin-walled composite tube under bending loading.

The thick-walled tube failed due to partial delamination of the outer layers and sliding of the delaminated layers parallel to the fibers direction towards the mid section of the tube. The loading capacity is dropped to half the recorded maximum loading applied on the tube.

Thin-walled composite tubes failed mainly due to buckling [36] and the loading capacity of the tube is dropped highly (catastrophic failure). For example ,the load is dropped to approximately 18% of the maximum loading capacity of the thermoplastic composite cone [28] ,shown in Figure 5.24

This presented difference can be explained to be due to the large wall thickness of the thick-walled tube. Although the outer layers are the main effective layers in the loading capacity of the tube, the inner layers are serving as stiffeners, uniformally distributed along the axial and circumferential directions of the outer layers. These stiffeners prevent the outer layers from buckling.

It is important to note that during testing of the second tube when delamination occurs for the outer layers (of thin wall thickness) the delaminated part exhibits a local buckling failure mode.

Chapter 6

Conclusions, contributions and future work

6.1 Conclusions

According to the thesis work, presented in previous chapters, the following points are concluded:

- The bending stiffness property of a composite tube is specified from the algebraic summation of the bending stiffness of the tube layers which in turn are controlled by two parameters for each layer: the layer moment of inertia and $E_{eff,n}$- which represent the layer mechanical properties contribution in its bending stiffness.
- Increasing tube wall thicknesses does not always improve the bending stiffness for either isotropic or composite tubes. Isotropic tube made of two thick layers of equal thickness and the inner layer is stiffer than the outer layer, the bending stiffness value decreases with increasing t/D_o ratio over specific value, noting that D_o is constant. For thick-walled composite tubes of $[\theta/-\theta]$ and equal layers thickness, the bending stiffness value also decreases when t/D_o exceeds specific value due to the effects of layer geometric parameters. These parameters reduce the contributions of the composite material properties in the outer layer compared to the inner layer, making $E_{eff,1}$ to be higher than $E_{eff,2}$. As if the inner layer is a stiffer one.
- The interaction between two adjacent layers of inclination angles θ and $-\theta$ in a composite tube highly improves the bending stiffness property. This improvement is due to the effect of coefficients of mutual influence ($\eta_{xy,x}$) and ($\eta_{x,xy}$) of these layers which increase the contribution of E_1 in the layers bending stiffness.

- Numerical differentiation provides a helpful tool in understanding the bending stiffness property of the composite tube, by specifying the effective parameters and contributions of the layers' mechanical properties in their bending stiffness.
- The new defined term ($E_{eff,n}$) serve as a measuring indicator for the interaction between layers in a composite tube under bending, such that for any two adjacent layers having high and close value of $E_{eff,n,}$ this implies better interaction between these layers. However, if $E_{eff,n}$ values for these layers have large difference, this means a lower interaction and a large stiffness mismatch between these two layers that is known to have bad effect on the strength of composite structure [37] adding to the lower bending stiffness property.
- $E_{eff,n}$ can be used as a tool to identify the balanced laminate configuration for tubes of thick layers using a 3D elasticity theory. It is for the first time to have this tool using 3D elasticity theory. And it is found that the balanced configuration does not always have layers of equal thickness as it was assumed in equivalent single layer theories.
- The geometric parameter t/D_o ratio of tubes made of two thick layers have any t_1/t ratio reduces $E_{eff,n}$ value and consequently reduces the bending stiffness.
- Multi-sublaminates composite tubes have higher bending stiffness compared to tubes made of two thick layers. Since multi-sublaminates configuration allows higher interaction effect and cancelation of the negative effect of t/D_o. This cancelation permits to have a simple and accurate equation to design the bending stiffness property.
- Manufacturing parameters of an AFP-made thermoplastic composite tube have a strong impact on its quality which is a key issue for strength of any composite structure. For example: using two compactions passes permits good contact between layers and minimizes the voids content.

- The idea of using LMPA with a large contact surface with the specimen permits firm and perfect gripping for the composite tube during the bending test. This idea can be applied in structural applications using an alternative material for the LMPA (epoxy as an example).
- The pure bending test setup is considered as a superior alternative testing method compared to the conventional 3-point and 4-point bending tests, since the bending moment is transferred to the test specimen in a smoother way without applying any concentrated loads. This smooth transfer allows the specimen to have an actual response for the bending moment and to specify the specimen actual bending stiffness and loading capacity.
- Despite that the inner layers of multi-sublaminates composite tubes have lower bending stiffness values, they play an important role in the tube strength, since they serve as stiffeners uniformly distributed in the axial and hoop directions for the tube outer layers. This prevents buckling of the tube under bending loading.
- The off axis Poisson's ratios of the layers such that (ν_{xy}) causes the existence of large hoop strain generated from the axial strain causing matrix failure in hoop direction, while (ν_{xz}) causes the existence of radial strain generated from the axial strain causing separation (delamination of mode I) between layers in the compression side of the tube.
- Increasing the interlaminar strength of the composite material can improve the resistance of the composite tube for delamination, which may increase its loading capacity.
- Thick-walled composite tubes can be considered as artificial trees since they provide large bending loading capacity-to-weight ratio compared to aluminum, and as they fail safely compared to thin-walled composite tubes (they still have some residual strength after failure).

6.2 Contributions

- Introducing and explaining the reasons for the decrease in bending stiffness values with increasing the wall thickness of thick-walled composite tubes made of [θ/-θ] stacking sequence, having equal layer thickness.
- Defining a new parameter ($E_{eff,n}$) for each layer in the composite tube under bending loading to identify the balanced laminate configuration using a 3D elasticity theory. This is the first time to have such parameter for a 3D theory.
- Understanding the bending stiffness property for composite tubes, specifying the effect of the layers' moment of inertia on their bending stiffness, and the variation of the contributions of the layers' material properties in their bending stiffnesses according to their geometry, location in the tube, and interaction with adjacent layers.
- Explaining the role of ($\eta_{xy,x}$) and ($\eta_{x,xy}$) in the interaction effect between adjacent layers of [θ/-θ] stacking sequence in composite tubes under bending and how they enhance the tube bending stiffness, using $E_{eff,n}$ as a quantifier for this interaction.
- Providing a simple and accurate equation to design the bending stiffness of multi-sublaminates composite tubes.
- Obtaining the process parameters to manufacture a thermoplastic composite tube with acceptable quality level.
- Validating the superiority of the pure bending test setup compared to the conventional 3-point and 4-point bending tests for testing thick-walled composite tubes.
- Experimental validation for the used 3D elasticity theory, and the derived simple equation to calculate the bending stiffness of thick-walled composite tubes.

- Specifying roles of inner & outer sublaminates in bending behavior of thick-walled tubes. The inner sublaminates has lower contribution in the tube bending stiffness while they serve as stiffeners, prevent the buckling of the outer sublaminates.
- Discovering the superior bending behavior of multi-sublaminates thick-walled composite tubes by testing them using an improved testing method, which permits us to specify the high strength of thick-walled tubes and to identify their mode of failure under bending accurately.
- Providing accurate experimental results for multi-sublaminates thick-walled tubes under bending.

6.3 Publications

- M. I. El-Geuchy, S. V. Hoa, F. Shadmehri, "Bending stiffness behavior of thick-walled composite tubes", accepted in the 19th international conference on composite materials, Montreal, Canada, July 2013.
- M. I. El-Geuchy, F. Shadmehri, S. V. Hoa, "Behavior of thick composite tubes under pure bending load", accepted in American Society for Composites 28th Technical Conference, Pennsylvania, USA, September 2013.
- J. Simpson, M. I. El-Geuchy, F. Shadmehri, S. V. Hoa, "Effect of processing behavior on the bending behavior of thermoplastic composite tubes made by automated fiber placement process", accepted in American Society for Composites 28th Technical Conference, Pennsylvania, USA, September 2013.

6.4 Poster

What is done of thick-walled composite tubes?

Designing <EI> simply & accurately

$$\langle EI \rangle = \frac{E_x}{1 - \eta_{xy,x}\eta_{x,xy}} I_T$$

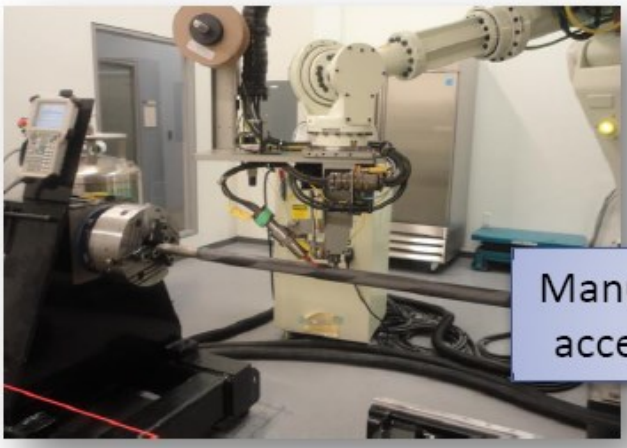

Manufacturing with acceptable quality

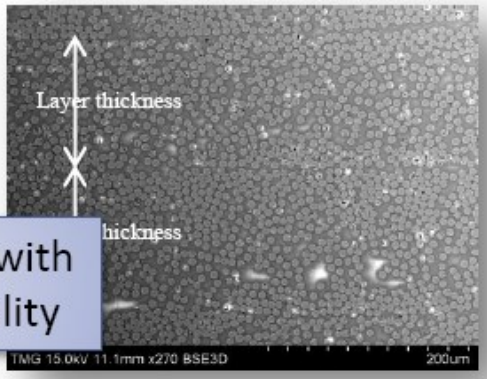

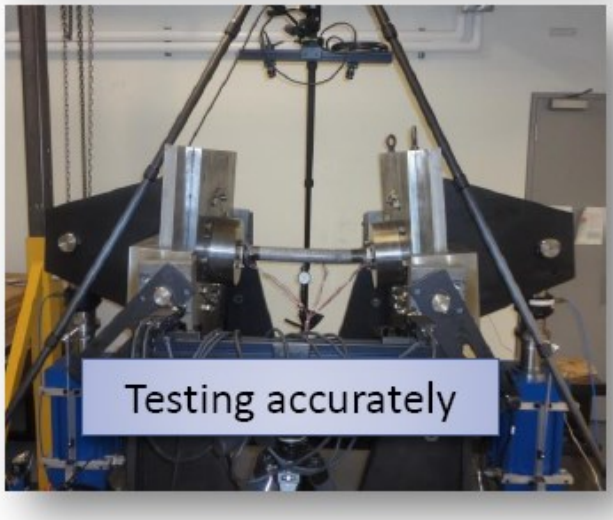

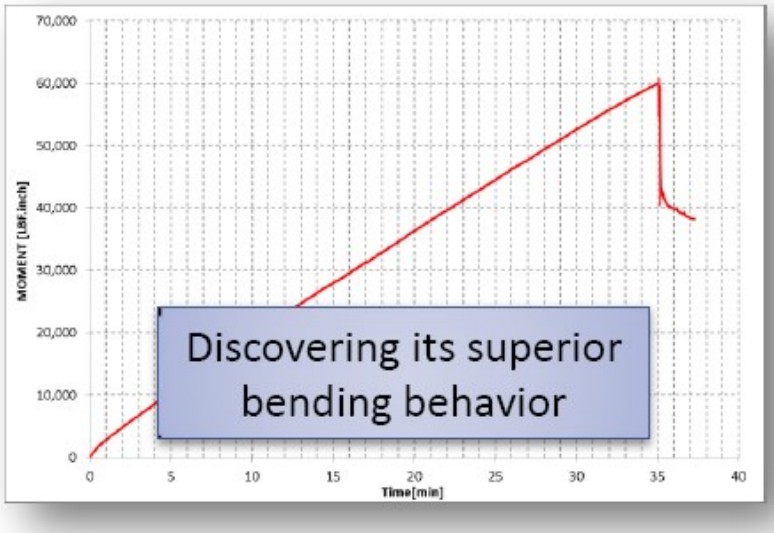

6.5 Future work

- Modeling the failure behavior of thick-walled composite tubes using finite element methods, making use of the obtained experimental results.
- Optimization of the laminate stacking sequence of a thick-walled composite tube in order to eliminate the observed positive radial strains generated in the compression side of composite tubes under bending. This radial strain has a negative effect on the tube strength since it may cause delamination between the tube layers.
- Applying the carried out parametric study with other load cases (extension and torsion) for thick-walled composite tubes using 3D elasticity theories.
- Working on layerwise methods for stress analysis of thick-walled composite tubes in order to handle transverse loading conditions.

Bibliography

[1] Derisi B., "Development of Thermoplastic Composite Tubes for Large Deformation," PhD Thesis, Concordia University, 2008.

[2] Lekhnitskii S. G., Theory of Elasticity of an Anisotropic Body, Moscow: Mir Publishers, 1981.

[3] Jolicoeur C.; Cardou A., "Analytical Solution for Bending of Coaxial Orthotropic Cylinders," *Journal of Engineering Mechanics,* vol. 120, no. 12, pp. 2556-2574, 1994.

[4] Tarn J.Q.; Wang Y.M., "Laminated Composite Tubes under Extension, Torsion, Bending, Shearing and Pressuring: a state space approach," *International Journal of Solids and Structures,* vol. 38, pp. 9053-9075, 2001.

[5] KHDEIR A. A.; REDDY J. N.; FREDERICK D., "A study of bending, vibration and buckling of cross-ply circular cylindrical shells with various shell theories," *Int. J. Engng .Sci.,* vol. 27, no. 11, pp. 1337-1351, 1989.

[6] Qatu M. S., "Accurate equations for laminated composite deep thick shells," *International Journal of Solids and Structures,* vol. 36, no. 19, p. 2917–2941, 1999.

[7] Qatu M. S.; Sullivan R. W.; Wang W., "Recent research advances on the dynamic analysis of composite shells: 2000–2009," *Composite Structures,* vol. 93, pp. 14-31, 2010.

[8] Asadi E., "Static and free vibration analyses of composite shells based on different shell theories," PhD Thesis, Mississippi State University, Mississippi State, Mississippi, December 2011.

[9] Xia M.;Takayanagi H.; Kemmochi K., "Bending behavior of filament-wound fiber-reinforced sandwich pipes," *Composite Structures 56,* vol. 56, pp. 201-210, 2002.

[10] Librescu L.; Song O., "Free vibration of anisotropic composite thin-walled beams of closed cross-section contour," *Journal of Sound and Vibration,* vol. V167, no. 1, pp. 129-147, 1993.

[11] Kim C.; White S. R., "Analysis of thick hollow composite beams under general loadings," *Composite Structures,* vol. 34, pp. 263-277, 1996.

[12] Reddy J. N., "A generalization of two-dimensional theories of laminated composite plates," *Communications in applied numerical methods,* vol. 3, pp. 173-180, 1987.

[13] Reddy J. N., "An evaluation of equivalent-single-layer and layerwise theories of composite laminates," *Composite Structures,* vol. 25, pp. 21-35, 1993.

[14] Reddy J. N., Mechanics of laminated composite plates and shells, Florida: CRC Press, 2004.

[15] Bathe K. J. ; Almeida C.A., "A simple and effective pipe elbow element-linear analysis," *Journal of Applied Mechanics,* 1980.

[16] YAN A. M.; JOSPIN R. J.; NGUYEN D. H., "An enhanced pipe elbow element-application in plastic limit analysis of pipe structures," *International journal for numerical methods in engineering,* vol. 46, pp. 409-431, 1999.

[17] Qi X. ; Jiang S., "Design and Analysis of A Filament Wound Composite Tube under General Loadings with Assitance of Computer," in *2nd international Conference on Education Technology and Computer (ICETC)*, 2010.

[18] Xu D.; Derisi B.; Hoa S.V.;Hojjati M.; Fews R., "Stress Distributions of Thermoplastic Composite Tubes Subjected to Four-Point Loading," in *The 1st Joint Canadian-American International Conference*, Delaware, USA, 2009.

[19] Tsai S.W. ; Hahn H. T., Introduction to Composite Materials, Section 7.2, Technomic Publishing Company, 1980.

[20] Chan W. S.; Demirhan K. C., "A Simple Closed-Form Solution of Bending Stiffness for Laminated Composite Tubes," *Journal of Reinforced Plastics and Composites,* vol. 19, no. 4, 2000.

[21] Cunha J. ; Piranda J., "Identification of stiffness properties of composite tubes from dynamic tests," *Experimental Mechanics,* vol. 40, no. 2, pp. 211-218, June 2000.

[22] Shadmehri F.; Derisi B.; Hoa S.V., "On bending stiffness of composite tubes," *Composite structures,* vol. V93, 2011.

[23] Khan M.A. ; Mitschang P. ; Schledjewski R., "Identification of some optimal parameters to achieve higher laminate quality thorugh tape placement process," *Advances in Polymer Technology,* vol. 29, no. 2, 2010.

[24] Croft K., "Experimental Characterization of Automated Fiber Placement Process Defects in Composite Structures," PhD Thesis, McGill University, Montreal, Canada, August 2010.

[25] Shadmehri F. ; Cai X. ; Hojjati M. ; Chen J. ; Hoa S. V., "Determination of Optimal Process Parameters for Manufacturing Thermoplastic Composite Rings by Automated Fiber Placement," in *26 American Society for Composites (ASC) annual technical conference (Second Joint US-Canada Conference on Composites)*, Montreal, Canada, September 2011.

[26] Saggar P., "Experimental study of laminated composite tubes under bending," Master Thesis, University of Texas, 2007.

[27] Fuchs J. P.; Hyer M. W.; Starnes,Jr J. H., "Numerical and Experimental Investigation of the Bending Response of Thin-Walled Composite Cylinders," NASA-CR-195730, Blacksburg, Virginia, September 1993.

[28] Shadmehri F., "Buckling of Laminated Composite Conical Shells; Theory and Experiment," PhD Thesis, Concordia University, Montreal, Quebec, Canada, September 2012.

[29] Hyer M., Stress analysis of fiber-reinforced composite materials, Destech publications, 2009.

[30] Hoa S. V., Principles of the manufacturing of composite materials, DEStech Publications, Inc, 2009.

[31] Cai X. ; Shadmehri F. ; Hojjati M. ; Chen J. ; Hoa S. V., "Determination of Optimum Process Conditions for Processing AS4/APC-2 Thermoplastic Composites by Automated Fiber Placement," in *The Society for the Advancement of Material and Process Engineering (SAMPE) conference*, Baltimore, May 2012.

[32] TenCate Advanced Composites, "TenCate Cetex Thermoplastic Advanced Composites Tehnical Data," TenCate Advanced Composites, 2012.

[33] Herbst C.; Splitthof K., "Basics of 3D digital image correlation," [Online]. Available: www.dantecdynamics.com/Default.aspx?ID=855..

[34] Correlated Solutions, "Deformation Measurment," www.correlatedsolutions.com/data/vic2d-vic3d-flyer.pdf. [Online].

[35] Leon G.F.; Hall J.C.; Kelly J.J.; Bohlmann R., "Design and testing of in-situ consolidated thick high performance thermoplastics," in *Proceedings of the Twelveth International Conference on Composite Materials*, Paris, July 1999.

[36] Brush D. O.; Almroth B. O., Buckling of bars, plates and shells, McGraw-Hill, Inc, 1975.

[37] Liu D., "Impact-Induced Delamination-A View of Bending Stiffness Mismatching," *Journal of Composite Materials,* vol. 22, p. 674, 1988.

Appendix A

Bending stiffness formulation based on 3D theory

This part is devoted to present the bending stiffness formulation for orthotropic circular tubes subjected to only bending Moment (M_x), causing bending curvature (k_x). This presented formulation is taken from [3].

$$M_x = (EI)k_x \tag{A.1}$$

Where:

$$(EI) = \sum_{n=1}^{N} \frac{\pi}{C_{33,n}} \left\{ \sum_{i=1}^{4} K_{i,n}[C_{13,n} + C_{23,n}(m_{i,n} + 1) - C_{34,n}g_{i,n}m_{i,n}] \frac{a_n^{m_{i,n}+2} - b_n^{m_{i,n}+2}}{m_{i,n}+2} + [\mu_{1,n}(C_{13,n} + 3C_{23,n}) - 2\mu_{2,n}C_{34,n} - 1] \frac{a_n^4 - b_n^4}{4} \right\} \tag{A.2}$$

By identifying the variables in equation (A.2), the bending stiffness can be calculated for the whole tube as will be presented in the following paragraphs

N…. Total number of layers of the composite tube

n…. Layer number from inside to outside

a,b …. Inner and outer radii for one layer

C_{ij} …. Elastic constants of transformed compliance matrix for one layer, shown in equation (A.3)

$$\begin{bmatrix} \varepsilon_r \\ \varepsilon_\alpha \\ \varepsilon_z \\ \gamma_{\alpha z} \\ \gamma_{rz} \\ \gamma_{r\alpha} \end{bmatrix} = \begin{bmatrix} C_{11} & C_{12} & C_{13} & C_{14} & 0 & 0 \\ C_{12} & C_{22} & C_{23} & C_{24} & 0 & 0 \\ C_{13} & C_{13} & C_{13} & C_{34} & 0 & 0 \\ C_{14} & C_{24} & C_{34} & C_{44} & 0 & 0 \\ 0 & 0 & 0 & 0 & C_{55} & C_{56} \\ 0 & 0 & 0 & 0 & C_{56} & \bar{S}_{66} \end{bmatrix}_{(n)} \begin{bmatrix} \sigma_z \\ \sigma_\alpha \\ \sigma_r \\ \tau_{r\alpha} \\ \tau_{rz} \\ \tau_{\alpha z} \end{bmatrix} \quad \text{(A.3)}$$

The strains and stresses in equation (A.3) are in cylindrical coordinates such that the stress components are defined as follows:

- In plane normal stresses: axial stress (σ_z), hoop stress (σ_α)
- In plane shear stress ($\tau_{\alpha z}$)
- Interlaminar normal stress: radial stress (σ_r)
- Interlaminar shear stresses ($\tau_{r\alpha}$,τ_{rz})

By reducing compliance matrix in z direction, the reduced matrix are obtained such that

$$\beta_{ij} = C_{ij} - \frac{C_{i3}C_{3j}}{C_{33}} \quad \text{(A.4)}$$

β_{ij} …. reduced elastic constants, such that: $\beta_{i3} = \beta_{3j} = 0$

$g_{i,n}$…. 4 variables for each layer, given by the following equation

$$g_{i,n} = \frac{\beta_{24}m_{i,n}^3 + (\beta_{14} + \beta_{24})m_{i,n}^2 - \beta_{24}m_{i,n}}{\beta_{44}m_{i,n}^2 - \beta_{55}} \quad \text{(A.5)}$$

Where:

$$
\begin{aligned}
m_{i,n} &= \pm\sqrt{\frac{-b \pm \sqrt{b^2 - 4ac}}{2a}} \\
a &= \beta_{22}\beta_{44} - \beta_{24}^2 \\
b &= \beta_{24}(2\beta_{14} + \beta_{24} + 2\beta_{56}) - \beta_{44}(\beta_{11} + 2\beta_{12} + \beta_{22} + \beta_{66}) - \beta_{22}\beta_{55} + \beta_{14}^2 \\
c &= \beta_{55}(\beta_{11} + 2\beta_{12} + \beta_{22} + \beta_{66}) - \beta_{56}^2
\end{aligned}
\tag{A.6}
$$

μ_1, μ_2 …. are calculated for each layer, using the following equation

$$
\begin{Bmatrix} \mu_1 \\ \mu_2 \end{Bmatrix} = \begin{bmatrix} -2\beta_{14} - 6\beta_{24} + \beta_{56} & 4\beta_{44} - \beta_{55} \\ -\beta_{11} - 2\beta_{12} + 3\beta_{22} - \beta_{66} & 2\beta_{14} - 2\beta_{24} + \beta_{56} \end{bmatrix}^{-1} \frac{1}{C_{33}} \begin{Bmatrix} 2C_{34} \\ C_{13} - C_{23} \end{Bmatrix} \tag{A.7}
$$

$K_{i,n}$…. four variables for each layer, these variables are defined assuming perfect bonding between layers such that the continuity is obvious in stresses (σ_r, $\tau_{r\alpha}$, τ_{rz}) and displacements (u_r, u_α, w). This condition leads to get a number of equations used to calculate ($K_{i,n}$) as follows:

1-Due to continuity of radial stress (σ_r) and shear stress ($\tau_{r\alpha}$):

$$
\sum_{i=1}^{4} K_{i,n} b^{m_{i,n}-1} - K_{i,n+1} b^{m_{i,n+1}-1} = (\mu_{1,n+1} - \mu_{1,n}) b \tag{A.8}
$$

2-Due to continuity of shear stress (τ_{rz}):

$$
\sum_{i=1}^{4} K_{i,n} g_{i,n} b^{m_{i,n}-1} - K_{i,n+1} g_{i,n+1} b^{m_{i,n+1}-1} = (\mu_{2,n+1} - \mu_{2,n}) b \tag{A.9}
$$

3-Due to continuity of displacement (u_r):

$$
\upsilon_n - \upsilon_{n+1} + \sum_{i=1}^{4} K_{i,n} U'_{i,n} b^{m_{i,n}} - K_{i,n+1} U'_{i,n+1} b^{m_{i,n+1}} = (U'_{5,n+1} - U'_{5,n}) b^2 \tag{A.10}
$$

4-Due to continuity of displacement (u_α):

$$\upsilon_n - \upsilon_{n+1} + \sum_{i=1}^{4} K_{i,n} U'_{i,n} b^{m_{i,n}} - K_{i,n+1} U'_{i,n+1} b^{m_{i,n+1}} = (U'_{5,n+1} - U'_{5,n}) b^2$$

$$\upsilon_n - \upsilon_{n+1} + \sum_{i=1}^{4} K_{i,n} V'_{i,n} b^{m_{i,n}} - K_{i,n+1} V'_{i,n+1} b^{m_{i,n+1}} = (V'_{5,n+1} - V'_{5,n}) b^2 \qquad \text{(A.11)}$$

5-Due to continuity of displacement (w):

$$\sum_{i=1}^{4} K_{i,n} W'_{i,n} b^{m_{i,n}} - K_{i,n+1} W'_{i,n+1} b^{m_{i,n+1}} = (W'_{5,n+1} - W'_{5,n}) b^2 \qquad \text{(A.12)}$$

Where:

$$U'_i = \frac{1}{m_i}[\beta_{11} + \beta_{12}(m_i + 1) - \beta_{14} g_i m_i]; \qquad i = 1 \text{ to } 4$$

$$U'_5 = \frac{1}{2}\left[\mu_1(\beta_{11} + 3\beta_{12}) - 2\beta_{14}\mu_2 + \frac{C_{13}}{C_{33}}\right]$$

$$V'_i = \frac{1}{m_i}[\beta_{11} + \beta_{12} - \beta_{22} m_i(m_i + 1) - g_i m_i(\beta_{14} - \beta_{24} m_i)]; \qquad i = 1 \text{ to } 4$$

$$V'_5 = \frac{1}{2}\left[\mu_1(\beta_{11} + \beta_{12} - 6\beta_{22}) - 2\mu_2(\beta_{14} - 2\beta_{24}) + \frac{C_{13} - 2C_{23}}{C_{33}}\right] \qquad \text{(A.13)}$$

$$W'_i = \frac{1}{m_i}(\beta_{55} g_i - \beta_{56}); \qquad i = 1 \text{ to } 4$$

$$W'_5 = \frac{1}{2}(\beta_{55}\mu_2 - \beta_{56}\mu_1)$$

ν_n…. is a constant for each layer such that: ν_0=0, the rest of (ν_n) are taken to be arbitrary value other than zero, to get a solution that satisfies the compatibility equations of the bent tube.

6-Equations due to free surfaces

There are free surfaces at the outer surface of the outer most layer (at $r=b_N$) and at the inner surface of the inner most layer (at $r=a_1$), in case of no core. At these free surfaces, the stresses ($\sigma_r=\tau_{r\alpha}=\tau_{rz}=0$) leading to the following equations

$$\sum_{i=1}^{4} K_{i,n} r^{m_{i,n}-1} = -\mu_{1,n} r \qquad \text{n=1 at r = } a_1 \text{ ,}$$

$$\sum_{i=1}^{4} K_{i,n} g_{i,n} r^{m_{i,n}-1} = -\mu_{2,n} r \qquad \text{n=N at r = } b_N \qquad \text{(A.14)}$$

Solving the system of equations, one can calculate $K_{i,n}$. The matrix equation of this system is of dimension equal to (5Nx5N). For a tube made of two layers, we have a matrix equation of 10x10, which is solved to get ten unknowns; four $K_{i,n}$ for each layer and ν_n. Substituting by all the obtained unknowns in equation (A.2), one can get the bending stiffness of the whole tube.

Appendix B

Designed parts

Mandrel technical drawing

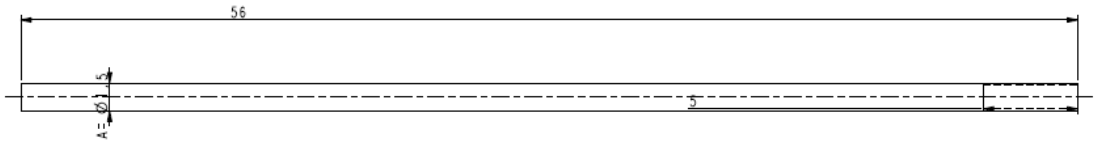

3 MANDREL ARE NEEDED
IST MANDREL: A=0.5 INCH
2ND MANDREL: A=1 INCH
3RD MANDREL: A=1.5 INCH

MANDRELS ARE STOCK BARS
WITH THE THREADED END

MATERIAL
1040 STEEL

ALL DIMENSIONS IN INCH

Rollers technical drawing

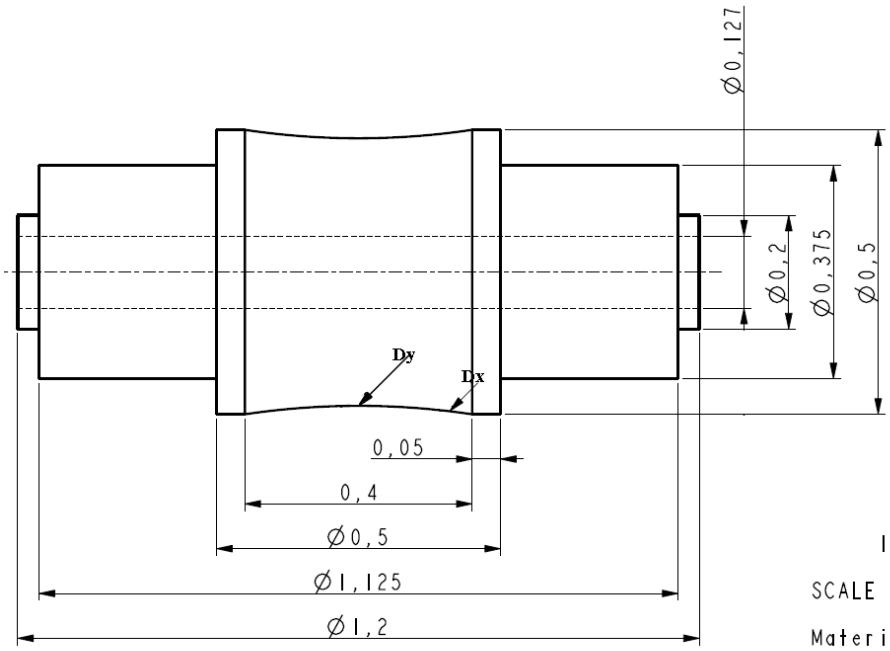

INCH Roller

SCALE 5,000

Material 316 STAINLESS STEEL
DIMENSIONS ARE IN INCHES

TOLERANCE NOT SPECIFIED
X.X +- 0.01
X.XX +- 0.005
X.XXX +-0.003

Adaptor Ring

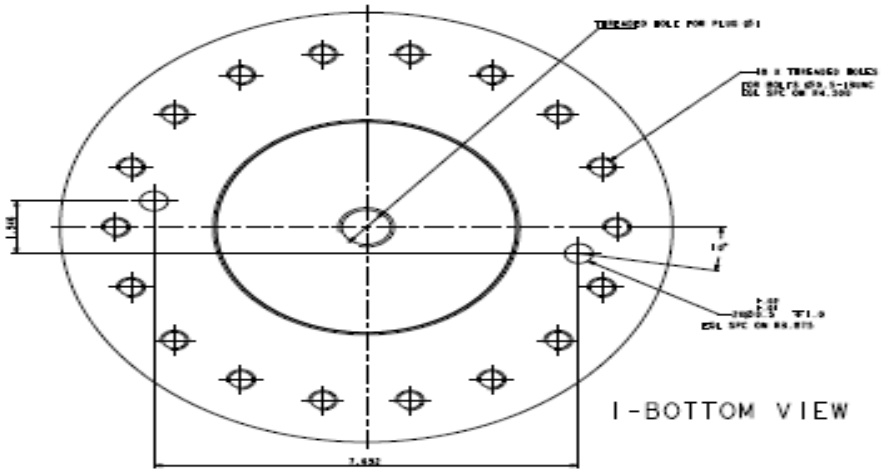

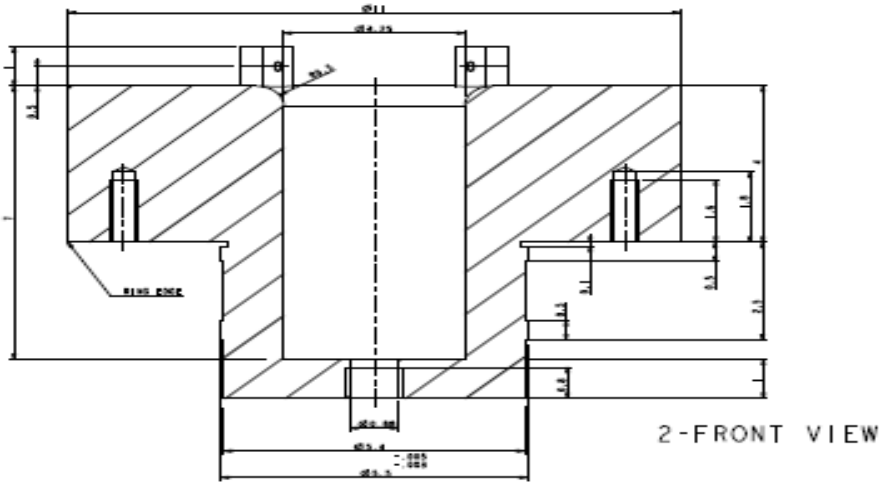

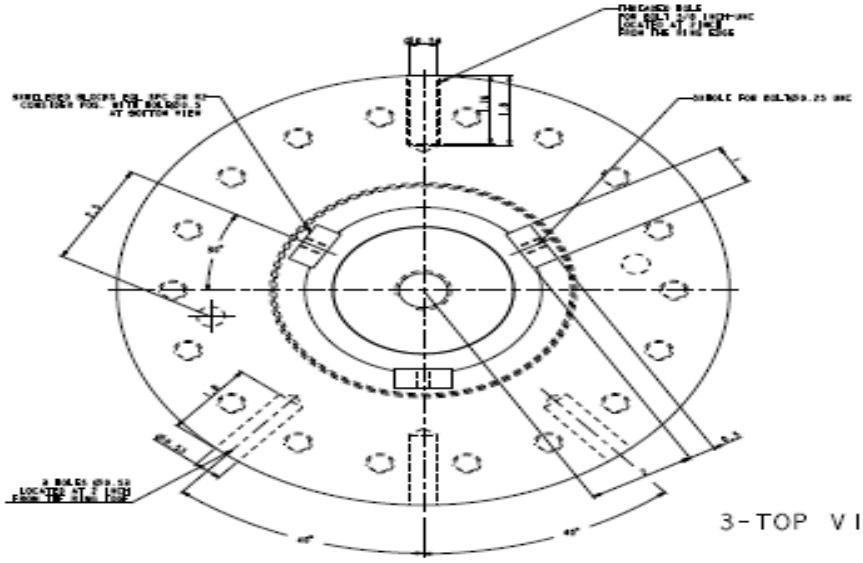

MATERIAL
4140 ALLOY STEEL

ALL DIMENSIONS IN INCH
TOLERANCE NOT SPECIFIED
X.X +-0.04
X.XX +-0.01
X.XXX +-.002

TWO PARTS ARE NEEDED

Appendix C

Stress analysis for composite tubes under pure bending

Using 3D elasticity theory presented in [3], the tube curvature is calculated using the following equation:

$$k_x = \frac{M_x}{\langle EI \rangle} \tag{C.1}$$

The total bending stiffness of a composite tube is calculated using Equation (2.25), and for the case of four-point bending, the bending moment M_x is calculated from the following form

$$M_x = P\frac{(L-a)}{4} \tag{C.2}$$

Where, (P) is the applied load, (L) is the length of the tube and (a) is the distance between the loading points in four-point bending test. Stress vector is calculated using the following equations for any point through the wall thickness of the composite tube, of cylindrical coordinate (r,α, z) as shown in Figure (C.1).

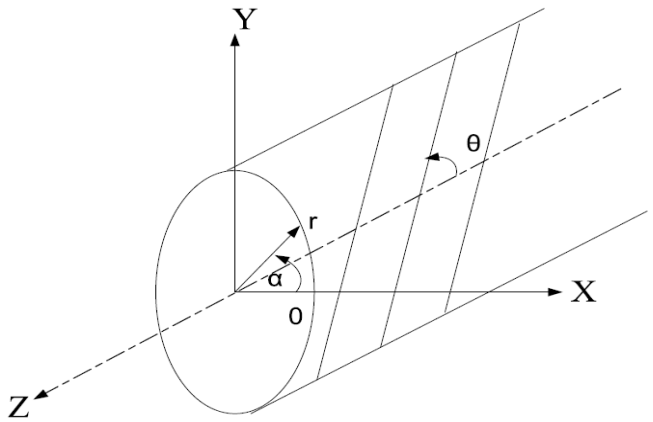

Figure C.1: Coordinate systems of a Composite tube

$$\sigma_r = (k_x \sin\alpha)\left(\sum_{i=1}^{4} K_{i,n} r^{m_{i,n}-1} + \mu_{1,n} r\right)$$

$$\sigma_\alpha = (k_x \sin\alpha)\left(\sum_{i=1}^{4} K_{i,n}(m_{i,n}+1) r^{m_{i,n}-1} + 3\mu_{1,n} r\right)$$

$$\tau_{r\alpha} = (k_x \cos\alpha)\left(-\sum_{i=1}^{4} K_{i,n} r^{m_{i,n}-1} - \mu_{1,n} r\right)$$

$$\tau_{rz} = (k_x \cos\alpha)\left(\sum_{i=1}^{4} K_{i,n} g_{i,n} r^{m_{i,n}-1} + \mu_{2,n} r\right) \qquad \textbf{(C.3)}$$

$$\tau_{\alpha z} = (k_x \sin\alpha)\left(-\sum_{i=1}^{4} K_{i,n} g_{i,n} r^{m_{i,n}-1} - 2\mu_{2,n} r\right)$$

$$\sigma_z = \frac{1}{\bar{S}_{11,n}}\left(k_x \, r \sin\alpha - \bar{S}_{13,n}\sigma_r - \bar{S}_{12,n}\sigma_\alpha - \bar{S}_{16,n}\tau_{\alpha z}\right)$$

σ_z *and* σ_α are the in-plane axial and hoop stresses, respectively. $\tau_{\alpha z}$ is the in-plane shear stress, σ_r is the out-of-plane radial stress, $\tau_{r\alpha}$ *and* τ_{rz} are the interlaminar transverse shear stresses. Strain vector at this point can be calculated using the following equation

$$\begin{bmatrix} \varepsilon_r \\ \varepsilon_\alpha \\ \varepsilon_z \\ \gamma_{\alpha z} \\ \gamma_{rz} \\ \gamma_{r\alpha} \end{bmatrix} = \begin{bmatrix} C_{11} & C_{12} & C_{13} & C_{14} & 0 & 0 \\ C_{12} & C_{22} & C_{23} & C_{24} & 0 & 0 \\ C_{13} & C_{13} & C_{13} & C_{34} & 0 & 0 \\ C_{14} & C_{24} & C_{34} & C_{44} & 0 & 0 \\ 0 & 0 & 0 & 0 & C_{55} & C_{56} \\ 0 & 0 & 0 & 0 & C_{56} & \bar{S}_{66} \end{bmatrix}_{(n)} \begin{bmatrix} \sigma_z \\ \sigma_\alpha \\ \sigma_r \\ \tau_{r\alpha} \\ \tau_{rz} \\ \tau_{\alpha z} \end{bmatrix} \qquad \textbf{(C.4)}$$

The Following figures present the calculated stresses and strains for the two tested composite tubes at M_x =1 kN.m, for α=90^o.

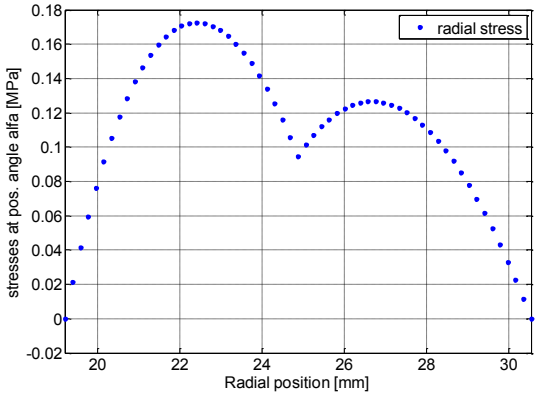

(a) Radial stress

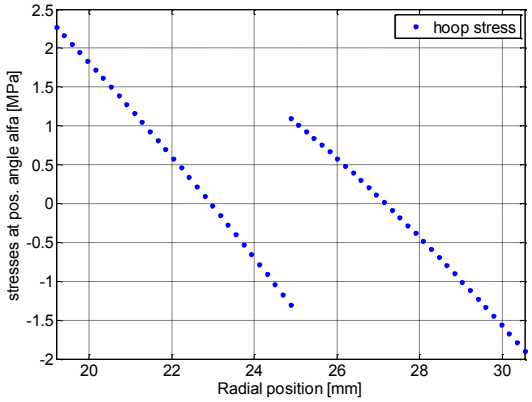

(a) Hoop stress

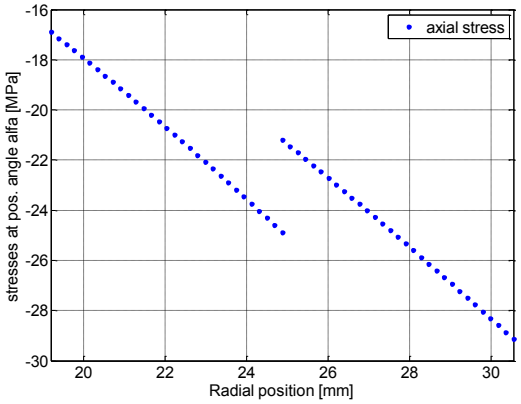

(a) Axial stress

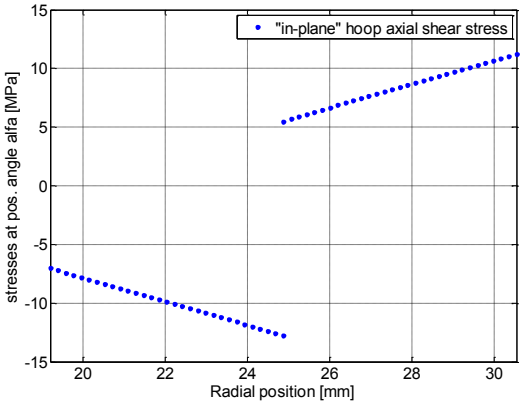

(a) in-plane shear stress

Figure C.2: Stresses in the first tube at $\alpha=90^{o}$, $M_x=1$kN.m

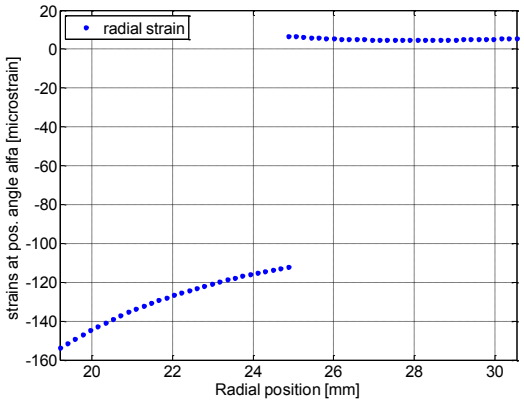

(a) Radial strain

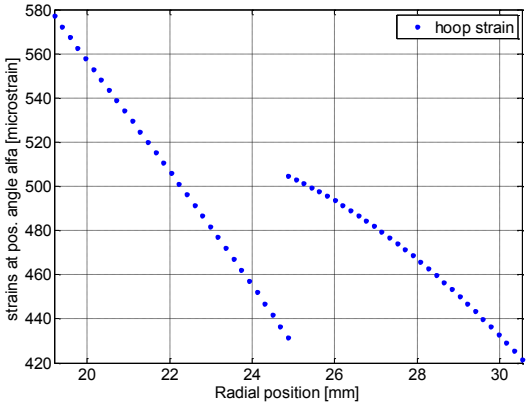

(a) Hoop strain

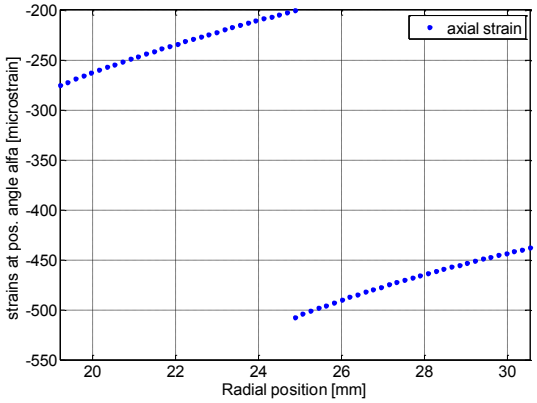

(a) Axial strain

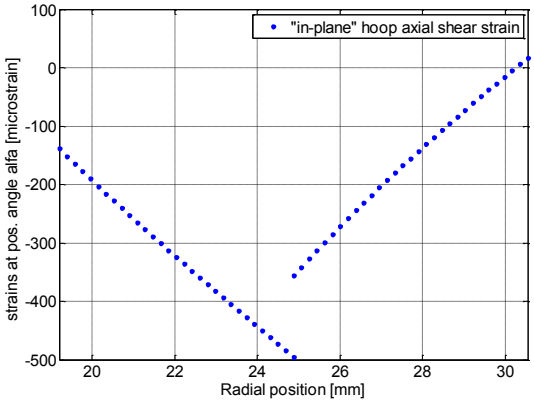

(a) in-plane shear strain

Figure C.3: Strains in the first tube at $\alpha=90^{o}$, $M_x=1$kN.m

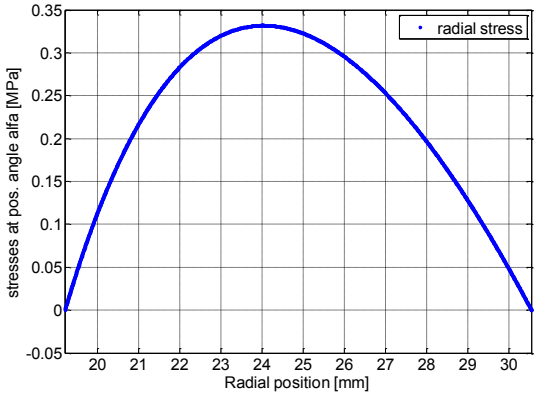

(a) Radial stress

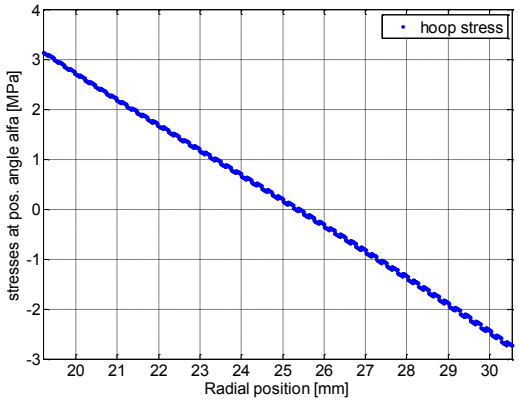

(a) Hoop stress

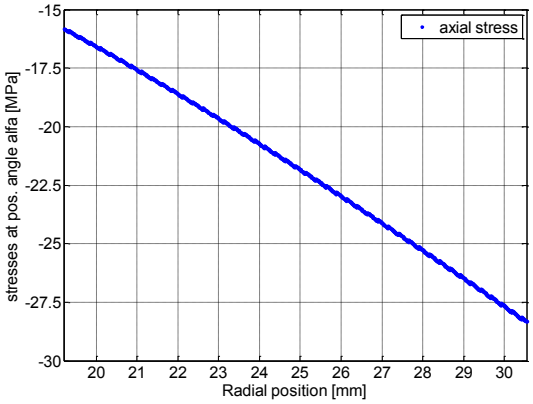

(a) Axial stress

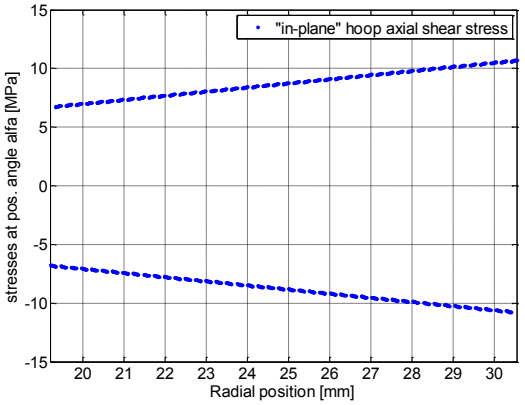

(a) in-plane shear stress

Figure C.4: Stresses in the second tube at $\alpha=90^{o}$, $M_x=1kN.m$

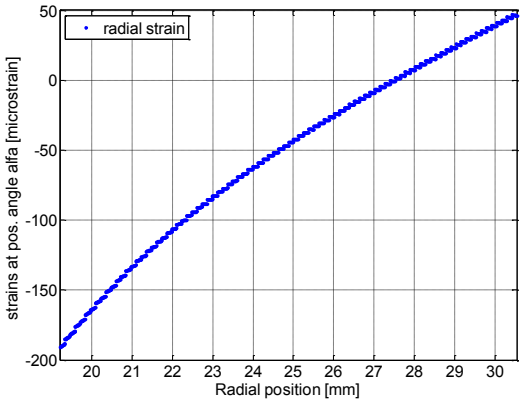

(a) Radial strain

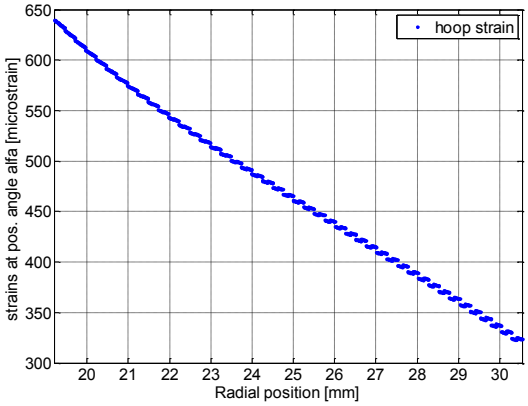

(a) Hoop strain

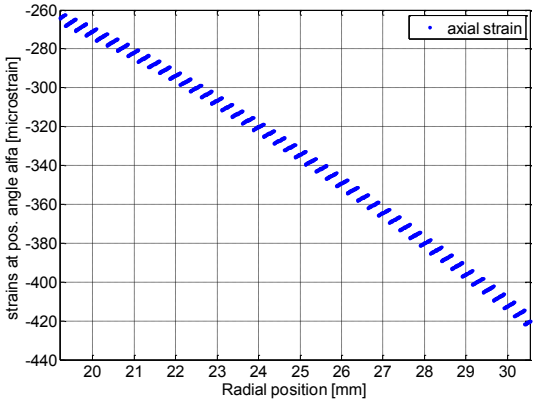

(a) Axial strain

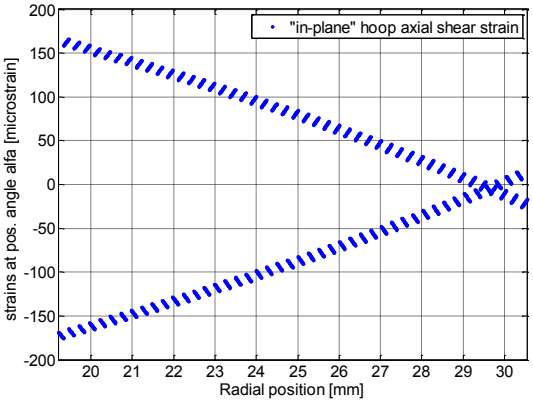

(a) in-plane shear strain

Figure C.5: Strains in the second tube at $\alpha=90^{o}$, $M_x=1kN.m$

Appendix D

MATLAB CODES

D.1 Code for calculating the tube bending stiffness, through thickness stresses and strains using [3]

```
 clc
 clear all
%=========================================================================
%constants
%=========================================================================
%Inputs
%for EI calculation
Douter=61.09;
thickness_Douter=0.45;
theta=25;
%for stress analysis
Mx=-1e6;    %N.mm
alfa=90;
points_layer=30; %no of calculation points within layer, to control precision
%% theta input
% making theta;-theta
N_layers=90;      %any number
theta_layer(1)=theta;
for n=2:N_layers
   if theta_layer(n-1)==theta
      theta_layer(n)=-1*theta;
   else
      theta_layer(n)=theta;
   end
end
theta_layer;
%% thickness ratio adjusting
%equal thickness
equal_thickness=1/N_layers;
thickness_ratio=ones(N_layers,1)*equal_thickness;
sum(thickness_ratio)              %checking
%% main program structure
total_thickness=thickness_Douter*Douter;
Dinner=Douter-total_thickness*2;
t_layers=thickness_ratio*total_thickness;
sum(t_layers)             %checking
%% Loop of inner and outer radii of cylinders
```

```
ra(1)=Dinner/2;
rb(1)=ra(1)+t_layers(1);
for n=2:N_layers
  ra(n)=rb(n-1);
  rb(n)=ra(n)+t_layers(n);
end
%% Loop of all needed coefficients
%initialization
%C(,n)
%Beta(,n)
%m(i,n)

for n=1:N_layers
   %initialization
   a=0; b=0; c=0; %mu_root1=0; mu_root2=0; nu(1)=0;

  C(:,:,n)=C_Matrix26022013(theta_layer(n));
  Beta(:,:,n)= C(:,:,n)-(C(:,3,n)*C(3,:,n)/C(3,3,n));

  a=Beta(2,2,n)*Beta(4,4,n)-Beta(2,4,n)^2;
  b=Beta(2,4,n)*(2*Beta(1,4,n)+Beta(2,4,n)+2*Beta(5,6,n))-
Beta(4,4,n)*(Beta(1,1,n)+2*Beta(1,2,n)+Beta(2,2,n)+Beta(6,6,n))-
Beta(2,2,n)*Beta(5,5,n)+Beta(1,4,n)^2;
  c=Beta(5,5,n)*(Beta(1,1,n)+2*Beta(1,2,n)+Beta(2,2,n)+Beta(6,6,n))-Beta(5,6,n)^2;

  m(1,n)=sqrt((-b+sqrt(b^2-4*a*c))/(2*a));
  m(2,n)=sqrt((-b-sqrt(b^2-4*a*c))/(2*a));
  m(3,n)=-sqrt((-b+sqrt(b^2-4*a*c))/(2*a));
  m(4,n)=-sqrt((-b-sqrt(b^2-4*a*c))/(2*a));

  mu_matrix=[-2*Beta(1,4,n)-6*Beta(2,4,n)+Beta(5,6,n) 4*Beta(4,4,n)-Beta(5,5,n);
     -Beta(1,1,n)-2*Beta(1,2,n)+3*Beta(2,2,n)-Beta(6,6,n) 2*Beta(1,4,n)-2*Beta(2,4,n)+Beta(5,6,n)];
  mu_vector=1/C(3,3,n)*[2*C(3,4,n);C(1,3,n)-C(2,3,n)];
  mu(:,n)=mu_matrix\mu_vector;

  for i=1:4
     g(i,n)=(Beta(2,4,n)*m(i,n)^2+(Beta(1,4,n)+Beta(2,4,n))*m(i,n)-
Beta(5,6,n))/(Beta(4,4,n)*m(i,n)^2-Beta(5,5,n));

     Uprime(i,n)=(1/m(i,n))*(Beta(1,1,n)+Beta(1,2,n)*(m(i,n)+1)-Beta(1,4,n)*g(i,n)*m(i,n));
     Vprime(i,n)=(1/m(i,n))*(Beta(1,1,n)+                    Beta(1,2,n)-Beta(2,2,n)*m(i,n)*(m(i,n)+1)-
g(i,n)*m(i,n)*(Beta(1,4,n)-Beta(2,4,n)*m(i,n)));
     Wprime(i,n)=(1/m(i,n))*(Beta(5,5,n)*g(i,n)-Beta(5,6,n));
  end
  Uprime(5,n)=0.5*(mu(1,n)*(Beta(1,1,n)+3*Beta(1,2,n))-
2*Beta(1,4,n)*mu(2,n)+C(1,3,n)/C(3,3,n));
```

```
  Vprime(5,n)=0.5*(mu(1,n)*(Beta(1,1,n)+Beta(1,2,n)-6*Beta(2,2,n))-2*mu(2,n)*(Beta(1,4,n)-
2*Beta(2,4,n))+(C(1,3,n)-2*C(2,3,n))/C(3,3,n));
  Wprime(5,n)=0.5*(Beta(5,5,n)*mu(2,n)-Beta(5,6,n)*mu(1,n));
end

%% section for Calculating K(i,n)
count=0;
dimension=5*(N_layers-1)+5;  %=5*N_layers

A_matrix=zeros(dimension,dimension);
A_matrices=zeros(dimension,dimension,N_layers);

B_vectors=zeros(dimension,1,N_layers);
B_vector=zeros(dimension,1);

%The main 5 equations at each interface
for n=1:(N_layers-1)
   for i=1:4
      A_matrices(1+count,i+count,n)=rb(n)^(m(i,n)-1);
      A_matrices(2+count,i+count,n)=g(i,n)*rb(n)^(m(i,n)-1);
      A_matrices(3+count,i+count,n)=Uprime(i,n)*rb(n)^(m(i,n));
      A_matrices(4+count,i+count,n)=Vprime(i,n)*rb(n)^(m(i,n));
      A_matrices(5+count,i+count,n)=Wprime(i,n)*rb(n)^(m(i,n));

      A_matrices(1+count,i+count+5,n)=-rb(n)^(m(i,n+1)-1);
      A_matrices(2+count,i+count+5,n)=-g(i,n+1)*rb(n)^(m(i,n+1)-1);
      A_matrices(3+count,i+count+5,n)=-Uprime(i,n+1)*rb(n)^(m(i,n+1));
      A_matrices(4+count,i+count+5,n)=-Vprime(i,n+1)*rb(n)^(m(i,n+1));
      A_matrices(5+count,i+count+5,n)=-Wprime(i,n+1)*rb(n)^(m(i,n+1));
   end

   A_matrices(3+count,5+count,n)=1;
   A_matrices(4+count,5+count,n)=1;

   A_matrices(3+count,5+count+5,n)=-1;
   A_matrices(4+count,5+count+5,n)=-1;

   B_vectors(1+count,1,n)=(mu(1,n+1)-mu(1,n))*rb(n);
   B_vectors(2+count,1,n)=(mu(2,n+1)-mu(2,n))*rb(n);
   B_vectors(3+count,1,n)=(Uprime(5,n+1)-Uprime(5,n))*rb(n)^2;
   B_vectors(4+count,1,n)=(Vprime(5,n+1)-Vprime(5,n))*rb(n)^2;
   B_vectors(5+count,1,n)=(Wprime(5,n+1)-Wprime(5,n))*rb(n)^2;

   count=count+5;
end

%the 5 equations of free surfaces "inner and outer cylinders"
```

```
for i=1:4
   A_matrices(1+count,i,N_layers)=ra(1)^(m(i,1)-1);
   A_matrices(2+count,i,N_layers)=g(i,1)*ra(1)^(m(i,1)-1);

   A_matrices(3+count,i+count,N_layers)=rb(N_layers)^(m(i,N_layers)-1);
   A_matrices(4+count,i+count,N_layers)=g(i,N_layers)*rb(N_layers)^(m(i,N_layers)-1);
end

A_matrices(5+count,5,N_layers)=1;

B_vectors(1+count,1,N_layers)=-mu(1,1)*ra(1);
B_vectors(2+count,1,N_layers)=-mu(2,1)*ra(1);
B_vectors(3+count,1,N_layers)=-mu(1,N_layers)*rb(N_layers);
B_vectors(4+count,1,N_layers)=-mu(2,N_layers)*rb(N_layers);
B_vectors(5+count,1,N_layers)=0;

%assembly of matrices
for n=1:N_layers
   A_matrix=A_matrix+A_matrices(:,:,n);
   B_vector=B_vector+B_vectors(:,:,n);
end

%Calculating K(i,n)

X=A_matrix\B_vector;

count=0;
for n=1:N_layers
   for i=1:4
      K(i,n)=X(i+count);
   end
   Nu(n)=X(5+count);
   count=count+5;
end

%% calculating the bending stiffness

for n=1:N_layers
   CoefPartA_I(n)=0;
   for i=1:4
      variable1(i,n)=(rb(n)^(m(i,n)+2)-ra(n)^(m(i,n)+2))/(m(i,n)+2);
      variable2(i,n)=(C(1,3,n)+C(2,3,n)*(m(i,n)+1)-C(3,4,n)*g(i,n)*m(i,n))*-1;
      K_var1_var2(i,n)=K(i,n)*variable1(i,n)*variable2(i,n);
   end
   CoefPartA_I(n)=sum(K_var1_var2(:,n));
   I(n)=(-pi/4)*(ra(n)^4-rb(n)^4);
```

```
   CoefPartA(n)=CoefPartA_I(n)*pi/I(n);
   CoefPartB(n)=(mu(1,n)*(C(1,3,n)+3*C(2,3,n))-2*mu(2,n)*C(3,4,n)-1)*-1;
   Coef(n)=CoefPartA(n)+CoefPartB(n);

   Ex(n)=1/C(3,3,n);
   Eeff(n)=Ex(n)*Coef(n);
   EI(n)=Ex(n)*Coef(n)*I(n);
end
EI_total=sum(EI)       %N.mm2
Ex_total=sum(Ex);
Coef_total=sum(Coef);
I_total=sum(I);

%% calculating stresses 1-radial axis
%inputs
%Mx=1e6;     %N.mm
%alfa=0;   %input('Enter the required position angle = ');
%points_layer=30; %no of calculation points withen layer, to control precision

% radial axis
radial_axis(1)=ra(1);
delta_radial=t_layers/points_layer;
counter=2;
for n=1:N_layers
   for o=1:points_layer
      radial_axis(counter)=radial_axis(counter-1)+delta_radial(n);
      counter=counter+1;
   end
   if n<N_layers
       radial_axis(counter)=radial_axis(counter-1);
       counter=counter+1;
   end
end

%% 2-stresses and strains
kx=Mx/EI_total; %1/mm
max=length(radial_axis);

% stresses loop
n=1;o=1;
for counter=1:max    %for o=1:(points_layer+1)
   for i=1:4
      segma_radialPartA(i)=K(i,n)*radial_axis(counter)^(m(i,n)-1);
      segma_hoopPartA(i)=K(i,n)*(m(i,n)+1)*radial_axis(counter)^(m(i,n)-1);
      segma_radialhoopPartA(i)=-1*K(i,n)*radial_axis(counter)^(m(i,n)-1);
      segma_radialaxialPartA(i)=K(i,n)*(g(i,n))*radial_axis(counter)^(m(i,n)-1);
      segma_hoopaxialPartA(i)=-1*K(i,n)*(g(i,n))*radial_axis(counter)^(m(i,n)-1);
```

```
   end
   %stresses
   segma_radial(counter)=kx*sind(alfa)*(sum(segma_radialPartA(:))+mu(1,n)*radial_axis(counter));

segma_hoop(counter)=kx*sind(alfa)*(sum(segma_hoopPartA(:))+3*mu(1,n)*radial_axis(counter));
   segma_radialhoop(counter)=kx*cosd(alfa)*(sum(segma_radialhoopPartA(:))-
mu(1,n)*radial_axis(counter));

segma_radialaxial(counter)=kx*cosd(alfa)*(sum(segma_radialaxialPartA(:))+mu(2,n)*radial_axis(co
unter));
   segma_hoopaxial(counter)=kx*sind(alfa)*(sum(segma_hoopaxialPartA(:))-
2*mu(2,n)*radial_axis(counter));
   segma_axial(counter)=Ex(n)*(kx*radial_axis(counter)*sind(alfa)-
Sbar13(n)*segma_radial(counter)-Sbar12(n)*segma_hoop(counter)-
Sbar16(n)*segma_hoopaxial(counter));


% strains

stress_vector(:,counter)=[segma_radial(counter);segma_hoop(counter);segma_axial(counter);segma_
hoopaxial(counter);segma_radialaxial(counter);segma_radialhoop(counter)];
   strain_vector(:,counter)=C(:,:,n)*stress_vector(:,counter);

   epslon_radial(counter)=strain_vector(1,counter)*1e6;
   epslon_hoop(counter)=strain_vector(2,counter)*1e6;
   epslon_axial(counter)=strain_vector(3,counter)*1e6;
   gama_hoopaxial(counter)=strain_vector(4,counter)*1e6;
   gama_radialaxial(counter)=strain_vector(5,counter)*1e6;
   gama_radialhoop(counter)=strain_vector(6,counter)*1e6;

   if o==(points_layer+1)
      n=n+1;
      o=0;
   end
    o=o+1;
end

%% Plotting stresses
%
figure(1)
plot(radial_axis,segma_radial,'.','LineWidth',2)
xlabel('Radial position [mm]','FontSize',16)
ylabel('stresses at pos. angle alfa [MPa]','FontSize',16)
xlim([radial_axis(1) radial_axis(max)])
grid on
legend ('radial stress')  %
```

```
figure(2)
plot(radial_axis,segma_hoop,'.','LineWidth',2)
xlabel('Radial position [mm]','FontSize',16)
ylabel('stresses at pos. angle alfa [MPa]','FontSize',16)
xlim([radial_axis(1) radial_axis(max)])
grid on
legend ('hoop stress')  %

figure(3)
plot(radial_axis,segma_axial,'.','LineWidth',2)
xlabel('Radial position [mm]','FontSize',16)
ylabel('stresses at pos. angle alfa [MPa]','FontSize',16)
xlim([radial_axis(1) radial_axis(max)])
grid on
legend ('axial stress')  %

figure(4)
plot(radial_axis,segma_hoopaxial,'.','LineWidth',2)
xlabel('Radial position [mm]','FontSize',16)
ylabel('stresses at pos. angle alfa [MPa]','FontSize',16)
xlim([radial_axis(1) radial_axis(max)])
grid on
legend ('"in-plane" hoop axial shear stress')  %

figure(5)
plot(radial_axis,segma_radialaxial,'.','LineWidth',2)
xlabel('Radial position [mm]','FontSize',16)
ylabel('stresses at pos. angle alfa [MPa]','FontSize',16)
xlim([radial_axis(1) radial_axis(max)])
grid on
legend ('"out-of-plane" radial axial shear stress')  %

figure(6)
plot(radial_axis,segma_radialhoop,'.','LineWidth',2)
xlabel('Radial position [mm]','FontSize',16)
ylabel('stresses at pos. angle alfa [MPa]','FontSize',16)
xlim([radial_axis(1) radial_axis(max)])
grid on
legend ('"out-of-plane" radial hoop shear stress')  %
%}

%% Plotting strains
%
figure(11)
plot(radial_axis,epslon_radial,'.','LineWidth',2)
xlabel('Radial position [mm]','FontSize',16)
ylabel('strains at pos. angle alfa [microstrain] ','FontSize',16)
```

```
xlim([radial_axis(1) radial_axis(max)])
grid on
legend ('radial strain')  %

figure(12)
plot(radial_axis,epslon_hoop,'.','LineWidth',2)
xlabel('Radial position [mm]','FontSize',16)
ylabel('strains at pos. angle alfa [microstrain] ','FontSize',16)
xlim([radial_axis(1) radial_axis(max)])
grid on
legend ('hoop strain')  %

figure(13)
plot(radial_axis,epslon_axial,'.','LineWidth',2)
xlabel('Radial position [mm]','FontSize',16)
ylabel('strains at pos. angle alfa [microstrain] ','FontSize',16)
xlim([radial_axis(1) radial_axis(max)])
grid on
legend ('axial strain')  %

figure(14)
plot(radial_axis,gama_hoopaxial,'.','LineWidth',2)
xlabel('Radial position [mm]','FontSize',16)
ylabel('strains at pos. angle alfa [microstrain]  ','FontSize',16)
xlim([radial_axis(1) radial_axis(max)])
grid on
legend ('"in-plane" hoop axial shear strain')  %

figure(15)
plot(radial_axis,gama_radialaxial,'.','LineWidth',2)
xlabel('Radial position [mm]','FontSize',16)
ylabel('strains at pos. angle alfa [microstrain] ','FontSize',16)
xlim([radial_axis(1) radial_axis(max)])
grid on
legend ('"out-of-plane" radial axial shear strain')  %

figure(16)
plot(radial_axis,gama_radialhoop,'.','LineWidth',2)
xlabel('Radial position [mm]','FontSize',16)
ylabel('strains at pos. angle alfa [microstrain]  ','FontSize',16)
xlim([radial_axis(1) radial_axis(max)])
grid on
legend ('"out-of-plane" radial hoop shear strain')  %
```

C_matrix26022013.m

```
function [C] = C_Matrix26022013(thetaD)
%disp('Layer material is Carbon/epoxy from Hyer');
E1=155e3;   %Megapascal
E2=12.1e3;  %Megapascal
E3=12.1e3;  %Megapascal
G12=4.4e3;  %Megapascal
G13=4.4e3;  %Megapascal
G23=3.2e3;  %Megapascal
nu12=0.248; %no unit
nu13=0.248; %no unit
nu23=0.458; %no unit
%% Main program
betaD=thetaD+90
m=cosd(betaD); %using betaD cardou
n=sind(betaD); %using betaD cardou

%initialization of the matrix
S=zeros(6,6);
T=zeros(6,6);
Sbar=zeros(6,6);
C=zeros(6,6);

% First part: Calculating S[]
S(1,1)=1/E1;
S(1,2)=-nu12/E1;
S(1,3)=-nu13/E1;

S(2,1)=S(1,2);
S(2,2)=1/E2;
S(2,3)=-nu23/E2;

S(3,1)=S(1,3);
S(3,2)=S(2,3);
S(3,3)=1/E3;

S(4,4)=1/G23;
S(5,5)=1/G13;
S(6,6)=1/G12;
S();

%2nd part:Calculating transfer matrix [T]
T(1,1)=m^2;
T(1,2)=n^2;
T(1,6)=2*m*n;
T(2,1)=n^2;
```

```
T(2,2)=m^2;
T(2,6)=-2*m*n;
T(3,3)=1;
T(4,4)=m;
T(4,5)=-n;
T(5,4)=n;
T(5,5)=m;
T(6,1)=-m*n;
T(6,2)=m*n;
T(6,6)=m^2-n^2;
T();

%3rd part:Calculating [Sbar]
%multiply by 0.5
for i=4:6
   for j=1:6
      S(i,j)=0.5*S(i,j);
   end
end
Sbar=T\S*T;
%then multibly by 2
for i=4:6
   for j=1:6
      Sbar(i,j)=2*Sbar(i,j);
   end
end
Sbar;        %for testing

%
%4th part:Calculating [C] which is the rearranged [S] due to Cardeau

C(1,1)=Sbar(3,3);
C(1,2)=Sbar(1,3);
C(1,3)=Sbar(2,3);
C(1,4)=Sbar(3,6);

C(2,1)=C(1,2);
C(2,2)=Sbar(1,1);
C(2,3)=Sbar(1,2);
C(2,4)=Sbar(1,6);

C(3,1)=C(1,3);
C(3,2)=C(2,3);
C(3,3)=Sbar(2,2);
C(3,4)=Sbar(2,6);

C(4,1)=C(1,4);
```

```
C(4,2)=C(2,4);
C(4,3)=C(3,4);
C(4,4)=Sbar(6,6);

C(5,5)=Sbar(4,4);
C(5,6)=Sbar(4,5);

C(6,5)=C(5,6);
C(6,6)=Sbar(5,5);
```

D.2 Program for calculating the material properties contributions

1- Material_Main_Program.m

```
N_layers=2;
%Inputs
E1=155e3;   %Megapascal
E2=12.1e3;  %Megapascal
E3=12.1e3;
G12=4.4e3;  %Megapascal
G13=4.4e3;
G23=3.2e3;  %Megapascal
nu12=0.248; %no unit
nu13=0.248; %no unit
nu23=0.458; %no unit
Douter=60;
thickness_Douter=0.05;
t1_total_thickness=0.5;
%=========================================================================
%main program structure
mat_props(1,1)=E1;
mat_props(2,1)=E2;
mat_props(3,1)=E3;
mat_props(4,1)=G12;
mat_props(5,1)=G13;
mat_props(6,1)=G23;
mat_props(7,1)=nu12;
mat_props(8,1)=nu13;
mat_props(9,1)=nu23;

theta=[0.01,5,10,15,22,25,30,35,40,45,60,75,89.99];
%% acquiring output from Sensitivity_Materials.m
for k=1:length(theta)
   soln_temp=  Sensitivity_Materials(  Douter,theta(k),thickness_Douter,t1_total_thickness,mat_props
);
   layer_soln_theta(k,:,1)=soln_temp(1,:);
   layer_soln_theta(k,:,2)=soln_temp(2,:);
end

layer1_soln=layer_soln_theta(:,:,1);
layer2_soln=layer_soln_theta(:,:,2);
```

```
function [ output_sensitivity_material ] =…
 Sensitivity_Materials( Douter,theta,thickness_Douter,t1_total_thickness,mat_props )
N_layers=2;
delta=0.5;
N_cases=6;
% main program structure
%% making material_plus,material_minus
E1=mat_props(1,1);
E2=mat_props(2,1);
E3=mat_props(3,1);
G12=mat_props(4,1);
G13=mat_props(5,1);
G23=mat_props(6,1);
nu12=mat_props(7,1);
nu13=mat_props(8,1);
nu23=mat_props(9,1);
 control=1;
factor=1+delta;
for i=1:2*N_cases
    if i==N_cases+1
        factor=1-delta;
        control=1;
    end
   switch (control)
          case 1,
              mat_props(1,1)=E1*factor;
              mat_props(2,1)=E2;
              mat_props(3,1)=E3;
              mat_props(4,1)=G12;
              mat_props(5,1)=G13;
              mat_props(6,1)=G23;
              mat_props(7,1)=nu12;
              mat_props(8,1)=nu13;
              mat_props(9,1)=nu23;
          case 2,
              mat_props(1,1)=E1;
              mat_props(2,1)=E2*factor;
              mat_props(3,1)=E3;
              mat_props(4,1)=G12;
              mat_props(5,1)=G13;
              mat_props(6,1)=G23;
              mat_props(7,1)=nu12;
              mat_props(8,1)=nu13;
              mat_props(9,1)=nu23;
          case 3,
              mat_props(1,1)=E1;
              mat_props(2,1)=E2;
```

```
            mat_props(3,1)=E3*factor;
            mat_props(4,1)=G12;
            mat_props(5,1)=G13;
            mat_props(6,1)=G23;
            mat_props(7,1)=nu12;
            mat_props(8,1)=nu13;
            mat_props(9,1)=nu23;
         case 4,
            mat_props(1,1)=E1;
            mat_props(2,1)=E2;
            mat_props(3,1)=E3;
            mat_props(4,1)=G12*factor;
            mat_props(5,1)=G13;
            mat_props(6,1)=G23;
            mat_props(7,1)=nu12;
            mat_props(8,1)=nu13;
            mat_props(9,1)=nu23;
         case 5,
            mat_props(1,1)=E1;
            mat_props(2,1)=E2;
            mat_props(3,1)=E3;
            mat_props(4,1)=G12;
            mat_props(5,1)=G13*factor;
            mat_props(6,1)=G23;
            mat_props(7,1)=nu12;
            mat_props(8,1)=nu13;
            mat_props(9,1)=nu23;
         case 6,
           mat_props(1,1)=E1;
            mat_props(2,1)=E2;
            mat_props(3,1)=E3;
            mat_props(4,1)=G12;
            mat_props(5,1)=G13;
            mat_props(6,1)=G23*factor;
            mat_props(7,1)=nu12;
            mat_props(8,1)=nu13;
            mat_props(9,1)=nu23;
   end

   if i>N_cases
      material_minus(:,control)=mat_props;
   else
      material_plus(:,control)=mat_props;
   end

    control=control+1;
end
```

```
delta_matrix=material_plus-material_minus;
delta_matrix=delta_matrix(1:6,:);
delta_vector= diag(delta_matrix);
%% calling function to obtain solns from
soln_plus=Coef_EI_solns( Douter,theta,thickness_Douter,t1_total_thickness,material_plus );
soln_minus=Coef_EI_solns( Douter,theta,thickness_Douter,t1_total_thickness,material_minus );


%% calculating  dX_dMaterial using Finite Difference
for n=1:N_layers
   dCoef_dMaterial(:,n)=(soln_plus(:,1,n)-soln_minus(:,1,n))./(delta_vector(:,1));
   dEx_dMaterial(:,n)=(soln_plus(:,2,n)-soln_minus(:,2,n))./(delta_vector(:,1));
   dCoef_Ex_dMaterial(:,n)=(soln_plus(:,3,n)-soln_minus(:,3,n))./(delta_vector(:,1));
   dEeff_minus_Ex_dMaterial(:,n)=((soln_plus(:,3,n)-soln_plus(:,2,n))-(soln_minus(:,3,n)-
soln_minus(:,2,n)))./(delta_vector(:,1));
end
dEI_dMaterial(:,1)=(soln_plus(:,4,n)-soln_minus(:,4,n))./(delta_vector(:,1));
%% output
for n=1:N_layers
output_sensitivity_material(n,:)=[dCoef_dMaterial(:,n)',0,0,0,0,...
dEx_dMaterial(:,n)',0,0,0,0,...
dCoef_Ex_dMaterial(:,n)',0,0,0,0,...
dEI_dMaterial',0,0,0,0,...
 dEeff_minus_Ex_dMaterial(:,n)'];
end


function [ output_Coef_EI ] =…
 Coef_EI_solns( Douter,theta,thickness_Douter,t1_total_thickness,material_matrix )
main program structure
%% getting soln and output
x=size(material_matrix);    %size of matrix
N_cases=x(1,2);
for i=1:N_cases
   soln=Cardou_solver_material(
Douter,theta,thickness_Douter,t1_total_thickness,material_matrix(:,i));

   for n=1:N_layers
      output_Coef_EI(i,1,n)=soln(n,3);  %Coefn
      output_Coef_EI(i,2,n)=soln(n,4);  %Exn
      output_Coef_EI(i,3,n)=soln(n,3)*soln(n,4);  %Coefn*Exn

      output_Coef_EI(i,4,n)=soln(3,1);  %EItotal
   end
end
```